DOCTOR OF PHILOSOPHY

Quantum dot-based semiconductor Terahertz transceiver systems

Leyman, Ross

Award date:
2014

Awarding institution:
University of Dundee

DOCTOR OF PHILOSOPHY

Quantum dot-based semiconductor Terahertz transceiver systems

Ross Leyman

2014

University of Dundee

University of Dundee

Doctoral Thesis

Quantum Dot-Based Semiconductor Terahertz Transceiver Systems

Author:
Ross Leyman

Supervisor:
Professor Edik Rafailov

A thesis submitted in fulfilment of the requirements for the degree of Doctor of Philosophy

in the

Photonics and Nanoscience Group
School of Engineering, Physics and Mathematics

January 2014

Declaration of Authorship

I, Ross Leyman, declare that this thesis titled, 'Quantum Dot-Based Semiconductor Terahertz Transceiver Systems' and the work presented in it are my own. I confirm that:

- This work was done wholly or mainly while in candidature for a research degree at this University.
- Where any part of this thesis has previously been submitted for a degree or any other qualification at this University or any other institution, this has been clearly stated.
- Where I have consulted the published work of others, this is always clearly attributed.
- Where I have quoted from the work of others, the source is always given. With the exception of such quotations, this thesis is entirely my own work.
- I have acknowledged all main sources of help.
- Where the thesis is based on work done by myself jointly with others, I have made clear exactly what was done by others and what I have contributed myself.

Signed: _____

Date: _____

"Science isn't about why – it's about why not!"

Cave Johnson, *Portal 2*

UNIVERSITY OF DUNDEE

Abstract

College of Art, Science and Engineering
School of Engineering, Physics and Mathematics

Doctor of Philosophy

Quantum Dot-Based Semiconductor Terahertz Transceiver Systems

by Ross Leyman

Terahertz (THz) technology is still currently a rapidly developing area of research with applications already demonstrated in the fields of biology [1, 2], medicine [2–4], security [5–7], chemical/materials inspection [8–11] and astrophysics [12] to name a few. The diversity of applications which require the generation and measurement of THz or sub-millimeter (sub-mm) electromagnetic (EM) signals is the result of the vast number of chemical elements and compounds which exhibit molecular transitions and vibrational behavior that occur at frequency ranges corresponding to the so-called "THz gap", roughly defined as 0.05-10 THz. The THz gap was named as such because of the relative difficulty in generating and analysing EM waves in this frequency band. This was due to the inherent challenges in generating either electrical signals with response periods below 1 picosecond (ps), or optical signals with wavelengths in the far-infrared (FIR) range. High absorption of THz signals in atmosphere via absorption by molecules such as H_2O also impeded early developments and is a key issue in THz systems even today.

There is now a wide variety of THz system solutions, each of which exhibits a different set of operational advantages and limitations. Arguably, the most well-established THz technique to date is based on the use of photoconductive antennas (PCAs) driven by ultrafast pulsed or dual-wavelength laser systems. This technique is the basis for the work presented in this thesis, which is an investigation into the potential utilisation of quantum dot (QD)-based semiconductor materials and devices in THz systems. This thesis discusses the work carried out in the development of a novel class of PCA devices which were postulated

to enable efficient optical-to-THz signal conversion, whilst also overcoming several major limitations normally exhibited by PCA devices such as limited optical wavelength pumping range and thermal breakdown. To summarise briefly, these issues were addressed by considering: the additional pump absorption energy ranges enabled by the inclusion of multiple bandgap-engineered semiconductor materials and quantum-confined structures; the higher thermal conductivity and hence pump tolerance exhibited by relatively high-quality (low defect) absorption layers; and by simultaneously harnessing the ultrafast charge carrier modulation exhibited by the integrated QDs. Additionally, some work was carried out using QD-based lasers as pump sources, with the initial intention to explore the feasibility of a fully QD-based THz transceiver system and draw some conclusions as to the future potential for ultra-compact or even lab-on-chip THz systems, for example. The outline of the thesis is as follows.

Chapter 1 discusses the development of optoelectronic techniques to date that are relevant to the current state-of-the-art in THz systems engineering. The establishment of various EM signal generation and detection methods are discussed, as well as modern and currently available THz system solutions with particular emphasis on PCA-based techniques. The predominant laser systems which are typically employed as optical pumps in THz systems are described, with some emphasis on laser diodes (LDs) as some of the work presented here is based on such devices. The relevant concepts in ultrafast semiconductor materials engineering are introduced, and the current primary alternative THz systems based on nonlinear crystals (NLCs) are briefly described.

Chapter 2 discusses the material and structural properties of InAs:GaAs QD-based semiconductor heterostructures. In particular, the predominant structure growth method, energy structure engineering and charge carrier control mechanisms are introduced with particular emphasis on their utilisation in LDs, SESAMs and the THz PCAs used in this work. The details of the QD-based semiconductor structures are presented, with some commentary on their potential performance as the active component in efficient THz PCA devices.

Chapter 3 gives an overview of the laser systems used in this work. This includes discussion of the laser driving and control methods for both ultrafast pulsed and continuous wave (CW) multi-wavelength systems. Applicable laser signal characteristics are presented as well as the measurement techniques which are used to

ascertain the suitability of such signals for use as optical pumps in THz systems. Results from setups designed as versatile, and in some cases novel, optical pump systems are presented, with the goal of generating either: sub-ps pulsed optical signals; tunable, narrowband dual- or multi-wavelength CW signals; or a 'hybrid' combination of the two regimes. The hybrid configurations were explored as the demonstrable versatility of QD LD devices allowed significant scope for temporal and spectral modulation of the optical output signal(s).

Chapter 4 presents the relevant details in the production and testing of PCA devices for readiness in THz systems. This includes discussion of the QD structures' design with regards to the optical pump signals that are used to drive them. Furthermore, the design and integration of metallic microantennas is presented. Also presented are details of the experimental setups for the generation of THz signals using the laser systems presented in Chapter 3 to drive the PCAs developed in this work.

Chapter 5 presents the main experimental results obtained in testing of optical systems and QD-based PCAs developed for this work. Three different detection methods were used, including: a low-temperature bolometer system; a Golay cell system; and a coherent emission/detection scheme utilising two PCA devices. The pre-calibrated bolometer system was used as the initial reference for THz power measurements, and as a reference for accurate THz power measurement calibration thereafter. Results are presented from tests of systems comprising: LD and Ti:Sapphire laser pumps; QD-based and commercially-available PCA devices for reference; and a range of QD semiconductor structures and microantenna geometries. Preliminary results from long-wavelength CW optical pumping of QD-based PCA devices are presented. THz output powers up to around 1 μW were achieved in 25-layer QD PCAs and the relevant device saturation effects are discussed. Coherent systems were used to characterise the THz frequency performance of QD PCA devices and results of early application in THz time-domain spectroscopy (TDS) systems are presented.

Chapter 6 gives a summary of the work presented in this thesis and the respective conclusions which may be drawn from the results. Advice on the further work may be done in the development of QD-based THz PCAs is given, and the potential future application and directions for QD-based THz transceiver systems is discussed.

Acknowledgements

I would like to acknowledge and thank all the people who have supported me throughout my time working on this project. First and foremost, I would like to thank my supervisor Professor Edik Rafailov for recruiting me for the duration of this project as part of the Photonics and Nanoscience group at the University of Dundee. I have learned a great deal from him in the past few years, and been given so many opportunities to explore the world of academia and to further my own knowledge and skills. His constant guidance and insight has allowed me to pursue my own creative insights in the fascinating field of THz optoelectronics, and to engage with many institutions and researchers in the field – I believe I am (slightly) more experienced now! I would also like to acknowledge the Engineering and Physical Sciences Research Council (EPSRC), UK, for the funding which made this project possible. Additionally, I would like to acknowledge the European Network for EXchange and PRototype Evaluation of photonicS componentS and Optical systems (Nexpresso) program for providing some of the financial and organisational support for the collaborative work with our European partner Innolume GmbH, Germany.

I would like to give thanks to the academic staff of the Electronic Engineering and Physics division at the university both past and present, specifically: Prof. Mervyn Rose for his additional supervision and ongoing support since the time of my MSci degree; Dr Natalia Bazieva for her ongoing support and guidance as investigator on this project; Prof. Gigorii Sokolovskii for his theoretical and experimental advice; Dr Stephen Reynolds for his creative insights and advice; Dr Andrey Dunaev for his interesting advice, musings on Modovan wine culture and for repeatedly testing me with the experimental LAKK-M biophotonic diagnosis equipment; Dr Yury Loika for his conceptual advice and LaTeX wizardry; Dr Yongchang Fan for his technical support and brilliant musings; Dr Ying Ding for his advice on cleanroom practice; and Dr Andrew Hourd for his technical advice. I would also like to thank the technical staff of the department who have advised me throughout my project and been patient with my various requests and mistakes, specifically: Dr Gary Callon; Grant Kydd; Stuart Anthony; Callum Moore; William Henderson; and a special thank you to Martin Kierans for his support with the electron microscope work and for the witty banter.

Additionally, I would like to thank the researchers of various positions and affiliations who have contributed to the work presented here, specifically: Dr Ksenia Fedorova; Dr Mantas Butkus; Tomasz Kruczek; Dr Daniil Nikitichev; Dr Chris Reardon; Dr Sebastian Schulz; Dr Li Chen; Dr Igor Krestnikov; Professor Arunas Krotkus; Juozas Adamonis; Dr Gediminas Molis; and Dr Andrei Gorodetsky. I have had the pleasure of working with many people from many different institutions throughout my studies – my apologies to anyone who I may accidentally have left out. A special thanks goes to Dr David Carnegie for his unflinching gusto in the face of innumerable technical 'challenges' – the achievements made in this work shall be royally celebrated at the next Gatty no doubt...

I would also like to show my sincerest appreciation for the support I have had from my family and friends throughout the ongoing duration of my studies. Firstly I would like to thank my parents, Sandra and Ron, for always being there to give me all the advice (and financial rescue) that I have ever needed. I would like to acknowledge the patience which my fiance, Sarah, has shown throughout my most stressful times. Also, I would like to give a huge thanks to the multitude of close friends who have been there to help keep me sane and remember how to party – you know who you are!

Contents

List of Figures

List of Tables

List Of Equations

Chapter 1:

1.2.1.1 $f_{osc} = \frac{c}{2n_{med}L_{cavity}}$

1.2.1.2 $\delta\tau_p = \frac{\beta}{\delta f}$

1.2.1.3 $P_G(t) = P_p \exp\left(-4ln2\left(\frac{t}{\tau_p}\right)^2\right)$

1.2.1.4 $P_S(t) = P_p sech^2\left(2ln(1+\sqrt{2})\frac{t}{\tau_p}\right)$

1.2.1.5 $P_L(t) = P_p\left(1+\frac{4}{1+\sqrt{2}}\left(\frac{t}{\tau_p}\right)^2\right)^{-2}$

1.2.1.6 $Duty\ cycle \equiv \delta\tau_p f_{rep} = \frac{P_{ave}}{P_p}$

1.2.2.1 $E_{THz}(t) \propto \frac{\delta^2 P}{\delta t^2}$

1.2.2.2 $\tan(\Theta) = n_{THz}/n_{IR}$

1.2.2.3 $\Lambda = \frac{\lambda_{THz}}{n_{IR}} \times cos(\Theta)$

1.2.4.1 $P_{THz} \propto V_{Bias}^2$

1.2.4.2 $P_{THz} \propto P_{Optical}^2$

1.2.4.3 $E_{THz} \propto \frac{\delta J^{real}(t)}{\delta t}$

1.2.4.4 $f_{res} \approx \frac{c}{2\times n_{GaAs}\times L_{dipole}}$

1.2.4.5 $P_i = P_{opt} + 2\sqrt{mP_1P_2}[\cos(2\pi(f_1-f_2)t) + \cos(2\pi(f_2+f_1)t)]$

1.2.4.6 $n(t) = \frac{\eta_e P_{opt}\tau}{hf_{ave}AL_a}\left(1+\frac{2\sqrt{mP_1P_2}\sin(\omega t+\phi)}{P_{opt}\sqrt{1+\omega^2\tau^2}}\right)$

1.2.4.7 $P_\omega = \frac{1}{2}(V_B G_{opt})^2 \frac{R_L}{[1+\omega^2\tau^2][1+(\omega R_L C)^2]}$

Chapter 2:

2.1.0.1 $h_c = \frac{a_S}{2\epsilon}$

2.1.0.2 $\frac{-h^2}{8\pi^2 m}\frac{\delta^2\Psi}{\delta x^2} = (E - V)\,\Psi$

2.1.0.3 $\Psi = A\sin\left(\sqrt{\frac{8\pi^2 mE}{h^2}}x\right) + B\cos\left(\sqrt{\frac{8\pi^2 mE}{h^2}}x\right)$

2.1.0.4 $\sqrt{\frac{8\pi^2 mE}{h^2}}x = n\pi$

2.1.0.5 $E_n = \frac{n^2h^2}{8md^2}$

2.1.0.6 $E_n = \frac{h^2\left(n_x^2+n_y^2+n_z^2\right)}{8md^2}$

2.1.0.7 $\Delta E = \frac{hc}{\lambda} = E_{BG} + \frac{h^2\left(n_x^2+n_y^2+n_z^2\right)}{8m_e^* d^2} + \frac{h^2\left(n_x^2+n_y^2+n_z^2\right)}{8m_h^* d^2}$

2.1.0.8 $\Delta E = \frac{hc}{\lambda} = E_{BG} + \frac{h^2\left(n_x^2+n_y^2+n_z^2\right)}{8m_e^* d^2} + \frac{h^2\left(n_x^2+n_y^2+n_z^2\right)}{8m_h^* d^2} - \frac{e^2}{8r\pi\epsilon}$

2.1.0.9 $\rho(E) = \frac{1}{V}\frac{\delta N}{\delta E}$

Chapter 3

3.2.2.1 $E_{THz} \propto \frac{\delta P(t)}{\delta t}$

Chapter 4:

4.1.3.1 $RL_{input} = 20\log_{10}|S_{11}|$

Chapter 5:

5.1.0.1 $R = R_0\exp(A/T)^{1/2}$

Appendix A:

A.0.0.1 $E_{BG}(x) = 1.425\ eV - x1.501\ eV + x^2 0.436\ eV$

A.0.0.2 $n = \sqrt{A + \frac{B}{1-\left(C\frac{E_{BG,GaAs}}{\lambda E_{BG}(x)}\right)^2}}$

List Of Publications

0.1 Publications in Peer-Reviewed Journals

[1] T. Kruczek, R. Leyman, D. Carnegie, N. Bazieva, G. Erbert, S. Schulz, C. Reardon, and E. U. Rafailov. Continuous wave terahertz radiation from an InAs/GaAs quantum-dot photomixer device. *Applied Physics Letters*, 101 (8):081114–4, 2012.

[2] R. Leyman, N. Bazieva, T. Kruczek, G. S. Sokolovskii, and E. U. Rafailov. Progress in compact room temperature thz radiation sources. *Recent Patents on Signal Processing*, 2(1):12–22, 2012.

[3] R. Leyman, D. I. Nikitichev, N. Bazieva, and E. U. Rafailov. Multimodal spectral control of a quantum-dot diode laser for THz difference frequency generation. *Applied Physics Letters*, 99(17), 2011.

0.2 Conference Contributions

[1] R. Leyman, D. Carnegie, N. Bazieva, K. A. Fedorova, D. Livshits, and E. U. Rafailov. Ultrabroad dual-mode spectral control of a quantum dot laser gain medium. In *3rd EOS Topical Meeting on Terahertz Science & Technology (TST 2012)*, 2012.

[2] R. Leyman, D. Carnegie, N. Bazieva, G. Molis, A. Arlauskas, A. Krotkus, S. Schulz, C. Reardon, E. Clarke, and E. U. Rafailov. Characterisation of InAs:GaAs Quantum Dot-Based Photoconductive THz Antennas. In *IEEE Photonics Conference*, 2013.

[3] R. Leyman, D. Carnegie, N. Bazieva, and E. U. Rafailov. Compact quantum-dot-based terahertz sources. In *SPIE Optics and Photonics*, 2013. **Invited**.

[4] R. Leyman, D. Carnegie, K. A. Fedorova, N. Bazieva, S. Schulz, C. Reardon, E. Clarke, and E. U. Rafailov. Thz emission from quantum dot-based thz antennas pumped by a tunable quantum-dot laser diode. In *European Conference on Lasers and Electro-Optics (CLEO)*, 2013.

[5] R. Leyman, T. Kruczek, N. Bazieva, D. Carnegie, G. Erbert, and E. U. Rafailov. Generation of continuous wave thz radiation from a quantum-dot photomixer device. In *2nd EOS Topical Meeting on Lasers (ETML'11)*, September 2011. **Best Student Presentation award**.

[6] G. Molis, A. Arlauskas, A. Krotkus, R. Leyman, N. Bazieva, and E. Rafailov. Thz emission spectroscopy of self-organized InAs quantum dot ensembles. In *Infrared, Millimeter, and Terahertz Waves (IRMMW-THz), 2012 37th International Conference on*, pages 1–2, 2012. doi: 10.1109/IRMMW-THz.2012.6380164.

[7] E. U. Rafailov, R. Leyman, and N. Bazieva. All quantum-dot based compact THz sources. In *Advanced Laser Technologies International Conference*, Budva, Montenegro, September 2013. **Invited**.

0.3 Authorship in Patents

[1] E. U. Rafailov, R. Leyman, N. Bazieva, and M. Butkus. Ultrafast Semiconductor Lasers As Optical Pump Sources In Terahertz Systems. GB1220460.8.

Abbreviations

ABS	**A**crylonitrile **B**utadiene **S**tyrene
Al	**Al**uminum
AR	**A**nti-**R**eflective
ASOS	**As**ynchronous **O**ptical **S**ampling
CMOS	**C**omplimentary **M**etal-**O**xide-**S**emiconductor
CPS	**Co**planar **S**tripline
DBR	**D**istributed **B**ragg **R**eflector
DC	**D**irect **C**urrent
DFB	**D**istributed **F**eed**b**ack
DFG	**D**ifference **F**requency **G**eneration
DMEM	**D**ulbeccos **M**odified **E**agle **M**edium
DOS	**D**ensity **o**f **S**tates
DWELL	**D**ot in **Well**
EM	**E**lectro**m**agnetic
ES	**E**xcited **S**tate
FFT	**F**ast **F**ourier **T**ransform
FIR	**F**ar-**I**nfra**r**ed
fs	**f**emto**s**econd
GaAs	**Ga**llium **As**enide
GHz	**G**iga**h**ert**z**
GS	**G**round **S**tate
GVD	**G**roup **V**elocity **D**ispersion
HDPE	**H**igh **D**ensity **P**oly**e**thylene

HWP	**H**alf-**W**ave **P**late
HR	**H**ighly-**R**eflective
HRFZ	**H**igh **R**esistivity **F**loat-**Z**one
IF	**I**ntermediate **F**requency
IMPATT	**Imp**act Ionisation **A**valanche **T**ransit-**T**ime
InAs	**In**dium **As**enide
$In_xGa_{1-x}As$	**In**dium **Ga**llium **As**enide
IPA	**I**so**p**ropyl **A**lcohol
IR	**I**nfra**r**ed
LD	**L**aser **D**iode
LHe	**L**iquid **He**lium
LIA	**L**ock-**I**n **A**mplifier
$LiNbO_3$	**Li**thium **N**io**b**ate
LN	**L**iquid **N**itrogen
LT-GaAs	**L**ow-**T**emperature Grown **Ga**llium **As**enide
LT-InGaAs	**L**ow-**T**emperature Grown **In**dium **Ga**llium **As**enide
M-S	**M**etal**-S**emiconductor
MIBK	**M**ethyl **I**so**b**utyl **K**etone
MBE	**M**olecular **B**eam **E**pitaxy
ML	**M**ono**l**ayer
MOCVD	**M**etal**o**rganic **C**hemical **V**apor **D**eposition
MMA	**M**ethyl **M**eth**a**cryllate
NEP	**N**oise-**E**quivalent **P**ower
NLC	**N**on**l**inear **C**rystal
NSL	**N**on-**S**aturable **L**osses
OPO	**O**ptical **P**arametric **O**scillator
PC	**P**hotoconductive
PCA	**P**hoto**c**onductive **A**ntenna
PCS	**P**hoto**c**onductive **S**witch
PG	**P**hoto**g**ap
PL	**P**hoto**l**uminescence

PMMA	**P**oly**m**ethyl **M**eth**a**crylate
PMT	**P**hoto**m**ul**t**iplier
PPLN	**P**eriodically-**P**oled **L**ithium **N**iobate
ps	**P**ico**s**econd
PSU	**P**ower **S**upply **U**nit
PTR	**P**hoto**t**hermo**r**efractive
QCL	**Q**uantum **C**ascade **L**aser
QD	**Q**uantum **D**ot
QPM	**Q**uasi **P**hase-**M**atching
QW	**Q**uantum **W**ell
RTA	**R**apid **T**hermal **A**nneal
RF	**R**adio **F**requency
RHEED	**R**eflection **H**igh **E**nergy **E**lectron **D**iffraction
S-K	**S**transki-**K**rastinow
S-Parameter	**S**cattering**-Parameter**
SEM	**S**canning **E**lectron **M**icroscope
SESAM	**Se**miconductor **S**aturable **A**bsorber **M**irror
SHG	**S**econd **H**armonic **G**eneration
Si	**Si**licon
TEC	**T**hermo**e**lectric **C**ooler
TDS	**T**ime-**D**omain **S**pectroscopy
THz	**T**era**h**ert**z**
Ti	**Ti**tanium
TBWP	**T**ime-**B**and**w**idth **P**roduct
TISE	**T**ime-**I**ndependent **S**chrödinger **E**quation
VBG	**V**olume **B**ragg **G**rating
VECSEL	**V**ertical **C**avity **S**urface **E**mitting **L**aser
WLT	**W**etting **L**ayer **T**hickness
Yb:KGW	**Yb**-doped Potassium **G**adolinium Tungstate

Physical Constants

Speed of Light	c	=	$2.997\ 924\ 58 \times 10^{8}\ \mathrm{ms}^{-1}$ (exact)
Permittivity of Free Space	ϵ_0	=	$8.854\ 187\ 82 \times 10^{-12}\ \mathrm{m}^{-3}\mathrm{kg}^{-1}\mathrm{s}^{-4}\mathrm{A}^{2}$ (exact)
Pi	π	=	3.141 592 65
Planck's Constant	h	=	$6.626\ 069\ 57 \times 10^{-34}\ m^2kg/s$
Elementary electric charge	e	=	$1.602\ 176\ 56 \times 10^{-19}C$

Symbols

a	lattice constant	nm
A	area	m^2
C	capacitance	F
d	potential well width	m
E	energy	W
f	frequency	Hz
G	conductance	Ω^{-1}
h_c	critical epitaxial layer thickness	nm
J	current	A
K	thermal conductivity	W/K/m
L	length	m
m	mass	kg
n	refractive index	
n_x	energy level (x-axis)	
n_y	energy level (y-axis)	
n_z	energy level (z-axis)	
N	number of states	
P	power	W (Js^{-1})
r	distance	m
R	resistance	Ω
S	S-parameter	dB
t	time	s
T	temperature	K

V	voltage	V
x	distance	m
Z	impedance	Ω
β	fitting parameter (TBWP)	
ϵ	epitaxial strain	
ϵ_r	relative permittivity	
Λ	poling period	m
λ	wavelength	m
η_e	external efficiency	$electrons/photon$
Ψ	wave-function	
ρ	density of states	$\mathrm{m}^{-3}eV^{-1}$
ρ_{mat}	material density	kgm^{-3}
τ_p	temporal pulse value	s
$\delta\tau_p$	pulsewidth	s
θ	poling angle	$^\circ$
ϕ	angular phase	rads
ω	angular frequency	rads^{-1}

For Smidge

Chapter 1

Introduction

"If I have seen farther than others, it is because I was standing on the shoulders of giants."

– Albert Einstein

1.1 The Emerging Terahertz Field

The discovery and exploration of EM radiation has been a continuous and widespread scientific endeavour in the 'modern' sense since the early 19^{th} century, with William Herschel's landmark investigation into the different "refrangibility" (now refered to as *refraction*) of visible and infrared (IR) radiation from the sun [13]. These tests were arguably the earliest characterisation of an IR radiation detection system and were based on the refraction of sun light through a glass prism and a set of thermometers placed in different colour bands in the refracted spectrum. The thermal energy imparted to the thermometers in each band was used as a measure of the fractional colour energy, and therefore the spectral power, of the respective wavelength.

In the late 1880's, Heinrich Hertz applied James Clerk Maxwell's theories of electromagnetic waves [14] to his work on the generation and detection of radio waves, leading to the unit of frequency being named as the *Hertz*. His work on electric and radio waves around 60 cm wavelength and the subsequent research

into progressively shorter electrical wavelengths below 1 cm [15] could be considered the earliest efforts to approach the study of THz radiation, or *sub-mm waves*, from EM frequencies *below* the THz gap. Conversely, the ongoing work into IR radiation techniques included development of systems for the identification of heat waves of 0.320 mm (320 μm) wavelength from a quartz mercury arc in 1911 [16] – which represented the first steps into the THz gap from EM frequencies *above* it. It was around this time that the THz gap came to be identified as such, with EM radiation in this range even being described as "artificial or purely products of laboratory manufacture" [17]. Figure 1.1 shows a reproduction of the EM spectrum described in the paper from 1923 that this quote is from and the 'new' unexplored wave region indicated here is, incredibly, still roughly accurate regarding today's limited far-IR and mm-wave technology applicable to the THz gap.

Importantly, Hertz's work into radio wave techniques included the development of relatively simple spark gap generators and antenna devices which became extremely ubiquitous as electric wave sources. A basic circuit schematic is given for the emitter device in Figure 1.2, which is recognisable as the commonly employed "Hertzian dipole antenna". The radiative element in this device is the length of wire which is current-loaded by using the low-power direct current (DC) source and induction coils to pass a high voltage pulse to the wire when the switch is closed. Capacity spheres are used at the wire ends for tuning of the resonant emission frequency. This method is still used today in antenna device design and fabrication, albeit significantly more elaborate now with the ubiquitous use of finely-tuned micro-antennas in integrated circuits. Hertzian dipole physics is an integral part of modern THz antenna design, as is described in Section 1.2.4 and applied later in Section 4.1.2 for this work.

The next main developments in sub-mm-wave technology were made during World War II by British and American scientists. This included the improvement of RADAR detection systems to operating frequencies into the K-band up to around 24 gigahertz (GHz), primarily to improve the spatial resolution of the systems. The efficiency of these systems as a 'real-world' application was reduced considerably by the attenuation of EM signals at the water absorption frequency around 22.3 GHz. This is perhaps the first identification of the major challenge in sub-mm and THz systems of strong absorption during atmospheric propagation,

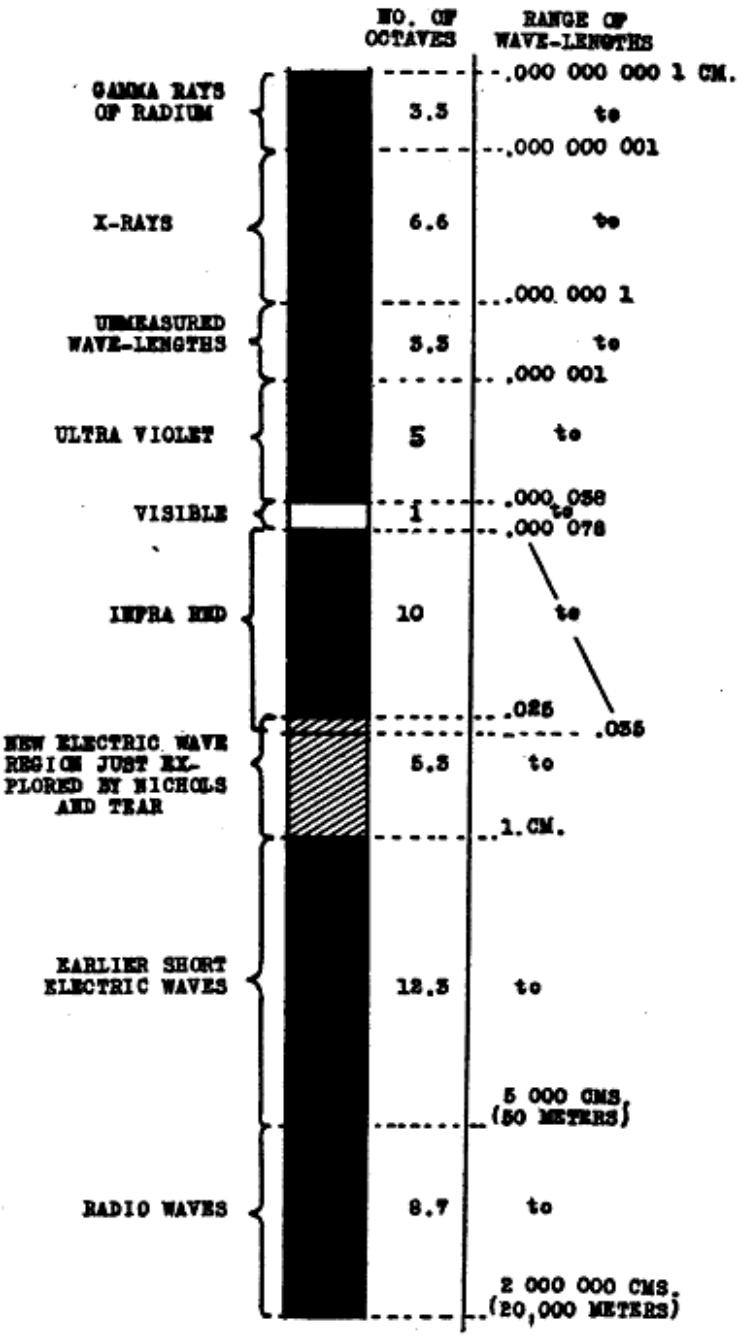

FIGURE 1.1: Early 20^{th}-century representation of the known EM spectrum, indicating the newly-accessed long-IR-wave/THz gap. Reproduced from Nichols, 1923.

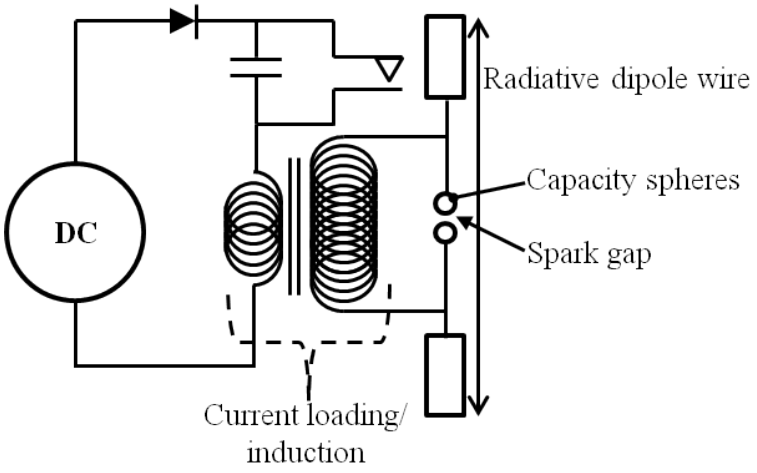

FIGURE 1.2: Circuit schematic of Heinrich Hertz's spark-gap EM signal emission system.

which of course is still a major consideration in THz systems development to this day. Another key development was made around the end of the war with the use of a 'klystron' system to generate high-power cm-wave electrical signals via electron-beam amplification of the 1 cm input signal. These signals were applied to a crystal harmonic generator and the 5 mm (60 GHz) second harmonic signal was used to measure the absorption of oxygen [18], as it was known at this time to strongly absorb 60 GHz waves. Although Beringer was unable to tune the device and map the absorption profile around this frequency, this may be the earliest reported spectral analysis of a chemical conducted in the now commonly recognised THz range.

Sub-cm-wave systems and spectroscopy rapidly became more popular and more versatile in the years following the remarkable demonstrations made using klystron-based systems. Notable methods for the generation and detection of far-IR radiation developed from grating-based spectroscopy and thermopile detectors, which were then made considerably easier with the invention of the Golay cell detector system [19]. As a point of interest, the Golay cell detector has undergone considerable refinement since its first implementation and is now an important tool in modern THz device testing – one such system is also used in this work, as described in Section 5.2.

A further improvement in IR radiation detection was the invention of semiconductor bolometer systems [20]. Although they were required to operate at liquid-helium (LHe) temperatures, they offered signal detectivity around 10–100 times

better than that of the room-temeprature Golay cell systems. They could also operate with much more practical time constants, as the semiconductor detector element could respond to incoming radiation and relax much faster than the gas-based Golay cell system. A bolometer system is also used as part of this work in the testing of novel THz emission devices, as discussed in Section 5.1.

The advent of lasers in the 1950's led to the development of high-power, coherent, sub-mm emission sources such as the hydrogen cyanide gas laser [21] and water vapor laser [22]. These operated at 890 GHz (0.337 mm) and 2.54 THz (0.118 mm), respectively, with multi-Watt peak powers. The disadvantage of these systems was the very narrow spectral linewidth which cannot be tuned, as is still the limitation of gas lasers in THz optoelectronics today. The exciting developments made in the laser field actually slowed the progress in sub-mm optoelectronics somewhat due to the subsequent widespread shift in project funding direction. However, important advances were still being made such as the discovery of the Gunn effect in Gallium Arsenide [23] and the "impact ionization avalanche transit-time" (IMPATT) oscillator [24]. Both of these methods allowed the generation of electrical signals at frequencies up to 35 GHz at this time and have since undergone considerable development. To date, these devices have demonstrated reliable operating frequencies up to around 0.5 THz for both IMPATT [25] and Gunn [26] diodes.

These developments and the work surrounding their inception essentially provided the technical foundations for the research we would now recognise as THz optoelectronics. The most significant advancements in sub-mm-wave and THz research was made shortly after in the fields of ultrafast lasers and semiconductors. Coherent light sources allowed the generation and analysis of CW and pulsed EM signals at the ps and femtosecond (fs) regime, which subsequently enabled the development of ultrafast electronics. The application of ultrafast EM signals to THz optoelectronics, insofar as the relevance to this work, is outlined in the following sections.

1.2 The Development of Modern Terahertz Systems

Both pulsed and CW THz optoelectronics research stems from the same fundamental work into materials which exhibit a component of nonlinear optical response in the THz frequency range, or which can electrically respond over ultrashort (picosecond or less) timescales. There have been many improvements in the efficiency of these systems, as well as several completely different approaches to the naturally difficult problem of generating signals within the THz gap. Predominant devices and methods of generating THz radiation to date include: exploitation of frequency conversion effects in NLCs (Section 1.2.2); emission from gas lasers [21, 22, 27–34]; quantum cascade lasers (QCLs) [35–42]; high frequency microwave electronics such as Gunn diodes and so-called uni-travelling-carrier-photodiodes [43–47]; gyrotrons [48] and pulsed or CW photoconductive THz antennas (Sections 1.2.4.1 and 1.2.4.2). These different approaches each have a range of advantages and limitations, the details of which are generally outwith the scope of this work – a summary of recent advances in research and patents pertaining to these systems is given in [49]. This chapter discusses the two most well-established methods of THz signal generation and detection driven by laser systems: NL crystals and PCAs, with emphasis on PCA techniques because this is the subject of this work.

The figures of merit in THz optoelectronics are typically considered to be the optical-to-THz efficiency, the relative simplicity and dimensions (therefore the general practicality), the operating temperature, the achievable output power and the THz frequency tunability of the system or device. Improvement of these aspects in each THz system is the motivation for research in the field. Early work in THz optoelectronics was based on materials and devices driven by fs optical pump signals generated by laser sources such as a Ti:Al_20_3 (Ti:Sapphire) or ring dye laser, discussed in Section 1.2.1. These systems are now capable of performing TDS and imaging [50] for a range of applications including the security [5–7] and biomedical [1–3] fields and the demand for the further development of devices capable of analysing the information-rich THz spectral region has led to the ongoing development of more compact, efficient and frequency-tunable THz sources. A more in-depth overview of the relatively recent state-of-the-art

in THz spectroscopy and imaging is given in [51], and such methods relevant to this work is discussed in Section 1.2.4.1. The following section outlines the principles of ultrashort laser pulse generation which enabled the development of THz systems.

1.2.1 Ultrafast Lasers

There are several techniques which can be used to generate ultrafast pulsed optical output signals from a laser system, including: gain switching [52], Q-switching [53] and mode-locking [54]. The earliest and most prominent of these is by mode-locking of the laser light within the cavity. This technique is generally based on the spatial and/or temporal separation and recombination of a broad range of laser light frequencies, and is discussed further in the following sections.

1.2.1.1 Mode-Locked Ultrafast Lasers

The initial demonstration of an ultrafast pulsed laser system in 1966, where 40 ps pulses from a mode-locked YAlG:Nd laser was reported [54]. The first demonstration of an ultrafast semiconductor LD was 12 years later when a 20 ps pulsed GaAlAs LD was reported in 1978 [52], and demonstration of 5 ps passively mode-locked pulses from a GaAlAs LD was reported in 1980 [55]. These were arguably the most notable advancements in the acceleration of the ps optoelectronics field in general. Advancement into the sub-ps arena was made with the demonstration of a mode-locked dye laser that generated 200 fs pulses [56], and pulse stretching and compression methods using diffraction gratings and dispersion prisms [57, 58] allowed the generation of even shorter fs optical pulses.

Mode-locking of gas or other solid-state laser types such as the Ti:Sapphire is still conducted today in much the same way as it was around the time of their first demonstration. The laser cavity itself is constructed with a certain length, L_{cavity}, which determines the oscillation frequency of the circulating longitudinal modes as described by the following equation:

$$f_{osc} = \frac{c}{2n_{med}L_{cavity}} \tag{1.2.1.1}$$

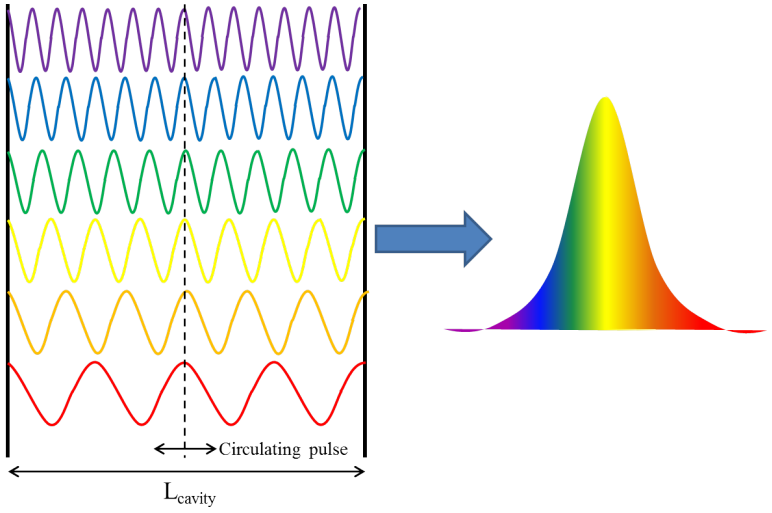

FIGURE 1.3: Principle of mode-locking of multiple oscillating longitudinal laser modes.

where n_{med} is the refractive index of the laser gain medium. Intuitively, this indicates that a longer cavity can support a greater number of oscillating longitudinal modes, and this is sketched in Figure 1.3. It should be noted here that the colours used in the pulse profile on the right of this sketch are simply to clarify that the pulse consists (optically) of the available modes oscillating as shown on the left, and give some idea of the separation of these constituent wavelengths throughout the pulse. This concept is useful in visualising the spectral distribution of optical pulses as discussed later in this section.

It can be seen that each *theoretically* supported longitudinal optical mode which interferes constructively in the cavity oscillates with a frequency difference of f_{osc}, but only those energies supported by the laser gain medium will be absorbed and/or emitted accordingly. This determines the gain bandwidth limits of the laser (range of supported optical modes) and this in turn sets the lower limits on the output pulsewidth and upper limits on energy, as we shall see. In the general case, the temporal overlap of circulating optical cavity modes is supported by the balance between the temporal 'lagging' effects of group velocity dispersion (GVD) and the 'accelerating' effects of self-phase modulation. The maintenance of the ultrashort pulse may be further enhanced by the 'self-starting' effect of Kerr lens mode-locking (KLM) [59], which utilises the inherent self-focussing of the beam due to the variance of refractive index with wavelength in the medium and the corresponding collapse of the modes' temporal spread. If the total bandwidth $\delta f = N \times f_{osc}$ is comprised of N number of modes each separated by an oscillating

frequency f_{osc}, the temporal spread $\delta\tau_p$ of the output pulse is given by Equation 1.2.1.2.

$$\delta\tau_p = \frac{\beta}{\delta f}, \tag{1.2.1.2}$$

where β is assigned here to account for the output pulse profile. The rise and fall times of the pulse determines which β-factor to use. For example, the propagation of a pulse with slowly rising and falling edges such as a saw-tooth 'delivers' the bulk of the pulse energy effectively over a longer time than a top-hat-like pulse profile, even if the full-width half-maximum (FWHM) happened to be the same for both pulses. It should be noted that neither of these pulse profile types will be observed in ultrafast laser pulses – Gaussian ($\beta = 0.4413$), sech^2 ($\beta = 0.315$) or Lorenzian ($\beta = 0.2206$) profiles are generally observed. These pulse profiles are used as 'templates' in the fitting of experimentally obtained laser pulses so that an accurate measurement of the pulse duration $\delta\tau_p$ can be made. The formulas for the approximation of the temporal intensity profile of each pulse type are given as:

$$P_G(t) = P_p \exp\left(-4ln2\left(\frac{t}{\tau_p}\right)^2\right), \tag{1.2.1.3}$$

$$P_S(t) = P_p \,\mathrm{sech}^2\left(2\ln(1+\sqrt{2})\frac{t}{\tau_p}\right), \tag{1.2.1.4}$$

$$P_L(t) = P_p \left(1 + \frac{4}{1+\sqrt{2}}\left(\frac{t}{\tau_p}\right)^2\right)^{-2}, \tag{1.2.1.5}$$

for Gaussian (P_G), sech^2 (P_S) and Lorentzian (P_L) pulses, respectively. P_p is the peak optical power.

The definition of τ_p and corresponding pulse profiles are essentially *ideal case* solutions for the minimum theoretical temporal spread of each pulse profile type. The product of $\delta\tau_p$ and δf is therefore a common measure of the 'purity' of a laser pulse, referred to as the *time-bandwidth product* (TBWP). The sketch in Figure 1.3 indicates some spectral spread in the mode-locked output pulse, although this is not intended as an accurate depiction of the frequency spread as such. An optical pulse in real laser systems consists of a broad range of longitudinal wavelengths which naturally propagate through the medium with different effective refractive indices, which gives rise to GVD. This delay between the long and short wavelengths is referred to as *chirp*.

The principles and management of spectral chirp in laser systems are relevant in this work to the extent that optical pump signals are generally chirp-compensated in real THz systems. In time-domain systems, the pump pulse should ideally be as short as possible to obtain a broad working THz spectral range, described in more detail in Section 1.2.4.1. Mode-locked laser pulses are short because the range of longitudinal modes have been 'locked' in phase-space such that there is a very narrow region of the propagating signal wherein the peaks of (ideally) all modes interfere constructively, and this amplitude peak circulates in the cavity. If there is a temporal offset between long-and short-wavelength mode peaks, τ_p will increase and the peak power will decrease accordingly. The peak power is dependent upon τ_p because optical energy which is restricted (or *well-defined*) in the time domain will correspondingly be amplified (or 'broadened') in the energy domain, according to the uncertainty principle. This leads to the relationship between the laser average optical power P_{ave}, peak power P_p, and 'duty cycle' as given by:

$$Duty\ cycle \equiv \delta\tau_p f_{rep} = \frac{P_{ave}}{P_p}, \tag{1.2.1.6}$$

where f_{rep} is the repetition rate of the circulating pulse in the cavity and the peak power in the pulse is inversely proportional to the pulsewidth as $P_p \approx E/\delta\tau_p$ where E is the total pulse energy.

Mode-locked femtosecond pulses are generated in a Ti:Sapphire laser system by considering these principles, among other design considerations. In this system, a green pump beam is used to optically pump the Ti:Sapphire crystal and, once properly aligned, allows a circulating beam of peak wavelength around 800 nm to be emitted from the crystal output facet. This may then be steered through focussing and compression optics to obtain a mode-locked optical pulse signal with a τ_p which may be finely controlled using a pair of compensation prisms as shown in Figure 1.4.

The first prism diffracts the incoming beam into a spatially separated range of wavelengths with a linearly increasing time-of-flight delay applied across the spectrum (part "A"). The second prism recollimates the diffracted beam, by which point each optical mode will have propagated the same optical path length and been delayed to roughly the same temporal location. This is effectively the actual spectral chirp compensation stage, but the beam then consists of a broad range of spatially *laterally* chirped wavelengths (part "B"). This is compensated

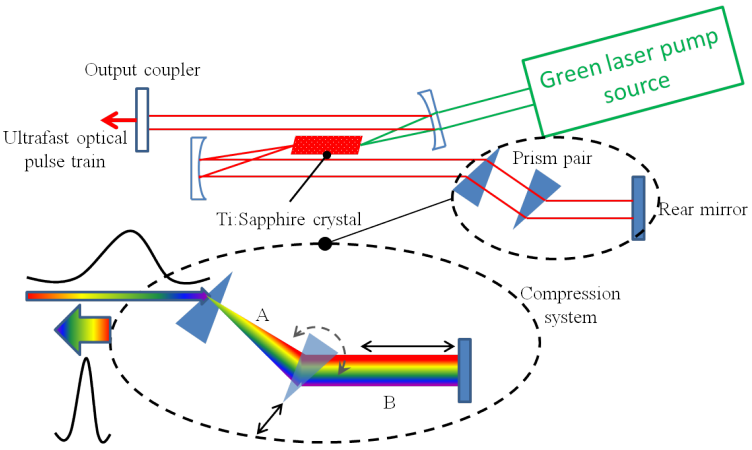

FIGURE 1.4: Basic optical schematic of the Ti:Sapphire laser system.

by retro-reflecting the beam back through the prism pair where they may be extracted as a refocussed, chirp-compensated simultaneous 'bunch' of modes as an ultrashort pulse.

This is now a well-established method for the generation of ultrashort laser pulses, and has been significantly developed and improved for the production of even shorter pulsewidths approaching the few-fs limit (e.g. [60]). The method for mode-locking of semiconductor LDs is somewhat different, and is discussed in the next section.

1.2.1.2 Ultrafast Laser Diodes

Semiconductor diode lasers are relatively very low-cost, ultra-compact and highly efficient light sources which may be implemented in a very broad range of applications. Improvements in their performance regarding ultrashort pulse generation, high beam quality, and high peak- and average-powers mean these devices are extraordinarily interesting and promising candidates for an extended variety of applications in industry and science, ranging from nonlinear biomedical imaging [61]; nano-surgery [62]; materials processing [63]; laser projector displays [64]; and optical fibre communications [65]. They are exceptionally versatile devices, and may be engineered to operate over a range of optical wavelengths and output powers with considerable scope for tunability and manipulation of these parameters by alteration of both the structural and material design, as well as optical system configuration. LDs may be designed with essential components such as

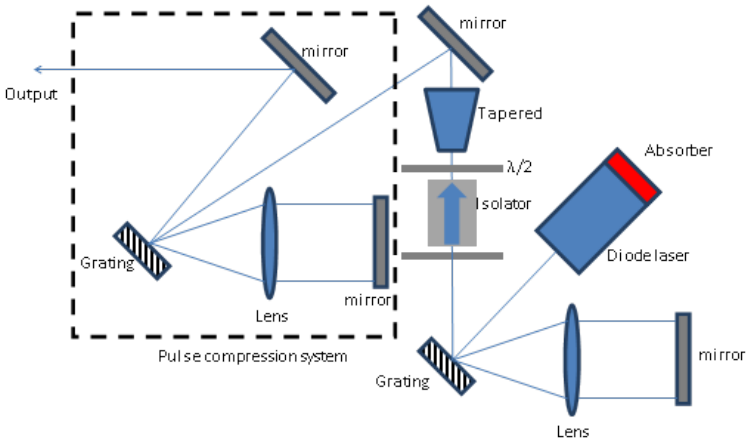

FIGURE 1.5: Optical schematic of a two-section diode laser operating in the pulse regime with a semiconductor optical amplifier and external pulse compressor. Reproduced from Jördens *et al.*, 2008.

the mirrored facets, gain medium, beam waveguide, electrical injection and distributed feedback wavelength tuning all monolithically integrated into the device [66], but may also be configured using external cavity setups [67].

External cavity configuration allows a wide variety of optical wavelength tuning and pulse generation and/or compression techniques to be implemented, and many systems have been developed to allow diode lasers to perform with the required ultrashort pulse durations, output powers and spectral range and bandwidths to achieve levels competitive with established lasers like the Ti:Sapphire. An ideal example is shown in Figure 1.5, where a two-section diode laser is passively mode-locked using the reverse-biased saturable absorber section. The LD is set up in an external cavity using a diffraction grating and an end mirror as both external feedback and tuning elements. This creates the first stage of output pulse lateral chirp. This output is then amplified using a semiconductor tapered amplifier and the resultant high-power output pulse is compensated using an external grating and retro-reflector – analogously to the compression scheme presented for the Ti:Sapphire laser in the previous section. This system allows a compact LD system to operate at around 830 nm wavelength with a pulsewidth around 0.66 ps, average output power of 500 mW (2.5 kW peak) and a resultant achievable working THz bandwidth of 1.4 THz [68]. Spectroscopic bandwidth of THz systems will be discussed later in Section 1.2.4.1.

When operated in the pulse regime, LDs have different design and operation parameters to Ti:Sapphire systems, for example, but operate on many of the

same fundamental principles. An LD initially operated in the CW regime may be used to generate ultrashort pulses in several different ways, including: gain switching [52]; Q-switching [53] and mode-locking [66]. A more in-depth overview and comparison of different semiconductor laser pulse regimes can be found in [69] – this section is focused specifically on mode-locking of LDs as this technique is applied for the experiments conducted in this work.

The primary method of ultrashort mode-locked pulse generation from LDs is by integrating a semiconductor saturable absorber mirror (SESAM) into either the external or internal laser cavity [70]. Saturable absorber mirrors have been used to assist or enhance the mode-locking performance of lasers since the early 1970's [71]. The function of the SESAM in ultrashort pulse management is essentially to act as a time-varying optically-lossy cavity mirror. As the absorber is irradiated by circulating photons in the cavity, electrons are stimulated to the conduction band. This gradually decreases the number of available absorption sites in the medium and the cavity loss is decreased. A "slow" absorber will do this over a time-scale that is long enough to support the formation of an energetic pulse and a net-gain will then be reached as the cavity losses very rapidly decrease. The absorber is then 'saturated' as Pauli blocking effects prevent the excitation of any additional energy states and $\delta a/\delta t = 0$, where a here represents photon absorption within the SESAM active region. $\delta a/\delta t$ then rapidly increases as excited carriers in the absorber thermally relax and then recombine so that once again photon absorption in the SESAM takes place and there is a net cavity loss. This process can occur over very short (ps) timescales, and may be further enhanced in a semiconductor absorber mirror by including dopants and carrier capture sites within the material. This allows further reduction of the carrier recombination time and therefore enables even faster modulation of the forming cavity pulse. This configuration is referred to as *passive* mode-locking as the device effectively modulated it's own ultrashort pulses. The advantage of SESAMs is the additional parameter of electrical control of the response, as a sloped potential may be applied across the absorber thereby further increasing carrier tunnelling, diffusion velocity and capture rate. This is described schematically in Figure 1.6.

The utilisation of electrically-assisted SESAMs in a LD device is classed as *hybrid* mode-locking, as the effect of the absorber mirror may be varied or modulated by the application of the reverse bias across it. The SESAM is typically placed at one

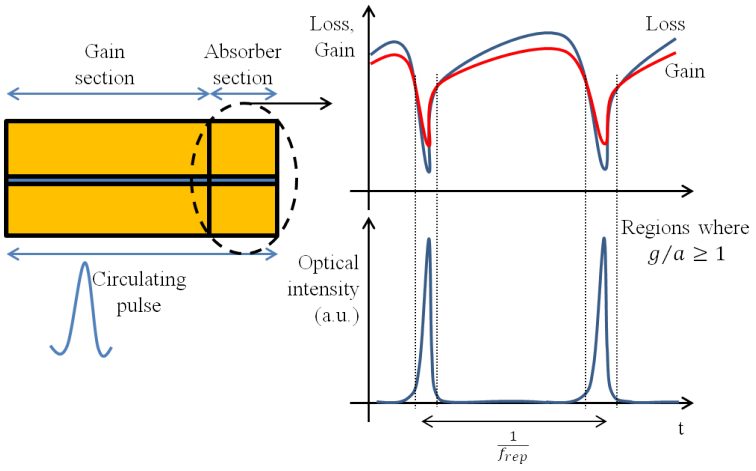

FIGURE 1.6: Schematic of the ultrashort pulse formation process in a SESAM-based mode-locked laser diode. Reproduced from Rafailov *et al.*, 2007.

end of the chip cavity, but may also be placed in the centre, for example, depending on the nature of the required pulse modulation. The example given in Figure 1.5 utilises such a technique with the addition of external GVD compensation and this is now common practise in such setups. Pulses as short as 200 fs have been directly generated using hybrid mode-locked quantum-well (QW)-based LD devices like this, with peak wavelength $\lambda_p = 830\ nm$ and $P_p > 160\ W$ [72]. Regarding longer-wavelength LD devices, passively mode-locked InGaAsP QW LDs have demonstrated pulsewidths $\tau_p < 650\ fs$ at $\lambda_p = 1560\ nm$ [73]. These techniques are employed in this work for the generation of ultrashort pulses from QD LDs as described in Section 2.2.4 and demonstrated in Sections 3.2.2 and 3.4.

1.2.2 Nonlinear Methods

Research in THz optoelectronic systems based on signals modulated via NLCs has seen some considerable advances in device performance, efficiencies and achievable output power. Under optical excitation by an ultrafast optical pulse, an NLC can undergo a change in polarisation within the volume. The NLC can re-emit an EM signal with an field strength proportional to the second derivative of the change in polarisation with respect to time, as described by:

$$E_{THz}(t) \propto \frac{\delta^2 P}{\delta t^2}. \tag{1.2.2.1}$$

The high $\mathcal{X}^{[2]}$ NL susceptibility of crystals such as ZnTe [74, 75] and periodically-poled $LiNbO_3$ (PPLN) [76, 77] allows the optical rectification of incoming EM waves as well as difference frequency generation (DFG) within the medium to achieve THz-range signal emission. The nonlinear susceptibility of such NLCs is used to generate both high power pulsed (via rectification) THz output signals and tunable CW THz output (via DFG, discussed later). In such crystals, phase matching of the pump and generated THz waves becomes important to ensure that the generated THz wave is not interfered with destructively before it can be outcoupled to free space. If a practical degree of phase-matching can be achieved, the generated THz output power may be proportional to the square of the pump power. This may be achieved in several ways, the most predominant of which are: by engineering of the birefringence of the crystal; by quasi-phase-matching (QPM) of propagating waves within the crystal; and by waveguiding.

Schulkin *et al.* developed a THz spectroscopy device (including the design of the device housing) in 2008 which is based on an NLC through which the components of EM polarisation of the pulsed pump and probe signals may be evaluated, and the resultant characterised THz radiation is passed through the target to be analysed which is placed in the housing in a small removable mount [78]. The THz signal which has been modulated by the target is then passed to another NLC for detection and analysis using a coherent THz spectroscopy method which is described in more detail in Section 1.2.4.1. This device has been marketed commercially under the title of the *Mini-Z* [79], and is technically a compact, room-temperature source of THz radiation (with integrated detector) for use in a broad range of THz frequencies (particularly 0.01-5 THz), but this is because the device must be driven by an external pulsed pump source such as a Ti:Sapphire laser and the operating frequency is determined by the temporal pulsewidth of the external pump.

Moloney *et al.* recently developed a highly effective system which utilises externally pumped vertical cavity surface emitting lasers (VECSELs) as the pump sources and a PPLN crystal as the active medium [80, 81]. This was engineered with all of the aforementioned phase-control mechanisms integrated in the design of the crystal and included additional outcoupling measures at the crystal-air interface to further reduce losses. In this setup, several configurations are employed

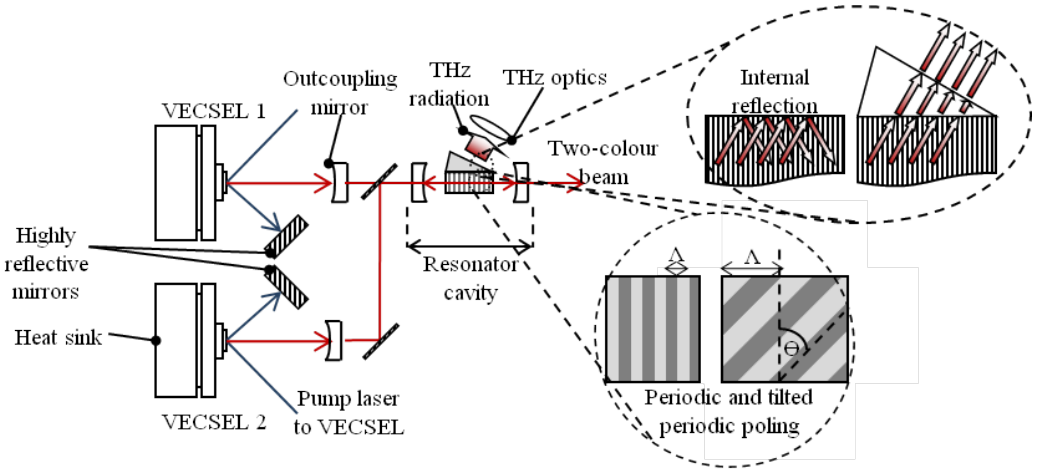

FIGURE 1.7: Optical schematic of a high-power two-VECSEL-pumped periodically-poled $LiNb0_3$-based THz source. Reproduced from Moloney *et al.*, 2010.

in which the VECSELs are pumped externally and operated at slightly offset optical wavelengths within an external cavity which the NLC is located. Figure 1.7 shows one such configuration.

DFG of the VECSEL pumps occurs within the crystal and this beating THz wave is propagated through the crystal volume, enhanced by its phase-matching properties, and is then outcoupled optically. The crystal birefringence (offset of refractive index between ordinarily and extraordinarily polarised propagating waves) is determined by the orientation of the crystal cleavage, and is chosen so to limit as far as possible the phase mismatch between the propagating ordinary and extraordinary EO signals. The crystal is periodically poled along the optical axis by applying a high electrical field across it, thereby creating opposite ferroelectric domains which typically vary periodically every half coherence length between the optical and THz wavevectors. More sophisticated poling profiles have been developed, however, for further enhancement of wavelength-specific propagation of pump and signal wave-vectors [82]. The developers in this case have used this concept to develop a crystal with poling period(s) which correspond to the coherence length of both the pump and generated THz waves. This ensures that the generated nonlinear signal is not dampened by the propagating pump signal, as the phase walk-off between the two signals is periodically 'reset' towards zero. Therefore, the amplitude of the propagating THz signal is increased quadratically as the pump is driven through each successive periodic domain. The associated patents and journal papers which were published include

a discussion on the use of poled domains which vary alternatingly in the pump beam direction through the crystal, as well as the use of tilted and aperiodic poling domains as shown in Figure 1.7(inset). Poling domains tilted at some angle Θ, which corresponds to the direction of the THz wave propagation, helps to compensate for the directional mismatch of the two propagating wavefront types. This also minimises the risk of destructive interference of the IR pump beam and the THz wave, and so the issue of divergence of the IR pump beam and subsequent reduction in the resultant THz output power is avoided. The tilt in the poling domains and the period of the poling is calculated by the following equations:

$$\tan(\Theta) = n_{THz}/n_{IR}, \quad (1.2.2.2)$$

$$\Lambda = \frac{\lambda_{THz}}{n_{IR}} \times cos(\Theta), \quad (1.2.2.3)$$

where n_{THz} and n_{IR} are the refractive indices of the crystal medium for the THz and IR pump waves respectively, λ_{THz} is the free-space THz wavelength and Λ is the poling period. The crystal is structured so to achieve identical effective refractive indices in the nonlinear medium of both the IR pump signal and the THz generated signal, and is done so using known strip, ridge and slab waveguide structuring techniques. To reduce losses due to internal reflection at the crystal-air interface an angled extension to the emission surface is included as shown in Figure 1.7(inset), which significantly improves outcoupling efficiency.

This system is perhaps the most efficient THz radiation source based on an NLC as the emission medium to date. Reported THz output power is in the milli-watt range and is potentially scalable up to the Watt-range. The THz output frequency is also tunable: it is determined by the difference frequency of the two VECSEL optical signals, which is tuned simply by rotating an etalon or coupled diffraction grating to separate or bring together the two permitted pump wavelengths. The system is also relatively cost-effective, as high-power VECSELs and PPLN may be produced comparatively economically, and may have the dimensions suitable for practical, table-top use. However, the optical-THz efficiency is still rather low, with the cavity optical power being around 500 W and strict temperature control of the NLC being required, despite including dopants such as MgO for thermal stability. The THz signal tuning range is also limited by the pre-determined poling of the crystal. Additionally, the requirement for a large,

high-power pump laser system and configuration of at least one VECSEL cavity means the system is overall still relatively complex, bulky, and mechanically sensitive.

1.2.3 Ultrafast Electronic Materials

An effective alternative to THz signal generation via NL methods is by using ultrafast semiconductor materials. Photoconductive (PC) materials which exhibit carrier lifetimes below 1 ps may be optically pumped by ultrashort laser pulses in order to generate a corresponding sub-ps electrical signal, which in turn may be utilised in the generation of THz EM signal generation. Materials traditionally used for this include: radiation-damaged silicon-on-sapphire (RD-SOS) [83–85] and low-temperature-grown GaAs or InGaAs (LT-GaAs [86] and LT-InGaAs [87], respectively) and are used because the growth process integrates lattice defects and carrier trapping sites throughout the bulk, which act to shorten carrier lifetimes and enable ultrafast switching.

GaAs is a well-established semiconductor material in the field of optoelectronics, and it was discovered that by growing the material at low temperature ($\lesssim 300°C$) using molecular beam epitaxy (MBE) with an arsenic overpressure, As interstitial defects were deposited at relatively high densities (up to $\sim 10^{20}/cm^3$) throughout the Ga crystal [88, 89]. Such defects have been shown to shorten carrier lifetimes in LT-GaAs down to around 0.2 ps, whilst still retaining relatively high carrier mobility ($\sim$ 1000 cm^2/Vs) that can be further enhanced by a post-growth annealing step [86, 90]. LT-GaAs also exhibits high performance in other important material requirements for THz signal modulation such as high electrical field (E-Field) breakdown ($\sim 300 - 500$ kV/cm), high dark resistivity ($\geq 10^6$ Ωcm) and high nonlinearity [91, 92]. While effective as an ultrafast PC material, LT-GaAs exhibits various limitations in it's optoelectronic performance, particularly relating to its application as an optically-pumped source of THz radiation. The most predominant limitations of LT-GaAs are the relatively low thermal conductivity and the optical energy range over which it may be pumped and a great deal of development in the field is dedicated to improvements in these parameters.

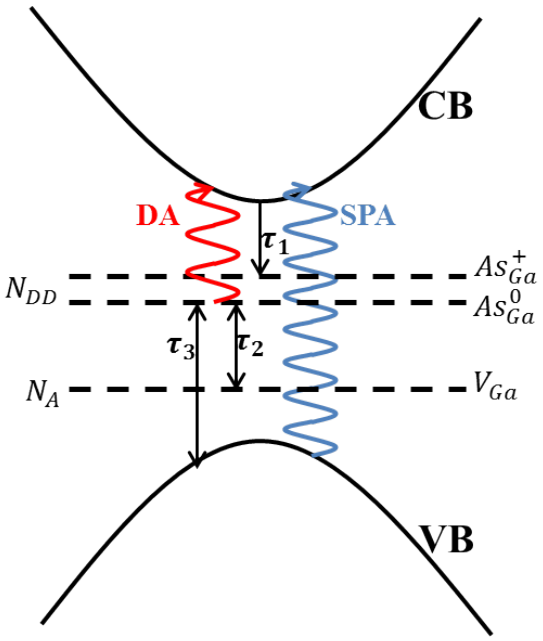

FIGURE 1.8: Illustration of the main energetic excitation and relaxation/recombination processes in LT-GaAs. VB – valence band; CB – conduction band; τ_1–τ_3 represent relaxation times; SPA – single photon absorption; DA – defect absorption; N_{DD} – donor states; N_A – acceptor states; As^+_{Ga} – ionised As defects in Ga; As^0_{Ga} – neutral defect sites; V_{Ga} – Ga valence band energy. Reproduced from von Gabriel, 2007.

The room-temperature energy bandgap of LT-GaAs is $\sim 1.42\ eV$, which corresponds to an optical absorption edge around 870 nm wavelength. This is acceptable for pumping with a Ti:Sapphire laser or GaAs-based LDs, for example, but many laser systems are necessarily developed with longer operating wavelengths towards the telecommunications ranges around 1.3 μm and 1.5 μm. Additionally, the relatively new generation of highly versatile QD-based semiconductor lasers typically operate in the $1.1 < \lambda_p < 1.3\ \mu m$ range where GaAs is effectively transparent and only two-photon absorption is possible. An illustration of excitation and relaxation processes in the optical pumping of LT-GaAs is given in Figure 1.8, but these processes are generally similar to most low-temperature-grown semiconductors and defect/trap-implanted PC materials for this application.

In the general case, the PC material(s) will absorb the pump photon via single photo absorption (SPA) and an electron is promoted from the valence band (VB) to the conduction band (CB). Alternatively, lower photon energies may be absorbed by the material defects (DA) which allows an additional channel of electron promotion to the CB. The electron may then be rapidly trapped by the

ionised As^{+}_{Ga} defect states. The donor states here may finally then be emptied via recombination into either the VB or the V_{Ga} acceptor level. All bandgap-engineered PC materials for ultrafast carrier modulation operate on this general principle, including the relatively novel QD-based PC structures which are presented in this work. This method of charge carrier excitation and trapping forms the basis for the ultrafast PC THz sources described in the following section, which is also the main subject of this work.

1.2.4 Photoconductive Switches and Antennas

In the 1980's, there was rapid development of lasers and semiconductor technology for both CW and pulsed EM wave emission and in 1983 a defining development in modern THz optoelectronics was reported by David Auston, working at Bell Laboratories at the time. Up to this point, he had been an important contributor to the establishment of important optoelectronic methods such as: electronic switching and gating [83]; sampling [84, 93, 94]; and microwave modulation [95]. The work published in 1983 was a study of the ps time-scale photoconductive response of semiconductor materials in transmission lines to ultrashort laser pulses, and is the seminal work for what became known as the "Auston Switch" [96]. The basic concept of this device is shown in Figure 1.9. Note that the circuit model represents the photoconductive gap in the transmission line as both: a time-varying capacitance $q(t)$, somewhat analogous to Hertz's early spark gap generator; and also a time-varying conductance, which is because the incoming gating signal is a time-varying pulse and the conductance of the gap is directly proportional to the pulse energy.

The photoconductive switch (PCS) is now a well-established method of detection of optical signals and conversion to electronic signals. Typically, a PCS is gated by an incident optical signal with photonic energy higher than the energy bandgap of the switch's active semiconductor material. This principle is further developed in the case of ultrafast PCAs, the basis of which is the control of the PCS behaviour via the optical signal, whereby the rapidly changing optical signal is represented as accurately as possible in the electronic response of the PCS. This ultrafast electronic response may then be utilised as a THz signal only if

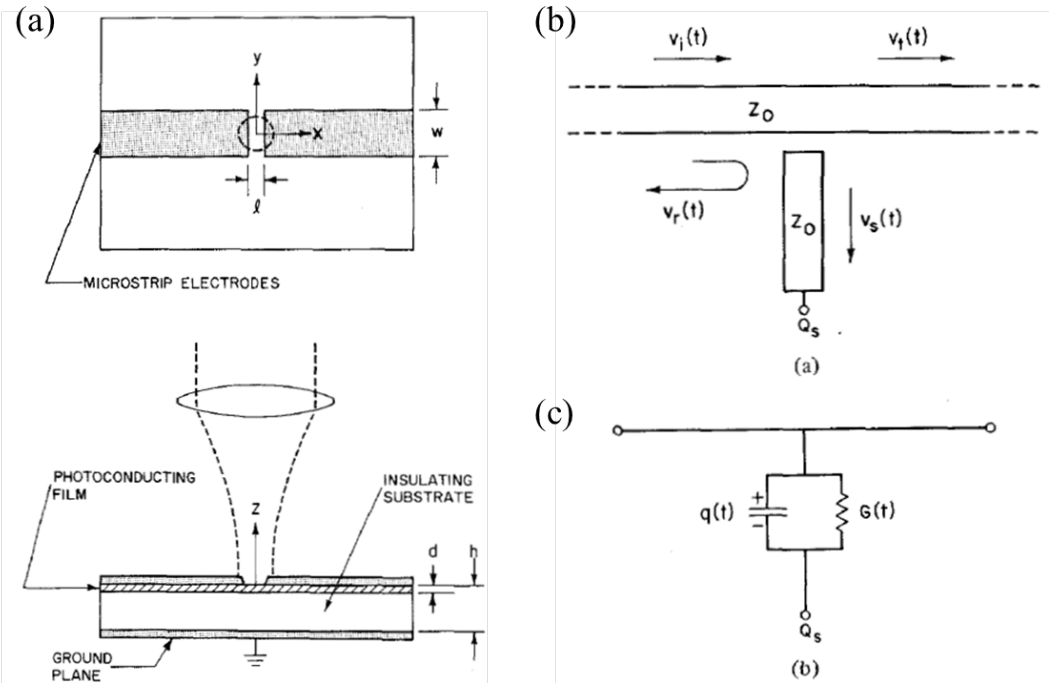

FIGURE 1.9: The Auston Switch concept. (a) is a schematic diagram of a thin photoconductive switch in a transmission line; (b) microstrip electrodes showing incident, reflected and transmitted waves; and (c) is the corresponding equivalent circuit model. l - photoconductive gap length; w - microstrip line width; d - photoconductive semiconductor film depth. Reproduced from Auston, 1983.

the optical and corresponding electronic signal is modulated at a high enough frequency, as discussed in Section 1.2.3.

The seminal research into PC THz devices [97] involved semiconductor materials which were optically pumped by laser sources with high peak power, ultrashort pulsed outputs as discussed above but modern PCA systems are based on both pulsed and CW optical pumping of PCS devices. Broadly speaking, in each case the performance of the THz PCA depends on: the speed and efficiency of the PC material/structure; the spectral and temporal characteristics of the pump beam; and the nature of the integration of antenna (switch) electrodes and E-field with the active PC medium. As the PCA is optically gated, electron-hole pairs are generated and a DC bias is applied across the device electrodes. The bias across the PC gap provides an E-field that can accelerate charge carriers, enhancing carrier velocities and accelerating the rate of carrier capture. This method also allows PCA operation analogously to a traditional Hertzian dipole antenna, as the periodic gating of the PC gap and tuning of the metallic contact

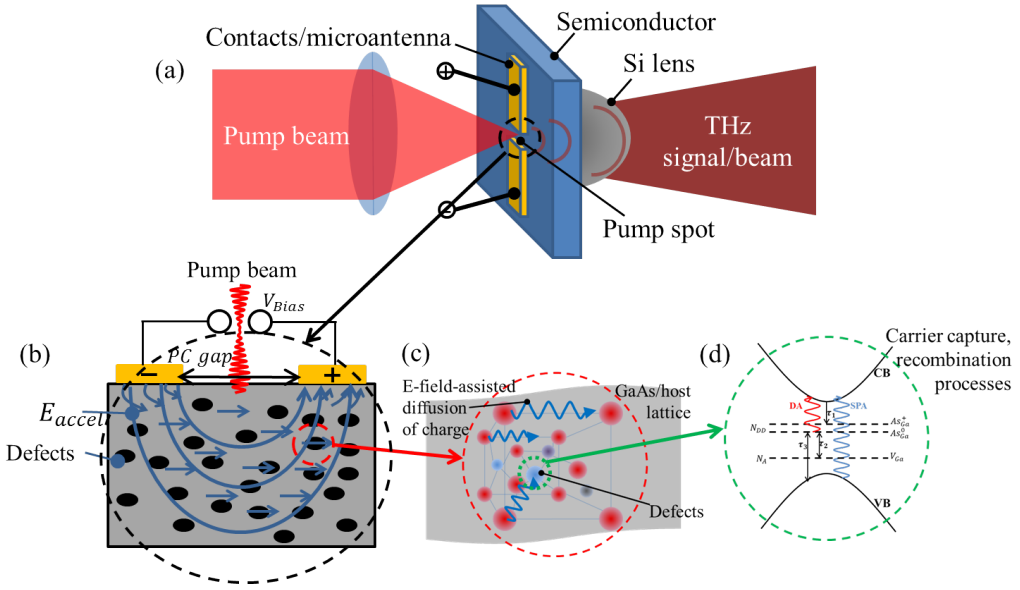

FIGURE 1.10: Schematics of (a) the general principle of PCA operation and (b) generation, diffusion and capture of carriers throughout defective photoconductive switch semiconductor. (c) is a more in-depth view of the diffusion of charge carriers through the host lattice and defect sites, and (d) is a still more in-depth schematic of the excitation and relaxation of carriers throughout available states in the semiconductor material (LT-GaAs here), including the defect trap states.

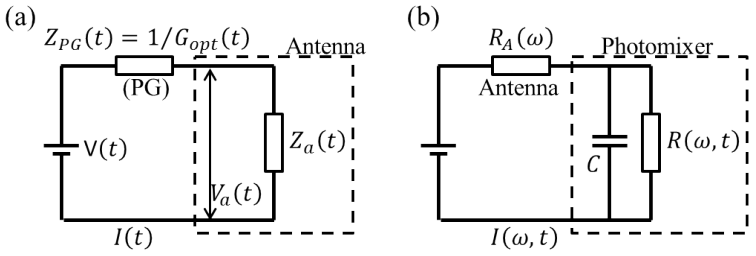

FIGURE 1.11: Equivalent circuit models for (a) wide-gap pulse-regime and (b) fine-gap CW-regime photomixer PCAs, respectively. PG – photo-gap.

features may be thought of as similar in principle to the spark gap generated discussed in Section 1.1. The generated THz wave may be 'captured' by the high dielectric constant PC medium and radiated into free space, optionally assisted by focussing from a Si lens abutted to the 'rear' facet of the PCA structure. This concept is sketched in Figure 1.10. Equivalent circuits for both pulsed and CW PCA devices are also given in Figure 1.11, as discussed in the following sections.

In practice, the optical pump beam is focused to the central gating spot between

the antenna contacts and the time-averaged photoconductance of the PCA increases. As the resistance across the PCA is minimized, the apparent optical beam absorption is maximised and the location of the optical spot is assumed then to be optimal. The PCA conditions may then be further adjusted via the bias level applied across the antenna contacts, which will enhance the E-field within the structure and subsequent carrier movement and capture. This generally increases the observed THz output signal power in accordance with the following equations:

$$P_{THz} \propto V_{Bias}^2, \tag{1.2.4.1}$$

$$P_{THz} \propto P_{Optical}^2, \tag{1.2.4.2}$$

where V_{Bias} is the applied voltage across the PCA contacts and $P_{Optical}$ is the optical pump power. Importantly, this relationship is accurate only until saturation behavior is observed at higher optical pump fluence and/or PCA bias, which is strongly affected by the conditions of the PC material (such as energy level saturation and charge screening) and the nature of the multi-layer PC structure in the active region, where appropriate. In this section, the design principle and performance of the THz PCA is discussed, to the extent that is relevant to the work presented in this thesis.

1.2.4.1 Pulsed and Time-Domain Antenna Systems

The seminal THz optoelectronics research was conducted using fs pulses from a mode-locked laser which switches the device by generating a photocurrent over the fs timescale. This allowed the device to re-emit a corresponding EM pulse in the temporal domain and the Fourier transform of the waveform described a broadband THz signal [97, 98]. This method allows the generation of relatively high-power broadband THz output signals above 100 μW at an optical pump power of several hundred milliwatts, and the bandwidth is determined by the pulsewidth of the pump signal. This output power is 2 orders of magnitude greater than that expected from the current most efficient CW systems. THz PCAs pumped by pulsed laser systems generally do not suffer from thermal breakdown associated with CW-regime devices because the high pump P_p is effective over a timescale too short to initiate the runaway thermal effect. However,

pulsed systems are still generally limited by the need for relatively powerful and bulky ultrafast laser systems and the control of THz bandwidth is rudimentarily based upon the pulse width of said lasers. An excellent comparison of recent state-of-the-art pulsed PCS's and CW operating conditions can be found in [99]. The equivalent circuit of a pulse regime PCA is given in Figure 1.11(a) [100], where the time-varying circuit bias $V(t)$, current $I(t)$ is applied over the circuit's photogap (PG) gate with impedance $Z(t)$ and corresponding conductance $G_{opt}(t)$. The time-varying antenna voltage $V_a(t)$ and impedance $Z_a(t)$ are also indicated and this relatively simple potential divider-type equivalent circuit is considered in the design of pulsed PCAs.

In pulse-regime THz PCA systems operation, an ultrashort gating pulse ($\tau_{pulse} \lesssim 150fs$) enables switching of the PCA over time-scales potentially as low as this duration, depending on the speed of the electronic response of PC material or structure. The emitted THz electric field amplitude is dependent upon the real component of this photocurrent J^{real} as described by the following equation [101]:

$$E_{THz} \propto \frac{\delta J^{real}(t)}{\delta t}. \tag{1.2.4.3}$$

The nature of the photocurrent response is typically ultrafast at the rising edge with a slower decay which is defined by the photocarrier relaxation dynamics of the PC medium, which is sketched in Figure 1.12. If the output pulse waveform can be measured with respect to time, it is then possible to extract frequency information by taking the Fourier transform of the temporal waveform. Additionally, by including a chemical or material sample in the THz beam path or as a reflecting element, the recovered THz waveform can then include spectral information of the sample. This is THz TDS and will be briefly outlined in this section, as this work includes TDS characterisation of PCA devices.

THz spectroscopy uncovers vast layers of valuable information that is almost impossible to extract any other way and is a unique method of determining the spectra of a huge variety of light molecules and chemical compounds. High-resolution molecular THz spectroscopy makes it possible to study very diverse objects, from the biological to the cosmic scales - including the absorption and emission spectra of chemicals and molecular transitions ranging from human tissue to stars, the light from which is composed predominantly of THz radiation [102, 103]. Recent years have brought the practical application of THz radiation

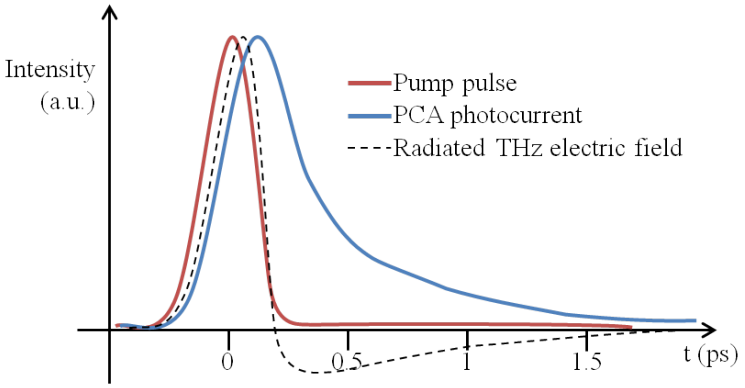

FIGURE 1.12: Sketch of the typical PCA photocurrent response trend to an ultrafast optical pump pulse, and corresponding waveform of the emitted THz field.

far beyond the limits of research laboratories. Radiation in the THz range is non-ionizing, which indicates expansive prospects for its application in medicine – for example, as implemented instead of X-rays in diagnostics. THz TDS and imaging is still a rapidly developing area of medical diagnostics. Despite the fact that the waves of this range are absorbed by water molecules, THz radiation is well established as a diagnostic method in dermatology [104], dentistry [105], and tablet analysis [2].

This technique involves both the generation and detection of THz signals using ultrafast PCAs, in a so-called *coherent* system. The ultrafast pulse pump beam is first split into two halves by a 50:50 beamsplitter. The transmitter (*emitter*) antenna is then excited by the pulse, the appropriate antenna bias is applied and the THz field is emitted. The THz beam is then directed to the rear-facet of the receiver (*detector*), which is also excited at the front facet by the other half of the pump beam. A photocurrent is generated in the detector antenna, which is biased by the electric field of the incoming THz pulse. If the THz pulse and detector optical pump arrive together, the convolution of the pump beam and the THz field effects allows the relative field amplitude to be examined by measurement of the detector antenna photocurrent or E-field. Varying the delay between the THz signal emission and detector pump pulse therefore allows the entire THz waveform to be extracted. It should be noted at this point that a major advantage of pulsed TDS systems is the inherently broadband working THz spectrum which is automatically achieved by using ultrafast signals and fast Fourier transform (FFT) analysis. Further experimental descriptions of such a

system are given in Section 5.3, including demonstrations of this technique for the purposes of testing the devices used in this work.

Considering this, it is intuitive that shorter optical pump pulses allow a broader THz spectral output – limited of course by the antenna photocurrent response time. The peak spectral power in the THz output pulse will be dependent on the overall response of the PCA, not just the pump pulse, which also includes the effects generated by the PCA electrode geometry. Such is the case with antenna devices in general, and resonant frequency characteristics of a THz antenna may be engineered by applying fundamental antenna principles to the microantennas which are used with these devices. Traditionally, simple antenna contact geometries such as co-planar stripline (CPS) and bow-ties are used in the more straightforward PCA tests. CPS antennas tend to be used when characterising the PC material of the PCA as the THz output signal in this case depends primarily on the charge modulation properties of the material, rather than the antenna contact geometry. Some studies have shown that the PC gap of a CPS antenna can slightly influence the PCA peak frequency response [106], for example, but the difference is typically relatively small. Hertzian dipole antennas have also been extensively used to refine the resonance response of PCAs, in both pulsed and CW regimes. A plot showing the calculated resonant frequency f_{res} of dipole antennas of length L_{dipole} over a GaAs-based substrate of refractive index n_{GaAs} is given in Figure 1.13, which is estimated according to the general condition given by the following equation:

$$f_{res} \approx \frac{c}{2 \times n_{GaAs} \times L_{dipole}}. \tag{1.2.4.4}$$

An enlarged view of the 0–3 THz frequency range is given in Figure 1.13(inset) as this is typically the THz spectral region of interest for much of the work presented in this thesis. These principles are introduced here as they are the basis for some of the design methods discussed in Section 4.1. Tuning the frequency response of a pulsed THz system is usually somewhat limited to the confinement of the peak frequency and narrow-band operation is inherently either not possible or inefficient. Narrowband operation may be achieved by implementation of a frequency-domain CW system, as discussed in the following section.

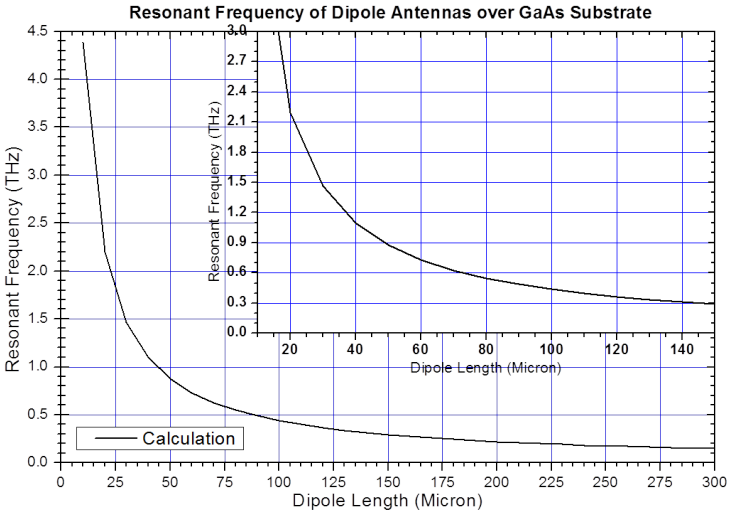

FIGURE 1.13: Theoretical resonance frequency of conductive a dipole antenna over a GaAs-based semiconductor substrate.

1.2.4.2 Continuous Wave and Frequency-Domain Antenna Systems

CW THz systems tend to be more complex than pulsed systems. This is because specific engineering of the laser pump system, the PCA semiconductor and the metallic antenna properties is required, with a wider range of considerations than the pumped system. CW systems are based on the principle of DFG via either optical parametric oscillation/conversion or photoconductive heterodyning (*photomixing*). The DFG method considers the superposition, or *beating*, of two offset optical modes generates a (down-converted) beat signal in the THz frequency range. This is used in both NLC- [107, 108] and PCA-based [109, 110] systems and PCA-based systems will be discussed here as the basis for this work. CW THz systems may also be operated in the coherent emission/detection regime similarly to pulsed systems but with the major advantage of tunability of the narrowband THz frequency which is used. This allows specific frequency-domain applications such as ultrahigh-speed communications and spectroscopy of particular chemicals [111] while enabling the system to avoid particular absorption frequencies of air, for example, which is achieved by tuning of the optical pump beam as discussed in this section.

Signal heterodyning techniques are now mature, and the method of superimposing two oscillating signals in a mixer device for analysis of a down-converted resultant signal has been applied for the purpose of THz DFG in devices based

on sub-ps PC materials for two decades now [99, 109, 112–114]. Instead of mixing incoming radiation with a local oscillator source, the active region in a THz photomixer is based on a material with high absorbance in the IR region and/or high nonlinear susceptibility, which is optically pumped by a dual-wavelength laser beam. The equivalent circuit of a CW regime PCA is given in Figure 1.11(b) [115], where the time and frequency-dependent circuit current $I(\omega, t)$ flows through the antenna with radiation resistance $R_a(\omega)$. The effects of the photomixer gap are modelled in the dashed box as a time- and frequency dependent gap resistance $R(\omega, t)$ and capacitance C which is caused by the very close distance of the electrode features that are typically used. This capacitance is one of the major limitations of CW PCA devices as discussed in the following paragraphs and this equivalent circuit model is always considered in the design of CW PCAs.

The laser signal may be set up by spatially combining two coherent optical beams [113], or by using a single beam generated by a coherent multi-mode source [116–120]. The resultant difference frequency between the two optical modes will be in the THz range and as the PC material absorbs the pump beam it is optoelectronically modulated at this frequency. A more in-depth discussion of the CW optical pumping systems for THz PCA devices specifically used for this work is given in Section 3.3. An example of a tunable dual-mode THz beat pump signal generated as part of this work is shown in Figure 1.14(a), and a sketch of the wave superposition principle is also given in (b). The optical spectra in this figure is obtained by using an ultrabroadband QD LD laser chip in a 'double-Littrow' configuration, discussed in Section 3.3.3.

The optical pump source in PCA-based CW THz systems typically comprise of two narrow-linewidth IR laser modes of wavelengths somewhere between 800-1550 nm. Each mode will have an energy above the bandgap of the photomixer active material, and their longitudinal wavelengths should be offset by say a few nm, depending on the spectral range they are at, whilst maintaining a suitable spatial overlap particularly as they are incident on the photomixer active layer. The modulation of electronic polarity within the active region will switch it electronically essentially between a conductive and non-conductive state, and this THz electrical signal is loaded by the integrated metallic antenna. The design of the photomixer device itself is relatively complex, and a great deal of

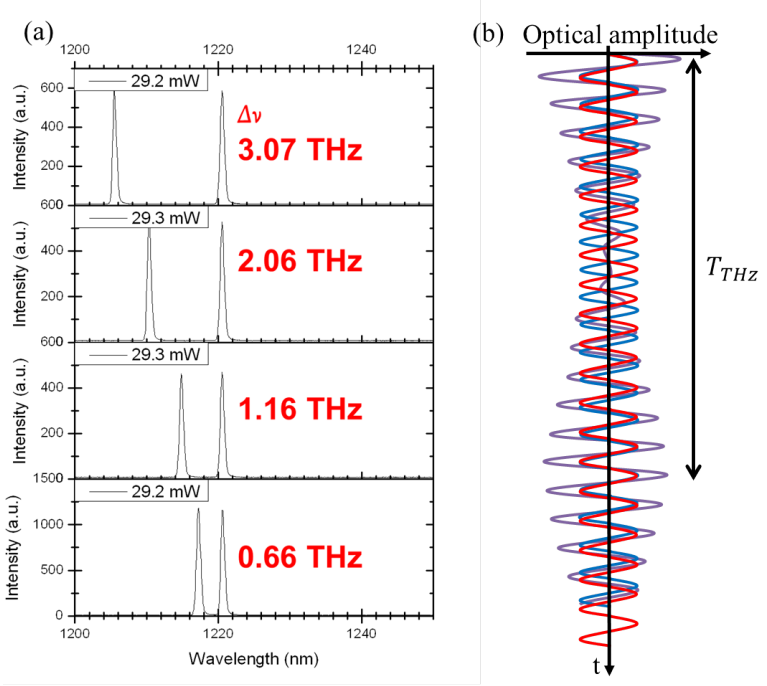

FIGURE 1.14: (a) example of a tunable dual-mode laser pump beam generated from a QD LD; and (b) a sketch of the basic principle of wave superposition for obtaining THz DFG.

work is going into a wide range of optimisations with the aim of improving the optical-THz efficiency of such devices.

The design and operational considerations for such devices begin with the definition of the optical pump beat profile, the power of which is esimated using the following equation:

$$P_i = P_{opt} + 2\sqrt{mP_1P_2}[\cos(2\pi(f_1 - f_2)t) + \cos(2\pi(f_2 + f_1)t)], \qquad (1.2.4.5)$$

where $P_{opt} = P_1 + P_2$ is the time-averaged incident optical power from both modes and m is the spatial mixing/overlap factor for the two modes. This demonstrates one of the advantages of using a single laser for the generation of both pump modes, as m can be fixed towards unity much easier than a combined beam from two separate lasers. The sum frequency power variation expressed in Equation 1.2.4.5, $\cos[2\pi(f_2 + f_1)t]$, may be neglected as this modulation frequency is far beyond the upper frequency response range of the PCA. We can then derive an expression for the time-varying photocarrier density $n(t)$ as in the following

equation [109]:

$$n(t) = \frac{\eta_e P_{opt} \tau}{h f_{ave} A L_a} \left(1 + \frac{2\sqrt{m P_1 P_2} \sin(\omega t + \phi)}{P_{opt} \sqrt{1 + \omega^2 \tau^2}} \right), \tag{1.2.4.6}$$

where η_e is the external quantum efficiency (photocarrier pairs generated per incident photon), τ is the photocarrier recombination time, hf_{ave} is the photon energy, $f_{ave} \equiv f_1 \approx f_2$, $\omega = 2\pi f_{ave}$ is the angular optical mode frequency, $\phi = \arctan(1/\omega\tau)$, L_a is the depth into the PC surface which is optically pumped and A is the PC area which is pumped. We may then consider the difference-frequency output power P_ω when at maximum, achieved only when $m = 1$ and $P_1 = P_2 = P_{opt}/2$, to be in the form described by the following equation:

$$P_\omega = \tfrac{1}{2} (V_B G_{opt})^2 \frac{R_L}{[1 + \omega^2 \tau^2][1 + (\omega R_L C)^2]}, \tag{1.2.4.7}$$

where V_B is the applied PCA bias, R_L is the effective load resistance of the metallic antenna, C is the antenna electrode capacitance and G_{opt} represents the time-varying conductance, which is a function of the photocarrier density. The main results of this expression are that one can expect the THz output power from a CW THz PCA to: vary quadratically with the applied PCA bias and the optical pump power; vary linearly with antenna load resistance (or *radiation resistance*); and to decrease as the carrier lifetime and/or RC-constant of the PCA increases [109]. The form of the THz output trend described by these equations therefore typically depends strongly on the geometry of the metallic antenna integrated with the PC material. This is because very fine features and short PC gaps are normally used for the purpose of increased PC gain and output powers tend to be dominated by electrode capacitance in the now commonly-employed sub-μm-gap finger contact PCAs.

At the heart of CW THz PCA research is also the issue of the growth, blend and structural conditions of ultrafast materials. Research effort is still ongoing to develop and improve materials with optimal characteristics as discussed previously, which must be considered more rigorously than in pulsed systems. This is because the electrical response of the PCA must follow the rapidly oscillating THz beat pump – whereas a PCA in a pulsed regime may rely to some extent on the initial fast response to the pump rising edge to generate the THz signal. CW THz radiation has been generated from materials such as LT-GaAs [109] and

GaAs with incorporated layers of self-assembled quantum-dot (QD) nanoislands [121, 122], as well as narrower bandgap materials such as: LT-GaBiAs [123–125]; InGaAs [126], LT-InGaAs [87, 127, 128], InGaAs with incorporated QDs [129–131] and InGaAs with dopants such as Fe [132]. The inclusion of In or Bi, for example, within the alloy blend allows the material to operate with optical pumps with up to telecoms-range wavelengths, whilst still retaining relatively high gain, and the inclusion of QD gain layers allows an extra degree of wavelength, gain and carrier trapping time tunability as discussed further in Chapter 2.

These materials all operate as effective THz photomixers at room temperature and allow the production of very compact THz sources, but are limited by crucial factors such as thermal breakdown [133] under modest CW pump power ($\sim$ 50 mW, depending on the thermal conductivity of the blend/structure) and quantum efficiency roll-off as the operating frequency increases above 1 THz due to carrier lifetime and RC-time factor constraints. Thermal conductivity of the active layer may be improved by inclusion of Al within the blend or multi-layered structure [134], for example. Heatsinking is improved by running the device at liquid nitrogen temperatures also, which allows the device to be pumped at higher power and thus to achieve higher THz output power [133] but this is not practical for the intended application(s). The quantum efficiency of the active region may be improved in many different ways, most notably by strengthening and further homogenising the electric-field throughout the depth of the active layer(s) using electrodes deposited over the entire active region depth, rather than just on the surface. Roehle *et al.* achieved enhanced THz efficiency of photomixer devices etched in a mesa-structure with contacts laid over various active layer depths [135], for example. Other attempts have been made to confine the optically active photomixer region to the layer surface where the E-field is strongest by using a buried distributed Bragg reflector (DBR) underneath the active layer [134, 136–138] to reflect the pump signal back and forth between the layer surface and the DBR and increase the effective absorption length, but the thermal constraints of the material(s) still apply and output powers are not particularly enhanced any more than with the inclusion of the thermal-conditioning Al-based layers.

Optimisation of the photomixers internal E-field characteristics leads into the investigation of antenna electrode structuring. Not only is the distribution of field strength within the active layer important, but the design of the antenna

electrode structure itself is crucial to its optoelectronic performance and the nature of the THz output signal. Early PC THz antennas were predominantly micron-scale Hertzian dipole antennas with $5 - 10\ \mu m$ PC gaps. This gave limited performance in the CW regime and since then, enhanced THz output has been investigated with the use of broadband-emission, higher power antennas such as self-complimentary spiral [133, 139] and circularly-toothed log-periodic designs [140–142], as well as traditional bow-tie designs. Examples of different broadband, CW microantenna designs used in this work are presented in Section 4.1.2.

Antenna structures like these allow the generation of broadband THz radiation to just beyond 1 THz. Beyond this, there is a signal power fall-off due to carrier lifetime and RC constraints and achievable output powers are typically up to around a few μW. The use of resonant dipole and dual-dipole structures allows higher powers to be generated around the specific respective resonant frequencies up to and beyond 2 THz [143] but this involves careful design and production of more detailed, sub-μm 'interdigitated' contact fingers which span the PC antenna gap. A periodic inductive 'choke' structure separated by a quarter resonant wavelength along the length of the antenna feed line, which can counter-act the capacitive effect of the electrode fingers and enhance the radiation efficiency. Interdigitated finger contacts were produced as part of this work, and presented in Section 4.1.4. The inductive choke features help balance the capacitive effects at the design frequency which otherwise would allow generated THz signals to 'leak' down the bias lines. The interdigitated fingers are normally etched by electron beam lithography, as the finger and inter-finger gap width are generally sub-micron. The reason for this is manifold: to enhance the quantum gain of generated photocurrent and improve coupling to the antenna for re-radiation – photocarriers must travel through the highly inter-atomically inconsistent crystal with very short lifetimes; thinner fingers reduce the amount of pump signal which is blocked over the active area; and capacitive effects are reduced if smaller electrodes are used while working at such a short separation. Sub-μm interdigitated-finger PCA gaps are also implemented at the heart of broadband emission structures for improved gain [140].

1.3 Summary and Conclusions

Presented in this chapter was a brief overview of the developments in technologies used for the generation and detection of EM signals which are relevant to the principles of current THz systems. The discovery and exploration of new regions of the EM spectrum have been introduced, from the first observation of IR radiation itself to the implementation of ultrafast optoelectronic signal emission and detection techniques for sophisticated sub-mm spectroscopic applications. This includes: ultrafast pulse laser systems; nonlinear down-conversion of coherent light in NLCs; ultrafast electronic signal modulation materials; and pulsed and CW PCA devices. PCA-based methods are potentially the most elegant solutions to the challenge of both THz signal generation and detection. This is because they offer inherent output signal parameter configuration such as frequency tunability and function over a range of driving conditions by which the performance of the system is controlled, such as tunable DFG laser pumping. Additionally, complete and tunable THz transceiver systems may be developed using all-semiconductor components operated at low power and room temperature. The current limitations in such systems are signal power – which is relatively low when compared with current record output powers from QCL- [144, 145] and NLC-based [80] THz sources – and optical pump restrictions. Both of these factors were motivations for the work presented in the following chapters.

1.4 References

[1] M. R. Scarfi, M. Romano, R. Di Pietro, O. Zeni, A. Doria, G. P. Gallerano, E. Giovenale, G. Messina, A. Lai, G. Campurra, D. Coniglio, and M. D'Arienzo. THz exposure of whole blood for the study of biological effects on human lymphocytes. *Journal of Biological Physics*, 29(2-3):171–177, 2003.

[2] Markus Schirmer, Makoto Fujio, Masaaki Minami, Jiro Miura, Tsutomu Araki, and Takeshi Yasui. Biomedical applications of a real-time terahertz color scanner. *Biomed. Opt. Express*, 1(2):354–366, Sep 2010. doi: 10.1364/BOE.1.000354. URL http://www.opticsinfobase.org/boe/abstract.cfm?URI=boe-1-2-354.

[3] H. B. Liu, Y. Q. Chen, and X. C. Zhang. Characterization of anhydrous and hydrated pharmaceutical materials with THz time-domain spectroscopy. *Journal of Pharmaceutical Sciences*, 96(4):927–934, 2007.

[4] Y. C. Shen and P. F. Taday. Development and application of terahertz pulsed imaging for nondestructive inspection of pharmaceutical tablet. *IEEE Journal of Selected Topics in Quantum Electronics*, 14(2):407–415, 2008.

[5] J. F. Federici, B. Schulkin, F. Huang, D. Gary, R. Barat, F. Oliveira, and D. Zimdars. THz imaging and sensing for security applications - explosives, weapons and drugs. *Semiconductor Science and Technology*, 20(7):S266–S280, 2005.

[6] A. Giles Davies, Andrew D. Burnett, Wenhui Fan, Edmund H. Linfield, and John E. Cunningham. Terahertz spectroscopy of explosives and drugs. *Materials Today*, 11(3):18–26, 2008.

[7] H. Quast and T. Loffler. Towards Real-Time Active THz Range Imaging for Security Applications. *ICEAA: 2009 International Conference on Electromagnetics in Advanced Applications, Vols 1 and 2*, pages 501–504, 2009. International Conference on Electromagnetics in Advanced Applications (ICEAA 2009) Sep 14-18, 2009 Torino, ITALY.

[8] D. Grischkowsky, Sren Keiding, Martin van Exter, and Ch Fattinger. Far-infrared time-domain spectroscopy with terahertz beams of dielectrics and semiconductors. *J. Opt. Soc. Am. B*, 7(10):2006–2015, 1990.

[9] D. Bigourd, A. Cuisset, F. Hindle, S. Matton, E. Fertein, R. Bocquet, and G. Mouret. Detection and quantification of multiple molecular species in mainstream cigarette smoke by continuous-wave terahertz spectroscopy. *Optics Letters*, 31(15):2356–2358, 2006.

[10] Markus Walther, Bernd Fischer, Alex Ortner, Andreas Bitzer, Andreas Thoman, and Hanspeter Helm. Chemical sensing and imaging with pulsed terahertz radiation. *Analytical and Bioanalytical Chemistry*, 397(3):1009–1017, 2010.

[11] Gianluca Pastorelli, Tanja Trafela, Phillip Taday, Alessia Portieri, David Lowe, Kaori Fukunaga, and Matija Strli? Characterisation of historic plastics

using terahertz time-domain spectroscopy and pulsed imaging. *Analytical and Bioanalytical Chemistry*, 403(5):1405–1414, 2012.

[12] C. E. Groppi and J. H. Kawamura. Coherent Detector Arrays for Terahertz Astrophysics Applications. *Terahertz Science and Technology, IEEE Transactions on*, 1(1):85–96, 2011.

[13] William Herschel. Investigation of the Powers of the Prismatic Colours to Heat and Illuminate Objects; With Remarks, That Prove the Different Refrangibility of Radiant Heat. To Which is Added, an Inquiry into the Method of Viewing the Sun Advantageously, with Telescopes of Large Apertures and High Magnifying Powers. By William Herschel, LL. D. F. R. S. *Philosophical Transactions of the Royal Society of London*, 90:pp. 255–283, 1800. ISSN 02610523. URL http://www.jstor.org/stable/107056.

[14] J. Clerk Maxwell. A Dynamical Theory of the Electromagnetic Field. *Philosophical Transactions of the Royal Society of London*, 155:pp. 459–512, 1865. ISSN 02610523. URL http://www.jstor.org/stable/108892.

[15] W. Möbius. The dispersion of water and ethyl alcohol between 7 and 35mm wavelengths and preliminary test for the application of even shorter electrical waves. *Annalen Der Physik*, 62(12):293–322, June 1920.

[16] H. Rubens and O. von Baeyer. On Extremely Long Waves, emitted by the Quartz Mercury Lamp. *Philosophical Magazine*, 21(125):689–695, May 1911. doi: 10.1080/14786440508637081.

[17] E. F. Nichols and J. D. Tear. Joining the Infra-Red and Electric Wave Spectra. *Proc Natl Acad Sci USA*, 9:211–214, 1923.

[18] Robert Beringer. The Absorption of One-Half Centimeter Electromagnetic Waves in Oxygen. *Phys. Rev.*, 70:53–57, Jul 1946. doi: 10.1103/PhysRev.70.53. URL http://link.aps.org/doi/10.1103/PhysRev.70.53.

[19] Marcel J. E. Golay. Theoretical Consideration in Heat and Infra-Red Detection, with Particular Reference to the Pneumatic Detector. *Review of Scientific Instruments*, 18(5):347–356, 1947. doi: http://dx.doi.org/10.1063/1.1740948. URL http://scitation.aip.org/content/aip/journal/rsi/18/5/10.1063/1.1740948.

[20] H. D. Drew and A. J. Sievers. A 3He-Cooled Bolometer for the Far Infrared. *Appl. Opt.*, 8(10):2067–2071, Oct 1969. doi: 10.1364/AO.8.002067. URL http://ao.osa.org/abstract.cfm?URI=ao-8-10-2067.

[21] H. A. Gebbie, N. W. B. Stone, and F. D. Findlay. A Stimulated Emission Source at 0.34 Millimetre Wave-length. *Nature*, 202(4933):685–685, 1964. 10.1038/202685a0.

[22] D.P. Akitt, W.Q. Jeffers, and P.D. Coleman. Water vapor gas laser operating at 118-microns wavelength. *Proceedings of the IEEE*, 54(4):547–551, 1966. ISSN 0018-9219. doi: 10.1109/PROC.1966.4773.

[23] J. B. Gunn. The discovery of microwave oscillations in gallium arsenide. *Electron Devices, IEEE Transactions on*, 23(7):705–713, 1976. ISSN 0018-9383. doi: 10.1109/T-ED.1976.18474.

[24] Jr. De Loach, B.C. The IMPATT story. *Electron Devices, IEEE Transactions on*, 23(7):657–660, 1976. ISSN 0018-9383. doi: 10.1109/T-ED.1976.18469.

[25] Moumita Mukherjee, Nilratan Mazumder, Sitesh Kumar Roy, and Kushalendu Goswami. Terahertz Frequency Performance of Double Drift IMPATT Diode Based on Opto-Sensitive Semiconductor. In *2007 ASIA PACIFIC MICROWAVE CONFERENCE, VOLS 1-5*, Asia Pacific Microwave Conference-Proceedings, pages 432–435, 2007. ISBN 978-1-4244-0748-4. Asia Pacific Microwave Conference, Bangkok, THAILAND, DEC 11-14, 2007.

[26] H. Eisele. 480 GHz oscillator with an InP Gunn device. *ELECTRONICS LETTERS*, 46(6):422–U62, MAR 18 2010. ISSN 0013-5194. doi: 10.1049/el.2010.3362.

[27] H. Hamster, A. Sullivan, S. Gordon, W. White, and R. W. Falcone. Subpicosecond, Electromagnetic Pulses from Intense Laser-Plasma Interaction. *Physical Review Letters*, 71(17):2725–2728, 1993.

[28] D. J. Cook and R. M. Hochstrasser. Intense terahertz pulses by four-wave rectification in air. *Optics Letters*, 25(16):1210–1212, 2000.

[29] T. Loffler and H. G. Roskos. Gas-pressure dependence of terahertz-pulse generation in a laser-generated nitrogen plasma. *Journal of Applied Physics*, 91(5):2611–2614, 2002.

[30] M. Kress, T. Loffler, S. Eden, M. Thomson, and H. G. Roskos. Terahertz-pulse generation by photoionization of air with laser pulses composed of both fundamental and second-harmonic waves. *Optics Letters*, 29(10):1120–1122, 2004.

[31] T. Bartel, P. Gaal, K. Reimann, M. Woerner, and T. Elsaesser. Generation of single-cycle THz transients with high electric-field amplitudes. *Optics Letters*, 30(20):2805–2807, 2005.

[32] X. Xie, J. M. Dai, and X. C. Zhang. Coherent control of THz wave generation in ambient air. *Physical Review Letters*, 96(7), 2006.

[33] C. D'Amico, A. Houard, M. Franco, B. Prade, A. Mysyrowicz, A. Couairon, and V. T. Tikhonchuk. Conical forward THz emission from femtosecond-laser-beam filamentation in air. *Physical Review Letters*, 98(23):235002, 2007.

[34] K. Y. Kim, J. H. Glownia, A. J. Taylor, and G. Rodriguez. Terahertz emission from ultrafast ionizing air in symmetry-broken laser fields. *Optics Express*, 15(8):4577–4584, 2007.

[35] R. F. Kazarinov and R. A. Suris. Possibility of Amplification of Electromagnetic Waves in a Semiconductor with a Superlattice. *Soviet Physics Semiconductors-USSR*, 5(4):707, 1971.

[36] J. Faist, F. Capasso, D. L. Sivco, C. Sirtori, A. L. Hutchinson, and A. Y. Cho. Quantum Cascade Laser. *Science*, 264(5158):553–556, 1994.

[37] M. Beck, D. Hofstetter, T. Aellen, J. Faist, U. Oesterle, M. Ilegems, E. Gini, and H. Melchior. Continuous wave operation of a mid-infrared semiconductor laser at room temperature. *Science*, 295(5553):301–305, 2002.

[38] R. Kohler, A. Tredicucci, F. Beltram, H. E. Beere, E. H. Linfield, A. G. Davies, D. A. Ritchie, R. C. Iotti, and F. Rossi. Terahertz semiconductor-heterostructure laser. *Nature*, 417(6885):156–159, 2002.

[39] G. Scalari, S. Blaser, J. Faist, H. Beere, E. Linfield, D. Ritchie, and G. Davies. Terahertz emission from quantum cascade lasers in the quantum Hall regime: Evidence for many body resonances and localization effects. *Physical Review Letters*, 93(23), 2004.

[40] M. Troccoli. Room temperature continuous-wave operation of quantum-cascade lasers grown by metal organic vapour phase epitaxy. *Electronics Letters*, 41(19):1059, 2005.

[41] B. S. Williams. Terahertz quantum-cascade lasers. *Nature Photonics*, 1: 517–525, 2007.

[42] M. A. Belkin, Q. J. Wang, C. Pflugl, A. Belyanin, S. P. Khanna, A. G. Davies, E. H. Linfield, and F. Capasso. High-Temperature Operation of Terahertz Quantum Cascade Laser Sources. *IEEE Journal of Selected Topics in Quantum Electronics*, 15(3):952–967, 2009.

[43] T. Ohno, S. Fukushima, Y. Doi, Y. Muramoto, and Y. Matsuoka. Application of uni-traveling-carrier waveguide photodiodes in base stations of a millimeter-wave fiber-radio system, 1999.

[44] Tadao Ishibashi, Tomofumi Furuta, Hiroshi Fushimi, and Hiroshi Ito. Photoresponse characteristics of uni-traveling-carrier photodiodes. In *Proc. SPIE 4283, Physics and Simulation of Optoelectronic Devices IX*, volume 4283, pages 469–479, 2001. doi: 10.1117/12.432597. URL http://dx.doi.org/10.1117/12.432597.

[45] T. Ishibashi, N. Shimizu, S. Kodama, H. Ito, T. Nagatsuma, and T. Furuta. Uni-traveling-carrier photodiodes. In *Tech. Dig. Ultrafast Electronics and Optoelectronics*, pages 83–87, 1997.

[46] T. Ishibashi, T. Furuta, H. Fushimi, S. Kodama, H. Ito, T. Nagatsuma, N. Shimizu, and Y. Miyamoto. InP/InGaAs uni-traveling-carrier photodiodes. *IEICE Transactions on Electronics*, E83C(6):938–949, 2000.

[47] H. Ito, S. Kodama, Y. Muramoto, T. Furuta, T. Nagatsuma, and T. Ishibashi. High-speed and high-output InP-InGaAs unitraveling-carrier photodiodes. *IEEE Journal of Selected Topics in Quantum Electronics*, 10 (4):709–727, 2004.

[48] VL Bratman, Yu K Kalynov, and VN Manuilov. Large-orbit gyrotron operation in the terahertz frequency range. *Physical review letters*, 102(24): 245101, 2009.

[49] R. Leyman, N. Bazieva, T. Kruczek, G. S. Sokolovskii, and E. U. Rafailov. Progress in Compact Room Temperature THz Radiation Sources. *Recent Patents on Signal Processing*, 2(1):12–22, 2012.

[50] Joo-Hiuk Son. Principle and applications of terahertz molecular imaging. *Nanotechnology*, 24(21):214001, 2013. URL http://stacks.iop.org/0957-4484/24/i=21/a=214001.

[51] Peter Uhd Jepsen, David G. Cooke, and Martin Koch. Terahertz spectroscopy and imaging - Modern techniques and applications. *Laser & Photonics Reviews*, 5(1):124–166, 2011.

[52] P.-. Ho, L. A. Glasser, E. P. Ippen, and H. A. Haus. Picosecond pulse generation with a cw GaAlAs laser diode. *Applied Physics Letters*, 33(3):241–242, 1978. doi: http://dx.doi.org/10.1063/1.90312. URL http://scitation.aip.org/content/aip/journal/apl/33/3/10.1063/1.90312.

[53] L.E. Holder, C. Kennedy, L. Long, and George Dube. One joule per Q-switched pulse diode-pumped laser. *Quantum Electronics, IEEE Journal of*, 28(4):986–991, 1992. ISSN 0018-9197. doi: 10.1109/3.135217.

[54] M. DiDomenico, J. E. Geusic, H. M. Marcos, and R. G. Smith. GENERATION OF ULTRASHORT OPTICAL PULSES BY MODE LOCKING THE YAIG: Nd LASER. *Applied Physics Letters*, 8(7):180–183, 1966. doi: http://dx.doi.org/10.1063/1.1754544. URL http://scitation.aip.org/content/aip/journal/apl/8/7/10.1063/1.1754544.

[55] E.P. Ippen, D. J. Eilenberger, and R.W. Dixon. Picosecond pulse generation by passive mode locking of diode lasers. *Applied Physics Letters*, 37(3):267–269, 1980. ISSN 0003-6951. doi: 10.1063/1.91902.

[56] J.-C. Diels, E. Van Stryland, and G. Benedict. Generation and measurement of 200 femtosecond optical pulses. *Optics Communications*, 25(1):93 – 96, 1978. ISSN 0030-4018. doi: http://dx.doi.org/10.1016/0030-4018(78)90096-2. URL http://www.sciencedirect.com/science/article/pii/0030401878900962.

[57] E. Treacy. Optical pulse compression with diffraction gratings. *Quantum Electronics, IEEE Journal of*, 5(9):454–458, 1969. ISSN 0018-9197. doi: 10.1109/JQE.1969.1076303.

[58] O.E. Martinez. Design of high-power ultrashort pulse amplifiers by expansion and recompression. *Quantum Electronics, IEEE Journal of*, 23(8):1385–1387, 1987. ISSN 0018-9197. doi: 10.1109/JQE.1987.1073518.

[59] D. E. Spence, P. N. Kean, and W. Sibbett. 60-fsec pulse generation from a self-mode-locked Ti:sapphire laser. *Opt. Lett.*, 16(1):42–44, Jan 1991. doi: 10.1364/OL.16.000042. URL http://ol.osa.org/abstract.cfm?URI=ol-16-1-42.

[60] Qiang Du, JiangFeng Zhu, Hao Teng, ChenXia Yun, and ZhiYi Wei. Carrier-envelope phase locking of 5 fs amplified Ti:sapphire laser pulse at 1 kHz repetition rate. *Chinese Science Bulletin*, 53(5):671–675, 2008. ISSN 1001-6538. doi: 10.1007/s11434-008-0160-5. URL http://dx.doi.org/10.1007/s11434-008-0160-5.

[61] Masaru Kuramoto, Nobuyoshi Kitajima, Hengchang Guo, Yuji Furushima, Masao Ikeda, and Hiroyuki Yokoyama. Two-photon fluorescence bioimaging with an all-semiconductor laser picosecond pulse source. *Optics Letters*, 32 (18):2726–2728, 2007.

[62] T. Shimada, W. Watanabe, S. Matsunaga, T. Higashi, H. Ishii, K. Fukui, K. Isobe, and K. Itoh. Intracellular disruption of mitochondria in a living HeLa cell with a 76-MHz femtosecond laser oscillator. *Optics Express*, 13(24): 9869–9880, 2005.

[63] Rafael R. Gattass and Eric Mazur. Femtosecond laser micromachining in transparent materials. *Nature Photonics*, 2(4):219–225, 2008.

[64] G. Hollemann, B. Braun, P. Heist, J. Symanowski, U. Krause, J. Kranert, and C. Deter. *High-power laser projection displays*, volume 4294 of *Proceedings of the Society of Photo-Optical Instrumentation Engineers (Spie)*, pages 36–46. 2001. Conference on Projection Displays VII Jan 24-25, 2001 San jose, ca Soc Imaging Sci & Technol; SPIE.

[65] M. Attygalle, A. Nirmalathas, and H. F. Liu. All-optical coding of mode-locked semiconductor laser pulse trains for high bit rate optical communications. *Optics Communications*, 217(1-6):161–167, 2003.

[66] E. U. Rafailov, M. A. Cataluna, and W. Sibbett. Mode-locked quantum-dot lasers. *Nature Photonics*, 1(7):395–401, 2007.

[67] B. Mroziewicz. External cavity wavelength tunable semiconductor lasers - a review. *Opto-Electronics Review*, 16(4):347–366, 2008. ISSN 1230-3402. doi: 10.2478/s11772-008-0045-9. URL http://dx.doi.org/10.2478/s11772-008-0045-9.

[68] C. Jördens, T. Schlauch, M. Li, M. Hofmann, M. Bieler, and M. Koch. All-semiconductor laser driven terahertz time-domain spectrometer. *Applied Physics B: Lasers and Optics*, 93(2):515–520, 2008.

[69] Kam Y. Lau. Short-pulse and high-frequency signal generation in semiconductor lasers. *Lightwave Technology, Journal of*, 7(2):400–419, 1989. ISSN 0733-8724. doi: 10.1109/50.17787.

[70] U. Keller, K.J. Weingarten, F.X. Kartner, D. Kopf, B. Braun, I.D. Jung, R. Fluck, C. Honninger, N. Matuschek, and J. Aus der Au. Semiconductor saturable absorber mirrors (SESAM's) for femtosecond to nanosecond pulse generation in solid-state lasers. *Selected Topics in Quantum Electronics, IEEE Journal of*, 2(3):435–453, 1996. ISSN 1077-260X. doi: 10.1109/2944.571743.

[71] B. K. Garside and T. K. Lim. Laser mode locking using saturable absorbers. *Journal of Applied Physics*, 44(5):2335–2342, 1973. doi: http://dx.doi.org/10.1063/1.1662561. URL http://scitation.aip.org/content/aip/journal/jap/44/5/10.1063/1.1662561.

[72] P.J. Delfyett, L.T. Florez, N. Stoffel, T. Gmitter, N.C. Andreadakis, Y. Silberberg, J.P. Heritage, and G.A. Alphonse. High-power ultrafast laser diodes. *Quantum Electronics, IEEE Journal of*, 28(10):2203–2219, 1992. ISSN 0018-9197. doi: 10.1109/3.159528.

[73] Young-Kai Chen and M.C. Wu. Monolithic colliding-pulse mode-locked quantum-well lasers. *Quantum Electronics, IEEE Journal of*, 28(10):2176–2185, 1992. ISSN 0018-9197. doi: 10.1109/3.159526.

[74] Q. Chen, M. Tani, Z. P. Jiang, and X. C. Zhang. Electro-optic transceivers for terahertz-wave applications. *Journal of the Optical Society of America B-Optical Physics*, 18(6):823–831, 2001.

[75] L. Rui, C. M. Gu, L. R. He, W. Sen, W. Z. Shen, O. Hiroshi, and Q. X. Guo. Generation of terahertz radiation via optical rectification and electro-optic detection in ZnTe crystals. *Acta Physica Sinica*, 53(4):1217–1222, 2004.

[76] K. Kawase, M. Sato, T. Taniuchi, and H. Ito. Coherent tunable THz-wave generation from LiNbO3 with monolithic grating coupler. *Applied Physics Letters*, 68(18):2483–2485, 1996.

[77] Y. S. Lee. Generation of narrow-band terahertz radiation via optical rectification of femtosecond pulses in periodically poled lithium niobate. *Applied Physics Letters*, 76(18):2505, 2000.

[78] B. Schulkin, X. C. Zhang, T. Tongue, J. Xu, and J. Chen. Systems, Methods and Devices for Handling Terahertz Radiation, 2008.

[79] Zomega Mini-Z THz TDS systems, 2013. URL http://www.z-thz.com/index.php?option=com_content&view=article&id=51&Itemid=59.

[80] Maik Scheller, Joe M. Yarborough, Jerome V. Moloney, Mahmoud Fallahi, Martin Koch, and Stephan W. Koch. Room temperature continuous wave milliwatt terahertz source. *Optics Express*, 18(26):27112–27117, 2010.

[81] J. V. Moloney, M. Faliahi, L. Fan, S. W. Koch, M. Koch, M. Scheller, and K. Banake. Terahertz and Millimeter Wave Source, 2010.

[82] J. A. L'Huillier, G. Torosyan, M. Theuer, Y. Avetisyan, and R. Beigang. Generation of THz radiation using bulk, periodically and aperiodically poled lithium niobate - Part 1: Theory. *Applied Physics B-Lasers and Optics*, 86 (2):185–196, 2007.

[83] D. H. Auston. Picosecond Optoelectronic Switching and Gating in Silicon. *Applied Physics Letters*, 26(3):101–103, 1975.

[84] D. H. Auston, A. M. Johnson, P. R. Smith, and J. C. Bean. Picosecond Optoelectronic Detection, Sampling, and Correlation-Measurements in Amorphous-Semiconductors. *Applied Physics Letters*, 37(4):371–373, 1980.

[85] P. R. Smith, D. H. Auston, A. M. Johnson, and W. M. Augustyniak. Picosecond Photoconductivity in Radiation-Damaged Silicon-on-Sapphire Films. *Applied Physics Letters*, 38(1):47–50, 1981.

[86] F. W. Smith, H. Q. Le, V. Diadiuk, M. A. Hollis, A. R. Calawa, S. Gupta, M. Frankel, D. R. Dykaar, G. A. Mourou, and T. Y. Hsiang. Picosecond GaAs-Based Photoconductive Optoelectronic Detectors. *Applied Physics Letters*, 54(10):890–892, 1989.

[87] C. Baker, I. S. Gregory, W. R. Tribe, I. V. Bradley, M. J. Evans, E. H. Linfield, and M. Missous. Highly resistive annealed low-temperature-grown InGaAs with sub-500 fs carrier lifetimes. *Applied Physics Letters*, 85(21): 4965–4967, 2004.

[88] F. W. Smith, A. R. Calawa, C. L. Chen, M. J. Manfra, and L. J. Mahoney. New MBE Buffer Used to Eliminate Backgating in GaAs-MESFETs. *IEEE Electron Device Letters*, 9(2):77–80, 1988.

[89] D. C. Look. Molecular-Beam Epitaxial GaAs Grown at Low-Temperatures. *Thin Solid Films*, 231(1-2):61–73, 1993.

[90] S. Gupta, J. F. Whitaker, and G. A. Mourou. Ultrafast Carrier Dynamics in III-IV Semiconductors Grown by Molecular-Beam Epitaxy at Very Low Substrate Temperatures. *IEEE Journal of Quantum Electronics*, 28 (10):2464–2472, 1992.

[91] David D. Nolte. Semi-insulating semiconductor heterostructures: Optoelectronic properties and applications. *Journal of Applied Physics*, 85(9): 6259–6289, 1999. ISSN 0021-8979. doi: 10.1063/1.370284.

[92] M. Haiml, U. Siegner, F. Morier-Genoud, U. Keller, M. Luysberg, R. C. Lutz, P. Specht, and E.R. Weber. Optical nonlinearity in low-temperature-grown GaAs: Microscopic limitations and optimization strategies. *Applied Physics Letters*, 74(21):3134–3136, 1999. ISSN 0003-6951. doi: 10.1063/1.124086.

[93] Robert A. Lawton and James R. Andrews. Optically strobed sampling oscilloscope. *Instrumentation and Measurement, IEEE Transactions on*, IM-25 (1):56–60, 1976. ISSN 0018-9456. doi: 10.1109/TIM.1976.6312306.

[94] D.H. Auston and P.R. Smith. Picosecond optical electronic sampling: Characterization of high-speed photodetectors. *Applied Physics Letters*, 41(7): 599–601, 1982. ISSN 0003-6951. doi: 10.1063/1.93612.

[95] A. M. Johnson and D. H. Auston. MICROWAVE SWITCHING BY PICOSECOND PHOTOCONDUCTIVITY. *IEEE Journal of Quantum Electronics*, QE11(6):283–287, 1975.

[96] D. H. Auston. Impulse-Response of Photoconductors in Transmission-Lines. *IEEE Journal of Quantum Electronics*, 19(4):639–648, 1983.

[97] P. R. Smith, D. H. Auston, and M. C. Nuss. Subpicosecond Photoconducting Dipole Antennas. *IEEE Journal of Quantum Electronics*, 24(2):255–260, 1988.

[98] J. T. Darrow, B. B. Hu, X. C. Zhang, and D. H. Auston. Subpicosecond Electromagnetic Pulses from Large-Aperture Photoconducting Antennas. *Optics Letters*, 15(6):323–325, 1990.

[99] E. R. Brown. *Advancements in photomixing and photoconductive switching for THz spectroscopy and imaging*, volume 7938. SPIE, 2011.

[100] C Loata von Gabriel. Investigation of low-temperature-grown GaAs photoconductive antennae for continous-wave and pulsed terahertz generation. 2007.

[101] L. Duvillaret, F. Garet, J. F. Roux, and J. L. Coutaz. Analytical modeling and optimization of terahertz time-domain spectroscopy experiments using photoswitches as antennas. *IEEE Journal of Selected Topics in Quantum Electronics*, 7(4):615–623, 2001.

[102] G. Neugebauer, C. A. Beichman, B. T. Soifer, H. H. Aumann, T. J. Chester, T. N. Gautier, F. C. Gillett, M. G. Hauser, J. R. Houck, C. J. Lonsdale, F. J. Low, and E. T. Young. Early Results from the Infrared Astronomical Satellite. *Science*, 224(4644):14–21, 1984. doi: 10.1126/science.224.4644.14. URL http://www.sciencemag.org/content/224/4644/14.abstract.

[103] Peter H. Siegel. THz instruments for space. *IEEE Transactions on Antennas and Propagation*, 55(11):2957–2965, 2007. Times Cited: 30 Part 1.

[104] R. M. Woodward, V. P. Wallace, R. J. Pye, B. E. Cole, D. D. Arnone, E. H. Linfield, and M. Pepper. Terahertz pulse imaging of ex vivo basal cell carcinoma. *Journal of Investigative Dermatology*, 120(1):72–78, 2003.

[105] D. A. Crawley, C. Longbottom, B. E. Cole, C. M. Ciesla, D. Arnone, V. P. Wallace, and M. Pepper. Terahertz pulse imaging: A pilot study of potential applications in dentistry. *Caries Research*, 37(5):352–359, 2003.

[106] Wei Shi, Lei Hou, Zheng Liu, and Thomas Tongue. Terahertz generation from SI-GaAs stripline antenna with different structural parameters. *J. Opt. Soc. Am. B*, 26(9):A107–A112, Sep 2009. doi: 10.1364/JOSAB.26.00A107. URL http://josab.osa.org/abstract.cfm?URI=josab-26-9-A107.

[107] T. Edwards, D. Walsh, M. Spurr, C. Rae, M. Dunn, and P. Browne. Compact source of continuously and widely-tunable terahertz radiation. *Opt. Express*, 14(4):1582–1589, 2006.

[108] Y. Geng, X. Tan, X. Li, and J. Yao. Compact and widely tunable terahertz source based on a dual-wavelength intracavity optical parametric oscillation. *Applied Physics B-Lasers and Optics*, 99(1-2):181–185, 2010.

[109] E. R. Brown, F. W. Smith, and K. A. McIntosh. Coherent Millimeter-Wave Generation by Heterodyne Conversion in Low-Temperature-Grown Gaas Photoconductors. *Journal of Applied Physics*, 73(3):1480–1484, 1993.

[110] S. Matsuura and H. Ito. Generation of CW terahertz radiation with photomixing. *Terahertz Optoelectronics*, 97:157–202, 2005.

[111] S. Preu, G. H. Döhler, S. Malzer, L. J. Wang, and A. C. Gossard. Tunable, continuous–wave terahertz photomixer sources and applications. *Journal of Applied Physics*, 109(6):061301, 2011. doi: http://dx.doi.org/10.1063/1.3552291. URL http://scitation.aip.org/content/aip/journal/jap/109/6/10.1063/1.3552291.

[112] E. R. Brown, K. A. McIntosh, K. B. Nichols, and C. L. Dennis. Photomixing up to 3.8-THz in Low-Temperature-Grown GaAs. *Applied Physics Letters*, 66(3):285–287, 1995.

[113] K. A. McIntosh, E. R. Brown, K. B. Nichols, O. B. McMahon, W. F. DiNatale, and T. M. Lyszczarz. Terahertz photomixing with diode lasers in low-temperature-grown GaAs. *Applied Physics Letters*, 67(26):3844–3846, 1995.

[114] S. Matsuura, M. Tani, and K. Sakai. Generation of coherent terahertz radiation by photomixing in dipole photoconductive antennas. *Applied Physics Letters*, 70(5):559–561, 1997.

[115] Ian S. Gregory, Colin Baker, William R. Tribe, I.V. Bradley, M.J. Evans, E.H. Linfield, Giles Davies, and M. Missous. Optimization of photomixers and antennas for continuous-wave terahertz emission. *Quantum Electronics, IEEE Journal of*, 41(5):717–728, 2005. ISSN 0018-9197. doi: 10.1109/JQE.2005.844471.

[116] T. Hidaka, S. Matsuura, M. Tani, and K. Sakai. CW terahertz wave generation by photomixing using a two-longitudinal-mode laser diode. *Electronics Letters*, 33(24):2039–2040, 1997.

[117] S. A. Zolotovskayaa and N. Daghestani. Stable dual-wavelength operation of InGaAs diode lasers with volume Bragg gratings. *Applied Physics Letters*, 91:171113, 2007.

[118] C. S. Friedrich, C. Brenner, S. Hoffmann, A. Schmitz, I. C. Mayorga, A. Klehr, G. Erbert, and M. R. Hofmann. New two-color laser concepts for THz generation. *IEEE Journal of Selected Topics in Quantum Electronics*, 14(2):270–276, 2008.

[119] S. A. Zolotovskaya, V. I. Smirnov, G. B. Venus, L. B. Glebov, and E. U. Rafailov. Two-Color Output From InGaAs Laser With Multiplexed Reflective Bragg Mirror. *IEEE Photonics Technology Letters*, 21(15):1093–1095, 2009.

[120] R. Leyman, D. I. Nikitichev, N. Bazieva, and E. U. Rafailov. Multimodal spectral control of a quantum-dot diode laser for THz difference frequency generation. *Applied Physics Letters*, 99(17), 2011.

[121] E. Estacio. Strong enhancement of terahertz emission from GaAs in InAs/-GaAs quantum dot structures. *Applied Physics Letters*, 94(23):232104, 2009.

[122] T. Kruczek, R. Leyman, D. Carnegie, N. Bazieva, G. Erbert, S. Schulz, C. Reardon, and E. U. Rafailov. Continuous wave terahertz radiation from an InAs/GaAs quantum-dot photomixer device. *Applied Physics Letters*, 101 (8):081114–4, 2012.

[123] K. Bertulis, A. Krotkus, G. Aleksejenko, V. Pacebutas, R. Adomavicius, G. Molis, and S. Marcinkevicius. GaBiAs: A material for optoelectronic terahertz devices. *Applied Physics Letters*, 88(20):201112–201112–3, 2006. ISSN 0003-6951. doi: 10.1063/1.2205180.

[124] V. Pacebutas, K. Bertulis, A. Biciunas, and A. Krotkus. Low-temperature MBE-grown GaBiAs layers for terahertz optoelectronic applications. *Physica Status Solidi C - Current Topics in Solid State Physics, Vol 6, No 12*, 6(12): 2649–2651, 2009. Krotkus, A Valusis, G Adomavicius, R 15th International Semiconducting and Insulating Materials Conference (SIMC-XV) Jun 15-19, 2009 Vilnius Univ, Vilnius, LITHUANIA.

[125] Andrius Arlauskas, Polina Svidovsky, Klemensas Bertulis, Ramūnas Adomavičius, and Arūnas Krotkus. GaAsBi Photoconductive Terahertz Detector Sensitivity at Long Excitation Wavelengths. *Applied Physics Express*, 5(2): 022601, 2012. doi: 10.1143/APEX.5.022601. URL http://apex.jsap.jp/link?APEX/5/022601/.

[126] J. B. D. Soole and H. Schumacher. Transit-Time Limited Frequency Response of InGaAs MSM Photodetectors. *IEEE Transactions on Electron Devices*, 37(11):2285–2291, 1990.

[127] B. Grandidier, H. J. Chen, R. M. Feenstra, D. T. McInturff, P. W. Juodawlkis, and S. E. Ralph. Scanning tunneling microscopy and spectroscopy of arsenic antisites in low temperature grown InGaAs. *Applied Physics Letters*, 74(10):1439–1441, 1999.

[128] Colin Baker, I. Gregory, M. Evans, W. Tribe, E. Linfield, and M. Missous. All-optoelectronic terahertz system using low-temperature-grown InGaAs photomixers. *Opt. Express*, 13(23):9639–9644, 2005.

[129] M. P. Hanson, D. C. Driscoll, E. Muller, and A. C. Gossard. Microstructure and electronic characterization of InGaAs containing layers of self-assembled ErAs nanoparticles. *Physica E: Low-dimensional Systems and Nanostructures*, 13(2-4):602–605, 2002.

[130] M. Griebel, J. H. Smet, D. C. Driscoll, J. Kuhl, C. A. Diez, N. Freytag, C. Kadow, A. C. Gossard, and K. Von Klitzing. Tunable subpicosecond optoelectronic transduction in superlattices of self-assembled ErAs nanoislands. *Nature Materials*, 2(2):122–126, 2003.

[131] M. Sukhotin, E. R. Brown, A. C. Gossard, D. Driscoll, M. Hanson, P. Maker, and R. Muller. Photomixing and photoconductor measurements on ErAs/InGaAs at 1.55 m. *Applied Physics Letters*, 82(18):3116–3118, 2003.

[132] C. D. Wood, O. Hatem, J. E. Cunningham, E. H. Linfield, A. G. Davies, P. J. Cannard, M. J. Robertson, and D. G. Moodie. Terahertz emission from metal-organic chemical vapor deposition grown Fe:InGaAs using 830 nm to 1.55 μm excitation. *Applied Physics Letters*, 96(19):194104, 2010.

[133] S. Verghese, K. A. McIntosh, and E. R. Brown. Highly tunable fiber-coupled photomixers with coherent terahertz output power. *IEEE Transactions on Microwave Theory and Techniques*, 45(8):1301–1309, 1997.

[134] A. Jackson. *Low-Temperature-Grown GaAs Photomixers Designed for Increased Terahertz Output Power*. PhD thesis, University of California, Santa Barbara, 1999.

[135] H. Roehle, R. J. B. Dietz, H. J. Hensel, J. Bottcher, H. Kunzel, D. Stanze, M. Schell, and B. Sartorius. Next generation 1.5 μm terahertz antennas: mesa-structuring of InGaAs/InAlAs photoconductive layers. *Optics Express*, 18(3):2296–2301, 2010.

[136] E. R. Brown. A photoconductive model for superior GaAs THz photomixers. *Applied Physics Letters*, 75(6):769–771, 1999.

[137] J. Darmo, T. Muller, G. Strasser, K. Unterrainer, and G. Tempea. Terahertz emitter with integrated semiconductor Bragg mirror. *Electronics Letters*, 39(5):460–462, 2003.

[138] R. Faulks. Enhanced Terahertz Receiver Using a Distributed Bragg Reflector Coupled to a Photoconductive Antenna. *IEEE Photonics Technology Letters*, 21(21):1603, 2009.

[139] K. A. McIntosh, E. R. Brown, K. B. Nichols, O. B. McMahon, W. F. DiNatale, and T. M. Lyszczarz. Terahertz measurements of resonant planar antennas coupled to low-temperature-grown GaAs photomixers. *Applied Physics Letters*, 69(24):3632–3634, 1996.

[140] R. Mendis, C. Sydlo, J. Sigmund, M. Feiginov, P. Meissner, and H. L. Hartnagel. Tunable CW-THz system with a log-periodic photoconductive emitter. *Solid-State Electronics*, 48(10-11):2041–2045, 2004. International Semiconductor Device Research Symposium (ISDRS 03) DEC 10-12, 2003 Washington, DC.

[141] C. Sydlo. Characterisation of a circularly-toothed planar logarithmic-periodic antenna for broadband power detection. *Frequenz*, 58(9-10):207, 2004.

[142] R. Mendis, C. Sydlo, J. Sigmund, M. Feiginov, P. Meissner, and H. L. Hartnagel. Spectral characterization of broadband THz antennas by photoconductive mixing: Toward optimal antenna design. *IEEE Antennas and Wireless Propagation Letters*, 4:85–88, 2005.

[143] S. M. Duffy, S. Verghese, K. A. McIntosh, A. Jackson, A. C. Gossard, and S. Matsuura. Accurate modeling of dual dipole and slot elements used with photomixers for coherent terahertz output power. *IEEE Transactions on Microwave Theory and Techniques*, 49(6):1032–1038, 2001.

[144] Martin Brandstetter, Christoph Deutsch, Michael Krall, Hermann Detz, Donald C. MacFarland, Tobias Zederbauer, Aaron M. Andrews, Werner Schrenk, Gottfried Strasser, and Karl Unterrainer. High power terahertz quantum cascade lasers with symmetric wafer bonded active regions. *Applied Physics Letters*, 103(17):171113, 2013. doi: http://dx.doi.org/10.1063/1.4826943. URL http://scitation.aip.org/content/aip/journal/apl/103/17/10.1063/1.4826943.

[145] C. Deutsch. The world's most powerful terahertz quantum cascade laser, 2013. URL http://phys.org/news/2013-10-world-powerful-terahertz-quantum-cascade.html.

Chapter 2

Semiconductor Quantum Dot Materials

The basis of this work is the exploration of basic THz system applications of quantum dot (QD)-based semiconductor materials and devices. This chapter outlines some important and relevant concepts regarding the production, material properties and applications of QDs as implemented in ultrafast optoelectronics and subsequently explores the motivations for this work.

2.1 Growth and Material Characteristics

QD semiconductor materials may be grown using molecular beam epitaxy (MBE). The MBE growth technique is now mature, having been invented in the late 1960's at Bell Laboratories, USA [1, 2], but is still a demanding and complicated science. The MBE system is used for high-precision deposition of binary, tertiary and quaternary blended semiconductor alloys, and is essentially an advanced vacuum deposition system. This is done by ejecting atomic beams of the respective materials from heated 'effusion' cells towards the central target wafer, where they form over the surface in layers potentially as thin as a single atom. The deposition progress may be monitored using methods such as reflection high energy electron diffraction (RHEED).

MBE is now a very effective and widespread method of semiconductor quantum well (QW) structure production [3] due to the precision and configurability of deposition and has been used in the development of the optoelectronics field in general for decades now. The ultra-high degree of uniformity and surface smoothness achieved using MBE deposition is ideal for the production of multi-layer semiconductor heterostructures, as well as pure crystalline bulk. It was also observed in the late 1980's that "nanoclusters" of semiconductor alloys could also be formed by depositing a layer with excessive strain over a different alloy blend [4].

The induced strain ϵ at a lattice-mismatched boundary between two alloys is given by $\epsilon = (a_L - a_S)/a_S$ where a_L is the larger overlayer lattice constant and a_S is the smaller underlayer constant. If grown carefully, the boundary strain may be small enough to allow deposition of the top layer, but large enough to encourage the reordering or 'self-assembling' of nano-scale islands of the top alloy [5]. These quasi-zero-dimensional islands became known as *quantum dots*. This happens because the contraction of InAs atoms in a planar layer into separated cluster sites is energetically favourable and the strain within the dots themselves is significantly reduced.

QDs are formed after the initial *wetting layer* has been deposited over GaAs. The wetting layer blend is then continually deposited up to a few nm depth, during which point the QDs will be formed, after which the GaAs capping layer may be introduced. This encourages the formation of a dilute InGaAs 'surrounding' lattice layer as shown in Figure 2.1. This dilute InGaAs layer surrounding the QDs is then considered the *effective* wetting layer of the structure and is approximated in practical terms as a QW, with QDs within it. As such, this configuration is similar but not identical to the so-called *dot-in-well* (DWELL) configuration, in which QDs are intentionally placed within existing InGaAs and capped with InGaAs [6, 7]. The growth thickness of the wetting layer is limited to the point of formation of lattice dislocations, which occurs when the thickness reaches a scale of roughly $1/\epsilon$. In general, the critical thickness h_c for which coherent lattice growth is possible is given by Equation 2.1.0.1. If the larger a_L overlayer goes beyond the critical thickness, the strain may increase to the point where it is forced to relax by completely dislocating from the underlayer, which would of course make the structure very inefficient in terms of carrier transport

and general optoelectronic performance.

$$h_c = \frac{a_S}{2\epsilon}. \tag{2.1.0.1}$$

The wetting layer is an $In_xGa_{1-x}As$ tertiary blend and has an intermediate lattice constant between the InAs:GaAs boundary alloys. Once the wetting layer thickness (WLT) has been reached, GaAs may once again be deposited over it. This top GaAs *spacer* layer may be grown up to tens of nm's depth, upon which another QD layer may be deposited, and so on. This method is known as the *Stranski-Krastanow* (S-K) growth regime, and these are the production constraints which were considered specifically in the design of materials for the PCA InAs:GaAs QD structures in this work. The wetting layer tertiary blend is limited by these parameters and an Indium content of 15% was used in all structures ($In_{0.15}Ga_{0.85}As$). An alternative method for the creation of InAs QDs within GaAs is to deposit a relatively low volume of InAs over the GaAs seed layer such that the required thickness for QD self-assembly is not reached, after which point multiple further GaAs host and thin InAs layers are deposited over this. This means that S-K growth of the QDs never occurs, but the increasing strain in the multi-layer lattice leads to the necessity for energetic relaxation of the thin InAs layers and QDs are formed within the host lattice without the surrounding wetting layer [8]. This method is known as *sub-monolayer* deposition, as the QD material layer is thinner than that required for self-assembly during their growth. This method was not used for the structures tested in this work, however, so is not discussed in significant detail here. It is worth noting, however, that QDs grown in the sub-monolayer regime have been shown to exhibit improved thermal management and faster carrier capture times compared with those grown in the S-K regime [9–11] – so this could be an important direction in the future research into efficient QD-based THz PCA devices.

QDs are often referred to as 'designer atoms' because they exhibit relatively discretised energy levels and are highly configurable in their properties. The nano-scale size of the dots means there is some significant degree of quantum confinement of excitons in all three spatial dimensions, compared with the confinement in one direction that is exhibited by semiconductor QWs, for example. By considering the 3D confinement conditions mathematically via established

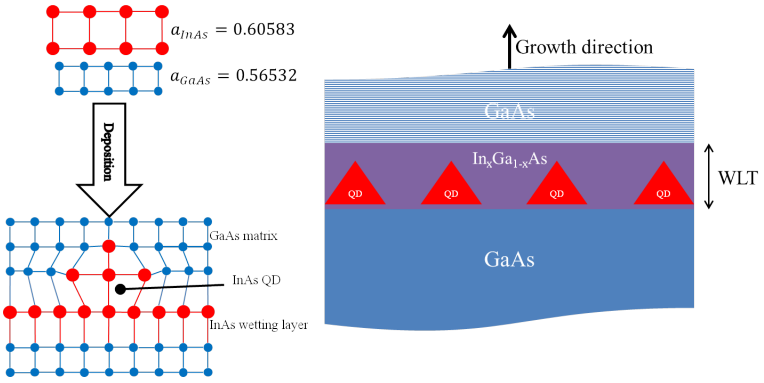

FIGURE 2.1: Diagram of epitaxial deposition of mismatched semiconductor alloys to form InAs:GaAs QDs. WLT – wetting layer thickness.

quantum mechanical concepts, it is possible to 'tune' the energy band structure of the dots by varying the dot size [12] and layer thickness [13]. QDs typically form with pyramidal physical profiles with dimensions on the order of $(15-25)\times(15-25)\times(5-15)$ nm (base width $\times$ base length $\times$ height), but this can be controlled somewhat by deposition conditions. In a simple approximation, the energy structure of each dot may be estimated by considering the quantum exciton confinement in each dimension using the time-independent Schrödinger equation (TISE) for the electron wavefunction Ψ, represented as follows:

$$\frac{-h^2}{8\pi^2 m}\frac{\delta^2\Psi}{\delta x^2} = (E-V)\,\Psi, \tag{2.1.0.2}$$

where h is Planck's constant, m is the effective mass of the electron, E is the energy, V is the well (dot) potential, and $0 \leq x \leq d$ is the position along the single axis under consideration. Taking the dot edges $x = 0$ and $x = d$ as boundary conditions and considering $V = 0$ here yields a periodic function when the TISE is solved for Ψ, shown below:

$$\Psi = A\sin\left(\sqrt{\frac{8\pi^2 mE}{h^2}}x\right) + B\cos\left(\sqrt{\frac{8\pi^2 mE}{h^2}}x\right), \tag{2.1.0.3}$$

where B then immediately goes to 0. Considering the 0-potential at the boundaries, we can see that the function within the sin() component must equal an integer number of π, i.e. $n\pi$ and satisfy the following equation:

$$\sqrt{\frac{8\pi^2 mE}{h^2}}x = n\pi. \tag{2.1.0.4}$$

We can then solve for the energy state as a function of the respective level n which yields the following:

$$E_n = \frac{n^2 h^2}{8md^2}, \tag{2.1.0.5}$$

where d is the width of the potential well (dot) in this dimension. In a QD, we can extend this to represent the energy structure all three independent dimensions in the following way:

$$E_n = \frac{h^2\left(n_x^2 + n_y^2 + n_z^2\right)}{8md^2}. \tag{2.1.0.6}$$

Extending this result for optoelectronic considerations, we consider that the energy different between electrons and holes with effective masses m_e^* and m_h^*, respectively, may be considered as follows:

$$\Delta E = \frac{hc}{\lambda} = E_{BG} + \frac{h^2\left(n_x^2 + n_y^2 + n_z^2\right)}{8m_e^* d^2} + \frac{h^2\left(n_x^2 + n_y^2 + n_z^2\right)}{8m_h^* d^2}, \tag{2.1.0.7}$$

where E_{BG} is the QD bandgap energy. Finally, if we include the exciton effect of the motion and Coulomb force between carrier pairs, we obtain the full general expression for the energy band structure experienced by photons absorbed or emitted from the QD as shown below:

$$\Delta E = \frac{hc}{\lambda} = E_{BG} + \frac{h^2\left(n_x^2 + n_y^2 + n_z^2\right)}{8m_e^* d^2} + \frac{h^2\left(n_x^2 + n_y^2 + n_z^2\right)}{8m_h^* d^2} - \frac{e^2}{8r\pi\epsilon_r}, \tag{2.1.0.8}$$

where r is the separation between respective excitons in each pair and ϵ_r is the dielectric constant or *relative permittivity* of the PC medium.

The result of the QD energy structure described above is that the density of states (DOS) in a QD is relatively low. The DOS $\rho(E)$ defines the number of states N which may be occupied at given energy level, normally defined in atomic studies by the electron degeneracy. The DOS in a volume V of semiconductor material given by Equation 2.1.0.9 and is generally confined only to the energy levels determined by the dot material and dimensions.

$$\rho(E) = \frac{1}{V}\frac{\delta N}{\delta E}. \tag{2.1.0.9}$$

An important consequence of this is illustrated in Figure 2.2. Bulk semiconductors exhibit carrier movement (or lack of carrier confinement) in all three dimensions, and as such the band structure simply shows an increasing DOS

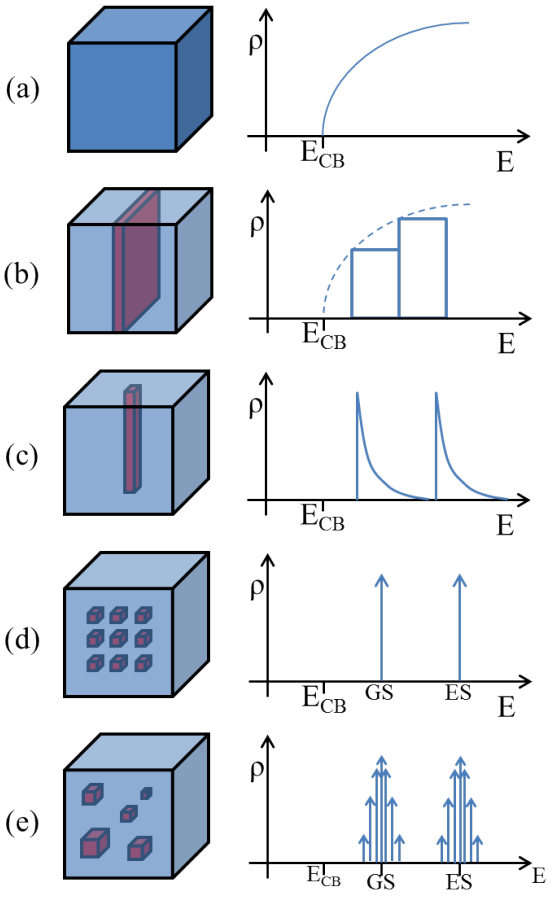

FIGURE 2.2: Illustration of the density-of-states distribution of: (a) 3D (bulk) semiconductor; (b) 2D (QW) heterostructure; (c) quantum-wire; (d) *ideal* QD; and (e) 'real' QDs. E_{CB} – conduction band energy level; E_{GS} – ground state energy level; E_{ES} – excited state energy level.

with increasing energy. QWs exhibit carrier confinement in one dimension, and a stepped DOS at the QW interface is observed. So-called "quantum wires" exhibit carrier confinement in two dimensions, and the DOS is confined to specific energy levels but with some smearing at the band edges due to the comparatively broad potential width in the unconfined direction. *Ideal* QDs exhibit carrier confinement in all three dimensions as discussed, and the discrete energy levels with well-defined DOS are formed. However, in real QD structures the DOS at each energy level is smeared over a Gaussian-type distribution do to the slight variation in deposited dot sizes inherent to the S-K growth regime.

The S-K growth regime is the predominant method by which low-bandgap semiconductor QDs may be integrated within a photoconductive structure. The optical, mechanical and thermal properties of such QD-based structures are still

being explored and they include a wide range of performance benefits and new applications in the optoelectronics field in general. These applications, predominantly to LDs and ultrafast EM signal management are discuss in the following sections with particular emphasis on their implementation as THz PCAs as this is the subject of this work.

2.2 Applications of Quantum Dot Materials

The reliable and repeatable deposition of QD-based structures is a major advantage of the MBE system, and has enabled the development of a broad range of devices and concepts. The use of QD-based semiconductors is quickly becoming ubiquitous in research and in commercial products. This stems from their inherent "customisable" properties and performance, and the early demonstrations of QD materials in heterostructure lasers and SESAMs was arguably the most important influence in the widespread use of them today. Engineering of QD LD properties is generally done by the configuration of such parameters as the QD size, density and number of layers in the gain volume. Engineering of QD properties for charge carrier control generally involves configuration of QD layer number, layer location with respect to the laser cavity modes and layer periodicity to name a few. However, all QD parameters listed here apply to both applications – in fact, in the case of ultrafast QD LDs both applications are utilised simultaneously. This section discussed such applications and how this relates to this work.

2.2.1 Quantum Dot Laser Diodes

An interesting development in laser diode technology was the incorporation of QD gain medium into the laser structure. The first demonstration of LDs utilising a QD-based gain medium was in 1994 [14, 15]. A major design goal at this time was to improve the lasing threshold and gain, and to reduce the limiting thermal rollover effects exhibited by LDs. The general principle was to consider a limited volume of isolated gain islands implanted within the laser volume, which would mean optically stimulating only a small amount of material at any given instant. Exceptionally low current density lasing thresholds were indeed demonstrated,

for example at 26 A/cm^2 for a single-layer InAs:GaAs QD LD with output λ_p at 1250 nm [16]; and as low as 17 A/cm^2 for a three-layer InAs QD LD with cleaved HR/HR facets with output λ_p at 1.3 μm [17]. Extremely high differential gain of $10^{-12} cm^{-1}$ and gain saturation of $1.5 \times 10^5 cm^{-1}$ has been demonstrated from InAs:GaAs LDs [18], making them far superior to QW LDs in terms of lasing efficiency. It has also been shown that the lasing threshold current in a QD LD gain medium can be almost completely insensitive to temperature compared with QW and bulk semiconductors [19, 20]. This is due to the low number of available states near to the ground and excited state lasing levels which may be thermally populated.

As the DOS is relatively low and distributed over a narrow range around the ground- and excited-states (*GS* and *ES*), it is also observed that gain saturation in the GS occurs at a relatively low injection current. As states in the GS are filled, this quickly leads to lasing in the ES as the Fermi level increases and the gain in the ES overtakes the GS gain. The gain will generally saturate at a much higher level while lasing at ES energies due to the higher carrier degeneracy and a proportionally higher optical power may be achieved than GS-only lasing [21]. For example, if the LD is driven at a relatively low current density the output beam may be of peak wavelength $\lambda_p \approx 1250\ nm$ and output power up to roughly 40 mW. Increasing the driving current density will begin to saturate the GS. Losses will slowly increase as the current is increased, which will begin to populate the ES levels and a small signal is observed at the ES output wavelength around 1185 nm. Further current increase will further populate the ES and increase ES gain such that simultaneous lasing at $\lambda_{p1} \approx 1185\ nm$ and $\lambda_{p2} \approx 1260\ nm$ is observed, with no significant emission at any wavelengths between these. The balance of gain and output power between ES and GS energies then increases towards the ES and lasing becomes fully dominated by the ES wavelength. This inherently dual-wavelength operation has been exploited for the purposes of THz optical pump signals in several ways, notably for the electrically-tunable generation of multiple simultaneous dual-mode pumps from a single QD LD [22]. This is discussed further in Section 3.3, as are the other optical systems and methods that were used in the generation of THz pump signals in this work.

Among these methods is the utilisation of an ultrabroadly-tunable QD LD. In this

LD, the gain bandwidth is extremely broad due to the inhomogeneous broadening of energy states exhibited by the dot layers. QDs which are implanted in layers of increasingly larger dot-size allows the DOS profile to extend over an extremely wide range, allowing efficient lasing over a peak wavelength of roughly 1122 $nm-$ 1324 nm from a single LD [23]. This was useful for this work as implemented in an ultrabroadly-tunable dual-wavelength optical signal which was capable of pumping QD PCA structures at a tunable THz difference frequency over an optical energy range which covers both the GS and ES regions [24], as discussed in Section 3.3.

2.2.2 Ultrafast Charge Carrier Modulation

QDs implanted within semiconductors have been shown to exhibit ultrashort carrier lifetimes [25], as they can act as mid-gap trapping and recombination sites within a photoconductive medium which is optically excited. This has been utilised in a variety of applications, most notably in SESAMs and passively/hybrid mode-locked QD LDs, as discussed in the following sections.

2.2.3 Quantum Dot Semiconductor Saturable Absorber Mirrors

SESAMs have been used in the passive mode-locking and sub-ps chirp compensation in the external cavity of solid-state lasers since the early 1970's [26], and QD-based SESAMs have been demonstrated for this use since the late 1990's [27–29]. QD SESAMs are usually produced in a heterostructure deposited over a semiconductor substrate and distributed Bragg reflector (DBR) with high reflectivity at the laser wavelength, but may also be used in transmission mode by excluding the DBR. A SESAM may be characterised primarily by factors such as the optically-influenced range of reflectivity and the 'speed' of the response [30].

The reflectivity may be characterised by: the difference in unsaturated and saturated reflectivity (*modulation depth*); the incident optical power density required to saturate the mirror; and the non-saturable losses (NSL), which is exhibited in real systems as losses in the SESAM material which do not contribute to

the modulation of the SESAM reflectivity. NSL should be minimised as far as possible as any cavity losses will affect the lasing efficiency of any system detrimentally, and is particularly low in QD-SESAMs due to the control of QD 'defect' implantation and the confinement of the DOS distribution [31]. The effective reflectivity is determined by saturation of the absorber, which in turn is determined by the relative excitation of the absorbing medium at the laser wavelength(s). As such, QD-SESAMs are typically used in laser systems operating in the wavelength range ∼1030-1400 nm and the SESAM heterostructure is designed with pump wavelengths in mind. A cavity structure is normally configured, which is either resonant or anti-resonant at the pump wavelength and the placement of the QDs in the cavity is designed with reference to the pump waveform [32]. This is done so as to configure the effective level of QD excitation and subsequent saturation level. QDs are particularly effective in this application because the modulation depth may be controlled by the absorber dot density (via MBE growth parameters such as temperature [31, 33]) and the effective optical fluence incident across the dot layers may be controlled via the cavity design and pump field enhancement.

Regarding the speed of the SESAM response, the ultrafast carrier capture dynamics exhibited by QD nanostructures is ideal for this application, and modulation of laser pulses to pulsewidths below 1 ps is readily achievable [25]. Additionally, the considerable reduction of NSL is achieved in QD-based SESAMs due to the high quality of the heterostructure epitaxial layers and the use of QDs instead of lattice defects for carrier lifetime control. Monitoring of the modulation speed of SESAMs such as these is made relatively simply by the use of a pump-reflective-probe technique. The pump beam excites carriers in the SESAM and the probe beam is incident and reflected from the SESAM at some angle. The time-dependent intensity of the reflected beam is then scanned and monitored using a time-of-flight beam delay line. Intuitively, it is observed that as the pump beam fluence is increased, the recombination time of the SESAM decreases due in part to the increase in saturable losses.

2.2.4 Ultrafast Pulsed Quantum Dot Laser Diodes

As discussed previously, a QD gain medium allows a broad gain bandwidth in the $1.03 - 1.4\ \mu m$ wavelength range and it can also exhibit ultrafast carrier recombination times. These characteristics enable the implementation of QD structures for the generation of high-power, ultrashort pulsed LD devices operating at these longer wavelengths [34–38]. The high output powers and ultrashort pulsewidths of signals generated by these semiconductor lasers, in addition to their relatively good beam quality and long operational wavelength makes them ideal candidates as the driving mechanism in a wide range of THz pulse generation systems based on both increasingly relevant, telecoms-wavelength PCAs as well as NLCs. Additionally, as these ultra-compact devices are designed with the active components such as a SESAM, spatial filtering waveguide, gain section and mirror facets monolithically integrated, the entire pump system is extremely compact, low power and need only include a few standard additional conditioning optics such as an optical isolator and coupling lenses [35, 38].

As discussed in Section 1.2.1.2, the use of a SESAM within the cavity of an LD can enable the generation of ultrashort optical pulses in the device. The operating principle of the SESAM is the ultrafast excitation, saturation and recombination of carriers within the PC SESAM structure. This is assisted by the use of dopants and mid-gap carrier capture sites throughout the SESAM which allows carriers to relax must faster than recombination in a more homogeneous crystalline structure. This may be enhanced even further with the use of a p-n junction across the absorber, which increases the movement and capture rate of charge carriers [39]. It follows then, that the ultrafast carrier modulation exhibited QD structures can be utilised in the absorber section of QD LDs to modulate sub-ps pulses in the cavity similarly to the method applied to QW LDs.

The performance of mode-locked QD LDs to date is impressive. The characteristics of various QD LD device structures and configurations includes: temporal pulsewidths as low as 390 fs [40]; peak powers on the order of 17 W [41, 42]; and repetition rates between 281 MHz [37] and several hundred GHz (e.g. [43]). Interestingly, Simultaneous mode-locking of both GS and ES wavelength pulses have also been demonstrated [44]. This makes these LD systems excellent candidates for use in THz optical pump systems, and a variety of two-section QD LD devices are tested in this work as discussed in Chapter 3.

The basic two-section QD LD layout is to use a straight waveguide between HR/AR cleaved facets, and a gain:absorber length ratio between 6:1 and 4:1. A variation on this is to replace the HR facet with an altered AR facet which utilises an angled waveguide to further reduce the reflectivity of this facet to around 10^{-5}. Another configuration was a tapered gain section and a (usually parallel) absorber section [41]. The parallel waveguide acts as a spatial filter within the cavity while the tapered section uses the increasing width of the gain medium to amplify the optical power. Tapered lasers may be designed in three different ways: fully index-guided, fully gain-guided or a combination of both designs. Such devices are now established as reliable semiconductor device configurations for the generation of high power, ultrashort optical pulses [45–47]. Gain-guided two-section tapered devices like these have demonstrated high peak output powers exceeding 17 W and enable the generation of Fourier-limited 0.672 ps pulsewidth optical signals [41].

2.2.5 Application to Terahertz Photoconductive Antennas

Recently, research into efficient ultrafast photoconductive materials and structures for ultrafast laser [25] and THz [48–51] applications has included the investigation of optically-pumped QD-based semiconductor structures with the primary function of utilising layers of implanted QDs as the photocarrier lifetime-shortening mechanism. The basis of this theorem is partly to take advantage of the high crystalline quality structure offered by MBE growth of all semiconductor materials in the device. This can potentially allow the production of a highly efficient, ultrafast device without introducing compromises between factors such as carrier mobility, PC gain, resistivity and carrier lifetimes as would normally be made in bulk-type PC THz materials. The use of essentially defect-free GaAs crystal layers in an InAs:GaAs QD structure allows carrier mobilities across the active region similar or higher to a bulk LT-GaAs structure but not as high as QD-free bulk GaAs [52], which is to be expected. It has been shown previously that QDs deposited within or over GaAs can efficiently shorten photocarrier lifetimes and generate THz signals when the structure is pumped by ultrafast optical pulses with wavelength $800 < \lambda_p < 895\ nm$ [53] and THz-range photomixing

Layer	Material	Repeats	Thickness (nm)	Comment
8	LT-GaAs	1	30	
7	GaAs	40	35	Active region
6	$In_{0.15}Ga_{0.85}As$	40	5	Active region
5	InAs QD	40	0.8	Active region
4	GaAs	1	35	Spacer layer
3	AlAs	25	100.46	DBR
2	GaAs	25	85.79	DBR
1	GaAs	1	100	Buffer layer
0	GaAs			3" SI substrate

TABLE 2.1: Epitaxial layer profile of QD-based antenna semiconductor "Structure 1". SI – semi-insulating.

operation of PCAs has been demonstrated using ErAs:GaAs nanoisland-based structures pumped at 800 nm using two Ti:Sapphire lasers [49].

These concepts and early results encourage the further development of QD-based THz PCA devices and this is the basis of this work. The PCA structures used in this work are InAs:GaAs QD structures of varying dot layer number and DBR reflectivity range, but are kept consistent in their material and layer thickness parameters. The epitaxial profile of each tested QD structure used in this work is given in Tables 2.1–2.3, and photoluminescence (PL) and optical reflectivity spectrum for each structure is shown in Figure 2.3.

Structure 1 described in Table 2.1 is the measured PL spectrum from a 40-layer QD structure which has a 25-layer DBR centred around 1180 nm wavelength. *Structure 2* described in Table 2.2 is a 25-layer structure with DBR centred around 1220 nm wavelength. *Structure 3* described in Table 2.3 is a 40-layer structure with DBR centred around 1220 nm wavelength. The PL spectrum of a QD-based structure is normally measured using a calibration sample of the same QD parameters but no additional features such as the DBR, shown in Figure 2.3(a,c). The PL spectrum shown in plot (e) is measured directly from the final heterostructure of Structure 2, and the effects of the DBR are recognisable by the enhancement of emission around the centre design wavelength of 1220 nm.

Figure 2.4 indicates the photocarrier dynamics in a multilayer structure consisting of three different possible semiconductor absorption materials, which can be very complex but effectively consist in charge carrier escape and/or capture

Layer	**Material**	**Repeats**	**Thickness (nm)**	**Comment**
Post-growth anneal				As_2 overpressure, 550°C, 10 mins
9	LT-GaAs	1	30	Grown at 190°C
8	GaAs	1	10	Spacer layer
7	GaAs	25	36	Active region
6	$In_{0.15}Ga_{0.85}As$	25	4	Active region
5	InAs QD	25	0.8	Active region
4	GaAs	1	75	Spacer layer
3	GaAs	30	89	DBR
2	AlAs	30	104	DBR
1	GaAs	1	300	Buffer layer
0	GaAs			3" SI substrate

TABLE 2.2: Epitaxial layer profile of QD-based antenna semiconductor "Structure 2". SI – semi-insulating.

Layer	**Material**	**Repeats**	**Thickness (nm)**	**Comment**
Post-growth anneal				As_2 overpressure, 450°C, 10 mins
9	LT-GaAs	1	30	Grown at 200°C
8	GaAs	1	10	Spacer layer
7	GaAs	39	35	Active region
6	$In_{0.15}Ga_{0.85}As$	40	4	Active region
5	InAs QD	40	0.8	Active region
4	GaAs	1	170	Spacer layer
3	GaAs	30	88.9	DBR
2	AlAs	30	104.5	DBR
1	GaAs	1	500	Buffer layer
0	GaAs			3" SI substrate

TABLE 2.3: Epitaxial layer profile of QD-based antenna semiconductor "Structure 3". SI – semi-insulating.

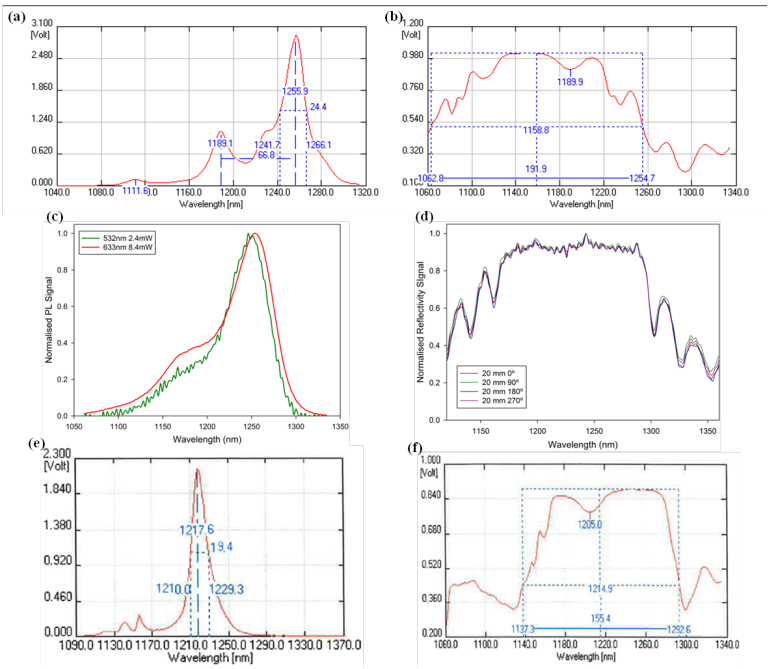

FIGURE 2.3: Photoluminescence and optical reflectivity spectrum of: (a-b) Structure 1; (c-d) Structure 2; and (e-f) Structure 3.

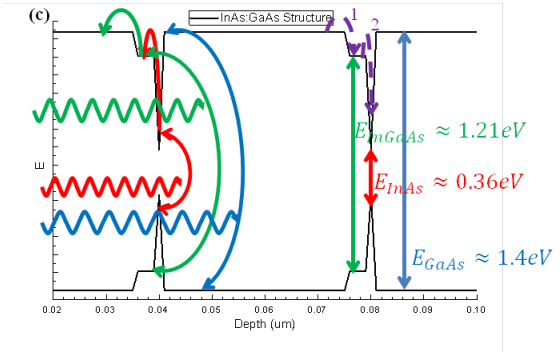

FIGURE 2.4: Sketch of the different possible mechanisms of charge carrier generation and movement between layers and materials in a QD structure grown in the Stranksi-Krastinow regime.

between the different materials. This plot is generated by custom simulation software which calculates refractive indices and energy bandgaps of the structure throughout the entire heterostructure depth, as discussed further in Section 4.1.1.

It should be noted that the values given here for the bandgap and refractive index of the InAs QD layers are typically 2–3 times higher than the levels given in this plot due to dot strain effects in the multi-layer heterostructure [54], but are still necessarily lower than the bandgap energies of the wetting layer and GaAs

spacer matrix. Carrier generation in GaAs barrier layers and subsequent capture into InGaAs capping and QD layers has already been demonstrated for different ultrafast optoelectronic applications such as the SESAMs discussed previously [53] and ultrafast lasers [41]. Presented in this work are also experimental investigations into the behaviour of similar InAs:GaAs structures operated in different charge transport regimes. The aim of this is to test the capacity for carrier escape specifically from InGaAs capping layers and the potential for 'inter-dot' carrier release and capture between adjacent QDs and QD layers when pumped around peak InAs ground and excited state energies. Ultrafast carrier relaxation has previously been demonstrated in QD-SESAMs pumped at longer wavelengths corresponding to absorption energies of the implanted QDs [25]. In these preliminary tests, pump wavelengths up to 1280 nm were employed using broadly tunable InAs:GaAs QD diode lasers in the CW dual-mode regime, some results of which are presented in Section 5.1.

Previous experiments have shown that different excitation energies in structures similar to this will involve a range of processes which occur over different timescales. The timescales of these processes depend upon which layer or material is optically excited; which layer/material charge carriers relax to; and the level of optical excitation applied [55, 56]. In the case for THz antenna devices there is the additional factor of the electric field applied across the active region, which contributes considerably to the movement of charge carriers particularly regarding movement speed and capture times [39], as discussed above and in Section 1.2.4.

Differential reflection measurements on QD layers of ∼100 nm vertical separation (*periodicity*) indicate sub-ps carrier capture from the GaAs bulk into the wetting layer of the QDs and a carrier capture time into the QDs themselves of ∼1.5 ps [57]. The periodicity of embedded QD layers has been shown to strongly influence the carrier capture time [58] and periodic 40 nm spacing of QD layers in structures such as those used in this work should theoretically enable the modulation of charge carrier relaxation down to timescales of roughly 450 fs. Carrier capture and recombination times in such InAs:GaAs QD structures have also been shown to be strongly dependent on the deposition depth of QD layers in terms of the number of dot monolayers (ML) [32]. Put simply, a higher ML number is likely to result in a higher number of potential carrier capture sites [59]

and higher dot density associated with higher QD layer depth also increases the inter-dot carrier capture probability [60] – both effects typically contributing to faster exciton capture and recombination. However, the S-K growth of QDs and the corresponding dot and carrier capture site density is *not* so straightforward as to mean that more MLs yield more 'useful' QD material in this sense. It should be noted that well-ordered QDs may *begin* to form once the appropriate InAs layer thickness is deposited [61] (depending upon the deposition conditions), but after formation the amount of material incorporated properly into the formed dots will saturate [62–64]. After this point, dislocations will begin to form as more material is added and the dot ensemble will exhibit less efficient thermal dissipation and carrier transport, potentially leading to an overall decrease in carrier generation and capture rate. Because of this, an optimal dot layer thickness should be chosen so as to maintain well-ordered QD structures whilst achieving a relatively high areal dot coverage. The structures used in this work are produced with InAs dot layer thickness of ∼2.3 ML, which should be high enough to support significant dot layer density without risking a high density of dislocations.

Ultrafast carrier processes in low-bandgap QD structures are governed by both radiative and non-radiative recombination and relaxation processes. It is observed that *radiative* recombination processes in InAs:GaAs QD structures (with no externally-applied E-field) pumped at wavelengths $\lesssim$800 nm can occur over timescales of several ps to hundreds of ps [65]. These timescales are determined by processes such as simultaneous state-filling of QD energy levels, subsequent energy-dependent exciton recombination and diffusion of carriers from GaAs spacer layers into the dots. As such, the timescales of PL recombination are dependent on the respective energy of the occupied dot level and subsequent emission, indicating a faster recombination time from excited states than from the ground state. Radiative recombination times are also strongly influenced by the photoexcitation power and availability of relaxation channels in this case, where increasing optical pump power leads firstly to saturation of the dot ground states and subsequently higher states as the power is increased [66].

Regarding *non-radiative* relaxation, the predominant processes of interest here are Auger effects [67] and step-wise (*intra-dot*) relaxation of excitons through subsequent QD energy levels. Again, such processes are intuitively dependent on

available intraband relaxation channels and phonon interaction [68]. The difference between carrier capture and relaxation in this case is defined by whether photocarriers are considered as *mobile*. Intra-dot processes are then not considered to be derived from mobile carriers, whereas capture (and also radiative recombination) of carriers generated in the barrier layers is considered as such. Intra-dot carrier processes may be investigated by resonant excitation of QD states, for example. In such a regime, intra-dot relaxation time reductions of 2.8 ps to 1.5 ps with increasing optical pump power, and 4.7 ps to 1.5 ps with increasing temperature (from 4 K to 300 K) have been demonstrated [69] and tend to support the Auger-based theory. As such, it was postulated that a many-layer InAs:GaAs QD structure could provide the necessary number and density of carrier capture sites and relaxation channels to support the ultrafast switching processes necessary for implementation in an optically-pumped ultrafast PCA device. Such a structure could potentially exhibit the ultrafast capture of mobile carriers generated in higher-bandgap spacer and wetting layers into QD layers and additionally exhibit ultrafast carrier intra-dot relaxation when pumped at lower photon energies corresponding to QD GS and ES PL peaks. Additionally, the suppression of PL emission from the structure may be assisted by the configuration of an optical cavity which is anti-resonant at the emission wavelength by utilisation of a DBR beneath the active region and inter-facial reflection at the structure-air boundary. Indeed, in this work measurements were carried out by optically pumping PCA structures with DBRs and consisting of different numbers of QD layers and hence different availability of carrier relaxation channels, the results of which are presented in Chapter 5.

It should be noted, however, that the operation of a PCA device in particular is based on the generation of photocurrent and the *movement* of charge carriers. Therefor, the mobility of carriers within the structure and between generation and capture sites is a prime concern in this application. The nature of *inter-dot* processes must be considered in the pumping of such structures at resonant QD energies. Such processes are governed by carrier escape from QD sites into the barrier layers, which is in part dependent on the relative energy mismatch between the QDs and wetting and spacer materials and potential tunneling between them. Previous experiments conducted using similar $In_{0.5}Ga_{0.5}As$:GaAs QD structures have demonstrated carrier recombination times reaching nearly 1 ns when excited from the QD GS into the barrier [56]. However, the experiments

in this case did not include investigation of the dynamics of carriers excited from higher dot energy levels, and no external E-field was applied. Application of an E-field across the QD layer region of an InAs:GaAs heterostructure under IR excitation has been previously demonstrated to enhance the movement and subsequent capture rate of charge carriers through such a structure to the extent that an increase the PL intensity at the respective QD energy levels is observed [70]. This has also been utilised as the carrier lifetime shortening mechanism in similar InAs:GaAs QD structures, to the extent that sub-ps carrier capture in an un-biased structure is not possible but is made possible in a biased structure [50] – an effect which is not observed in more homogeneous, bulk semiconductors grown at low temperatures. The extent of these effects are explored further in this work, and discussed in Chapter 5.

2.3 Summary and Conclusions

In this chapter, the production and application of InAs:GaAs QD semiconductor structures was discussed, with particular emphasis on QD structures and applications in SESAMs and LDs. A description of the S-K growth regime was given, which is the basis of QD layer production. The method of QD bandgap engineering was described with application to the design of structures with controllable optical absorption and emission properties. The ultrafast charge carrier modulation of multi-layered QD-based heterostructures was also discussed, which is fundamental in the design of efficient SESAM structures and a key concept in the interpretation of the main results presented later in Chapter 5.

2.4 References

[1] A.Y. Cho. Film Deposition by Molecular-Beam Techniques. *Journal of Vacuum Science and Technology*, 8(5):S31–S38, 1971. ISSN 0022-5355. doi: 10.1116/1.1316387.

[2] A.Y. Cho and J.R. Arthur. Molecular beam epitaxy. *Progress in Solid State Chemistry*, 10, Part 3(0):157 – 191, 1975. ISSN 0079-6786.

doi: http://dx.doi.org/10.1016/0079-6786(75)90005-9. URL http://www.sciencedirect.com/science/article/pii/0079678675900059.

[3] B A Joyce. Molecular beam epitaxy. *Reports on Progress in Physics*, 48(12): 1637, 1985. URL http://stacks.iop.org/0034-4885/48/i=12/a=002.

[4] L. Goldstein, F. Glas, J. Y Marzin, M.N. Charasse, and G. Le Roux. Growth by molecular beam epitaxy and characterization of InAs/GaAs strained-layer superlattices. *Applied Physics Letters*, 47(10):1099–1101, 1985. ISSN 0003-6951. doi: 10.1063/1.96342.

[5] P.M. Petroff and S.P. DenBaars. {MBE} and {MOCVD} growth and properties of self-assembling quantum dot arrays in III-V semiconductor structures. *Superlattices and Microstructures*, 15(1):15 –, 1994. ISSN 0749-6036. doi: http://dx.doi.org/10.1006/spmi.1994.1004. URL http://www.sciencedirect.com/science/article/pii/S0749603684710044.

[6] Kenichi Nishi, H. Saito, Shigeo Sugou, and Jeong-Sik Lee. A narrow photoluminescence linewidth of 21 mev at 1.35 μm from strain-reduced InAs quantum dots covered by $In_{0.2}Ga_{0.8}$as grown on GaAs substrates. *Applied Physics Letters*, 74(8):1111–1113, 1999. ISSN 0003-6951. doi: 10.1063/1.123459.

[7] V.M. Ustinov, N.A. Maleev, A.E. Zhukov, A.R. Kovsh, A. Yu Egorov, A.V. Lunev, B. V. Volovik, I.L. Krestnikov, Yu G. Musikhin, N. A. Bert, P.S. Kopev, Zh.I. Alferov, N.N. Ledentsov, and D. Bimberg. InAs/InGaAs quantum dot structures on GaAs substrates emitting at 1.3 μm. *Applied Physics Letters*, 74(19):2815–2817, 1999. ISSN 0003-6951. doi: 10.1063/1.124023.

[8] IL Krestnikov, NN Ledentsov, A Hoffmann, and D Bimberg. Arrays of two-dimensional islands formed by submonolayer insertions: growth, properties, devices. *PHYSICA STATUS SOLIDI A APPLIED RESEARCH*, 183(2): 207–233, 2001.

[9] N.N. Ledentsov, D. Bimberg, F. Hopfer, A. Mutig, V.A. Shchukin, A.V. Savelev, G. Fiol, E. Stock, H. Eisele, M. Dhne, D. Gerthsen, U. Fischer, D. Litvinov, A. Rosenauer, S.S. Mikhrin, A.R. Kovsh, N.D. Zakharov, and P. Werner. Submonolayer Quantum Dots for High Speed Surface

Emitting Lasers. *Nanoscale Research Letters*, 2(9):417–429, 2007. ISSN 1931-7573. doi: 10.1007/s11671-007-9078-0. URL http://dx.doi.org/10.1007/s11671-007-9078-0.

[10] F. Hopfer, A. Mutig, G. Fiol, M. Kuntz, V.A. Shchukin, V.A. Haisler, T. Warming, E. Stock, S.S. Mikhrin, I.L. Krestnikov, D.A. Livshits, A.R. Kovsh, C. Bornholdt, Andrea Lenz, H. Eisele, M. Dahne, N.N. Ledentsov, and D. Bimberg. 20 Gb/s 85°C Error-Free Operation of VCSELs Based on Submonolayer Deposition of Quantum Dots. *Selected Topics in Quantum Electronics, IEEE Journal of*, 13(5):1302–1308, 2007. ISSN 1077-260X. doi: 10.1109/JSTQE.2007.905133.

[11] N. N. Ledentsov, F. Hopfer, A. Mutig, V. A. Shchukin, A. V. Savel'ev, G. Fiol, M. Kuntz, V. A. Haisler, T. Warming, E. Stock, S. S. Mikhrin, A. R. Kovsh, C. Bornholdt, A. Lenz, H. Eisele, M. Dähne, N. D. Zakharov, P. Werner, and D. Bimberg. Novel concepts for ultrahigh-speed quantum-dot vcsels and edge-emitters. volume 6468, pages 64681O–64681O–15, 2007. doi: 10.1117/12.717248. URL http://dx.doi.org/10.1117/12.717248.

[12] M. Grundmann, N. N. Ledentsov, O. Stier, J. Böhrer, D. Bimberg, V. M. Ustinov, P. S. Kop'ev, and Zh. I. Alferov. Nature of optical transitions in self-organized InAs/GaAs quantum dots. *Phys. Rev. B*, 53:R10509–R10511, Apr 1996. doi: 10.1103/PhysRevB.53.R10509. URL http://link.aps.org/doi/10.1103/PhysRevB.53.R10509.

[13] A. Y. Egorov, A. E. Zhukov, P. S. Kopev, N. N. Ledentsov, M. V. Maksimov, V. M. Ustinov, A. F. Tsatsulnikov, Z. I. Alferov, D. L. Fedorov, and D. Bimberg. Optical emission range of structures with strained InAs quantum dots in GaAs. *Semiconductors*, 30(8):707–710, August 1996.

[14] N. N. LEDENTSOV, V. M. USTINOV, A. Y. EGOROV, A. E. ZHUKOV, M. V. MAKSIMOV, I. G. TABATADZE, and P. S. KOPEV. Optical-properties of Heterostructures With Ingaas-gaas Quantum Clusters. *Semiconductors*, 28(8):832–834, August 1994.

[15] N. KIRSTAEDTER, N. N. LEDENTSOV, M. GRUNDMANN, D. BIMBERG, V. M. USTINOV, S. S. RUVIMOV, M. V. MAXIMOV, P. S. KOPEV, Z. I. ALFEROV, U. RICHTER, P. WERNER, U. GOSELE, and

J. HEYDENREICH. Low-threshold, Large T-o Injection-laser Emission From (inga)as Quantum Dots. *Electronics Letters*, 30(17):1416–1417, August 1994. doi: 10.1049/el:19940939.

[16] G. T. Liu, A. Stintz, H. Li, K.J. Malloy, and L.F. Lester. Extremely low room-temperature threshold current density diode lasers using InAs dots in $In_{0.15}Ga_{0.85}As$ quantum well. *Electronics Letters*, 35(14):1163–1165, 1999. ISSN 0013-5194. doi: 10.1049/el:19990811.

[17] H. Y. Liu, D. T. Childs, T. J. Badcock, K. M. Groom, I. R. Sellers, M. Hopkinson, R. A. Hogg, D. J. Robbins, D. J. Mowbray, and M. S. Skolnick. High-performance three-layer 1.3 μm InAs-GaAs quantum-dot lasers with very low continuous-wave room-temperature threshold currents. *IEEE Photonics Technology Letters*, 17(6):1139–1141, 2005.

[18] D. Bimberg, M. Grundmann, F. Heinrichsdorff, N.N. Ledentsov, V.M. Ustinov, A.E. Zhukov, A.R. Kovsh, M.V. Maximov, Y.M. Shernyakov, B.V. Volovik, A.F. Tsatsulnikov, P.S. Kopev, and Zh.I. Alferov. Quantum dot lasers: breakthrough in optoelectronics. *Thin Solid Films*, 367(12):235 – 249, 2000. ISSN 0040-6090. doi: http://dx.doi.org/10.1016/S0040-6090(00)00697-0. URL http://www.sciencedirect.com/science/article/pii/S0040609000006970.

[19] ZHORES I. ALFEROV. THE DOUBLE HETEROSTRUCTURE: CONCEPT AND ITS APPLICATIONS IN PHYSICS, ELECTRONICS AND TECHNOLOGY. *International Journal of Modern Physics B*, 16(05): 647–675, 2002. doi: 10.1142/S0217979202010233. URL http://www.worldscientific.com/doi/abs/10.1142/S0217979202010233.

[20] S S Mikhrin, A R Kovsh, I L Krestnikov, A V Kozhukhov, D A Livshits, N N Ledentsov, Yu M Shernyakov, I I Novikov, M V Maximov, V M Ustinov, and Zh I Alferov. High power temperature-insensitive 1.3 μm InAs/InGaAs/GaAs quantum dot lasers. *Semiconductor Science and Technology*, 20(5):340, 2005. URL http://stacks.iop.org/0268-1242/20/i=5/a=002.

[21] Viktor Michajlovič Ustinov. *Quantum dot lasers*, volume 11. Oxford University Press, 2003.

[22] R. Leyman, D. I. Nikitichev, N. Bazieva, and E. U. Rafailov. Multimodal spectral control of a quantum-dot diode laser for THz difference frequency generation. *Applied Physics Letters*, 99(17), 2011.

[23] K. A. Fedorova, M. A. Cataluna, I. Krestnikov, D. Livshits, and E. U. Rafailov. Broadly tunable high-power InAs/GaAs quantum-dot external cavity diode lasers. *Optics Express*, 18(18):19438–19443, 2010.

[24] R. Leyman, D. Carnegie, N. Bazieva, K. A. Fedorova, D. Livshits, and E. U. Rafailov. Ultrabroad Dual-Mode Spectral Control of a Quantum Dot Laser Gain Medium. In *3rd EOS Topical Meeting on Terahertz Science & Technology (TST 2012)*, 2012.

[25] E. U. Rafailov, S. J. White, A. A. Lagatsky, A. Miller, W. Sibbett, D. A. Livshits, A. E. Zhukov, and V. M. Ustinov. Fast quantum-dot saturable absorber for passive mode-locking of solid-State lasers. *Photonics Technology Letters, IEEE*, 16(11):2439–2441, 2004.

[26] B. K. Garside and T. K. Lim. Laser mode locking using saturable absorbers. *Journal of Applied Physics*, 44(5):2335–2342, 1973. doi: http://dx.doi.org/10.1063/1.1662561. URL http://scitation.aip.org/content/aip/journal/jap/44/5/10.1063/1.1662561.

[27] P. T. Guerreiro, S. Ten, N. F. Borrelli, J. Butty, G. E. Jabbour, and N. Peyghambarian. PbS quantum-dot doped glasses as saturable absorbers for mode locking of a Cr:forsterite laser. *Applied Physics Letters*, 71(12):1595–1597, 1997. doi: http://dx.doi.org/10.1063/1.119843. URL http://scitation.aip.org/content/aip/journal/apl/71/12/10.1063/1.119843.

[28] R. Paschotta, G. J. Spühler, D. H. Sutter, N. Matuschek, U. Keller, M. Moser, R. Hövel, V. Scheuer, G. Angelow, and T. Tschudi. Double-chirped semiconductor mirror for dispersion compensation in femtosecond lasers. *Applied Physics Letters*, 75(15):2166–2168, 1999. doi: http://dx.doi.org/10.1063/1.124953. URL http://scitation.aip.org/content/aip/journal/apl/75/15/10.1063/1.124953.

[29] A. M. Malyarevich, V. G. Savitski, P. V. Prokoshin, N. N. Posnov, K. V. Yumashev, E. Raaben, and A. A. Zhilin. Glass doped with PbS quantum

dots as a saturable absorber for 1-μm neodymium lasers. *J. Opt. Soc. Am. B*, 19(1):28–32, Jan 2002. doi: 10.1364/JOSAB.19.000028. URL http://josab.osa.org/abstract.cfm?URI=josab-19-1-28.

[30] U. Keller. Recent developments in compact ultrafast lasers. *Nature*, 424 (6950):831–838, 2003.

[31] A.A. Lagatsky, C.G. Leburn, C.T.A. Brown, W. Sibbett, S.A. Zolotovskaya, and E.U. Rafailov. Ultrashort-pulse lasers passively mode locked by quantum-dot-based saturable absorbers. *Progress in Quantum Electronics*, 34(1):1 – 45, 2010. ISSN 0079-6727. doi: http://dx.doi.org/10.1016/j.pquantelec.2009.11.001. URL http://www.sciencedirect.com/science/article/pii/S0079672709000299.

[32] DJHC Maas, AR Bellancourt, M Hoffmann, B Rudin, Y Barbarin, M Golling, T Südmeyer, and U Keller. Growth parameter optimization for fast quantum dot SESAMs. *Opt. Express*, 16(23):18646–18656, 2008.

[33] C. Y. Ngo, S. F. Yoon, and J. H. Teng. Bandgap engineering of 1.3 μm quantum dot structures for terahertz (THz) emission. *Journal of Crystal Growth*, 323(1):211–214, 2011.

[34] Matthias Kuntz, Gerrit Fiol, Matthias Laemmlin, Christian Meuer, and Dieter Bimberg. High-speed mode-locked quantum-dot lasers and optical amplifiers. *Proceedings of the Ieee*, 95(9):1767–1778, 2007.

[35] E. U. Rafailov, M. A. Cataluna, and W. Sibbett. Mode-locked quantum-dot lasers. *Nature Photonics*, 1(7):395–401, 2007.

[36] Mark G. Thompson, Alastair R. Rae, Mo Xia, Richard V. Penty, and Ian H. White. InGaAs Quantum-Dot Mode-Locked Laser Diodes. *IEEE Journal of Selected Topics in Quantum Electronics*, 15(3):661–672, 2009.

[37] Maria Ana Cataluna, Ying Ding, Daniil I. Nikitichev, Ksenia A. Fedorova, and Edik U. Rafailov. High-Power Versatile Picosecond Pulse Generation from Mode-Locked Quantum-Dot Laser Diodes. *IEEE Journal of Selected Topics in Quantum Electronics*, 17(5):1302–1310, 2011.

[38] E.U. Rafailov, M.A. Cataluna, and E.A. Avrutin. *Ultrafast Lasers Based on Quantum Dot Structures: Physics and Devices*. Wiley-VCH, 2011.

[39] A.A. Lagatsky, E.U. Rafailov, W. Sibbett, D.A. Livshits, A.E. Zhukov, and V.M. Ustinov. Quantum-dot-based saturable absorber with p-n junction for mode-locking of solid-state lasers. *Photonics Technology Letters, IEEE*, 17(2):294–296, 2005. ISSN 1041-1135. doi: 10.1109/LPT.2004.839387.

[40] E.U. Rafailov, M.-A. Cataluna, W. Sibbett, N.D. Ilinskaya, Yu M. Zadiranov, A.E. Zhukov, V.M. Ustinov, D.A. Livshits, A.R. Kovsh, and N.N. Ledentsov. High-power picosecond and femtosecond pulse generation from a two-section mode-locked quantum-dot laser. *Applied Physics Letters*, 87 (8):081107–081107–3, 2005. ISSN 0003-6951. doi: 10.1063/1.2032608.

[41] D. I. Nikitichev, Y. Ding, M. A. Cataluna, E. U. Rafailov, L. Drzewietzki, S. Breuer, W. Elsaesser, M. Rossetti, P. Bardella, T. Xu, I. Montrosset, I. Krestnikov, D. Livshits, M. Ruiz, M. Tran, Y. Robert, and M. Krakowski. High peak power and sub-picosecond Fourier-limited pulse generation from passively mode-locked monolithic two-section gain-guided tapered InGaAs quantum-dot lasers. *Laser Physics*, 22(4):715–724, 2012.

[42] Y. Ding, D.I. Nikitichev, I. Krestnikov, D. Livshits, M.A. Cataluna, and E.U. Rafailov. Quantum-dot external-cavity passively modelocked laser with high peak power and pulse energy. *Electronics Letters*, 46(22):1516–1518, 2010. ISSN 0013-5194. doi: 10.1049/el.2010.2336.

[43] A.R. Rae, M.G. Thompson, R.V. Penty, I.H. White, A.R. Kovsh, S.S. Mikhrin, D.A. Livshits, and I.L. Krestnikov. Harmonic Mode-Locking of a Quantum-Dot Laser Diode. In *Lasers and Electro-Optics Society, 2006. LEOS 2006. 19th Annual Meeting of the IEEE*, pages 874–875, 2006. doi: 10.1109/LEOS.2006.279085.

[44] Maria Ana Cataluna, Daniil I. Nikitichev, Spiros Mikroulis, Hercules Simos, Christos Simos, Charis Mesaritakis, Dimitris Syvridis, Igor Krestnikov, Daniil Livshits, and Edik U. Rafailov. Dual-wavelength mode-locked quantum-dot laser, via ground and excited state transitions: experimental and theoretical investigation. *Opt. Express*, 18(12):12832–12838, Jun 2010. doi: 10.1364/OE.18.012832. URL http://www.opticsexpress.org/abstract.cfm?URI=oe-18-12-12832.

[45] M. T. Kelemen, J. Weber, G. Kaufel, G. Bihlmann, R. Moritz, M. Mikulla, and G. Weimann. Tapered diode lasers at 976 nm with 8 W nearly diffraction limited output power. *Electronics Letters*, 41(18):1011–1013, 2005.

[46] K. Kim, S. Lee, and P. J. Delfyett. 1.4kW high peak power generation from an all semiconductor mode-locked master oscillator power amplifier system based on eXtreme Chirped Pulse Amplification(X-CPA). *Optics Express*, 13(12):4600–4606, 2005.

[47] N. Michel, M. Ruiz, M. Calligaro, Y. Robert, M. Lecomte, O. Parillaud, M. Krakowski, I. Esquivias, H. Odriozola, J. M. G. Tijero, C. H. Kwok, R. V. Penty, and I. H. White. *Two-sections tapered diode lasers for 1 Gbps free-space optical communications with high modulation efficiency*, volume 7616 of *Proceedings of SPIE*, page 76161F. 2010. Conference on Novel In - Plane Semiconductor Lasers IX Jan 25-28, 2010 San Francisco, CA Spie.

[48] W. E. Kerr, A. Pancholi, and V. G. Stoleru. Quantum dot molecules: A potential pathway towards terahertz devices. *Physica E-Low-Dimensional Systems & Nanostructures*, 35(1):139–145, 2006.

[49] C. Kadow. Self-assembled ErAs islands in GaAs for THz applications. *Physica. E, Low-dimensional systems & nanostructures*, 7(1-2):97, 2000.

[50] N. S. Daghestani, M. A. Cataluna, G. Berry, G. Ross, and M. J. Rose. Terahertz emission from InAs/GaAs quantum dot based photoconductive devices. *Applied Physics Letters*, 98(18), 2011.

[51] T. Kruczek, R. Leyman, D. Carnegie, N. Bazieva, G. Erbert, S. Schulz, C. Reardon, and E. U. Rafailov. Continuous wave terahertz radiation from an InAs/GaAs quantum-dot photomixer device. *Applied Physics Letters*, 101(8):081114–4, 2012.

[52] D. Turchinovich, K. Pierz, and P. Uhd Jepsen. InAs/GaAs quantum dots as efficient free carrier deep traps. *physica status solidi (c)*, 0(5):1556–1559, 2003.

[53] E. Estacio. Strong enhancement of terahertz emission from GaAs in InAs/-GaAs quantum dot structures. *Applied Physics Letters*, 94(23):232104, 2009.

[54] E.C. Le Ru, A.J. Bennett, C. Roberts, and R. Murray. Strain and electronic interactions in InAs/GaAs quantum dot multilayers for 1300 nm emission. *Journal of Applied Physics*, 91(3):1365–1370, 2002. ISSN 0021-8979. doi: 10.1063/1.1429797.

[55] D. Turchinovich, H. P. Porte, N. Daghestani, K. G. Wilcox, E. U. Rafailov, and P. U. Jepsen. Capture and release of carriers in InGaAs/GaAs quantum dots. In C. Palermo and G. Bastard, editors, *16th International Conference on Electron Dynamics in Semiconductors, Optoelectronics and Nanostructures*, volume 193 of *Journal of Physics Conference Series*, Bristol, 2009. IOP Publishing Ltd.

[56] H. P. Porte, P. Uhd Jepsen, N. Daghestani, E. U. Rafailov, and D. Turchinovich. Ultrafast release and capture of carriers in InGaAs/GaAs quantum dots observed by time-resolved terahertz spectroscopy. *Applied Physics Letters*, 94(26), 2009.

[57] Hai-Ying Liu, Zi-Ming Meng, Qiao-Feng Dai, Li-Jun Wu, Qi Guo, Wei Hu, Song-Hao Liu, Sheng Lan, and Tao Yang. Ultrafast carrier dynamics in undoped and p-doped InAs/GaAs quantum dots characterized by pump-probe reflection measurements. *Journal of Applied Physics*, 103(8):083121, 2008.

[58] C. Kadow, S. B. Fleischer, J. P. Ibbetson, J. E. Bowers, A. C. Gossard, J. W. Dong, and C. J. Palmstrom. Self-assembled ErAs islands in GaAs: Growth and subpicosecond carrier dynamics. *Applied Physics Letters*, 75 (22):3548–3550, 1999.

[59] Peter C. Sercel. Multiphonon-assisted tunneling through deep levels: A rapid energy-relaxation mechanism in nonideal quantum-dot heterostructures. *Phys. Rev. B*, 51:14532–14541, May 1995. doi: 10.1103/PhysRevB.51.14532. URL http://link.aps.org/doi/10.1103/PhysRevB.51.14532.

[60] Yu.I. Mazur, Zh M. Wang, G.G. Tarasov, Min Xiao, G.J. Salamo, J.W. Tomm, V. Talalaev, and H. Kissel. Interdot carrier transfer in asymmetric bilayer InAs/GaAs quantum dot structures. *Applied Physics Letters*, 86 (6):063102–063102–3, 2005. ISSN 0003-6951. doi: 10.1063/1.1861980.

[61] D. Leonard, K. Pond, and P. M. Petroff. Critical layer thickness for self-assembled InAs islands on GaAs. *Phys. Rev. B*, 50:11687–11692, Oct 1994. doi: 10.1103/PhysRevB.50.11687. URL http://link.aps.org/doi/10.1103/PhysRevB.50.11687.

[62] J. M. Moison, F. Houzay, F. Barthe, L. Leprince, E. André, and O. Vatel. Self-organized growth of regular nanometer-scale Inas dots on GaAs. *Applied Physics Letters*, 64(2):196–198, 1994. doi: http://dx.doi.org/10.1063/1.111502. URL http://scitation.aip.org/content/aip/journal/apl/64/2/10.1063/1.111502.

[63] N.P. Kobayashi, T.R. Ramachandran, P. Chen, and A. Madhukar. In situ, atomic force microscope studies of the evolution of InAs three-dimensional islands on GaAs(001). *Applied Physics Letters*, 68(23):3299–3301, 1996. ISSN 0003-6951. doi: 10.1063/1.116580.

[64] T. J. Krzyzewski, P. B. Joyce, G. R. Bell, and T. S. Jones. Scaling behavior in InAs/GaAs(001) quantum-dot formation. *Phys. Rev. B*, 66:201302, Nov 2002. doi: 10.1103/PhysRevB.66.201302. URL http://link.aps.org/doi/10.1103/PhysRevB.66.201302.

[65] K. Neudert, F. Trojnek, K. Kuldov, J. Oswald, A. Hospodkov, and P. Mal. Ultrafast photoluminescence spectroscopy of InAs/GaAs quantum dots. *physica status solidi (c)*, 6(4):853–856, 2009. ISSN 1610-1642. doi: 10.1002/pssc.200880597. URL http://dx.doi.org/10.1002/pssc.200880597.

[66] R Heitz, A Kalburge, Q Xie, M Grundmann, P Chen, A Hoffmann, A Madhukar, and D Bimberg. Excited states and energy relaxation in stacked InAs/GaAs quantum dots. *PHYSICAL REVIEW B*, 57(15):9050–9060, APR 15 1998. ISSN 0163-1829. doi: {10.1103/PhysRevB.57.9050}.

[67] F Adler, M Geiger, A Bauknecht, F Scholz, H Schweizer, MH Pilkuhn, B Ohnesorge, and A Forchel. Optical transitions and carrier relaxation in self assembled InAs/GaAs quantum dots. *JOURNAL OF APPLIED PHYSICS*, 80(7):4019–4026, OCT 1 1996. ISSN 0021-8979. doi: {10.1063/1.363361}.

[68] J. Siegert, S. Marcinkevi˘ cius, and Q. X. Zhao. Carrier dynamics in modulation-doped InAs/GaAs quantum dots. *Phys. Rev. B*, 72:085316,

Aug 2005. doi: 10.1103/PhysRevB.72.085316. URL http://link.aps.org/doi/10.1103/PhysRevB.72.085316.

[69] T. Muller, F. F. Schrey, G. Strasser, and K. Unterrainer. Ultrafast intraband spectroscopy of electron capture and relaxation in InAs/GaAs quantum dots. *Applied Physics Letters*, 83(17):3572–3574, 2003. ISSN 0003-6951. doi: 10.1063/1.1622432.

[70] Evgenii S. Moskalenko, Mats Larsson, K. Fredrik Karlsson, Per Olof Holtz, Bo Monemar, Winston V. Schoenfeld, and Pierre M. Petroff. Enhancement of the Luminescence Intensity of InAs/GaAs Quantum Dots Induced by an External Electric Field. *Nano Letters*, 7(1):188–193, 2007. doi: 10.1021/nl062417u. URL http://pubs.acs.org/doi/abs/10.1021/nl062417u.

Chapter 3

Laser Pumping of Terahertz Systems

In this chapter, the design and implementation the optical driving schemes used for testing devices is discussed. Several different laser systems were employed, including: laser diodes; solid-state lasers; and optical parametric oscillator systems. This includes both pulsed and CW laser systems, utilising well-established pumping methods as well as novel regimes. Section 1.2.4 gives a more in-depth description of the implementation of optical pumps in 'full' THz systems, so descriptions in this chapter are confined as much as possible to the optical systems presented here only.

3.1 Laser Measurement and Control Systems

The various equipment and experimental setups used in the driving of laser systems are discussed in this section and the characterisation of their optical signals is described. The systems used in this work were driven electrically in the case for laser diodes and optically in the case for Ti:Sapphire lasers. Laser systems were controlled in each case via beam alignment elements and thermal stabilisation, using different methods for each system type. There were several important signal parameters requiring different measurement techniques, predominantly including: the optical power and spectrum; temporal optical pulsewidth (where appropriate); and pulse repetition rate (where appropriate).

3.1.1 Laser Control Systems

Each laser system used in these experiments was tested ultimately for their use in an effective, stable, efficient THz transceiver system, and must be stable and predictable in their operation. To this end, a high degree of thermal and/or electrical control was employed in the driving of every laser system presented here. In each case, the laser gain medium must be kept thermally stable so to avoid any changes in refractive index, physical dimensions and spectral gain, for example, as much as possible during operation. In the case for semiconductor lasers, there was the additional constraint of electrical driving stability, as fluctuation or noise in the gain current can significantly affect the output power and wavelength, which in turn may lead to energy drift effects particularly in external feedback cavity setups.

The Ti:Sapphire system used in this work was driven optically by a solid-state green pump laser at 532 nm wavelength (Finesse), which in turn was kept thermally and electrically stable using a separate drive/control unit (Laser Quantum). The pump laser was initially set to an output power of 5.3 W, at which point an optimal alignment through the Ti:Sapphire crystal was achieved using simple beam steering optics placed before the Ti:Sapphire and compression cavity. The Ti:Sapphire crystal itself was additionally kept thermally stable using a water cooling system (NanoTherm3$^{\text{TM}}$) at a fixed temperature setting of $20°C$. The pump laser power was then reduced to 4.6 W to maintain the optimal conversion state in the crystal cavity and the system was then left for at least 20 minutes to ensure that again a state of thermal stability was reached.

In the case for all LDs, the chips were maintained at a steady temperature using a thermoelectric cooler (TEC) controlled by either a high-precision bipolar temperature controller (ICE-BLOC TC-4 [1]) provided by M^2 Lasers [2], or a unipolar temperature controller (LDD1-1T-D) with a temperature stability of $0.1°C$ provided by AlphaLas [3]. For each LD, the gain current was delivered using either a laser diode current driver (DD70) with a current noise level of $<0.01\%$ provided by M^2 Lasers, or by the LDD1-1T-D unit that was also used as the TEC controller. It was found that the TC-4 and DD70 TEC and current controllers were most stable and had a more sophisticated software-based control suite, and so they were predominantly used. In the case for two-section QD LDs,

the reverse bias voltage was applied to the absorber section using a Thurlby Thandar PL330 power supply unit.

For all laser systems, the optical power was measured using either a ThorLabs S121C Si photodiode or S144C InGaAs photodiode detector head, which was monitored using ThorLabs' corresponding PM100D power meter. The S121C is used to measure the power at optical wavelengths of 400–1100 nm and the S144C is used at wavelengths of 800–1700 nm.

3.1.2 Optical Spectrum Analyser

As discussed in Section 1.2.4, the operational optical spectral range of our laser pump system was a crucial factor in the pumping efficiency of our photoconductive antenna devices. The spectrum of our laser systems were measured using a compact A.P.E. USB-interface "waveScan" spectrometer.

This system operates on the principle of spectral separation and measurement using a diffraction grating, shown in Figure 3.1. The diffraction grating is rotated continuously at a rate of 6 Hz, which is controlled and tracked with high precision by the on-board drive electronics. The output from this was focussed to a Si-based photodetector and an optical intensity measurement was taken continuously throughout the rotational scanning. This allows measurement of the intensity of small portions of the optical spectrum over the full effective spectral range of the grating and detectivity range of the photodetector. The resolution of each measurement is therefore determined by the temporal window over which each intensity measurement is made, and how accurately this can be coordinated with the rotation of the grating. This constitutes a comparatively simple, high refresh-rate spectrometer with spectral resolution around 0.2 nm and spectral analysis range of 800-1600 nm. As such, the waveScan unit was sufficient for alignment and tuning of optical systems presented in this work.

3.1.3 Autocorrelation System

The effectiveness of pulsed-laser-driven photoconductive THz systems is based fundamentally on the speed of the ultrashort driving laser pulses (see Section

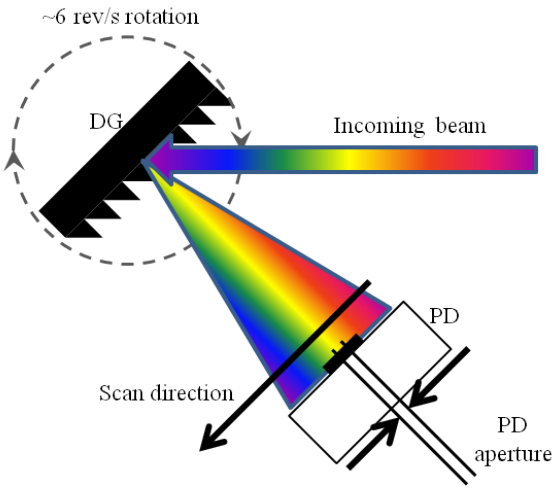

FIGURE 3.1: Schematic of the A.P.E. "waveScan" optical spectrum analyser basic operating principle. DG - diffraction grating; PD - photodetector.

1.2.4.1), so in the case for pulsed laser systems, the output signals must be characterised in terms of their temporal pulsewidths. For this, a Femtochrome FR-103XL rapid scanning auto/crosscorrelator system based on SHG autocorrelation was used.

This type of system operates by splitting the test beam into two parts, applying a pre-determined variation to the time-of-flight of one part, then recombining it with the first (reference) part to monitor the time-varying interference between the two parts and thereby retrieve the temporal structure information of the pulse. The time-of-flight variation was applied using a rotating parallel mirror set, the interaction between the delayed beam and the reference beam was achieved by combining the beams in a nonlinear crystal and monitored by a photodetector, and the determination of time-of-flight variation and calibration of output signal temporal scale was achieved using a micrometer delay line on the reference beam as shown in Figure 3.2. The input beam (shown in red) was either free-space or fibre-coupled. RM1 and RM2 rotate at a continuous speed and provide the varying time-of-flight delay over a scan range determined by the alteration in beam path length during rotation. The split beam was recombined in the NLC and the second harmonic signal generated was analysed at the photomultiplier (PMT). The PMT output signal was monitored using an oscilloscope and it was found that 1 ms on the oscilloscope timebase corresponded to 19.1 ps in 'real-world' beam time-of-flight, calibrated by altering the delay-line path length and monitoring the shift in the pulse profile on-screen. As the

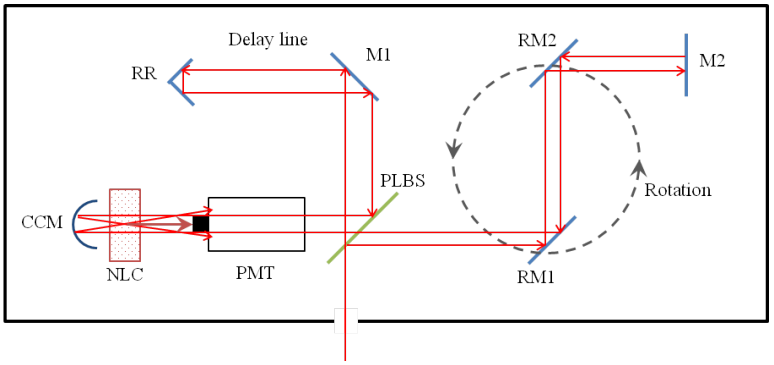

FIGURE 3.2: Optical schematic of the FR-103XL auto/crosscorrelator system. PLBS - pellical beamsplitter. M1 and M2 - stationary metallised mirrors. RM1 and RM2 - rotating mirrors. RR - retroreflector. CCM - concave mirror. NLC - nonlinear crystal. PMT - photomultiplier.

delay-line length was increased by say 1 mm (equal to a time-of-flight change of $(1 \times 10^{-3}) / (3 \times 10^{8}) \approx 3.33ps$) using the micrometer control, the corresponding temporal shift in the pulse peak position (in ms) on the oscilloscope could be read. This FR-103XL system was capable of resolving temporal beam features to <1 fs over an optical wavelength range of 800-3000 nm. The scan range was >185 ps and the PMT detector could detect a signal of minimum power $P_{av} \times P_{peak} = 10^{-7}\ W^2$.

3.1.4 Radio Frequency Spectrum Analyser

The pulse repetition rate of a laser system is determined by a multitude of crucial features in the layout of the cavity itself and conveys important information regarding the nature of the output signal. For example, the duty cycle of a pulsed laser system is inherently related to the repetition rate and associated peak and average powers; and the distribution of signal peaks in the radio frequency (RF) operating spectrum of a mode-locked laser strongly indicates the system's mode-locking stability. The pulse-to-pulse stability of a laser pump source for THz systems is of high importance in the stability and accuracy of the system as a whole, as artefacts such as timing jitter can introduce phase shifts and subsequent spectral measurement errors in the generated THz signals. The RF spectrum analyser used to measure laser outputs in this work was a Rohde and Schwarz RSP Spectrum analyzer FSP-40.

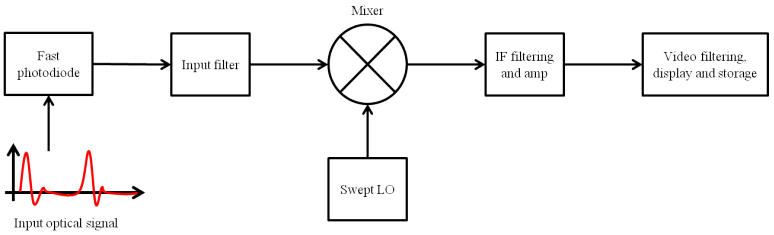

FIGURE 3.3: System schematic of the RF spectrum analyser. IF - intermediate frequency. LO - local oscillator. The fast photodiode shown here is a separate unit which connects to the system input, and the filtered output signal is plotted on a small LCD screen on the system housing.

This system operates essentially on the principle of heterodyning (mixing) of an incoming pulse signal with a locally generated oscillating signal and a basic system schematic is shown in Figure 3.3. The incoming optical pulse train was sent via fibre to a 29 GHz D-15 Newport fast photodiode detector, which converts the optical signal to a varying electrical signal. This signal was then mixed with the sweeping local oscillator source, and the resulting intermediate frequency (IF) at each mixed frequency interval was amplified and this narrowband GHz frequency amplitude was recorded and displayed at the corresponding location on the RF spectrum plot. This means that an optical input pulse with a very well-defined fundamental pulse repetition rate at say 1 GHz would be represented as a very narrow peak at the 1 GHz, with further harmonic peaks at consecutive 1 GHz intervals thereafter, and any additional spectral features (e.g. sidebands) would be caused by interference modulation within (most likely) the optical cavity or drive system of the laser source.

3.2 Ultrafast Laser Systems

Ultrafast lasers provide the most effective pump signals for THz systems. The reasons for this are manifold as discussed in Section 1.2.4.1, but this is predominantly because of the high peak pump powers which can be introduced into the photoconductive emitter and corresponding high optical-to-THz conversion efficiency, as the emitted THz output power is a superlinear function of optical pump power (see Equation (1.2.4.2)). For this reason, various different pulsed laser systems were considered in the development of the systems presented here,

as a significant aspect of this work was investigation of the possibility to optically pump THz PCA devices over different wavelengths in the same setup (see Section 4.1) and the conversion efficiency in these cases should be as high as possible. This section outlines the characteristics of the pulse-regime optical pump systems used for the various experiments presented here.

3.2.1 Ti:Sapphire Lasers

An in-depth description of the operation principles of Ti:Sapphire systems in general is given in Section 1.2.1. The Ti:Sapphire laser used in this work was provided by M^2 Lasers (Sprite). The system was relatively compact and stable, and provides a reliable pump signal for systematic testing of photoconductive devices based on $In_xGa_{1-x}As$, LT-GaAs and GaAsBi semiconductor materials as the operating wavelength $\lambda_{peak} \approx 810\ nm$ ($\approx 1.56\ eV$) is readily absorbed in such tertiary blends throughout the entire $0 \leq x \leq 1$ range. The custom Sprite laser was pumped by a green CW laser (Finesse) operating at 532 nm wavelength and 4.6 W power. The mode-locked output pulse repetition rate was $f_{rep} \approx 99.5\ MHz$ and pulsewidth $\tau_p \approx 100\ fs$. The compression optics in this system were based on a prism pair, knife-edge and rear reflector as discussed in Section 1.2.1 and Figure 1.4. This output beam had an average power which could be varied between 4 mW and 320 mW using an optical neutral density (broadband) filter with corresponding peak powers between roughly 400 W and 32 kW. Exemplary optical, autocorrelation and RF spectrum are given in Figure 3.4, showing a broad optical output spectrum with $\sim 70\ nm$ bandwidth; ultrashort pulse with a FWHM of $\sim 97\ fs$; and RF linewidth of $\sim 0.1\ kHz$.

3.2.2 Ultrafast Quantum Dot Diode Lasers

For generating high power ultrashort pulses in these experiments, various different diode laser devices were used and device descriptions are given here with exemplary optical, autocorrelation and RF spectral characteristics, where appropriate. A more in-depth description of two-section, QD-based ultrafast pulsed diode laser principles and properties is given in Section 2.2.4. As described, these devices were operated much like traditional laser diodes but with a gain

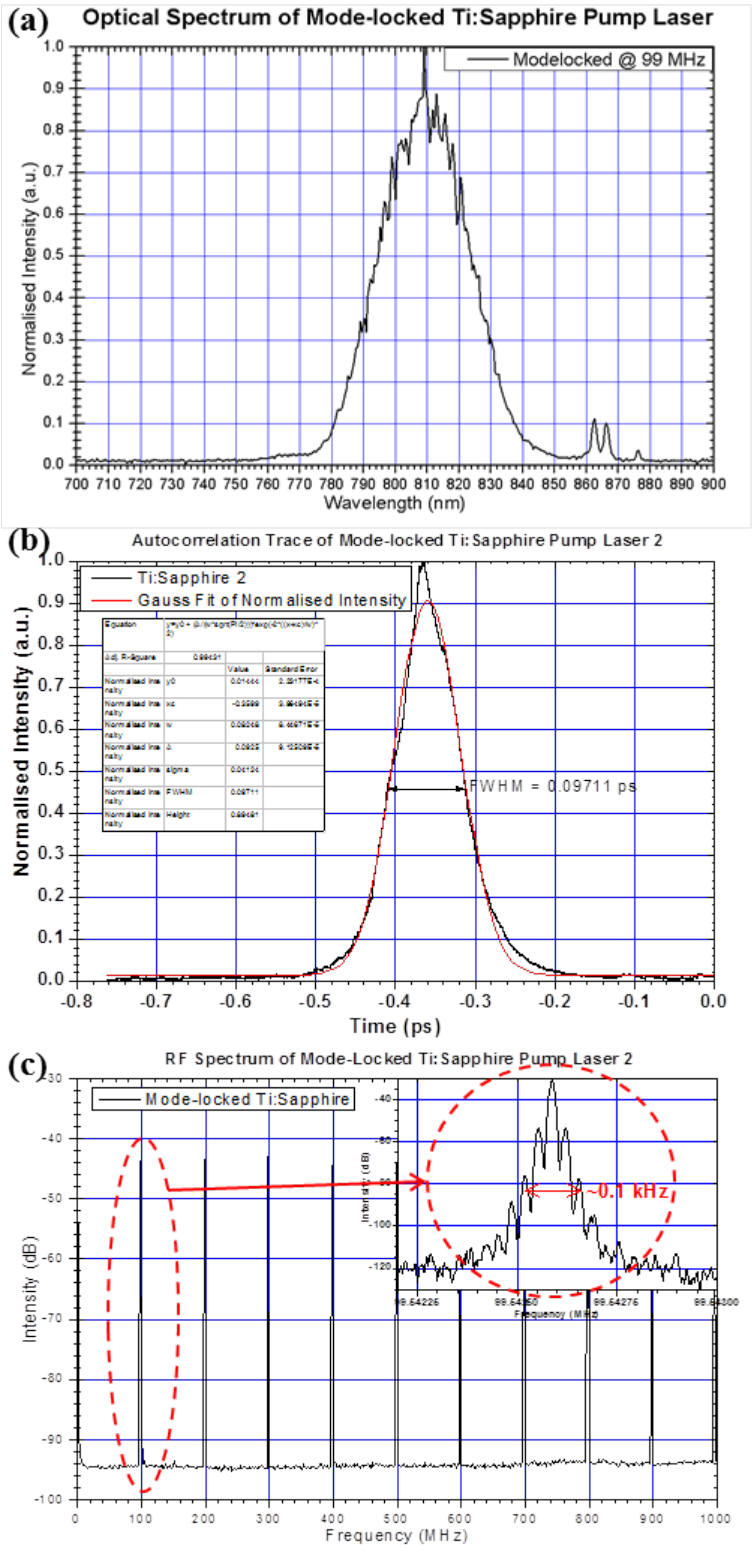

FIGURE 3.4: Exemplary (a) optical; (b) autocorrelation (time-domain); and (c) RF spectrum for the "Sprite" Ti:Sapphire laser system.

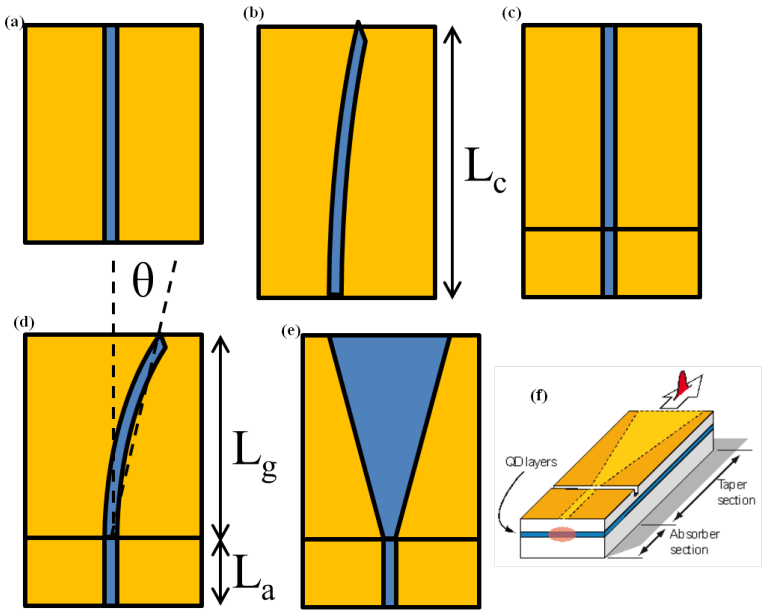

FIGURE 3.5: Configurations of the various different QD LD chips tested. (a) single-section with straight-waveguide and HR/AR facets; (b) single-section angled waveguide with high-AR/AR facets; (c) two-section with straight-waveguide and HR/AR facets; (d) two-section angled waveguide with high-AR/AR facets; (e) tapered waveguide gain section and straight waveguide absorber section; and (f) is a cartoon of the general layout of devices over their gain medium. L_a - absorber length; L_g - gain section length; L_c - laser chip length; θ - waveguide angle.

medium which extends the gain bandwidth over 200 nm in the $1.1-1.3\ \mu m$ range [4], with the addition of a saturable absorber section that acts as an ultrafast time-varying mirror within the laser cavity to engage optical mode-locking with ultrashort temporal pulsewidths. A range of different LD device configurations were investigated, summarised in Figure 3.5, including a range of structural laser layout as well as QD layer numbers, QD size/material variation and different external cavity configurations. The structure variations included a range of laser chip lengths (L_c); gain/absorber length (L_g/L_a) ratios; and when angled waveguides were used, θ was typically 7°. Presented here is data pertaining to the tuning of these devices with the aim of implementation as ultrafast pulse pump sources for THz systems.

The simplest configuration was a two-section device with a straight waveguide, a highly-reflective (HR) and an anti- reflective (AR) facet, 10 QD gain layers, and a gain:absorber section ratio of 4:1. This chip type was used predominantly for the characterisation of volume Bragg Grating (VBG) elements [5] in the CW regime

as discussed in Section 3.3, and also served as an effective device in pulsed tests. This was simply because there were more variations of this chip type available than any other and these had a variety of operational characteristics such as: repetition rates of 5–20 GHz [6]; average output powers up to 200 mW; and gain bandwidths centred around either *or both* ground- and first-excited-state wavelengths [5, 7], which was extremely useful for multi-wavelength tests. Various tapered gain section devices were also tested with different lengths, gain:absorber ratios and QD layer numbers. Exemplary mode-locked RF, optical and autocorrelation spectrum of a mode-locked 8 mm tapered two-section QD LD are given in Figure 3.6.

The output pulse performance data is presented here as an example of the pulsewidth shortening behaviour which was achieved by altering the reverse bias across the absorber section of these devices, and was crucial in the process of configuration as effective pulsed pump sources. The figure indicates a mode-locked pulse repetition rate at 10 GHz and that as the reverse bias was increased and gain current was reduced, the pulsewidth can be gradually reduced to a few picoseconds FWHM in this sample, but has been demonstrated to below 1 ps [8]. The RF linewidth of the mode-locked pulse in this case was also somewhat broad, but can be reduced and 'cleaned' with further tuning and improved alignment of the cavity. The only variation in angled-waveguide laser chips was whether they were one- or two-section, i.e. CW or pulse regime, and all such samples were chirped-gain medium type.

To gain further insight into the practical interpretation of the achievable output pulse performance from mode-locked QD LD's, mathematical evaluations of the temporal pulse properties were often conducted. For this, output pulse autocorrelation spectra were firstly modeled using either Gaussian, Lorenzian or sech^2 power fitting curves as described in Equations 1.2.1.3-1.2.1.5. This was done to recover accurate estimation of temporal pulse FWHM and corresponding TBWP, which in turn allows some evaluation of the extend of pulse broadening through chirp effects. As typical examples of this process, the fitted output pulse curves for the Ti:Sapphire laser and a tapered two-section QD LD are given in Figure 3.7.

These autocorrelation spectra indicate firstly that each pulse is closely modeled using a Gaussian pulse profile, and also that the Ti:Sapphire exhibits a much

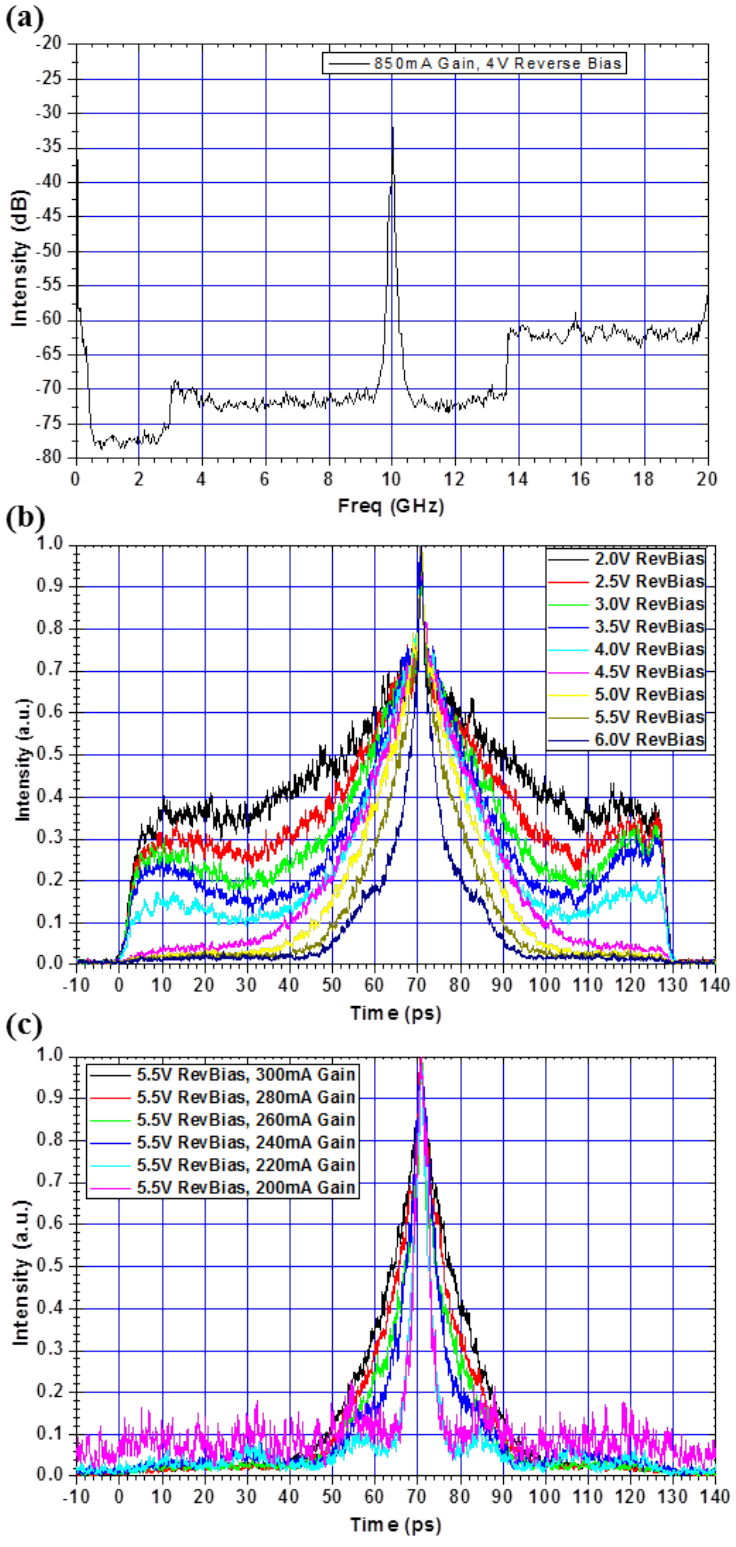

FIGURE 3.6: Example (a) RF and (b,c) autocorrelation spectrum taken from a tapered two-section QD LD, indicating a 10 GHz mode-locked pulse repetition rate and output pulsewidth which is electrically tunable down to a few ps in this case.

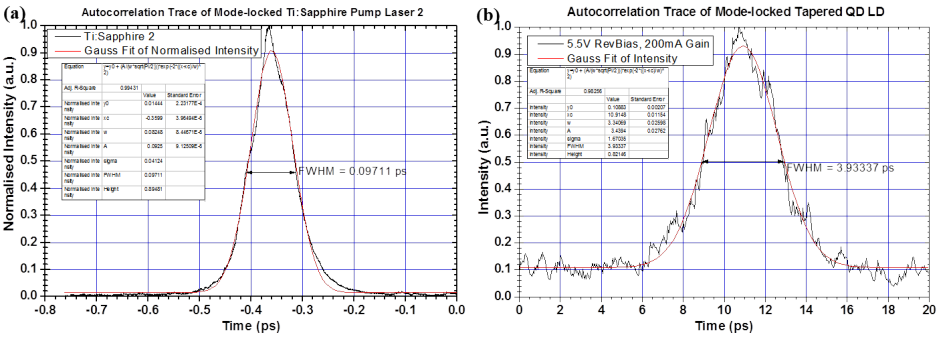

FIGURE 3.7: Exemplary autocorrelation spectrum taken from (a) the Ti:Sapphire laser and (b) a tapered two-section QD LD, with mathematically-fitted pulse models shown in red.

shorter pulsewidth compared with the QD LD, as was typically the case. The pulsewidth of the QD LD output in this example was estimated by the fitting program (Origin Pro) as 3.93 ps. This pulsewidth is essentially too long to be used efficiently as an optical pump signal in THz systems for two main reasons. Firstly, this length of optical excitation will tend to 'smear' most of the sub-ps photocarrier generation and relaxation processes in the THz PCA, inhibiting THz EM pulse generation. Additionally, a more rigorous mathematical evaluation of the pulse reveals that Fourier-transformed signal frequency spectrum of the changing electric field $\delta E/\delta t$ results in a peak spectral amplitude at sub-THz frequencies that rapidly decays before reaching the $\gtrsim 300\ GHz$ range of interest. For comparison, plots of the temporal evolution of the pulse power derivative $\delta P/\delta t$ from both the Ti:Sapphire laser and the same QD LD are given in Figure 3.8. Plot 3.8(c) here is given simply as a clearer comparison of the relative pulse power derivatives with respect to time for each output pulse signal. The x-axis here is normalised to the maximal and minimal extents of the pulse profile in time, taken as the minimum and maximum x-axis points in the fitted curves (red) shown in Figure 3.7; and the y-axis is the calculated derivative $\delta P/\delta t$ of the normalised Gaussian-fitted pulse power profile. As such, this was plotted as a demonstration of the difference in $\delta P/\delta t$ for each pulse only and any temporal overlap between features of the two curves are not relevant – the Ti:Sapphire pulse has essentially been 'stretched' in time to allow for a clearer graph. Plot 3.8(d) here shows the Fourier transform power spectrum (black curve) of the mode-locked QD LD optical pulse power derivative shown in plot (b).

It can be seen from Figure 3.8(c) that the value of the pulse power derivative

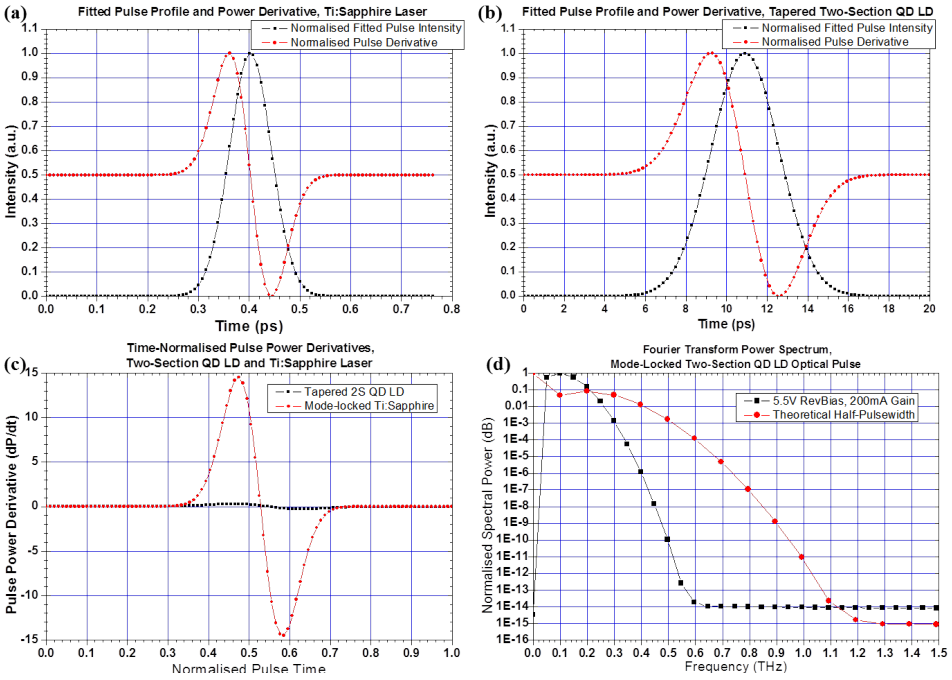

FIGURE 3.8: Derivatives of the pulse power with respect to time for (a) the Ti:Sapphire laser and (b) a tapered two-section QD LD. For reference, (c) is a 'time-normalised' plot of the *un-normalised* power derivatives of the fitted pulse profile from each system. (d)(black curve) shows the calculated Fourier transform frequency power spectrum of the derivative of the mode-locked QD LD output pulse in plot (b); and (d)(red curve) shows the power spectrum of the same pulse profile compressed to exactly half the FWHM.

for the mode-locked tapered QD LD output is relatively low compared with that of the Ti:Sapphire laser. It should be noted that the field amplitude of the THz output signal in a pulse-regime PCA-based THz system is related to the generated PCA photocurrent as in Equation 1.2.4.3 and the time-dependent optical pump power $P(t)$ as below:

$$E_{THz} \propto \frac{\delta P(t)}{\delta t}. \tag{3.2.2.1}$$

As such, it is reasonable to infer that this particular LD sample is less effective than the Ti:Sapphire laser as an optical pump source for a PCA-based THz system. The peak Fourier-transformed spectral power amplitude of the Ti:Sapphire when calculated using the same methods is at roughly 3.9 THz and shows a gradual power decay over tens of THz, which is in stark contrast to the power spectrum of the mode-locked QD LD optical pulse as shown in plot 3.8(d). This frequency power spectrum plot represents the relative optical pump efficacy

across the expected maximum working THz spectral range of a PCA-based THz source pumped by this particular LD. As such, these results and evaluations build a picture of the actual practical effectiveness which may considered in the design of a THz source (and by extension a complete THz transceiver system) and the relative efficacy of the LD pump system may be evaluated. As further demonstration of this, the red curve in plot 3.8(d) is the resultant calculated frequency bandwidth of an optical pulse of exactly half the temporal pulsewidth (2 ps) of the QD LD pulse corresponding to the black curve. Indeed, the peak spectral power is at effectively double that of the black curve, indicating that a reduction of the pulsewidth by only a factor of two in this case can extend the working spectral range of the system to twice the THz frequency. This would of course still be limited by the active PC materials in the PCA for a real THz system, but it is observed that continuously decreasing the optical pulsewidth yields a continuously increasing THz spectral bandwidth.

Similar mathematical evaluation techniques of generated ultrafast EM output waveforms are typically applied for the analysis of PCA performance in THz systems, as applied in Section 5.3.2 for the devices presented in this work. It is worth noting in this case that several of the two-section QD LD's used in this work had previously been demonstrated to exhibit optical pulsewidths around 1 ps, but the complexity of the laser monitoring systems and the subsequent GVD that was likely induced in the pulses made identification of such signals difficult. As such, the lowest *measured* optical pulsewidths from all two-section QD LDs were on the order of 2 ps and were not transform-limited upon measurement at the autocorrelator.

Two-section pulsed devices involve overall perhaps the simplest optical setups regarding LD pump sources due to the monolithic integration of fundamental features and 'direct' thermal or electrical control of output signal properties (see Section 2.2.1), but the scope for further configuration of these devices, particularly in the CW regime, is considerable and some of the implemented external cavity setups for dual- and multi-mode operation is discussed in the next section.

3.3 Dual- and Multi-Mode Laser Systems

As discussed in Section 1.2.4.2, the generation of CW THz signals in PCA-based systems is based upon the photomixing principle and use of dual-modal optical pump signals. The generation of such optical pump signals for THz photomixers has been accomplished in several different ways. This includes: systems of tunable multiterahertz difference frequency generation via two-wavelength LD arrays [9]; spatial combination of two pulsed Ti:Sapphire lasers or CW LDs [10]; single monolithic dual-longitudinal-mode LDs [11]; spectral tuning of a single LD using gratings and an etalon [12]; dual-mode tuning of a single LD using single [13] and/or multiple ("multiplexed") VBGs in an external cavity [5, 14]; and tunable systems using a single LD in a 'double-Littrow' configuration [15, 16]. Described here is the configuration of several different optical systems, all based on laser diodes, which were implemented in this work as dual-mode optical pump sources.

3.3.1 Dual Distributed Feedback Laser Setups

Discussed earlier (Section 3.2.1) was the use of the Ti:Sapphire laser a high-power pulsed pump source operating at optical wavelengths readily absorbed by the entire $In_xGa_{1-x}As$ tertiary blend range, and the traditionally employed CW 'alternative' at this wavelength range is the two-distributed feedback (DFB) laser pump system [10]. This was constructed using a pair of DFB laser diodes provided by G. Erbert of the Ferdinand-Braun-Institut [17] which operated at wavelengths around 847 nm and 850 nm [18], the difference frequency between which could be tuned in the range 0.76–1.31 THz by varying their operating temperature using a thermoelectric element as shown in Figure 3.9. The output from each LD was collected and collimated by an aspheric lens, then refocussed by similar apsheric lenses to be introduced into a 2:1 polarisation-maintaining fibre splitter/combiner. This allows a high degree of spatial overlap between the two beams to be achieved before collection, refocussing and introduction to the PCA active region. The CMOS camera was employed with a telescopic zoom lens here to precisely monitor the focussed pump beam alignment to the appropriate location between the PCA contacts.

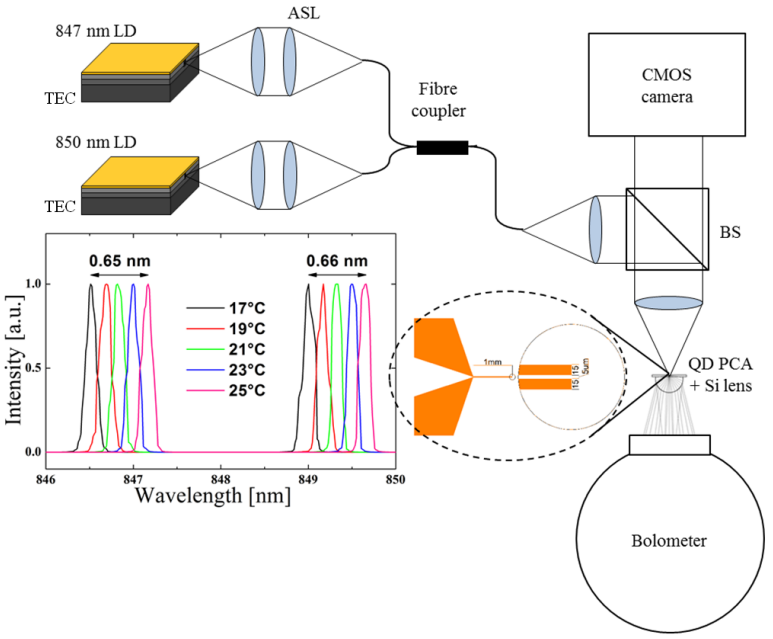

FIGURE 3.9: Optical schematic of the two-DFB LD optical pump system. ASL - aspheric lens; TEC - thermoelectric coolers; BS - beamsplitter; QD PCA - quantum dot photoconductive antenna. Shown insets are the respective operating wavelengths and zoomed view of example antenna contacts.

3.3.2 Multiplexed Volume Bragg Gratings

VBGs are essentially customisable Bragg gratings which are 'implanted' throughout the volume of a small photothermorefractive (PTR) glass window using material doping and holographic writing techniques. PTR glass is a silicate glass doped with Ce, Ag, F and Br and is photosensitive. Under UV holographic exposure and a thermal development process, a refractive index change was induced in the window volume within the features defined by holographic pattern, which may be designed as successive planes throughout the window to form a Bragg grating [19], hence it is referred to as a "volume Bragg grating". VBGs have been shown to exhibit exceptional stability as wavelength modulators in external feedback laser systems [20], giving stable operation over a wide range of operating temperature for example. It is also possible to develop more than one Bragg grating throughout the glass volume, each designed to reflect a different narrow optical wavelength, and these so-called 'multiplexed' VBGs may be designed to reflect two specific closely-spaced wavelengths when they are interlaced within the window. This essentially creates an external cavity optical feedback element which allows laser operation at two simultaneous wavelengths, which constitutes

VBG Label	λ_1 (nm)	λ_2 (nm)	Difference Frequency (THz)
VBG 1	977	980	0.9400
VBG 2	1177	1182	1.0782
VBG 3	1257	1262	0.9456
VBG 4	1180	1260	16.1421

TABLE 3.1: Volume Bragg gratings used in dual-wavelength laser system tests.

a fixed dual-mode optical pump signal with a different frequency at a pre-defined THz value.

In the systems used here, four different VBG elements were used, characterised by their respective reflected wavelengths. A summary of the VBGs used, their peak reflected wavelengths and respective modal difference frequencies is given in Table 3.1.

All VBGs are referred to as *reflection* VBGs when operated in this regime. VBGs 2–4 had a diffraction efficiency of $15 \pm 1\%$ and window dimensions around $4 \times 3 \times 4\ mm$. VBG 1 was effective at a different wavelength range than the others, has a diffraction efficiency of 30% and was used in external feedback configuration with a 150 μm broad area stripe quantum-well InGaAs–GaAs LD in the CW regime. This broad stripe LD could be driven at gain currents up to 3 A, generating an output power up to 2 W. VBGs 2–4 were effective at longer wavelengths corresponding to the spectral gain regions of the various QD LDs used here, which typically were driven at lower gain currents between 40 mA and 1.5 A and generated output powers between 30 mW [5] and 1.7 W [14], depending on the LD type being used. Exemplary optical spectral outputs are given for each case in Figure 3.10, with corresponding LD type, operating characteristics and output powers indicated. Additionally, a table at the end of this chapter fully summarises the range of LD's used and corresponding characteristics.

3.3.3 Tunable Double-Littrow Configuration

Described here is the novel use of ultrabroadly-tunable QD-based laser diodes as a dual-mode CW optical pump source for driving a THz PCA. As discussed in Section 2.2.1, configuration of the operational wavelengths, or gain bandwidth,

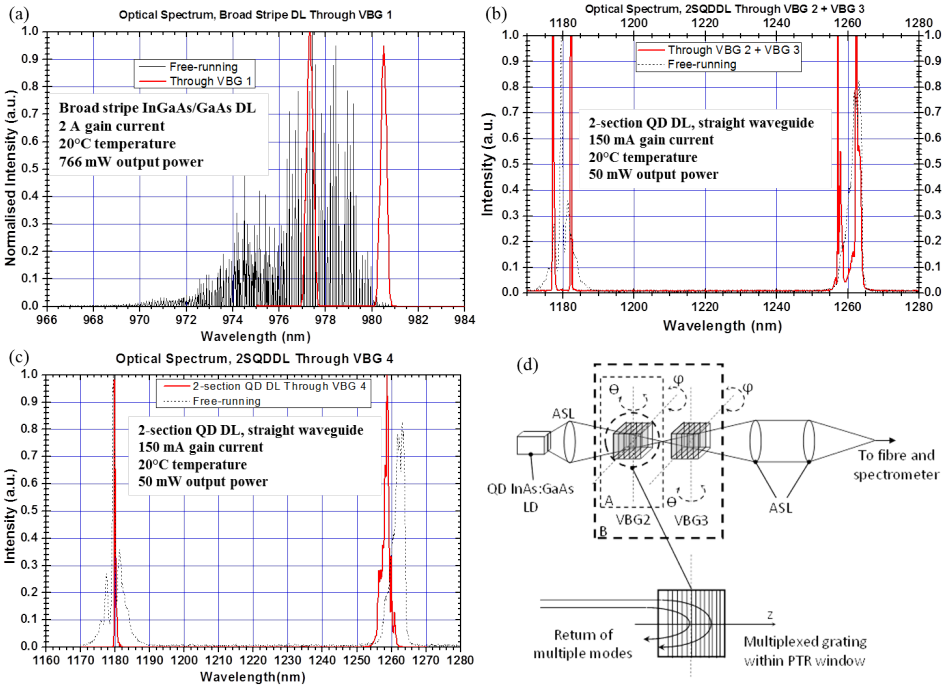

FIGURE 3.10: Exemplary optical spectrum from different QD LDs operating in an external cavity setup with the various VBGs presented here. (a) Broad stripe InGaAs/GaAs QW LD through VBG 1; (b) 2-section QD LD through VBGs 2 + 3; (c) 2-section QD LD through VBG 4; and (d) is a schematic of the beam propagation through either one (A) or two (B) VBGs. θ and φ are the angles used when tuning VBG retroreflection alignment; ASL - aspheric lens.

of QD-based LDs is engineered in part by the semiconductor deposition/growth process during production of the device. Using standard MBE techniques, the material grower may deposit layers of QDs with a range of physical sizes, dot density and layer spacing, for example. Much of the work presented here was related to the configuration of QD LD-based setups in a so-called 'chirped gain bandwidth' device [4]. This method involves the deposition of multiple layers of QDs with a variety of dot dimensions, allowing a broad range of operational energies/wavelengths. This solution was a highly versatile one as it was operational and tunable over a very wide spectral range at long (near telecoms-range) wavelengths by utilising the inhomogeneous broadening of the QD gain medium [16]. A one-section device with highly anti-reflecting end facets was employed in this case in a double-Littrow configuration as shown in Figure 3.11, such that two longitudinal modes may be circulated and continuously tuned whilst maintaining a single multi-mode output beam via extraction from the opposite facet of the device. Exemplary optical spectrum from this setup is also shown in Figure 3.11.

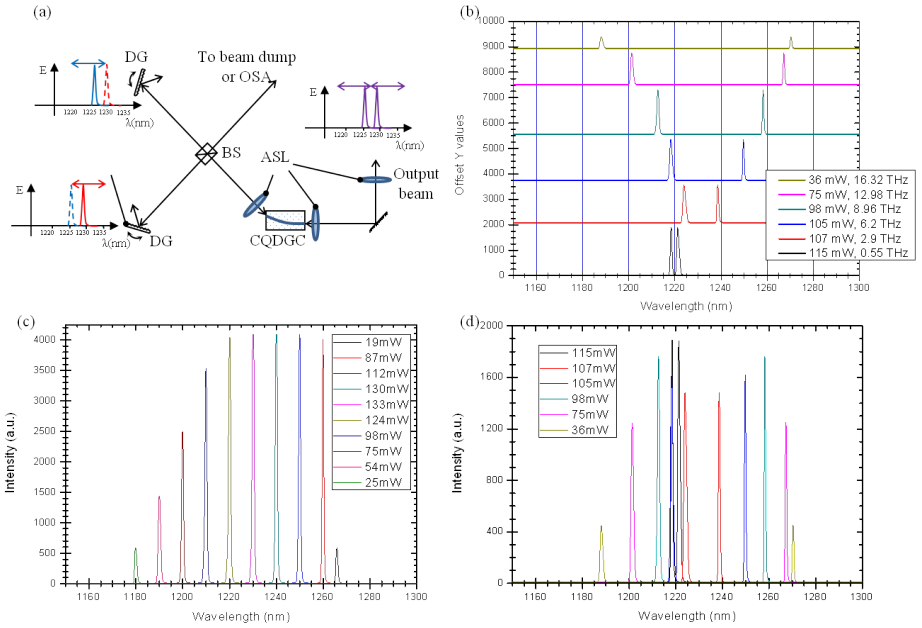

FIGURE 3.11: Tunable double-Littrow configuration of a chirped QD LD. (a) shows the optical schematic, CQDGC - chirped quantum dot gain chip, ASL - aspheric lens, BS - beamsplitter, DG - diffraction grating; (b) example broadly separated simultaneous dual-mode operation; (c) plots the the ultra-broad gain bandwidth; and (d) is graph (b) replotted on the same axes for further comparison.

As discussed in Section 3.2.2, these ultra-broadband chirped gain chips are extremely versatile and may be produced as two-section devices which could potentially be used for ultrashort pulse operation in a dual-wavelength or dual-repetition-rate regime, discussed further in the next section.

3.4 'Hybrid' Dual-Mode Pulsed Regimes

The spectral and temporal operational versatility of QD-based ultrafast LDs as discussed so far also allows scope for 'hybrid' pump systems, which may take advantage of both of these elements to produce a highly efficient optical solution. Two-section tapered devices such as the one shown in 3.5(d) may be configured in an external cavity setup to provide an extra degree of output tunability. Presented here firstly is a method involving the use of VBGs as external feedback elements, the novelty of which was the implementation of the system in simultaneous dual-wavelength and pulsed regime.

A VBG may be used in an external cavity configuration with a two-section QD LD to allow the generation of ultrashort pulses of dual-wavelength light, which provides a method for producing high peak power dual-mode pump signals to PC and EO THz emitters. This is particularly advantageous in PCA devices as ultrashort pulses with high peak powers impart significantly lower thermal energy to the device, thereby reducing the risk of thermal breakdown, whilst still imparting very high optical pump energy and hence high THz output power as discussed in Section 1.2.4.1. Optical schematics and some exemplary performance data of tapered two-section QD LDs in this configuration are given in Figure 3.12. The two 'effective' optical modes of the VBG at 1257 nm and 1262 nm wavelengths can be resolved, although with significant sidebands, and a typical temporal pulse FWHM of around 13 ps was acheived. As such, the operating conditions of such a system are so far demonstrably not fully suited to immediate application as a pulsed THz system optical pump source. However, this proof of concept was encouraging enough to merit further work on such configurations as an ultracompact, hybrid pulsed dual-mode optical pump source such as this could prove to be a fascinating and effective solution.

This main advantage of the setup would theoretically be the ability to generated a narrowband THz frequency signal via DFG in a photomixing antenna with high conversion efficiency without encountering the usual thermal constraints of a photomixer device. The THz difference frequency would be fixed by the VBG reflected modes but a suitable VBG may be pre-configured for a particular THz frequency of choice, for example in applications where only a specific chemical with a known THz spectral fingerprint is to be analysed or detected. It is likely, however, that further work will need to be done specifically regarding the spatial and temporal overlap of the optical modes. Interestingly, it was observed that the two different modes pulsed at two slightly offset repetition rates; around 9.75 GHz and 10 GHz as shown in plot (d), which may be due to the optical dispersion through the laser chip material [21]. This could indeed confirm the separate operation of the two wavelengths as two separate pulses from the same cavity but whereas this would be a disadvantage in terms of DFG and photomixing applications, this could potentially be utilised instead for example as an optical source as part of an ultrafast "asynchronous optical sampling" (ASOS) system [22]. This is because the system utilises two optical beams with slightly offset pulse repetition rate as the delay scanning mechanism. For this to be feasible,

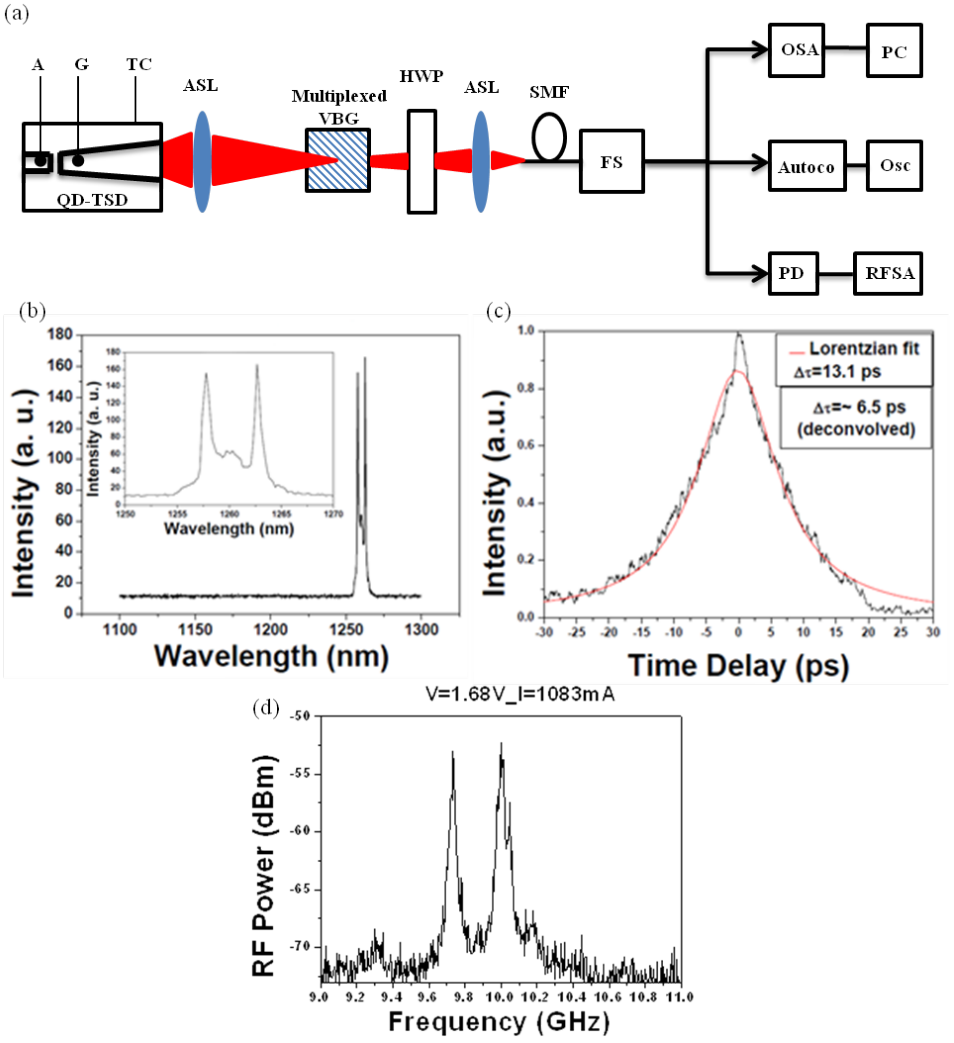

FIGURE 3.12: 'Hybrid' ultrafast pulsed dual-mode optical pump system based on a two-section QD LD and a multiplexed VBG in an external cavity configuration. (a) shows the optical schematic of the full characterisation setup and typical (b) optical, (c) autocorrelation and (d) RF spectrum from the system are given. A - absorber section; G - gain section; TC - temperature controller; ASL - aspheric lens; VBG - volume Bragg grating; HWP - half wave plate; SMF - single-mode fiber; FS - fiber splitte; OSA - optical spectrum analyzer; PC - personal computer; Autoco - autocorrelator; Osc - oscilloscope; PD - photodetector; RFSA - RF spectrum analyzer.

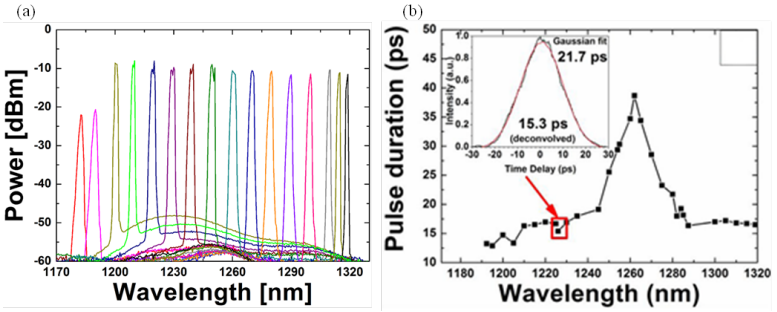

FIGURE 3.13: Exemplary output characteristics of a pulsed two-section ultra-broadband chirped QD LD. (a) shows the full gain bandwidth achievable and (b) shows the typical variation in temporal pulsewidth. Reproduced from Nikitichev *et al.*, 2012a.

the temporal pulsewidth(s) of the modes in this setup would both of course have to be reduced to below 1 ps, which would also involve a broadening of the optical wavelength FWHM of each mode.

Broadly tunable QD LDs such as the devices described in Section 3.3.3 above may also be configured as two-section devices, potentially enabling the device to produce ultrashort pulses while operating over a very broad spectral range [23]. Figure 3.13 shows an exemplary gain bandwidth of such a device in a 'traditional' Littrow configuration, indicating operation over the wavelength range $1.18-1.32\ \mu m$ and (b) shows the typical range of output pulse durations demonstrated over this tuning range. The variation in pulsewidth with optical wavelength is significant and generally is on the order of tens of picoseconds, but this could conceivably be reduced with further optimisation of the QD attributes and additional external cavity configuration.

This system was also tested in a dual-mode, double-Littrow configuration similar to the setup described in Section 3.3.3 above. The goal of this work was to generate either: an ultrashort circulating optical pulse with two distinct optical wavelengths; two circulating ultrashort optical pulses at two distinct optical wavelengths; or two circulating ultrashort pulses at the same optical wavelengths at continuously tunable, distinct repetition rates. It was found that stable mode-locking operation of a single pulse could be achieved whilst one tuning 'arm' of the setup dominated the QD chip gain, but obtaining stable mode-locking operation from the two separate arms simultaneously was more difficult. Tests did show, however, that when the two tuning arms were locked to the same optical wavelength and cavity length, a mode-locking regime could be achieved. Figure

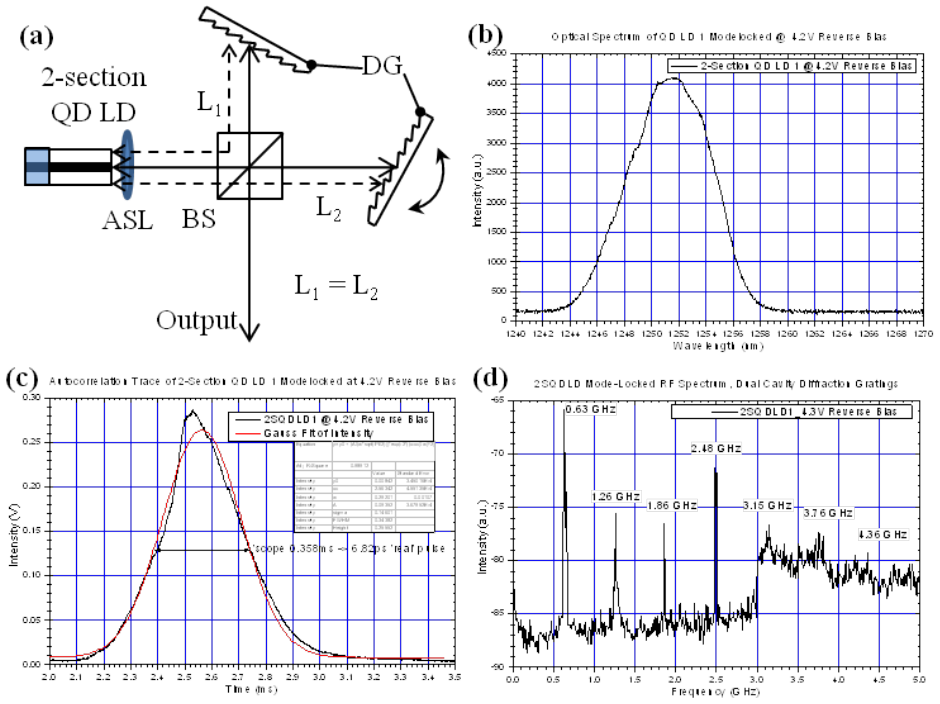

FIGURE 3.14: Modelocking of a two-section QD LD in the double-Littrow configuration showing: (a) the optical schematic; (b) free-running mode-locked optical spectrum; (c) free-running mode-locked autocorrelation trace, Gaussian pulsewidth ~ 6.82 *ps*; and (d) double-Littrow RF spectrum. ASL - aspheric lens; BS - beamsplitter; DG - diffraction gratings; L_1 and L_2 are the lengths of cavity arm 1 and arm 2, respectively.

3.14 gives exemplary data from such a setup, with RF spectrum showing the achieved fundamental mode-locking repetition rate at 630 MHz, corresponding to the return trip time in the ~ 23 cm dual external cavity.

To clarify, the cavity length in this setup was the defined by the external cavity formed by each diffraction grating as an end-mirror component and each cavity arm was made identical in length. In this case, a straight-waveguide two-section QD LD was used with a gain current of 130 mA and a reverse bias applied to the absorber section of 4.2–4.3 V. It was possible to achieve two distinct circulating pulses offset at slightly tunable repetition rates. The benefit of stable operation in this regime would be the possibility to configure a complete THz transceiver system using only a single QD LD as the pump source in an ASOS-based system as mentioned earlier. However, further tests are required to establish the stability of pulses in this regime. Theoretically, there is some minimum carrier relaxation time required between pulse formations and so there may be some periodic occurrence where at least one pulse cannot be resolved, for example, if

it arrives at the gain medium simultaneously or too soon after a pulse from the other tuning arm. This may be countered by further optimisation of the QD gain for ultrafast carrier capture, and controlled to some extent by the level of reverse bias applied to the chip's absorber section, but this limitation will always be in place due to the fundamental mode-locking principle in such semiconductor LD devices.

3.5 Summary and Conclusions

In this chapter, descriptions of the laser systems used in this work were given. The characterisation systems which were used to measure laser output characteristics were firstly described. These signal characterisation processes were necessary in the evaluation of a laser system's suitability as an optical pump for THz systems. Optical, autocorrelation and RF characteristics were presented, where appropriate, and many of the experimental optical pump systems presented in this work were evaluated based on their spectral, temporal and mode-locking stability performance. It was shown that the most effective (pulsed) optical pump system is the Ti:Sapphire laser due to the very low pulsewidth, extremely stable mode-locking, narrow Rf linewidth (low jitter), practical peak wavelength (absorbed by all $In_xGa_{1-x}As$) and high power range. LD-based pump systems were also investigated, and were shown to be very practical in their application as dual-wavelength CW optical pumps, conceivably practical as pulsed sources and a very interesting solution as a 'hybrid' combination of the two regimes. Many of these systems were implemented in the tests which are reported in the main results in Chapter 5.

3.6 References

[1] M-Squared Lasers 'ICE-BLOC' laser temperature controllers, 2013. URL http://www.m2lasers.com/products/instrumentation/diode-laser-temperature-controllers.aspx.

[2] M-Squared Lasers, 'Sprite' systems, 2013. URL http://www.m2lasers.com/products/laser-systems/femtosecond-laser.aspx.

[3] AlphaLas laser diode and thermoelectric cooler drivers, 2013. URL http://www.alphalas.com/products/laser-diode-drivers-and-tec-controllers/laser-diode-and-tec-peltier-drivers-tec-modules.html.

[4] K. A. Fedorova, M. A. Cataluna, I. Krestnikov, D. Livshits, and E. U. Rafailov. Broadly tunable high-power InAs/GaAs quantum-dot external cavity diode lasers. *Optics Express*, 18(18):19438–19443, 2010.

[5] R. Leyman, D. I. Nikitichev, N. Bazieva, and E. U. Rafailov. Multimodal spectral control of a quantum-dot diode laser for THz difference frequency generation. *Applied Physics Letters*, 99(17):171107, 2011.

[6] Maria Ana Cataluna, Ying Ding, Daniil I. Nikitichev, Ksenia A. Fedorova, and Edik U. Rafailov. High-Power Versatile Picosecond Pulse Generation from Mode-Locked Quantum-Dot Laser Diodes. *IEEE Journal of Selected Topics in Quantum Electronics*, 17(5):1302–1310, 2011.

[7] M. A. Cataluna, W. Sibbett, D. A. Livshits, J. Weimert, A. R. Kovsh, and E. U. Rafailov. Stable mode locking via ground- or excited-state transitions in a two-section quantum-dot laser. *Applied Physics Letters*, 89(8):081124, 2006.

[8] D. I. Nikitichev, Y. Ding, M. A. Cataluna, E. U. Rafailov, L. Drzewietzki, S. Breuer, W. Elsaesser, M. Rossetti, P. Bardella, T. Xu, I. Montrosset, I. Krestnikov, D. Livshits, M. Ruiz, M. Tran, Y. Robert, and M. Krakowski. High peak power and sub-picosecond Fourier-limited pulse generation from passively mode-locked monolithic two-section gain-guided tapered InGaAs quantum-dot lasers. *Laser Physics*, 22(4):715–724, 2012.

[9] C. L. Wang and C. L. Pan. Tunable Multiterahertz Beat Signal Generation from a 2-Wavelength Laser-Diode Array. *Optics Letters*, 20(11):1292–1294, 1995.

[10] K. A. McIntosh, E. R. Brown, K. B. Nichols, O. B. McMahon, W. F. DiNatale, and T. M. Lyszczarz. Terahertz photomixing with diode lasers in low-temperature-grown GaAs. *Applied Physics Letters*, 67(26):3844–3846, 1995.

[11] T. Hidaka, S. Matsuura, M. Tani, and K. Sakai. CW terahertz wave generation by photomixing using a two-longitudinal-mode laser diode. *Electronics Letters*, 33(24):2039–2040, 1997.

[12] C. S. Friedrich, C. Brenner, S. Hoffmann, A. Schmitz, I. C. Mayorga, A. Klehr, G. Erbert, and M. R. Hofmann. New two-color laser concepts for THz generation. *IEEE Journal of Selected Topics in Quantum Electronics*, 14(2):270–276, 2008.

[13] S. A. Zolotovskayaa and N. Daghestani. Stable dual-wavelength operation of InGaAs diode lasers with volume Bragg gratings. *Applied Physics Letters*, 91:171113, 2007.

[14] S. A. Zolotovskaya, V. I. Smirnov, G. B. Venus, L. B. Glebov, and E. U. Rafailov. Two-Color Output From InGaAs Laser With Multiplexed Reflective Bragg Mirror. *IEEE Photonics Technology Letters*, 21(15):1093–1095, 2009.

[15] Haim Lotem, Zeqi Pan, and Mario Dagenais. Tunable dual-wavelength continuous-wave diode laser operated at 830 nm. *Appl. Opt.*, 32(27):5270–5273, 1993.

[16] R. Leyman, D. Carnegie, N. Bazieva, K. A. Fedorova, D. Livshits, and E. U. Rafailov. Ultrabroad Dual-Mode Spectral Control of a Quantum Dot Laser Gain Medium. In *3rd EOS Topical Meeting on Terahertz Science & Technology (TST 2012)*, 2012.

[17] Ferdinand-Braun Institut, diode lasers, 2013. URL http://www.fbh-berlin.com/business-areas/diode-lasers.

[18] T. Kruczek, R. Leyman, D. Carnegie, N. Bazieva, G. Erbert, S. Schulz, C. Reardon, and E. U. Rafailov. Continuous wave terahertz radiation from an InAs/GaAs quantum-dot photomixer device. *Applied Physics Letters*, 101(8):081114–4, 2012.

[19] O. M. Efimov, L. B. Glebov, L. N. Glebova, K. C. Richardson, and V. I. Smirnov. High-efficiency Bragg gratings in photothermorefractive glass. *Applied Optics*, 38(4):619–627, 1999.

[20] G. B. Venus, A. Sevian, V. I. Smirnov, and L. B. Glebov. High-brightness narrow-line laser diode source with volume Bragg-grating feedback. *High-Power Diode Laser Technology and Applications III*, 5711:166–176, 2005. Zediker, MS Conference on High-Power Diode Laser Technology and Applications III Jan 24-25, 2005 San Jose, CA.

[21] M. Bagnell, J. Davila-Rodriguez, A. Ardey, and P. J. Delfyett. Dispersion measurements of a 1.3 μm quantum dot semiconductor optical amplifier over 120 nm of spectral bandwidth. *Applied Physics Letters*, 96(21):211907, 2010.

[22] Takeshi Yasui, Eisuke Saneyoshi, and Tsutomu Araki. Asynchronous optical sampling terahertz time-domain spectroscopy for ultrahigh spectral resolution and rapid data acquisition. *Applied Physics Letters*, 87(6):061101–3, 2005.

[23] D. I. Nikitichev, K. A. Fedorova, Y. Ding, A. Alhazime, A. Able, W. Kaenders, I. Krestnikov, D. Livshits, and E. U. Rafailov. Broad wavelength tunability from external cavity quantum-dot mode-locked laser. *Applied Physics Letters*, 101(12):121107, 2012a.

Chapter 4

Quantum Dot-Based Terahertz Photoconductive Antennas

Discussed in this chapter are the the methods of generating THz EM signals which were used in this work. This refers primarily to the methods of optical pumping of photoconductive THz antenna devices using the ultrafast pulsed or multi-modal CW laser systems discussed in Chapter 3, but also described here are the relevant details in the process of designing and producing such antenna devices. There is still currently a great deal of research dedicated to the design of THz antennas in almost every aspect of the device, ranging from the semiconductor lattice engineering of the active photoconductive medium to the geometrical considerations of the radiative integrated metallic antenna contacts and subsequent outcoupling of THz EM beams. Presented here are design considerations for the semiconductor materials in our novel QD-based photoconductive antenna structures; optoelectronic simulations of such structures when pumped over a broad range of optical wavelengths; example simulations for metallic microantenna design; methods for reproducible production of antenna devices; and their implementation as part of a complete THz source or transceiver system.

4.1 Photoconductive THz Antennas

As discussed in Section 1.2.4, photoconductive materials and structures are generally designed with the optical pumping scheme in mind. This means that the

design of the active medium must take into account factors such as the pump wavelengths; pump powers; beam shape and/or size; number of pump beams; and temporal pulsewidth or CW beat frequency. In particular, the medium *ideally* should readily absorb the pump beam and be capable of switching between a state of near-insulator to a state of high conductivity and then, importantly, return to the non-conductive 'off' state — all within a period significantly lower than 1 ps. This is now possible in many semiconductor materials, but achieving these operational characteristics will typically involve considerable thermal constraints in the device and some limitations on the range of optical pump wavelengths (and hence limitations on the laser systems) which can be used to pump it. These limiting factors are in fact still the major obstacles to be overcome in the development of photoconductive THz antennas, and this has been the motivation for the work presented here.

4.1.1 Quantum Dot Structure Design

The properties of QD semiconductor materials are discussed in depth in Chapter 2 and their potential for use specifically in THz photoconductive antennas are discussed in Section 2.2.5 – discussed here are only the specifics of the structure designs used in the antenna devices developed as part of this work and brief explanations for such designs.

Three different QD structure designs were used in this work, characterised primarily by the number of QD layers throughout the active region. All semiconductor structures were grown by MBE in the S-K regime, with a very thin (30 nm) top layer of LT-GaAs to take advantage of the high electrical breakdown field threshold, and the 'active' QD layer region was immediately beneath this. Tests were carried out using three different structures, each comprising of either 25 or 40 layers of InAs QDs. In all cases, the QD layers were each capped by 4–5 nm $In_{0.15}Ga_{0.85}As$ wetting layer and separated by 35–36 nm GaAs spacer layers — giving a total active region depth between $1-1.7$ μm over either twenty-five or forty 40 nm PC sections. This is comparable with active region depths of more well-established PC antenna structures previously demonstrated (for example see [1] and [2]. Beneath the active generation layer, a 'spacer' layer of GaAs was grown, followed by an AlAs/GaAs DBR of either 25 or 30 layers. This was

used for several reasons: to reflect the pump beam when at longer wavelengths not absorbed by the GaAs and only partially absorbed by the wetting and QD layers; to allow scope for full optical cavity-type optimisation of the structure; and also to act to some extent as a long-pass filter and reduce the 'leaked' IR beam power at the output.

The epitaxial layer scheme of each structure type was introduced in Section 2.2.5 and Tables 2.1–2.3. Structure 1 was grown by Innolume GmbH [3], Germany, and included 40 QD layers and a 25-layer DBR centred around 1180 nm wavelength. Structure 2 was grown by the EPSRC National Centre for III-V Technologies at the University of Sheffield [4], UK, and included 25 QD layers and a 30-layer DBR centred around 1220 nm. Structure 3 was grown by Innolume and included 40 QD layers and a 30-layer DBR. The QD layer periodicity, deposited QD material properties, QD size and wetting layer blends were intentionally kept as similar as possible between structures.

There were effectively three different semiconductor materials in these structures, integrated in distinct layers throughout the active region, and so the corresponding variation in energy bandgap and refractive index was simulated using a custom software package, written in C++ language. Details of the software package can be found in Appendix A, and is referred to from herein by it's working title 'Opto-InGaAsP'. This was done because the incoming optical pump beam will experience these distinct layers sequentially, and the difference in layer properties at each interface could potentially affect the pump beam significantly. These properties are summarised in Figure 4.1, which also includes a sketch of the variance of material bandgaps with structure depth. This gives some indication of the various possible charge carrier generation, relaxation and capture processes that could occur between adjacent layers in the active region, discussed in more detail previously in Section 2.2.

The Opto-InGaAsP program was used to further simulate the expected behaviour of a broad range of optical pump signals within the device structures. It was expected that pump beams at wavelengths around 850 nm and below would be strongly absorbed by the active region and that any cavity optimisation of the region would have only a small overall effect. For pump wavelengths above this, the beam is not completely absorbed by the relatively small absorptive material volume (i.e. the cumulative $In_{0.15}Ga_{0.85}As$ and InAs QD volume) and so the

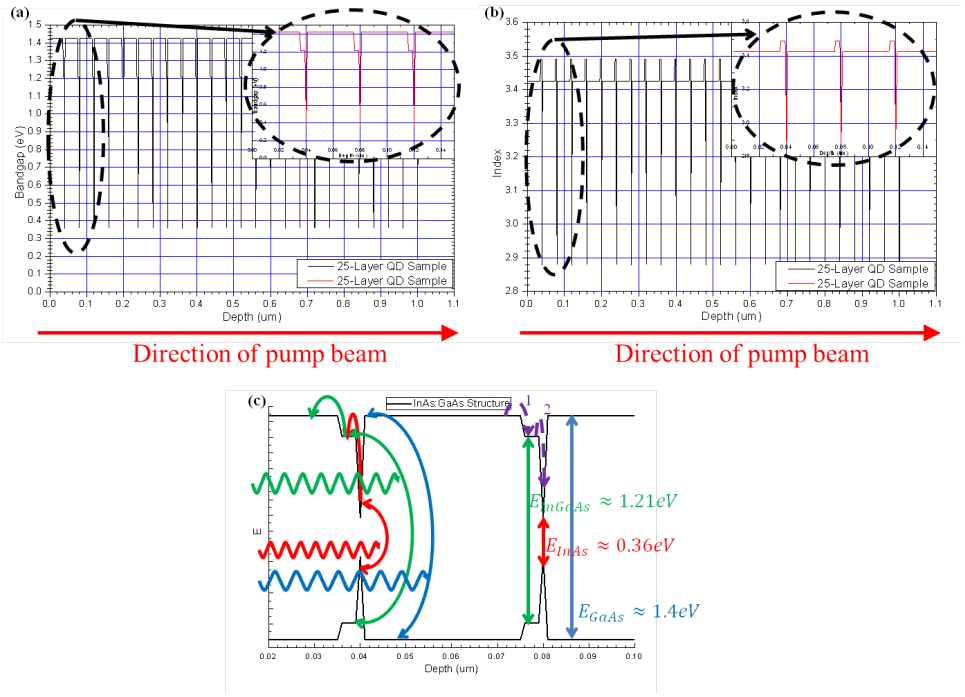

FIGURE 4.1: Variation in PC structure bandgap(s) throughout a 25-layer QD antenna structure. (a) shows the calculated bandgap distribution throughout the whole structure, with top surface zoomed inset; (b) shows the corresponding refractive index variation throughout the structure; and (c) is a sketch of the different possible mechanisms of charge carrier generation and movement between layers/materials.

returned beam intensity post-DBR and subsequent cavity behaviour becomes important. Some exemplary simulations of the evolution of pump beam propagation and structure cavity configuration are shown in Figure 4.2. Structure cavity configurations were considered similarly to the design of QD-SESAMs discussed in Section 2.2.3. Plot (c) in this Figure 4.2 gives some indication of the considerable difference in pump beam intensity throughout the structure volume when either a resonant or anti-resonant cavity is considered, with respect to the pump beam wavelength(s). As such, it should be noted that these designs were each anti-resonant for the longer pump wavelengths of interest around the 1200 nm range. It is evident that there are significant phase shifts at sequential layer interfaces through the QD layer region, but the overall wave profile is relatively unaffected due to the comparatively low volume of InAs and $In_{0.15}Ga_{0.85}As$. The small dips and peaks occurring periodically (every 40 nm) in the waveforms correspond to QD locations and the effect on the pump beam phase as it passes through the material interfaces at each of these regions.

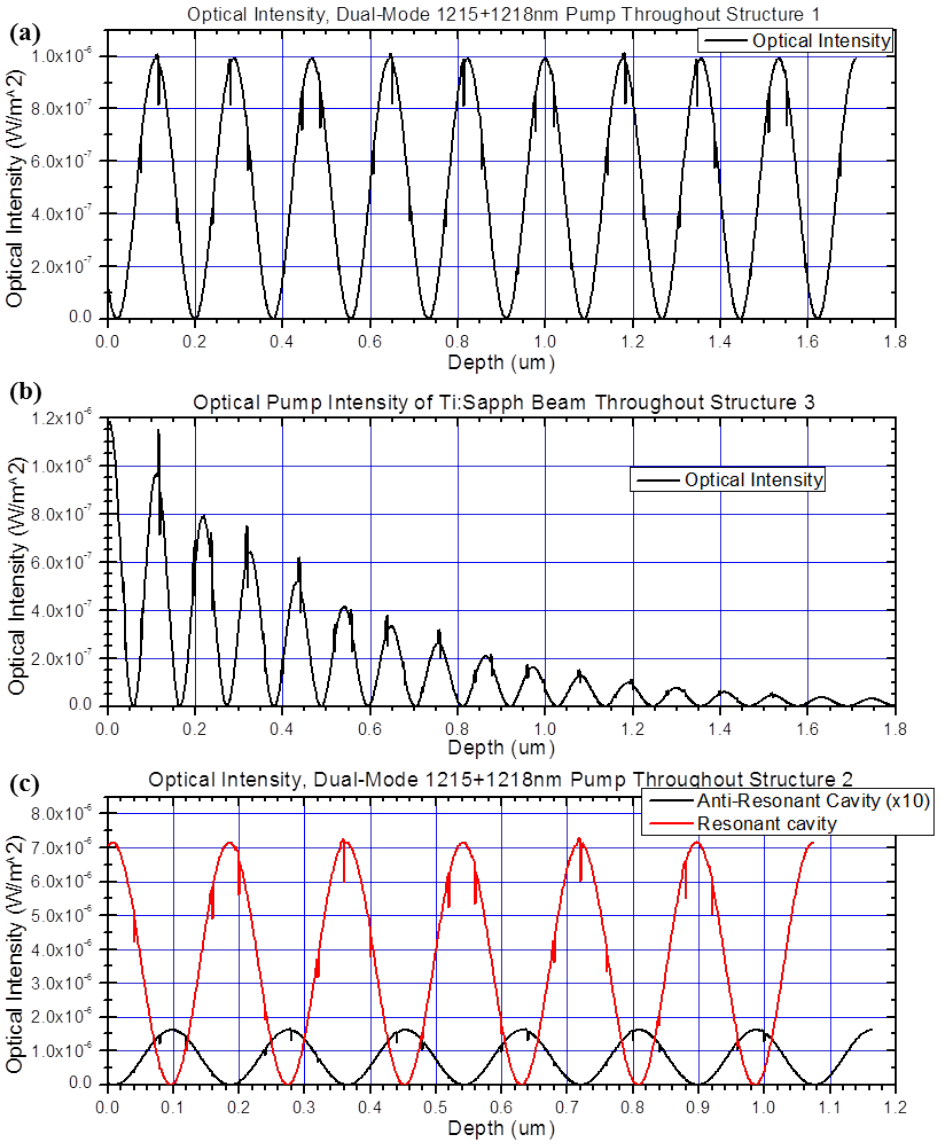

FIGURE 4.2: Example simulated antenna structure cavity configurations and pump beam propagation at different pump wavelengths. (a) shows a dual-mode pump beam of average wavelength 1216.5 nm through Structure 1; (b) the Ti:Sapphire pump beam through Structure 3; and (c) a dual-mode CW beam at around 1216.5 nm average wavelength through Structure 2.

Post-growth PL spectrum were measured from each structure type, shown earlier in Figure 2.3. These plots show both the structure PL and the optical reflectance spectrum which gives a good indication of the *effective* reflectivity of the DBR beneath the QD region. The calculated reflectivity of the DBRs show that they were >99% reflective around 1180 nm wavelength in Structure 1 and >99% over the 1180–1260 nm range in Structures 2 and 3. The ground state emission of the QDs in each case is around 1260 nm ($\approx 0.98\ eV$); first excited state around 1180 nm ($\approx 1.05\ eV$); and second excited state around 1111 nm ($\approx 1.12\ eV$). The observed relative PL intensities were modulated by the presence of the cavity due to the DBR as described previously, and indicate the effective wavelength enhancement of the cavity as shown in Figure 2.3(e). However, the calibration samples grown without DBR indicate the 'true' PL spectrum of the QD materials and were used as a measure of the inherent PL emission spectrum of each sample. These characteristics allowed testing over the important energy range of $0.98 - 1.12\ eV$ to investigate the effects of pumping at energies specific to different QD states for example, which is also the emission range of the QD LD pump systems presented previously in Chapter 3. Together with these pump systems, it was postulated that an all-QD-semiconductor THz signal generation and detection system could be configured. This could potentially constitute the basis for an ultracompact THz transceiver system.

According to the observed dependence of carrier lifetimes on QD layer periodicity [5], it is reasonable to assume that electron lifetimes can be *potentially* reduced down to $\sim 0.45ps$ in the structures tested here. This depends on the nature of charge carrier generation and movement, which in turn is determined by factors such as the optical pump energy and fluence [6, 7] and the lateral E-field applied across the active region [8, 9] as discussed in Section 2.2.5.

To investigate the influence of microantenna geometry on device performance, Ti/Au metallic contact antennas in various geometries were integrated over the top surface of all PC structures, the design and production of which is described in the next section.

4.1.2 Microantenna Design

As discussed previously (Section 2.2.2), sub-picosecond charge carrier capture times are readily achievable using QD-based PC structures — but the generation and propagation of THz EM signals from an ultrafast switch depends also on the nature of the signal emitter/radiator element which is integrated with the structure. In this case, we refer to the metallic antenna integrated over the top surface of the PC structure.

As in the case for radiative signal antennas in other applications, microantennas for THz PCA devices are designed with the principles of the resonant current-loading frequencies and radiation resistance in mind (see examples of both broadband [10] and narrowband [11, 12]), with the additional contributing factors and limitations from the ultrafast PC structure that it is bonded with. In general, however, relatively simple antenna configurations were used here, including: CPS; Hertzian-type dipoles; bow-ties; and log-spiral or log-periodic 'toothed' geometries. In each case, the antenna is loaded and gated by the photocurrent generated by the incoming pump beam, which is focussed to the appropriate loading point located typically in the very centre of the antenna between the two contacts. An overview of the microantenna geometries tested here is given in Figure 4.3. Figure 4.3(g) here is one of many custom experimental designs which operate at multiple resonant frequencies, defined by the variety of dipole and inductive choke lengths along the antenna profile; and (h) is an example of an exported dipole antenna design under simulation testing, discussed in Section 4.1.3. Most antennas typically used here were for broadband THz signal generation, indicated by their lack of distinct geometrical resonance features. The three-turn, self-complimentary log-spiral and log-periodic geometries 4.3(d-e) are typically used in the CW regime. This is because they feature very small photoconductive gaps ($\lesssim 5\ \mu m$) which improve photoconductive gain and also a self-complimentary geometry which allows a relatively large emitter area with a well-defined output signal polarisation (circularly for spirals, linearly for toothed geometries [13]) to be produce. Further optimisation of these geometries for CW operation can be made by developing sub-μm-scale interdigitated metallic 'fingers' across the PC gap — thereby decreasing the effective gap width to around $0.4 - 0.8\ \mu m$ and increasing the PC gain considerably. This is useful in the CW regime as it compensates for the relatively low optical-to-THz conversion

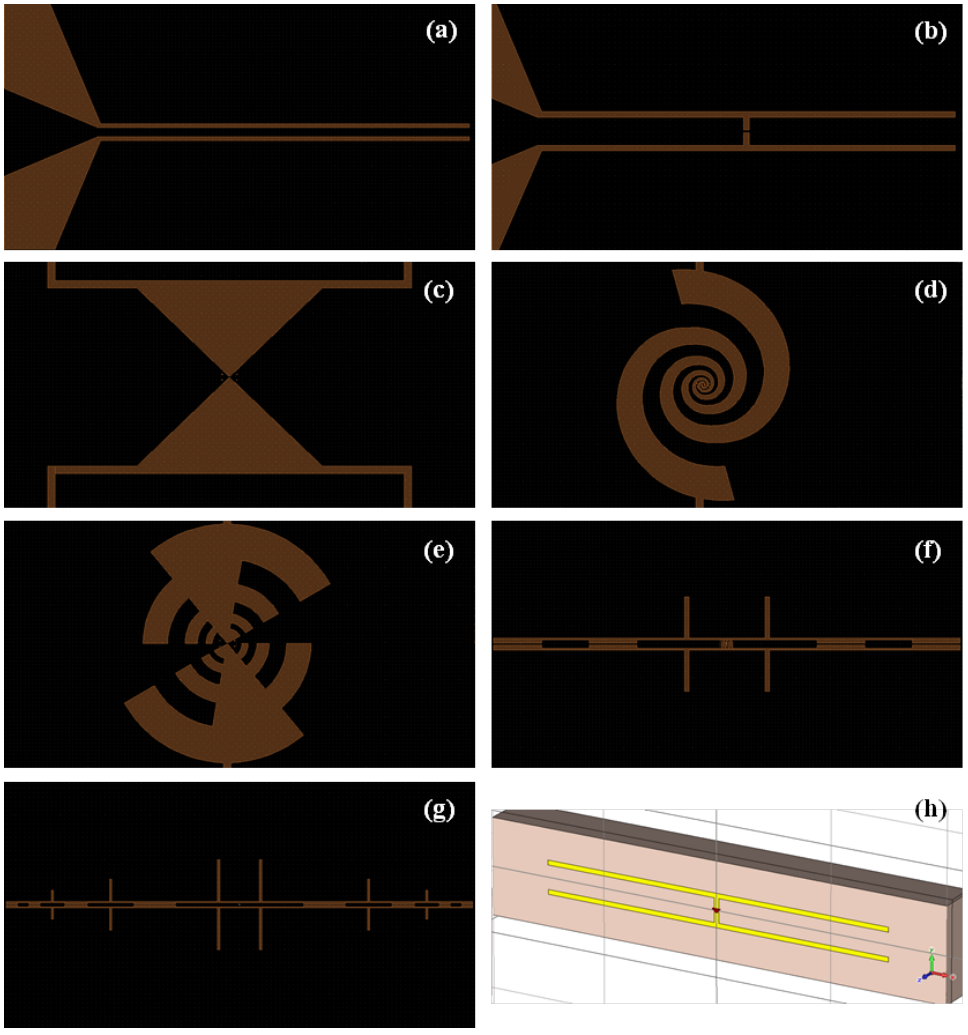

FIGURE 4.3: Overview of THz microantenna designs taken by the LayoutEditor software. (a) is the coplanar stripline design; (b) dipole; (c) bow-tie; (d) three-turn spiral; (e) log-periodic toothed; (f) dual-dipole; (g) custom multi-frequency tri-dipole; and (h) is an example exported dipole design situated in a full EM simulation.

efficiency imposed by CW optical pumping and associated thermal constraints. It does, however, involve an additional specialist production step (see Section 4.1.4.2) and also imposes restrictions on the tolerable antenna voltage level before device failure, as the avalanche breakdown voltage limit defined by the top surface material still applies.

As microantennas were produced using lithography techniques (see Section 4.1.4), the actual design was done using printed circuit board design software package, LayoutEditor [14]. This software allows CAD-like precision design and editing of metallic contact features to be prepared for etching onto photo-lithographic mask

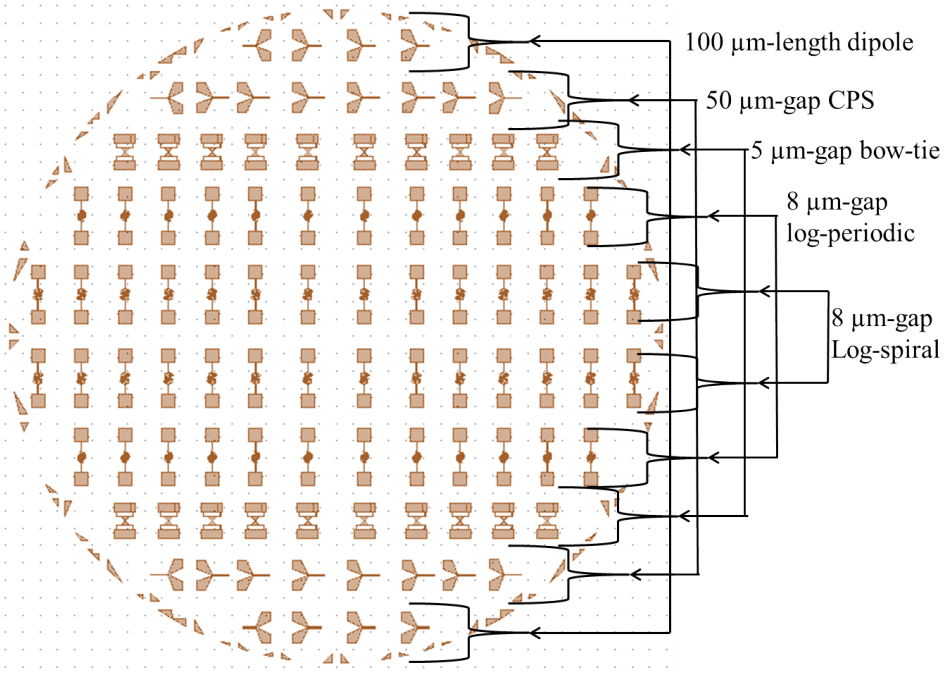

FIGURE 4.4: Example design of a THz antenna array for production over a 3-inch semiconductor wafer.

plates, which in turn were to be formed over the surface of the PCA semiconductor structures. It includes multi-layer design capability and import/export in the necessary '.gds' file formats used in mask production. A notable example of the use of this design software is given in Figure 4.4, which shows the design of an array of antennas for production over an entire 3" semiconductor wafer. The antenna arrangement is symmetrical about the central horizontal axis (but features were not simply mirrored about this axis) and different types are labelled and arranged in rows. Mask features were arranged as such so that a selection of different antenna geometries could be removed easily as a single section from the wafer if necessary. The outer ring of small features represents the outer circumference of the 3" semiconductor wafers used and is there to assist the alignment of the laser cleaving process.

Exemplary properties of the actual output signals generated by the devices described here are given in Chapter 5. Indeed, they were typically broadband THz signals but for the purposes of future work in more specific frequency-domain systems and also to explore and confirm the expected behaviour of all microantennas, computer simulations were run and are discussed in the next section.

Parameter	Symbol	Value	Unit
Relative permittivity	ϵ_r	12.94	
Material density	ρ_{mat}	5320	kg/m^3
Thermal conductivity	K	54	W/K/m
Heat capacity	C	0.33	kJ/K/kg

TABLE 4.1: Relevant material specifications of the lossy GaAs substrates used in PCA EM simulations.

4.1.3 Simulation

PCA simulations were conducted using CST Microwave Studio EM simulation software [15]. This software was used to import microantenna designs and model their EM behaviour using a finite element method as metallic objects over semiconductor substrates. Once the microantenna .gds files were imported, they were scaled appropriately and assigned their metallic properties, for example as highly conductive gold, and an object thickness is chosen. A substrate is then generated with user-defined dimensions and the appropriate material is assigned to it. In these simulations, typically a "lossy" GaAs substrate is used. This means that all the relevant characteristics of a 'non-perfect' GaAs substrate were assigned to the block of material used in the simulation such as the relative permittivity, thermal and electrical conductivity and heat capacity. Material parameters for the lossy GaAs substrates used are summarised in Table 4.1:

The substrate thickness should represent asaccurately as possible that of the real antenna structures, as this affects the far-field radiation pattern of the THz output signal, for example, amongst other effects.

An excitation signal is then defined, which will be applied to the antenna, and a power "port" can be connected to monitor several relevant parameters such as antenna voltage, current and as such the subsequent signal frequency response of the microantenna-over-semiconductor may be retrieved. Excitation signals can include a variety of energetic inputs such as a single ultrashort electrical pulse or an incoming plane wave at a particular direction and polarisation. Figures 4.5–4.8 gives some exemplary simulation results of antenna resonance properties and 3D simulation diagrams for four different microantenna types: (Fig 4.5) a 2 mm-long CPS antenna; (Fig 4.6) a 100 μm-long dipole antenna; (Fig 4.7) an 'ideal' tuned 55.4 μm dual-dipole antenna similar to the designs presented in [11]; and (Fig 4.8)

a 5 μm-gap log-periodic antenna. Antennas as presented over visible substrate 'bricks' in some of these figures, but this is for visual clarification of the simulation setup. Antennas were in fact generally situated over semi-infinite GaAs planes or within a pure GaAs surrounding medium for the purposes of reducing the simulation time and complexity without sacrificing numerical accuracy.

The two main parameters of interest are plotted here: the scattering parameter (S-Parameter) and radiation resistance. The S-Parameter, or more specifically the "reflection coefficient" in this case, is used in the measurement of the return loss of the antenna. This is a common figure of merit in transmission line analysis and can provide information on the passage of the electrical signal through the microantenna. The signal applied across the antenna terminals experiences some loss in transmission and some degree of reflection as it propagates through different material interfaces and impedances. This loss and reflection is generally frequency-dependent, even in 'broadband' antenna designs, so simulating this phenomenon can help further characterise the expected frequency-dependent performance of the PCA devices. This was typically sampled at frequency intervals of roughly 3 GHz over the 0.05–3 THz range of interest and the sample frequency with the lowest return loss essentially indicates the highest signal resonance and gives it's 'resonant operating frequency'. The return loss of a resonant antenna, in dB, may be estimated as:

$$RL_{input} = 20 \log_{10} |S_{11}| \ , \tag{4.1.3.1}$$

where S_{11} is the only S-matrix parameter for each simulation as only one input signal port is used here. The radiation resistance is an estimate of the microantenna load resistance (V_{ant}/I_{ant}) as an EM radiating circuit element, as discussed in Section 1.2.4. A range of resonance features appear in all antenna tests, which must be accounted for particularly in the interpretation of experimental results later.

The CPS antenna results shown in Figure 4.5 were essentially dominated by modulation features which were caused by contact length at the low frequencies and contact width at around 1.65 THz, and other than these features there is relatively little enhancement of any specific operating frequencies. The dipole antennas tested in these examples had resonant frequencies at around 0.34 THz for the 100 μm dipole antenna as shown in Figure 4.6. Figure 4.7 indicates at

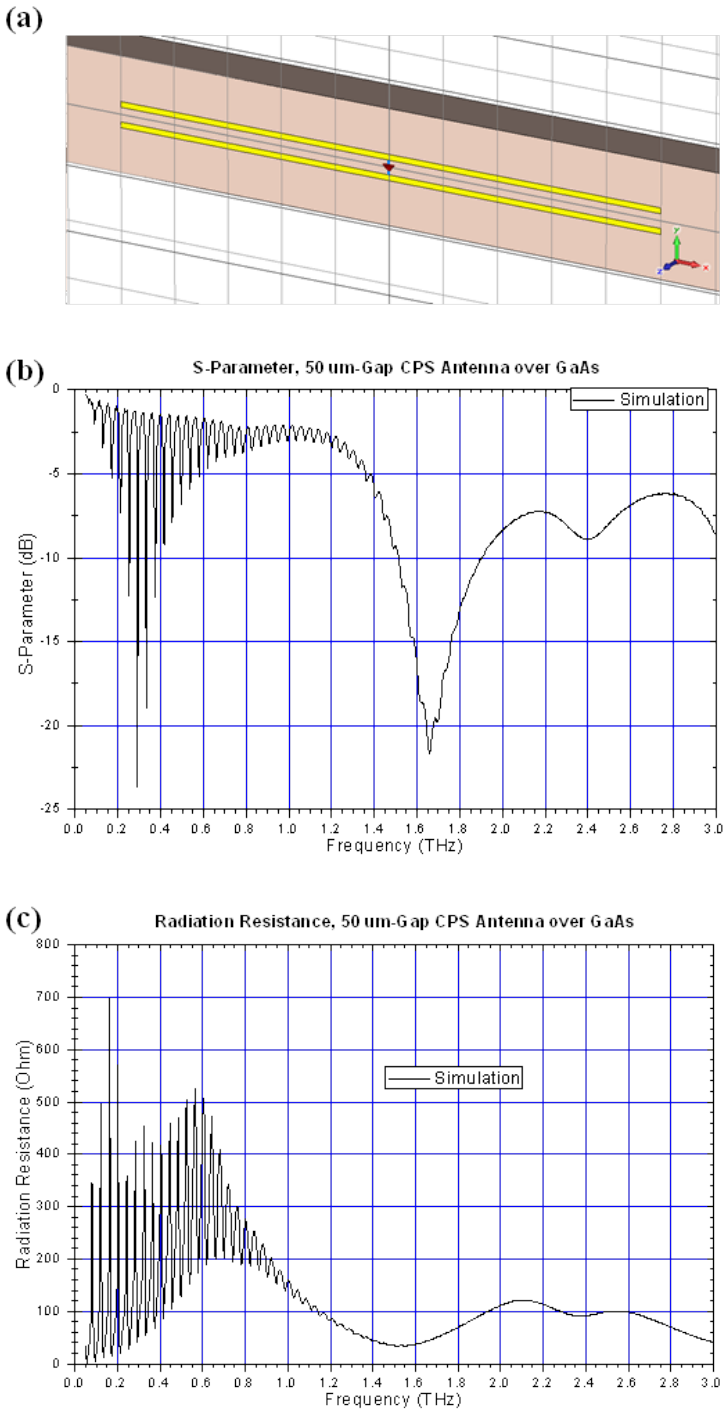

FIGURE 4.5: Simulated electrical response of a 50 μm-gap CPS antenna. (a) shows the 3D simulation layout; (b) shows the obtained S-Parameter; and (c) shows the radiation resistance data over the 0.05–3 THz range of interest.

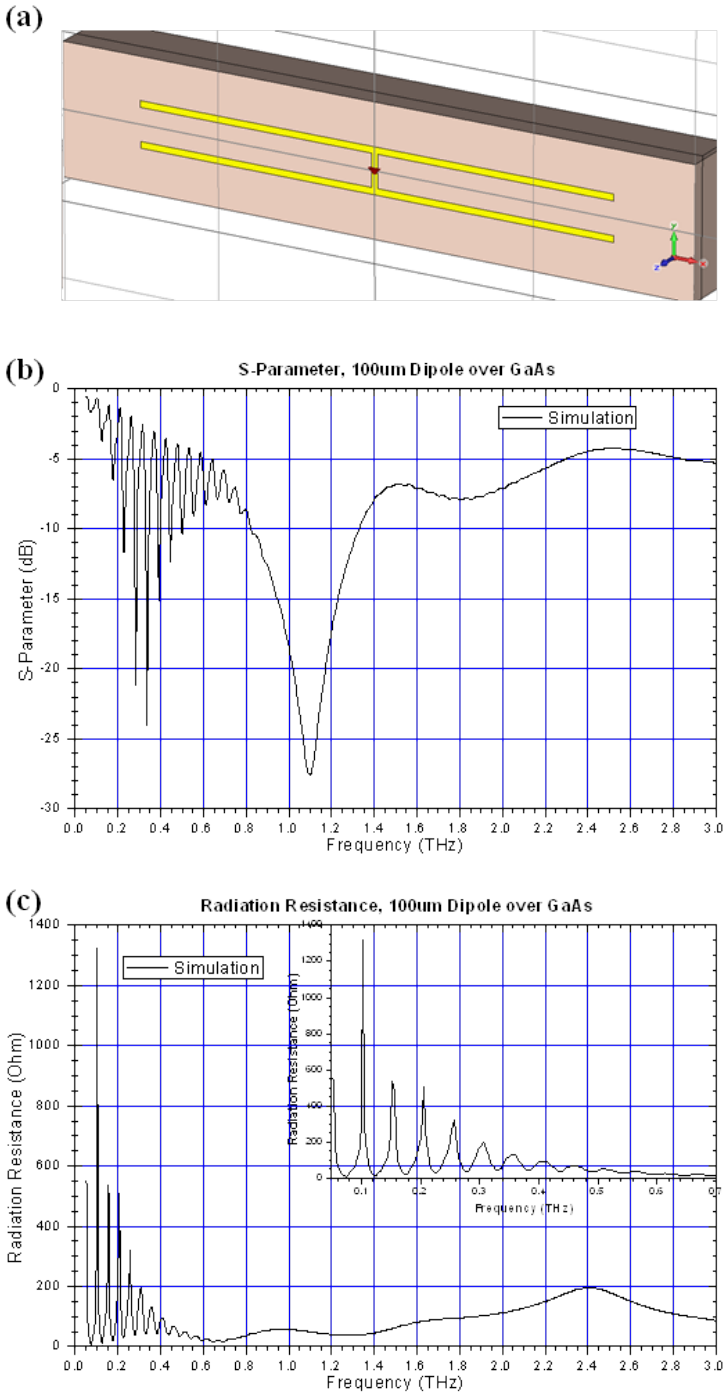

FIGURE 4.6: Simulated electrical response of a 100 μm-length, 10 μm-gap dipole antenna. (a) shows the 3D simulation layout; (b) shows the obtained S-Parameter; and (c) shows the radiation resistance data over the 0.05–3 THz range of interest.

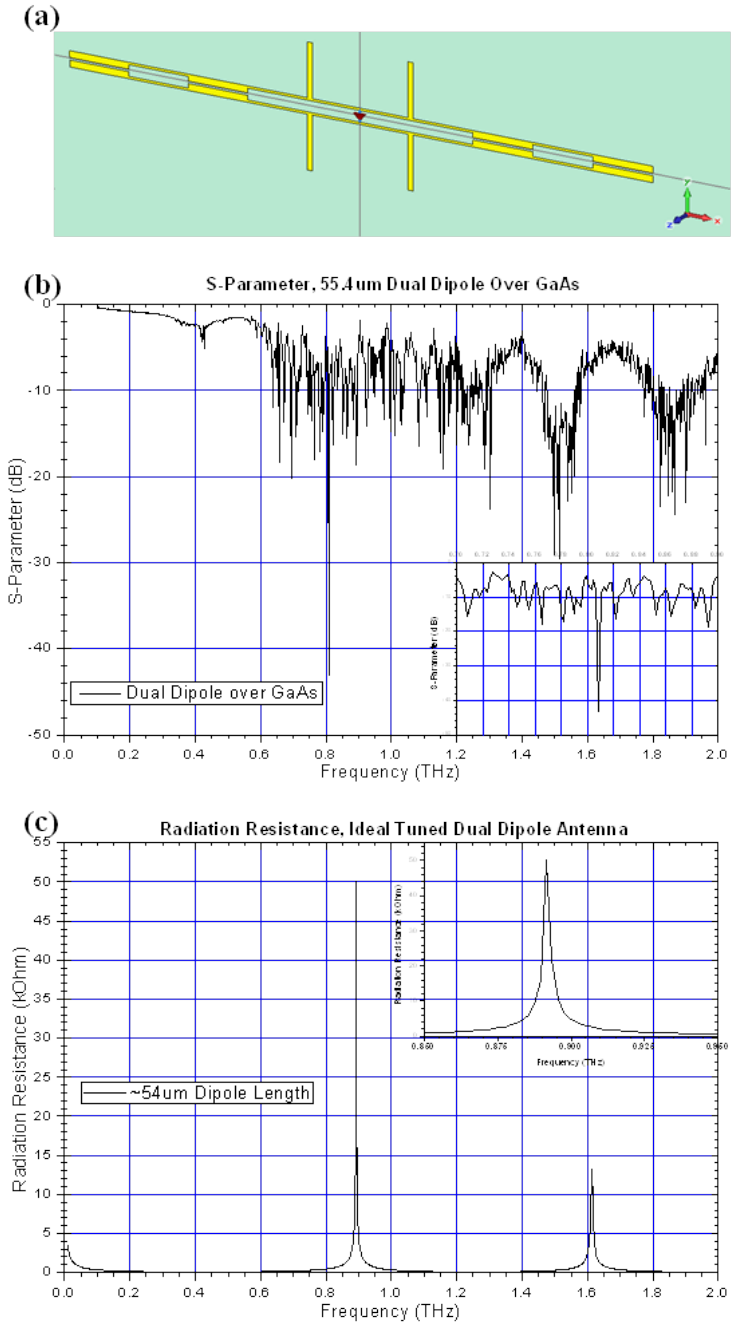

FIGURE 4.7: Simulated electrical response of an 'ideal' tuned dual-dipole antenna. (a) shows the 3D simulation layout; (b) shows the obtained S-Parameter; and (c) shows the radiation resistance data over the 0.05–2 THz range of interest.

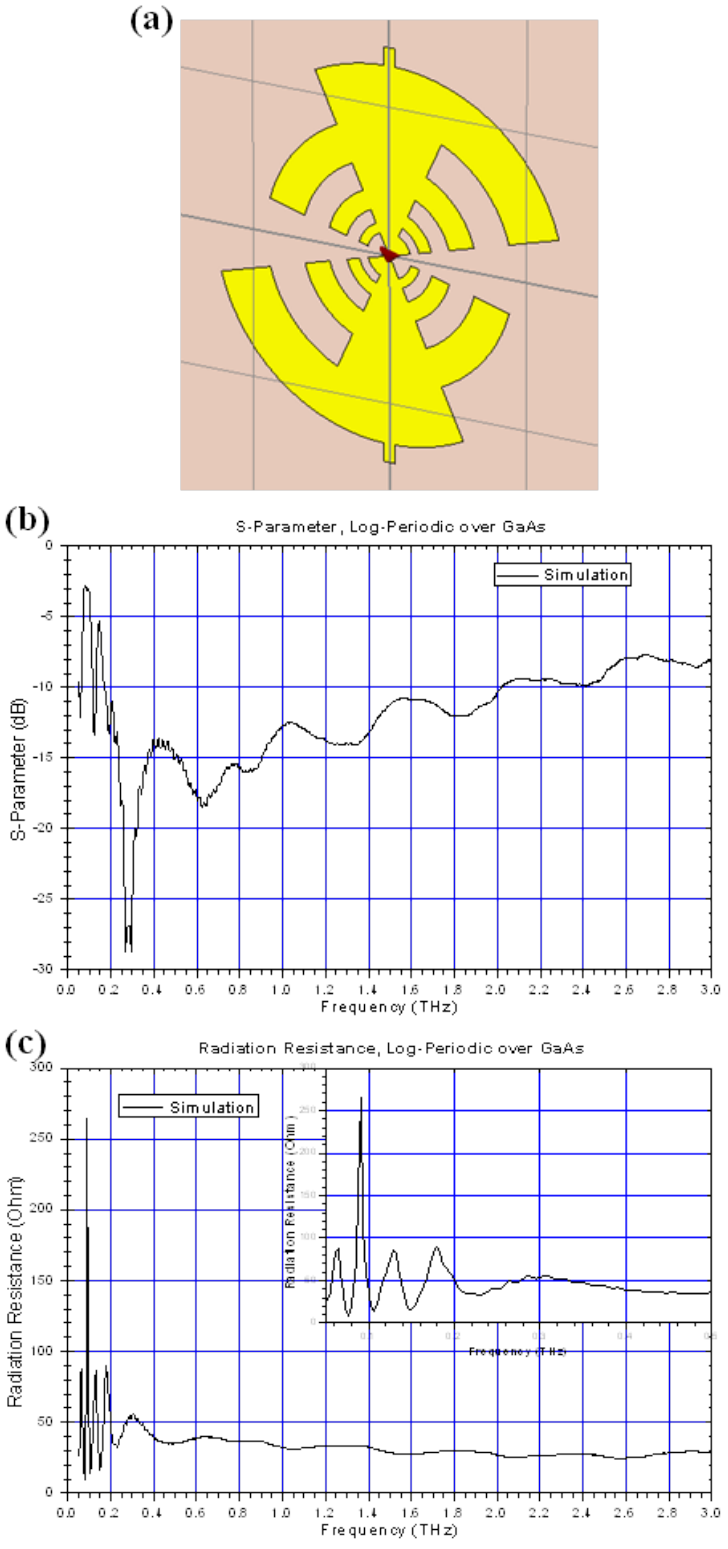

FIGURE 4.8: Simulated electrical response of a broadband, log-periodic toothed antenna. (a) shows the 3D simulation layout; (b) shows the obtained S-Parameter; and (c) shows the radiation resistance data over the 0.05–3 THz range of interest.

resonant response predominantly located around 0.83 THz for the tuned 55.4 μm dual-dipole antenna, as expected from Equation 1.2.4.4. Strong modulating harmonics were also observed at low frequencies and a large response around 1.1 THz due to the geometries of the long lengths and narrow widths of the Au antenna feed lines, but in practice the low frequency harmonics would not give these sharp peaks due to the roughness of the 'real-world' etch and surface features. The radiation resistance plot for the dual-dipole antenna as shown in Figure 4.7(c) is calculated after the structure has been simplified to remove such features not relevant to the basic design principle and gives an idea of the intended resonance properties of the design. This resonance curve is much more simple and indicates a much clearer resonance enhancement at the design frequency, and is typically observed in real devices [11]. Low-frequency resonance behavior is also observed in the log-periodic antenna as shown in Figure 4.8, where multiple strong resonance features were observed which correspond to the different tooth lengths and the inner bow-tie geometry, but a more constant response over the THz range of interest is also observed as expected.

4.1.4 Production

4.1.4.1 Antenna Metallisation and UV Lithography

Production of metallic microantennas over semiconductor substrates was done using standard UV photolithography and wet etching of surface Ti/Pt/Au features, and a post-process anneal to increase Ohmic contact between antenna metal and GaAs surface. First, the contact metals were deposited using an Edwards Auto-306 electron-beam sputtering system. This system allows several metals to be deposited sequentially in a single chamber without breaking vacuum, and so typically the metallisation recipe was either:

- 40 nm Ti + 210 nm Au or,
- 25 nm Ti + 40 nm Pt + 100 nm Au

in order from the bottom-most surface layer upwards. Initially, Ni was used in place of Ti and the overall thickness of the contact layer was around 300 nm, as it sufficed for the production of early sample characterisation — then later a

smaller overall contact thickness of 165 nm was used as critical feature dimensions decreased towards $\sim 2\ \mu m$, and Ni was replaced with Ti and Pt was added because the Au was found to be diffusing through the Ni barrier. Ti was used in each case because it enables a high degree of metal-semiconductor (M-S) adhesion whilst still adequately preventing softer metal diffusion from above. These details are mentioned here because Ohmic M-S contact production methods is in fact an area of research unto itself (e.g. see [16] which includes work determining Ohmic and Schottky contact properties of Au/Ti over doped GaAs substrates), and naturally the electrical contact and lateral current movement between terminals of an ultrafast photoswitch or PCA will affect the performance considerably [17]. The GaAs used in these structures is undoped, and M-S contact properties are simpler in this case compared with doped GaAs photoswitches. After metallisation is complete, the lithography process is used to define the microantenna pattern to be etched. The process for this was as standard:

1. Cleaning of metallised substrate, acetone + DI water + isopropyl alcohol (IPA)
2. Spin-coating of S1813 G2 positive photoresist over substrate at 4000 rpm for 60 seconds
3. Softbake at 115°C for 60 seconds
4. UV exposure of antenna pattern through UV mask using a Karl Suss MJB3 alignment system for 21 seconds at 4 mW/cm^2 fluence
5. Development in MF-319 developer for 60 seconds, with some sample agitation
6. 'Hard' bake at 120°C for 3 minutes
7. Etching of resultant antenna features into metallised surface
8. Acetone bath to remove residual photoresist over surface
9. Rapid thermal anneal (RTA) in an East Star labs RTP-300 RTA oven at 410°C for 3 minutes

The antenna feature etching in this case may be done using different methods. 'Dry' processes such as reactive ion beam etching and chemically-assisted ion

beam etching were trialled as high-definition, non-isotropic methods of metallic feature definition. The definition quality of antenna features that were achieved using such methods was indeed very high, but the ion beam had difficulty removing the Ti under-layers and so the method was abandoned. A lithographic lift-off process was also trialled. This involved similar processing steps as outlined above, except the metallisation was done instead of etching after the antenna pattern was UV-exposed and developed. The exposure pattern in this case was of the opposite 'polarity' – the antenna features were defined as the region of the sample not covered by photoresist. This meant that after metallisation, an acetone bath could be used to lift and remove the photoresist and metal surrounding the central antenna. However, this method was relatively difficult to repeatably achieve accurate results with and so was also abandoned. 'Wet' chemical etching processes were then generally used for the samples prepared for this work. These methods were perhaps less sophisticated and offered less accurate definition of very fine antenna features than the dry methods, but allowed some extra degree of control and could selectively remove Ti surface layers with relatively little effect on the Au top layer. This could be achieved using different blends and water-diluted concentrations of hydrofluoric acid, which also determined the vertical etch rate. Etching of the Au top layer could be done using a potassium iodide solution.

An example of a finished log-periodic THz PCA device is given in Figure 4.9. All devices defined using UV lithography were made with Ohmic contact to the substrates and smallest feature sizes down to $\sim 2\ \mu m$. An additional step was made in some samples to add sub-μm interdigitated contact fingers to the central photo-gap spot, which was done using electron-beam lithography as described in the next section.

4.1.4.2 Electron Beam Lithography and Imaging

For the production of high-gain CW regime PCA device contacts, sub-μm contact finger features were defined and etched over pre-defined log-periodic and log-spiral antennas using electron beam writing facilities at the University of Leeds. The preparation process was as follows:

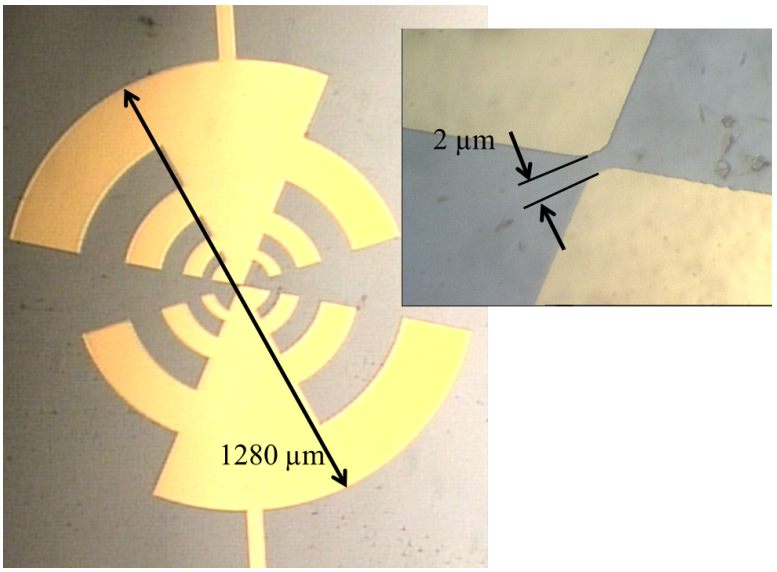

FIGURE 4.9: 'Finished' log-periodic toothed antenna with a 2 μm photoconductive gap.

1. Cleaning of PCA surface, acetone rinse for 5 minutes then IPA rinse for 5 minutes
2. Spin-coating of methyl methacryllate (MMA) copolymer at 2500 rpm for 45 seconds
3. Bake at 150°C on hotplate for 10 minutes
4. Spin-coating of polymethyl methacrylate (PMMA) 950 A4 at 4000 rpm for 45 seconds
5. Bake at 180°C on hot plate for 10 minutes
6. E-beam writing done using a JBX 6300FS at 100kV mode 6 with 100pA probe current
7. Develop in methyl isobutyl ketone (MIBK):IPA (1:3) for ∼1 minute
8. Rinse in IPA and blow dry
9. Metal deposition: Ti 25nm + Au 90nm
10. Lift off procedure using Acetone

The samples were then annealed to improve the M-S contact using the RTP-300 RTA oven. Alignment of the writing pattern is absolutely crucial, as the 8×6 μm

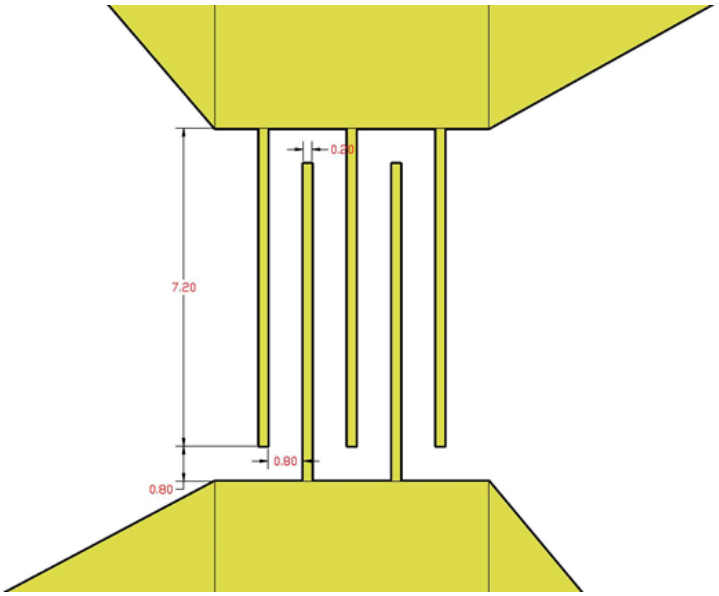

FIGURE 4.10: Sub-μm interdigitated finger design for high-gain CW PCA devices.

working area of the finger pattern must be placed at the existing electrodes' centre as accurately as possible. This was assisted using alignment cross-hairs which were deposited around the centre of the existing antenna contacts in the previous UV lithographic process. A relatively 'standard' [18] interdigitated finger design was used, which consisted of five 7.2 μm-long fingers of 0.2 μm-width and separated by 0.8 μm across an 8 μm initial contact gap, as shown in Figure 4.10.

To confirm the accuracy of the sub-μm feature production and placement over PC gaps, scanning electron microscope (SEM) images were taken of the relevant PCA samples. SEM imaging was conducted at the Wellcome Trust laboratories at the University of Dundee [19] by mounting samples on Hitachi stubs using double-sided carbon adhesive tabs and examined in a Hitachi S-4700 FEG scanning electron microscope. The scanning electron microscope operated at an accelerating voltage of 15kV for the work presented here, and examples of the images taken are presented in Figure 4.11. For ease of alignment and to account for any inaccuracy in the larger, pre-defined antenna structure below, the fingers were designed in the LayoutEditor software first with large contact pads at the base of each finger set. It can be seen that the fingers could be deposited very accurately aligned with the bases at the edges of the larger contacts with only a very slight offset towards one contact. This could mean that the PC gaps at the tips of one set of fingers were closer to the antenna edge that the other

set, potentially leading to a concentration of the PCA E-field at this side and additional high-precision E-field analysis tools are required to measure this. The afore-mentioned alignment cross-hairs are also visible around the finger area in Figure 4.11(a) here.

4.1.4.3 Custom Antenna Mounts

Additionally, some effort was put into the mounting of test antenna structures. This was necessary as the samples must be situated in housing which is mechanically stable so as to avoid misalignment of the pump-beam during testing and must also include an effective method of stably abutting the hyperhemispherical high-resistivity float-zone (HRFZ) Si collimating lens to the rear facet of the sample. We took the opportunity here to develop several iterations of our custom sample housing to include stability, versatility and the ability to change samples as conveniently as possible. Some examples of the design and use of our custom mounts are shown in Figure 4.12, the designs of which were assisted by Tomasz Kruczek. Initially, systems consisting of two copper plates and a copper-coated PCB plate were used to hold the sample and press the Si lens to the rear facet with springs. It became apparent that significant control of the Si lens X-Y location on the sample facet was needed for optimisation of THz signal collection and output beam collimation, so a more versatile design was made using AutoCAD design software and printed by a 3D acrylonitrile butadiene styrene (ABS) plastic printer. This included small sliding Si lens mounting brackets within the housing which were spring-loaded and pushed in both X and Y directions using external threaded plastic screws. This material was considered ideal for use in the use of custom components in THz systems also because they are also relatively transparent at the frequency range of interest, ∼0.1–3 THz [20].

4.2 Experimental Setups

In this section, an overview of the experimental setups used in this work is presented. This includes the methods of driving PCA devices and generating THz optical and electrical signals. The methods presented here were based mainly on the application of the optical pump signals discussed in Chapter 3 and also

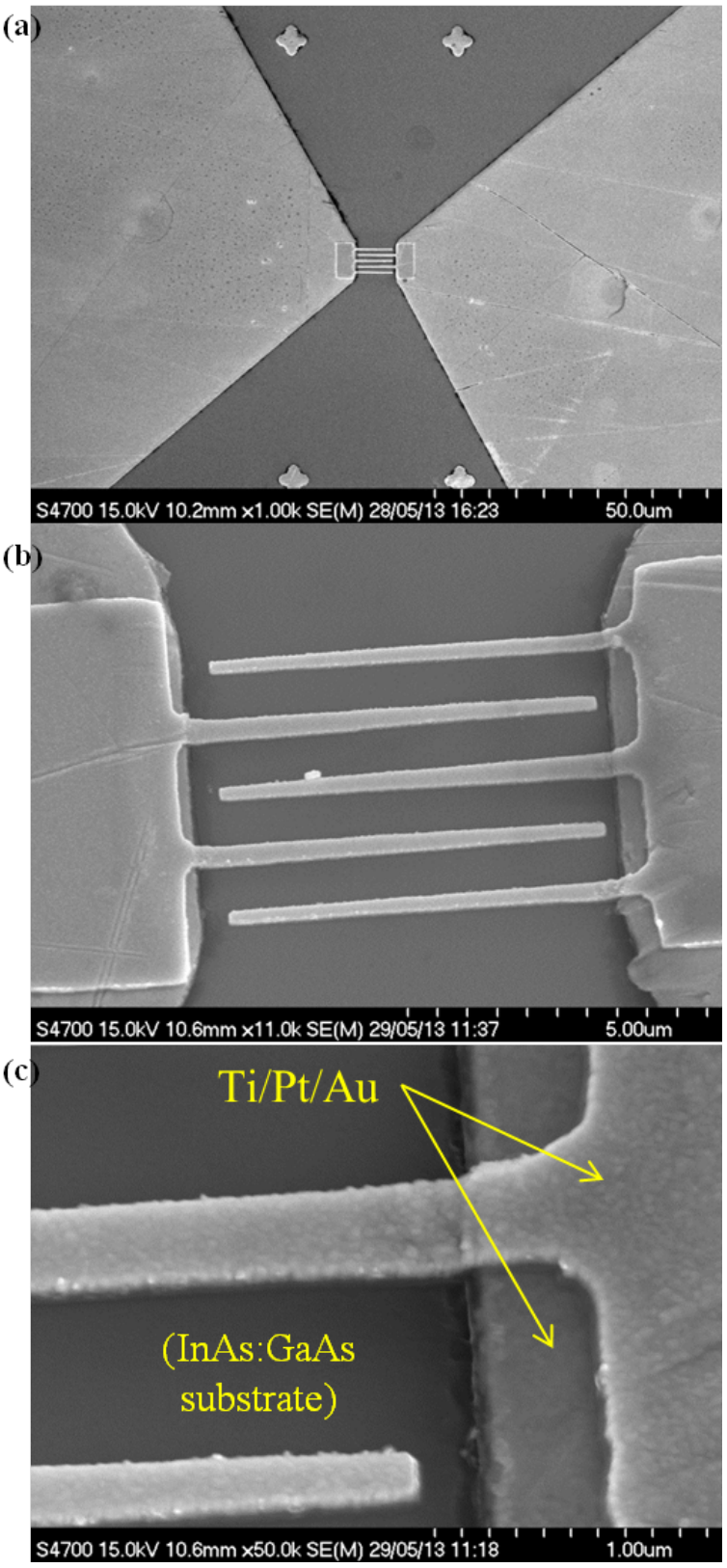

FIGURE 4.11: SEM imagery of the sub-μm metallic fingers produced over CW PCA contacts. (a) is a wide view showing the situation of the fingers in the antenna centre; (b) is a zoomed view showing the placement of the finger base pads over the existing contacts; and (c) is a further zoom showing the fine-structure of the overlapping metal contact materials.

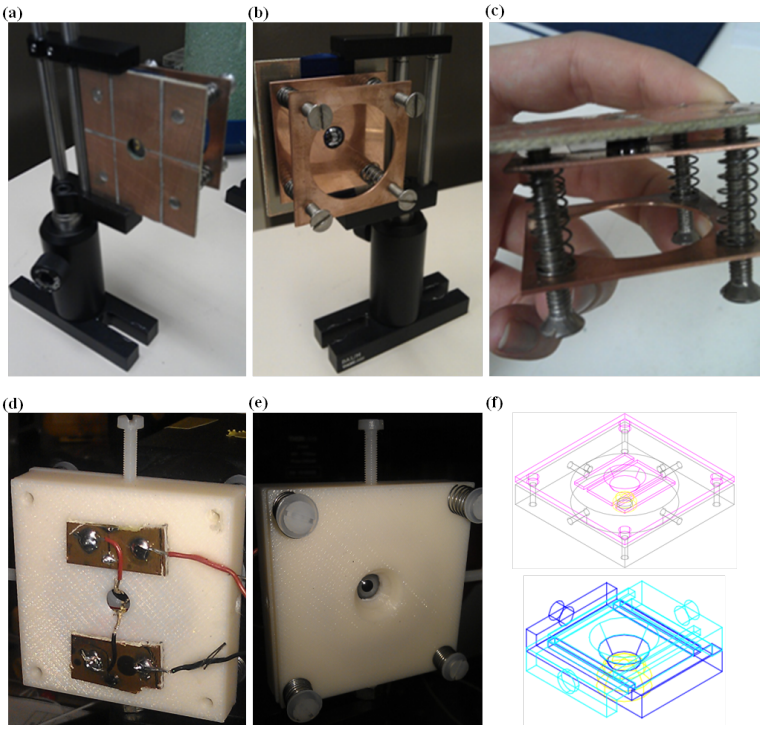

FIGURE 4.12: Examples of custom PCA device testing mounts. (a-c) were made from a copper-coated PCB board and thin copper plates with apertures for both the Si lens and the THz output beam; (d-f) was the latter iteration of the mount, which was designed in AutoCAD then printed in ABS plastic. (f,top) is the outer housing and (f,bottom) is the inner lens translation brackets.

discuss the equipment used to power and measure the response of the PCAs under testing.

Figure 4.13 shows a general schematic of the test setups used in this work. The optical pump signal is collected from the laser system being used and applied to the PC gating gap of the PCA. A beamsplitter is placed before the PCA focusing optics to part-off enough of the optical beam power to continuously monitor its optical, temporal and/or RF properties during pumping of the device. The optimal focus and alignment of the pump beam must then be obtained, which is monitored in several ways. Primarily, the resistance across the antenna contacts was monitored, as the optimal pump focusing condition was generally achieved when the antenna resistance was at a minimum. However, some of the antenna geometries under testing include some complicated features, and several *local* resistance minima will be found before the global minimum is achieved. This was assisted in some cases with the use of a CMOS camera and a beamsplitter,

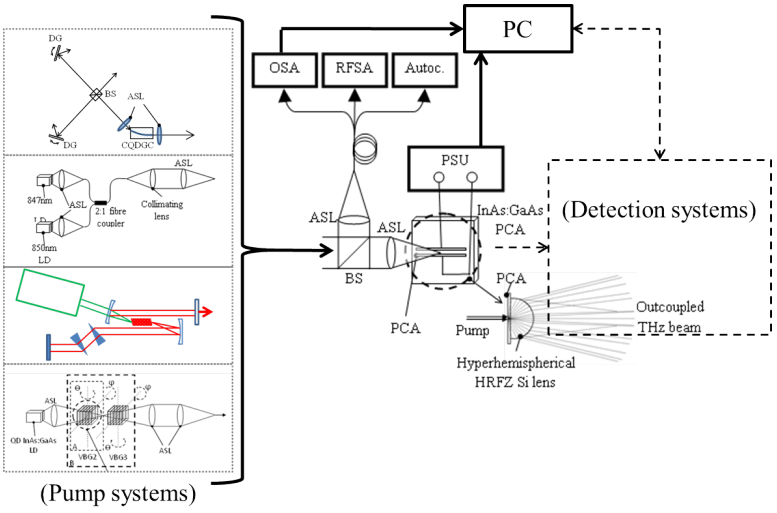

FIGURE 4.13: Schematic of the experimental setup for the pumping of test PCA devices and generation of THz signals. ASL - aspheric lens; BS - beam-splitter; PCA - photoconductive antenna; PSU - power supply unit; OSA - optical spectrum analyser; RFSA - radio frequency spectrum analyser; Autoc. - autocorrelator; PC - computer system.

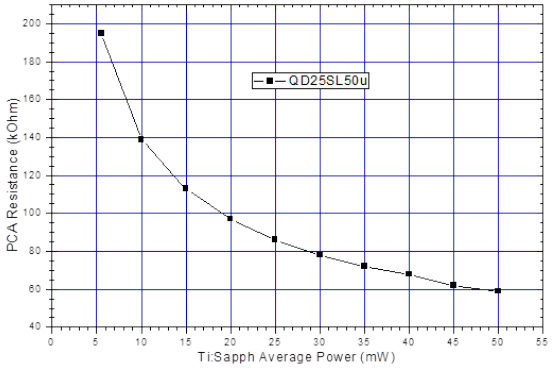

FIGURE 4.14: 50 μm-gap CPS antenna deposited over QD Structure 2: (photo)resistance as a function of Ti:Sapphire laser pump power.

which allowed real-time optical monitoring of beam alignment using a zoom lens (see Figure 3.9).

Once the pump beam is aligned optimally, continuously increasing the optical pump power will alter the PCA (photo)resistance in a trend similar to those presented in Figures 4.14–4.16. Figure 4.14 shows the resistance trend in a 50 μm-gap CPS antenna deposited over QD Structure 2 as a function of Ti:Sapphire laser pump power.

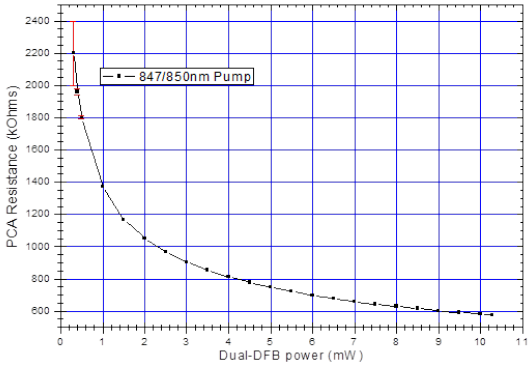

FIGURE 4.15: 5 μm-gap log-periodic antenna deposited over QD Structure 1: (photo)resistance as a function of dual-DFB LD system pump power.

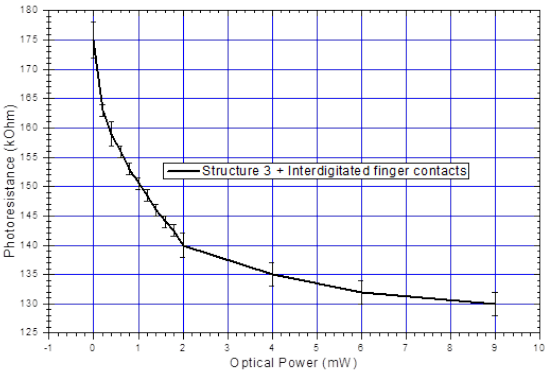

FIGURE 4.16: Log-periodic antenna with 0.2 μm contact fingers separated by 0.8 μm gaps over QD Structure 3: (photo)resistance as a function of tunable InAs:GaAs QD LD pump power.

Figure 4.15 shows the resistance trend in a 5 μm-gap log-periodic antenna deposited over QD Structure 1 as a function of dual-DFB LD system pump power.

Figure 4.16 shows the resistance trend in a log-periodic antenna with 0.2 μm contact fingers separated by 0.8 μm gaps on QD Structure 3 as a function of dual-wavelength InAs:GaAs QD LD pump power operated at an average wavelength of 1220 nm.

Additionally, an example of CMOS camera-assisted alignment of the pump beam with the PCA photo-gap is given in Figure 4.17. The bowtie antenna in this case was pumped by a CW InAs:GaAs QD LD modulated for dual-wavelength output at 1257 nm and 1262 nm using VBG 2.

To confirm that the contact between the metallic antenna and the PC structure

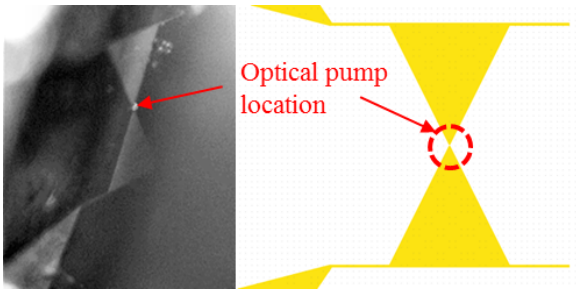

FIGURE 4.17: CMOS camera-assisted alignment of the pump beam with the PCA photo-gap (left), with corresponding antenna design for clarification (right).

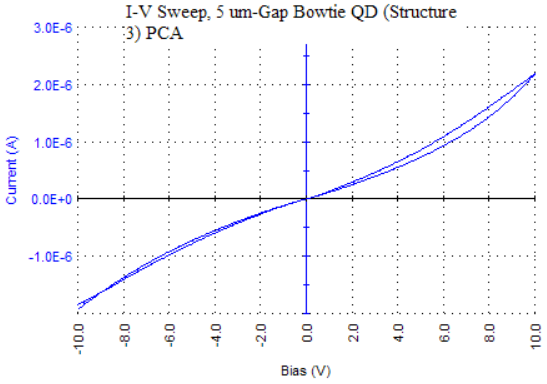

FIGURE 4.18: I-V characterisation of a 5 μm-gap bow-tie PCA over QD Structure 3.

was Ohmic after annealing, I-V tests were made of many different PCA configurations. Figure 4.18 shows an example of an I-V sweep of a 5 μm-gap bow-tie PCA over QD Structure 3. This was done in a sealed, dark test environment using a Kiethley 4200-SCS Semiconductor Characterization System. A bias voltage was applied across the PCA contacts and swept between -10 V and 10 V in most cases – for PCAs with sub-μm photogaps, -5 V to 5 V was used to avoid the risk of electrical breakdown. Measurements were made in 0.05 V increments and swept in both directions. As Figure 4.18 indicates, there is some evidence of slight hysteresis but overall the trend in current with respect to applied bias is very much Ohmic in nature. This was found to be the case for all antennas which were thermally annealed and tested.

The power supply unit (PSU) used to drive the antennas was a programmable control unit (PLH-P [21]) provided by Thurlby Thandar, which could apply a maximum bias voltage of 250 V across the contacts, to within an accuracy of 0.05%. The accuracy and precision of the applied PCA voltage may not be

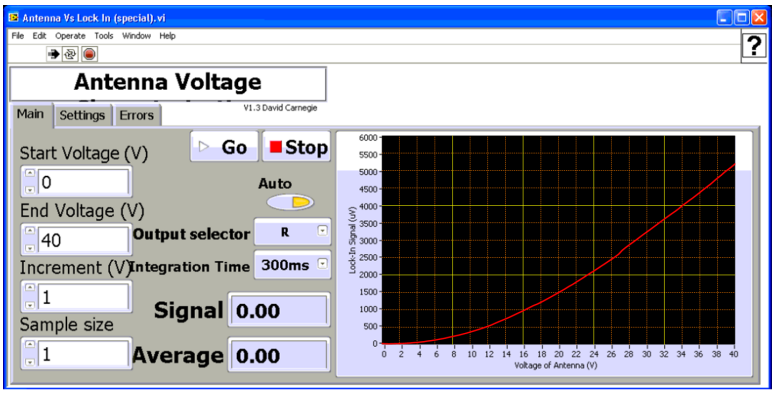

FIGURE 4.19: Screenshot of the PCA bias characterisation program.

as fine as the PSU, however, due to losses in the calbing and custom terminal bonds at the PCA mounting assembly. This unit could also be controlled via USB connection using the computer, and custom control software written in LabVIEW. A useful method for characterising the THz output power trend from the PCAs was to apply a sweeping voltage up to say 40 V in 1 V steps and plot the output power at each step, which was accomplished using the control program. Exemplary results taken using this software are given in Figure 4.19. This software was developed with the help of Dr David Carnegie.

4.3 Summary and Conclusions

In this chapter, the design principles and production methods of custom QD-based PCA devices were described. The epitaxial details of the InAs:GaAs semiconductor structures used in this work were described, as was the subsequent integration of metallic microantenna contacts over these structures. Simulations of the microantenna electrical responses were presented, including a discussion of the expected resonance properties, where appropriate. The further work into e-beam lithographic and imaging techniques were introduced. Additionally, the custom mounting assemblies were presented.

Also discussed is the experimental setups which were used in the generation of THz signals using the prepared PCA devices and the next chapter discusses the main results obtained using such materials, devices and experimental setups.

4.4 References

[1] E. R. Brown. A photoconductive model for superior GaAs THz photomixers. *Applied Physics Letters*, 75(6):769–771, 1999.

[2] H. Roehle, R. J. B. Dietz, H. J. Hensel, J. Bottcher, H. Kunzel, D. Stanze, M. Schell, and B. Sartorius. Next generation 1.5 μm terahertz antennas: mesa-structuring of InGaAs/InAlAs photoconductive layers. *Optics Express*, 18(3):2296–2301, 2010.

[3] Innolume GmbH quantum-dot semiconductor wafers, 2013. URL http://www.innolume.com/products/e_optoelectronics.htm.

[4] The EPSRC National Centre for III-V Technologies, 2013. URL http://www.epsrciii-vcentre.com/Home.aspx.

[5] C. Kadow, S. B. Fleischer, J. P. Ibbetson, J. E. Bowers, A. C. Gossard, J. W. Dong, and C. J. Palmstrom. Self-assembled ErAs islands in GaAs: Growth and subpicosecond carrier dynamics. *Applied Physics Letters*, 75 (22):3548–3550, 1999.

[6] D. Turchinovich, H. P. Porte, N. Daghestani, K. G. Wilcox, E. U. Rafailov, and P. U. Jepsen. Capture and release of carriers in InGaAs/GaAs quantum dots. In C. Palermo and G. Bastard, editors, *16th International Conference on Electron Dynamics in Semiconductors, Optoelectronics and Nanostructures*, volume 193 of *Journal of Physics Conference Series*, Bristol, 2009. IOP Publishing Ltd.

[7] H. P. Porte, P. Uhd Jepsen, N. Daghestani, E. U. Rafailov, and D. Turchinovich. Ultrafast release and capture of carriers in InGaAs/GaAs quantum dots observed by time-resolved terahertz spectroscopy. *Applied Physics Letters*, 94(26), 2009.

[8] Evgenii S. Moskalenko, Mats Larsson, K. Fredrik Karlsson, Per Olof Holtz, Bo Monemar, Winston V. Schoenfeld, and Pierre M. Petroff. Enhancement of the Luminescence Intensity of InAs/GaAs Quantum Dots Induced by an External Electric Field. *Nano Letters*, 7(1):188–193, 2007. doi: 10.1021/nl062417u. URL http://pubs.acs.org/doi/abs/10.1021/nl062417u.

[9] N. S. Daghestani, M. A. Cataluna, G. Berry, G. Ross, and M. J. Rose. Terahertz emission from InAs/GaAs quantum dot based photoconductive devices. *Applied Physics Letters*, 98(18), 2011.

[10] R. Mendis, C. Sydlo, J. Sigmund, M. Feiginov, P. Meissner, and H. L. Hartnagel. Spectral characterization of broadband THz antennas by photoconductive mixing: Toward optimal antenna design. *IEEE Antennas and Wireless Propagation Letters*, 4:85–88, 2005.

[11] S. M. Duffy, S. Verghese, K. A. McIntosh, A. Jackson, A. C. Gossard, and S. Matsuura. Accurate modeling of dual dipole and slot elements used with photomixers for coherent terahertz output power. *IEEE Transactions on Microwave Theory and Techniques*, 49(6):1032–1038, 2001.

[12] M. I. Kazim, P. U. Jepsen, and V. Krozer. Design of THz Antennas for a Continuous-Wave Interdigitated Electrode Photomixer. *2009 3rd European Conference on Antennas and Propagation, Vols 1-6*, pages 1560–1564, 2009. 3rd European Conference on Antennas and Propagation Mar 23-27, 2009 Berlin, GERMANY.

[13] E.N. Grossman. Lithographic antennas for submillimeter and infrared frequencies. In *Electromagnetic Compatibility, 1995. Symposium Record., 1995 IEEE International Symposium on*, pages 102–107, 1995. doi: 10.1109/ISEMC.1995.523527.

[14] LayoutEditor PCB design software, 2013. URL http://www.layouteditor.net/index.php5.

[15] CST Microwave Studio simulation software, 2013. URL http://www.cst.com/Content/Products/MWS/Overview.aspx.

[16] RV Ghita, C Logofatu, C Negrila, AS Manea, M Cernea, and MF Lazarescu. STUDIES OF OHMIC CONTACT AND SCHOTTKY BARRIERS ON. *Journal of Optoelectronics and Advanced Materials*, 7(6):3033–3037, 2005.

[17] Hou Lei, Shi Wei, Han Xiaowei, and Yan Zhijin. Enhanced terahertz emission from photoconductive antenna with ohmic contact electrodes biased by out-of-phase voltages. *Electronics Letters*, 48(13):780–781, 2012.

[18] M. Mikulics, M. Marso, M. Lepsa, D. Grutzmacher, and Peter Kordos. Output Power Improvement in MSM Photomixers by Modified Finger Contacts Configuration. *Photonics Technology Letters, IEEE*, 21(3):146–148, 2009. ISSN 1041-1135. doi: 10.1109/LPT.2008.2008202.

[19] Wellcome Trust electron beam imaging facilities, 2013. URL http://www.wellcome.ac.uk/Education-resources/Education-and-learning/Big-Picture/All-issues/The-Cell/Videos-Types-of-microscopy/WTDV030800.htm.

[20] H. Wang, Y. He, and D. Guo-Zhong. Terahertz Spectroscopic Inspection of Several Kinds of Plastic. *Acta Photonica Sinica*, 39:1185–1188, 2010.

[21] Thurlby Thandar PLH power supply units, 2013. URL http://www.tti-test.com/products-tti/psu/plh-series.htm.

Chapter 5

Evaluation of Compact Terahertz Transceiver Systems

In this chapter, the experimental methods and results obtained in the detection and characterisation of THz signals are described. This includes an overview of all detection methods tested, each of which is characterised by different signal input limitations; different control conditions; and different levels of 'practicality' and accuracy. Most systems were 'direct' detection methods that function based on their sensitivity to a very broad range of IR and thermal energy. These systems were used to directly measure the THz output signal power from a PCA device under test and in this work, a low-temperature bolometer and a Golay cell detector was used. One method, the 'coherent' detection scheme, was used for further characterisation of devices in terms of their THz frequency performance and is also the primary method used for the now commonly-employed THz spectroscopic and hyperspectral imaging systems [1, 2]. This method will be expanded on the most here, as it was both the most complicated but also the most informative experimental system. It should be noted here that both the bolometer (Section 5.1) and the Golay cell (Section 5.2) systems measure the incoming energy as an average over a relatively long integration time due to the required relaxation time of the active detection element, and were not able to measure peak THz pulse powers or waveform information without additional optical systems such as an interferometer.

In all experiments, the output signal was monitored with the use of a SR830 lock-in amplifier (LIA) system developed by Stanford Research Systems [3]. This was connected directly to the output terminal of the detector system and an appropriate chopping frequency was set using a Thorlabs MC2000 optical chopper unit and a blade with a suitable number of slots. The chop rate was set by the controller and both the target and actual chop rates were fed to the LIA, which will then analyse the output from the connected detector at this chop frequency. This is relevant because the chop rate of each system varies greatly, was dependent upon the nature of the detector response and can significantly affect the accuracy of the results if the chop rate was offset from the optimal detectivity rate of the detector. This is generally the case for incoherent thermal detector systems [4]. The LIA could also be controlled and monitored using custom software written in LabVIEW, which vastly expanded and accelerated our experimental results but was also necessary to operate the coherent detector system, discussed in Section 5.3.

5.1 Low Temperature Bolometer Detection

The bolometer system used in this work was based on an ultra-sensitive doped germanium semiconductor detector/absorber chip [5]. The effective temperature-dependent resistance of the chip (given below) was accurately calibrated by the manufacturer to give a corresponding read-out of the level of incident energy over the chip surface.

$$R = R_0 \exp(A/T)^{1/2}. \tag{5.1.0.1}$$

The Ge chip is (carefully) soldered into a circuit with a balanced load resistor and electrical connection to the chip is very specifically configured. The connection leads (typically indium) that are directly in contact with the chip and the first stage signal amplifier are held also in the ultra-cooled chamber to significantly eliminate the amplification of microphonic noise in the wiring, and bandpass filters are connected directly after this to eliminate all expected low-frequency noise. In fact, the performance and sensitivity of such bolometer systems can be generally improved if the entire detector chip enclosure can be surrounded by a liquid helium (LHe) shield and LHe-temperature RF filters are used [6], which was the case for the system used here.

Parameter	**Value**	**Unit**
Bandwidth	2–2000	μm
Filtered bandwidth	0.05–7	THz
NEP	2×10^{-12}	$W/Hz^{1/2}$
Optical Responsivity	780	kV/W
Chop rate	80	Hz

TABLE 5.1: Relevant technical specifications of the bolometer THz detector system.

A composite Ge/Si bolometer provided by QMC Systems [7] was used for much of the preliminary device calibration work. This was because of the accurate factory pre-calibration, exceptional sensitivity, and ultra-low noise-equivalent power (NEP), offered by the LHe-cooled system. The NEP of a detector system represents the value of incident signal power which is equivalent to the noise level of the system measurement so a THz detector for initial device testing and optimisation should have an NEP level as low as possible. The technical specifications of the bolometer system are summarised in Table 5.1.

Figure 5.1 shows a schematic section through the full system. The beam entrance aperture was of 15 mm diameter, behind which was a feed horn that focusses the incident beam to the chip active area of 9 mm^2. The operating resistance of the chip was 1–10 MΩ. The detector circuit features a low noise ULN40 preamplifier which is optimised for use with composite bolometer detector integration as indicated previously. The system was cooled cryogenically, using both liquid nitrogen (LN) and LHe. In preparation for operation, the LN reservoir within system was first filled and kept topped up for roughly 12-17 hours to fully cool the 77 K shielding. At this point, the LHe could be introduced to the central reservoir with the abutted chip mount plate below. Several litres of LHe was sacrificed in immediate insertion boil-off in this process just to bring the reservoir itself down to $\sim$ 4.2 K even before the He could be introduced in liquid form. However, once the reservoir was filled it was possible to run the system continuously with adequate LHe supply for up to several days at a time if the LN was regularly topped up.

The entrance window of the bolometer system was fitted with a high density polyethylene (HDPE) lowpass mesh filter which was designed specifically to strongly attenuate EM signals outwith frequencies $0.05 \lesssim f_{input} \lesssim 6.5$ THz and

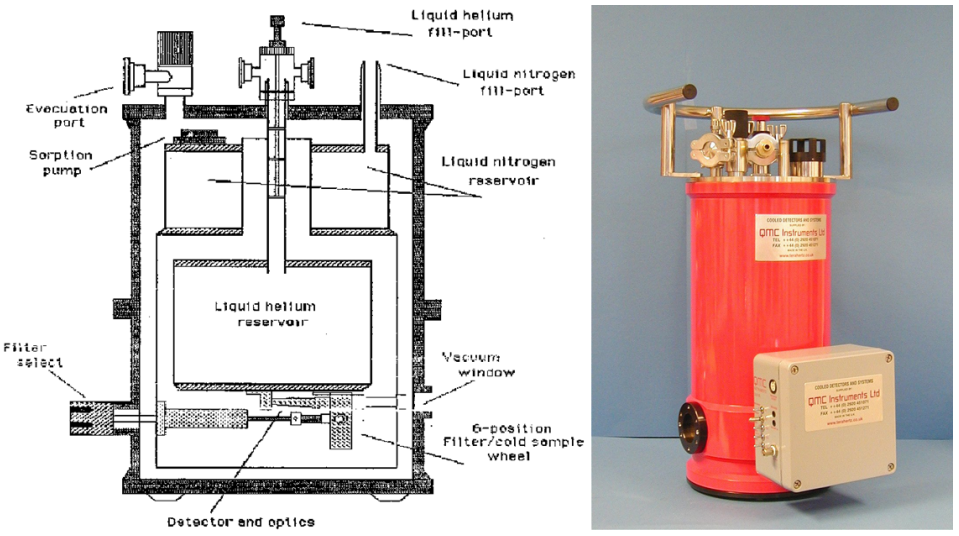

FIGURE 5.1: Schematic section and photograph of the cryogenic bolometer detector system. The "vacuum window" here is the signal entrance aperture.

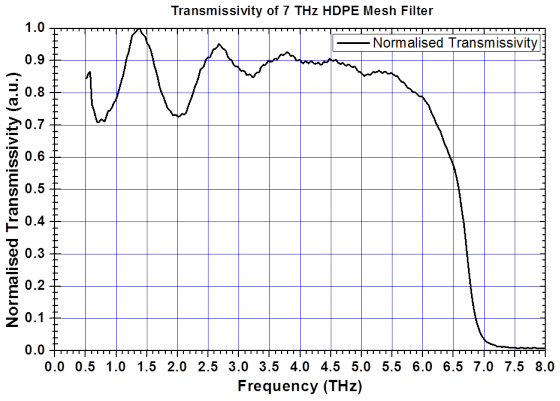

FIGURE 5.2: Transmissivity plot of the bolometer entrance window HDPE mesh filter.

the transmission plot for this is shown in Figure 5.2. Polyethylene and HDPE are commonly used in THz optics because of the relatively high transmissivity at commonly-used THz frequencies [8]. Once the system was cooled and running, the output from the test PCA device was focused directly into the bolometer entrance window. Either the optical pump beam or the THz output beam was chopped at 80 Hz. The preamplifier circuitry was located on the side of the system, the output from which was connected via BNC cables directly to the LIA and the bolometer response was monitored either directly from the LIA display or via the plotter software installed on the connected PC system. A basic system schematic is shown in Figure 5.3, which was similar for tests using both the bolometer and Golay cell systems.

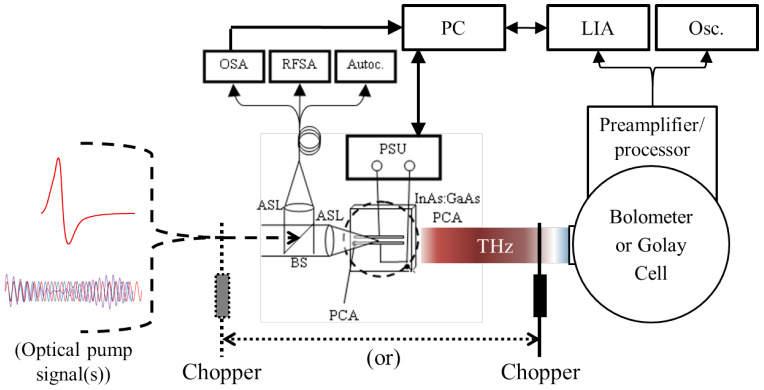

FIGURE 5.3: Schematic of the 'direct' generation and detection experimental setup. ASL - aspheric lens; BS - beamsplitter; PCA - photoconductive antenna; PSU - power supply unit; OSA - optical spectrum analyser; RFSA - radio frequency spectrum analyser; Autoc. - autocorrelator; PC - computer system; LIA - lock-in amplifier; Osc. - oscilloscope.

Semiconductor Structure	**Antenna Geometry**	**PC Gap (μm)**	**Optical Pump**	**Figure**
LT-GaAs	CPS	50	Dual-DFB	5.4
LT-GaAs	CPS	50	Ti:Sapphire	5.5
Structure 1	CPS	5	Dual-DFB	5.6
Structure 2	LP	5	QD Double-Littrow	5.7

TABLE 5.2: Table of THz signal measurements presented here which were taken with the bolometer detector system using different optical pump systems and PCA types.

Figures 5.4–5.7 presented in the following sections show exemplary THz signal output power trends measured using this bolometer system, including tests of a range of PCA devices as summarised in Table 5.2. Note that descriptions of QD Structures 1–3 are given in Section 2.2.5.

5.1.1 Signal Calibration Tests with LT-GaAs-Based Antennas

Figure 5.4 shows results obtained in the measurement of THz output power trends from a 50 μm-gap coplanar stripline (CPS) LT-GaAs PCA pumped by the two distributed feedback (DFB) LD system with average wavelengths around 848 nm. The observed THz output power trend is quadratic as we would expect. In this measurement, the frequency difference between the two optical signals was tuned

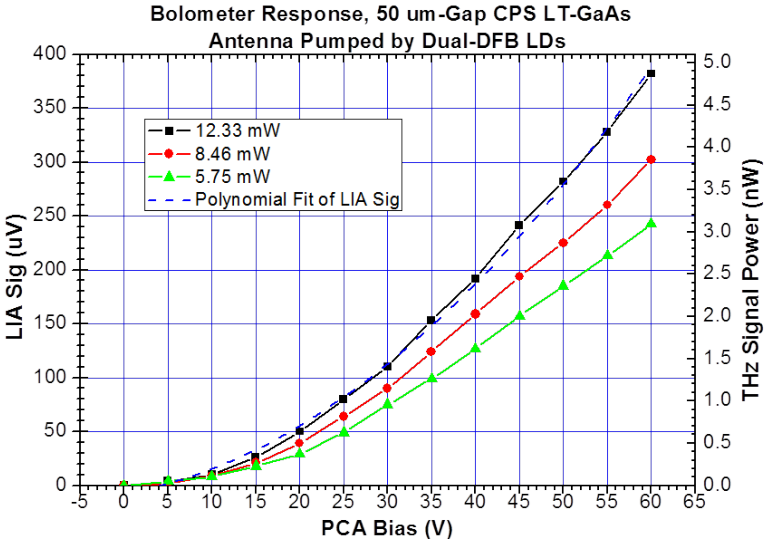

FIGURE 5.4: Bolometer-measured THz output power trend from an 50 μm-gap CPS LT-GaAs PCA pumped by the dual-DFB laser setup at three different optical powers with increasing applied voltage to the PCA.

to 1 THz. The polarisation of the combined beam was closely monitored using a linear polariser at the fibre output and the input polarisations of the beams were equalised by using a half-wave plate at the fibre input from one of the LDs. The absolute polarisation of the combined dual-mode beam is not a critical factor here because the PC gap was much larger than the pump wavelength [9], but they must both match to ensure electric dipole modulation in the same direction for photomixing. The output power is relatively low here due to the very large PC gap and subsequently low gain – 50 μm is well above the typically-used CW PCA gap width. However, this setup was used in initial testing because the commercially-available pre-mounted LT-GaAs THz PCA provided by TeraVil, Lithuania [10] was a suitable reference sample. Moreover, such results could be used to confirm the successful alignment of the pump system and allow the straightforward replacement of PCA devices for further tests in the same setup.

Figure 5.5 shows results obtained in the measurement of the THz output signal power from the same 50 μm-gap CPS LT-GaAs PCA pumped using the Ti:Sapphire laser. Again we observed quadratically increasing THz power trends as the Ti:Sapphire pump power or PCA bias was increased. This was tested up to a PCA bias of 60 V and average pump power of 50 mW, at which point a THz output power just below 1.3 μW was observed. This is a typical performance level from such a device, and corresponds to an optical-to-THz conversion

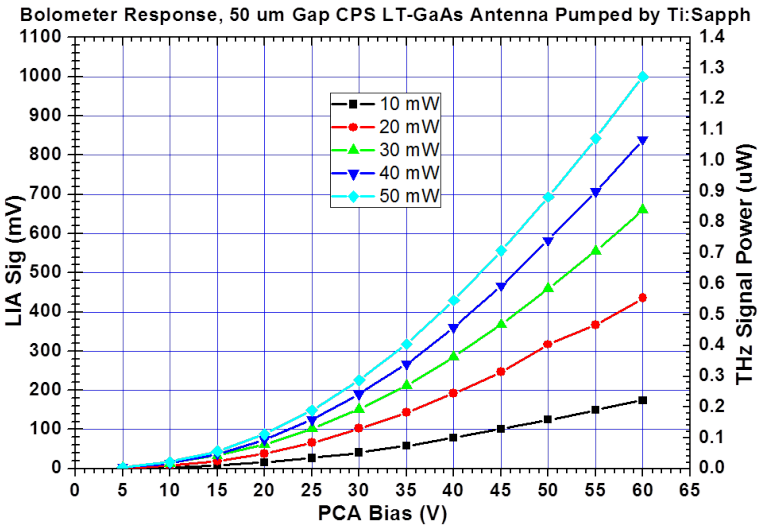

FIGURE 5.5: Bolometer-measured THz output power trend from a 50 μm-gap CPS LT-GaAs PCA pumped by the Ti:Sapphire laser with increasing applied voltage to the antenna.

efficiency of 2.6×10^{-5}.

5.1.2 QD-Based Antenna Tests with Bolometer Detection

Figure 5.6 shows results obtained in the measurement of THz output power from a 5 μm-gap CPS QD (Structure 1) PCA pumped using the two-DFB LD system. These particular measurements were taken over a relatively modest PCA bias and pump power range. As such, the measurement range does not indicate a proper quadratic output trend but the results presented in this plot were repeatable and averaged over multiple measurements to verify the accuracy of the plot. The output power in these measurements is relatively low, but again this is due to the highly unoptimised nature of the antenna contacts and the low expected conversion efficiency of CW regime operation (see Section 1.2.4.2).

Figure 5.7 shows results obtained in the measurement of THz output power from a broadband 5 μm-gap log-periodic QD (Structure 2) PCA pumped using a tunable QD LD in the double-Littrow configuration, and the corresponding optical spectrum which was used for this test. Again, the use of a 5 μm-gap PCA of any geometry is not optimal but the THz output power trend was repeatable and quadratically increased with increasing PCA bias. Interestingly, it was found that

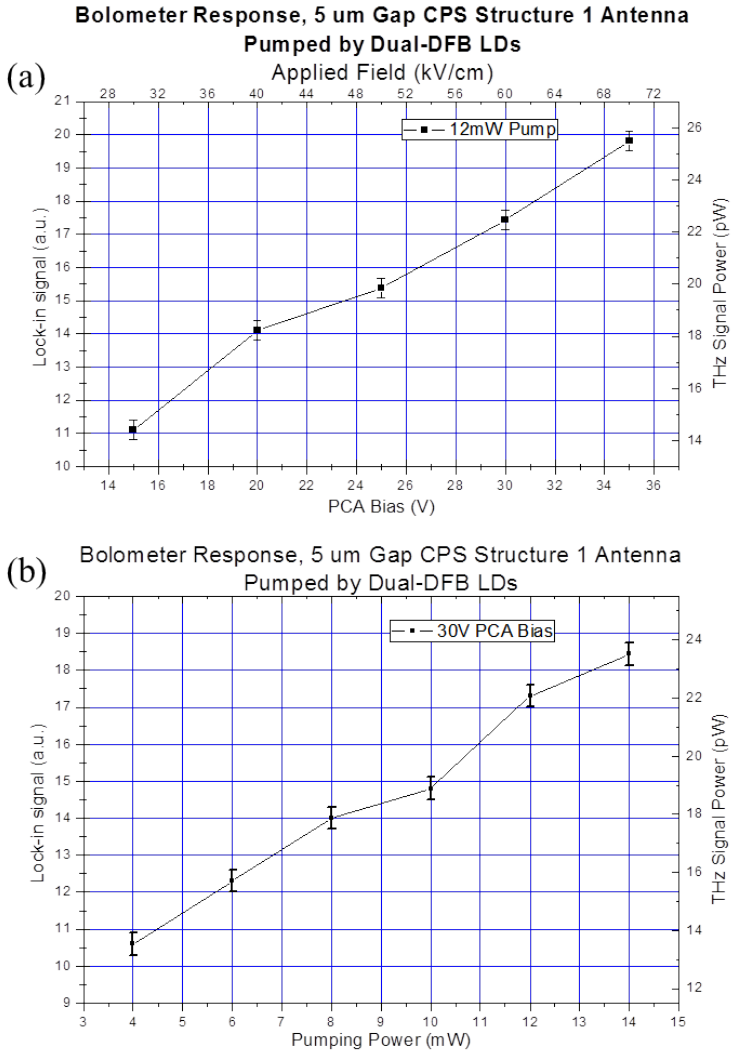

FIGURE 5.6: Bolometer-measured THz output power trend from a 5 μm-gap CPS PCA over QD Structure 1 pumped by the dual-DFB laser setup with (a) increasing applied voltage to the PCA and (b) increasing optical pump power.

the highest conversion efficiency from this device was obtained while pumping the structure at wavelengths between the peak QD ES PL energy and the photomixer cavity resonance peak at $\sim 1220\ nm$. This is perhaps further indication that the higher degeneracy and gain saturation of the ES is better suited to supporting carrier generation, relaxation and recombination mechanisms. Indeed, it has been previously demonstrated that the fast component of carrier recovery in such InAs:GaAs QD heterostructures may be further reduced by excitation of the dots near the ES PL peak(s) [11]. This observation is in agreement with the concepts of carrier dynamics in bandgap-engineered QD heterostructures that were discussed in Section 2.2.5. These discussions indicated the likeliness of accelerated ultrafast carrier dynamics when optically exciting carriers to excited

QD states and applying a lateral E-field across the active volume. Such effects are investigated further in Section 5.3. No *observable* THz EM signals were generated when the PCA was pumped around the QD GS energy. It is possible that optical-to-THz signal conversion processes were initiated in this regime, but carrier escape and recombination will likely have occurred over longer timescales and the subsequent output signal power in this case may have simply been too low.

Additionally, it is worth noting that throughout the PC heterostructure QD layers are not simply 'bunched' at the pump wave nodes (as might be the case for QD-SESAMs) but are distributed periodically throughout the entire standing wave of the *internal* PCA 'cavity' (see Figure 4.2). Therefore, some layers are subject to higher optical excitation than others. If we consider that this effect is crucial in the carrier dynamics for effective saturation control of ultrafast QD-SESAMs as discussed in Section 2.2.3, we begin to see the possibility of QD layers being saturated at different rates throughout the volume. Therefore, it is possible that some layers may be more susceptible to pump absorption and carrier generation and others more susceptible to carrier capture and relaxation. The variation in the layer-to-layer behaviour in this case would depend on the pump wavelength (and corresponding standing wave pattern), the respective availability of energy states in each layer, and would be most noticeable at the QD ES energies due to their higher degeneracy and saturation fluence.

5.2 Golay Cell Detection

The Golay cell detector system used in this work was provided by Tydex, Russia [12] and was based on the original principle developed in 1947 [13]. Generated THz beams were focused and transmitted through the 11 mm entrance cone aperture through a low-pass filter to remove any IR laser light. The beam was then absorbed by an element immediately inside the entrance aperture which is enclosed within a gas cell. When irradiated, the absorber passes heat to the gas causing it to expand, which then acts on a membrane at the rear cell facet. The deformation of the expanding membrane is monitored using a small light source and photodiode pair which is located at the other side. This allowed extremely sensitive monitoring of a very broad range of visible-to-THz frequencies, filtered

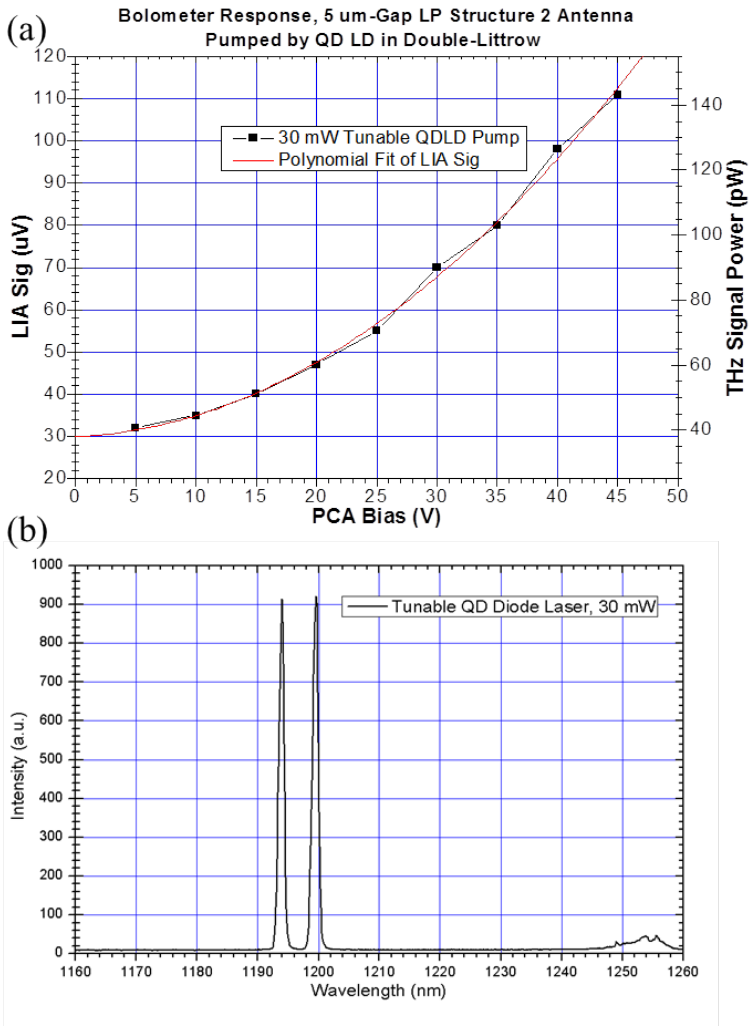

FIGURE 5.7: Bolometer-measured THz output power trend from a 5 μm-gap LP PCA over QD Structure 2 pumped by the tunable double-Littrow QD LD setup with (a) increasing applied voltage to the PCA; and (b) shows the corresponding optical spectrum of the tunable QD LD pump used in this experiment.

by a mesh filter similar to the one used with the bolometer window. The transmissivity of the mesh filter used with the Golay cell is given in Figure 5.8. A table of technical specifications for the Golay cell system is given in Table 5.3.

The optical responsivity of the system as given in Table 5.3 was the noted factory value, but each system was calibrated independently by Tydex and so this value was checked for this specific model by comparing identical THz system measurements taken with the bolometer and the Golay cell. The corresponding optical responsivity trend was obtained as shown in Figure 5.9. This yielded an effective optical responsivity for this detector unit of $\gtrsim 300 \pm 45\ kV/W$, which is a factor of

Parameter	Value	Unit
Bandwidth	15–8000	μm
Filtered bandwidth	$\lesssim 3$	THz
NEP	1×10^{-10}	$W/Hz^{1/2}$
Optical Responsivity	≥ 150	kV/W
Chop rate	15	Hz

TABLE 5.3: Relevant technical specifications of the Golay cell THz detector system.

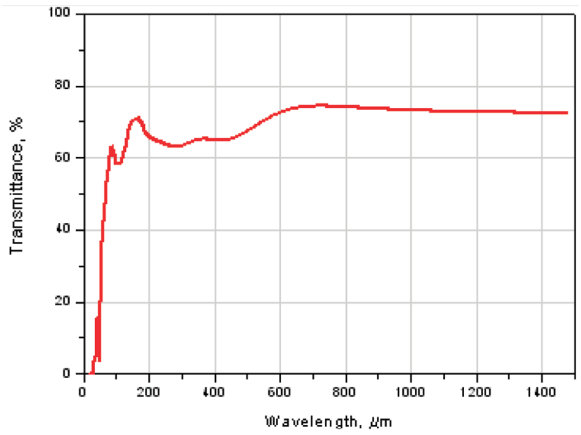

FIGURE 5.8: Transmissivity plot of the low-pass THz mesh filter used with the Golay cell detector system.

two greater than the factory rating, even when taking the margin of uncertainty into account. The calibration was repeated, again referring to the pre-calibrated bolometer system values and still the same value was obtained. This responsivity is large but not outwith reason, and so it was used for the conversion of Golay response to THz input power for the measurements presented here. For reference, the difference in responsivity between the Golay cell and bolometer detector systems can be seen in Figure 5.10, where the responsivity of each system is plotted as a function of incident THz signal power. Simply put, the response from the bolometer system is always around three times greater than that of the Golay cell at the same incident power level. This allows measurements of much lower THz power levels and also means that the bolometer is considerably more accurate at lower signal levels that would normally be approaching the NEP of the Golay cell.

The Golay cell was much more convenient to use than the bolometer system due to the room-temperature operation and acceptable NEP level – a minimum

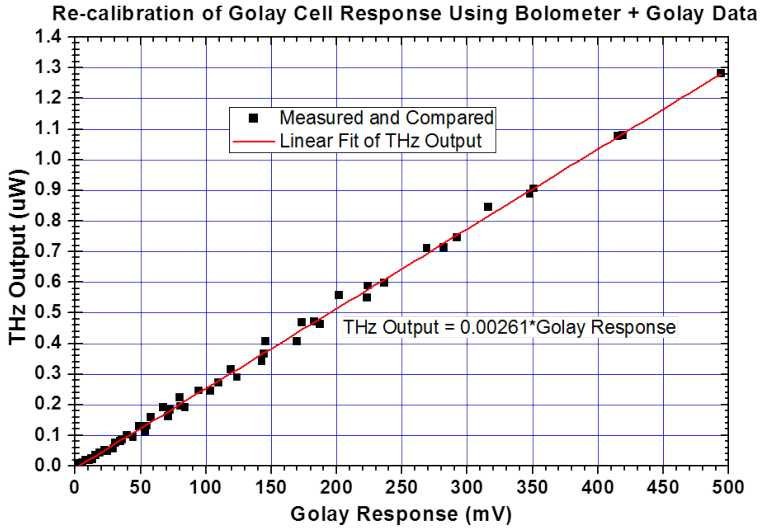

FIGURE 5.9: Re-calibration of optical responsivity data for the Golay cell detector.

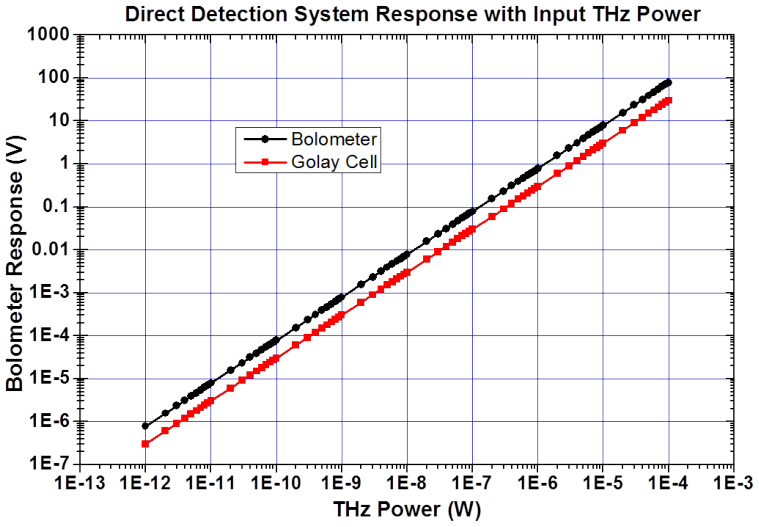

FIGURE 5.10: Comparison of theoretical optical responsivity trends between the Golay cell and bolometer detector systems.

detectable THz signal level of $\gtrsim 0.1\ nW$ should be sufficient to measure any 'practical' THz signal that was generated. This meant that many more experiments were made using the Golay cell detector and an overview of these measurement results is presented in the Figures 5.11–5.13 as described in Table 5.4.

Semiconductor Structure	Antenna Geometry	PC Gap (μm)	Optical Pump	Figure
LT-GaAs	CPS	50	Ti:Sapphire	5.11
QD Structure 2	CPS	30	Ti:Sapphire	5.12
QD Structure 3	CPS	50	Ti:Sapphire HF	5.13
QD Structure 3	Dipole	10	Ti:Sapphire	5.14
LT-GaAsBi	CPS	50	T2S QD LD	5.16

TABLE 5.4: Table of THz signal measurements presented here that were taken with the Golay cell detector system using different optical pump systems and PCA types. T2S QD LD – tapered-gain two-section quantum dot laser diode; HF – high optical fluence.

5.2.1 Golay Cell Detection of LT-GaAs-Based THz Antenna Signals

Figure 5.11 shows an example of typical results obtained via the Golay cell measurement of THz output power from a 50 μm-gap LT-GaAs CPS PCA pumped using the Ti:Sapphire laser, in the same experimental conditions as the calibration tests made in Section 5.1.1. These were the first tests which were made using the Golay cell detector to ensure that the system's response exhibited no unexpected non-linearity, for example. The resulting output trends are similar as measured using the bolometer system and THz signal power quadratically increases with PCA bias and optical pump power up to a level of 1.29 μW. Again, this output power was measured when at an average pump power of 50 mW, indicating an optical-to-THz conversion efficiency of 2.6×10^{-5}, as before.

5.2.2 Golay Cell Detection of QD-Based THz Antenna Signals

Figure 5.12 shows results obtained via the Golay cell measurement of THz output power from a 50 μm-gap QD (Structure 2) CPS PCA pumped using the Ti:Sapphire laser. It was generally found that this structure exhibited the highest optical-to-THz conversion efficiency, typically generating ~ 0.9 μW output power at an average pump power of 50 mW. This corresponds to a conversion efficiency of 1.8×10^{-5}.

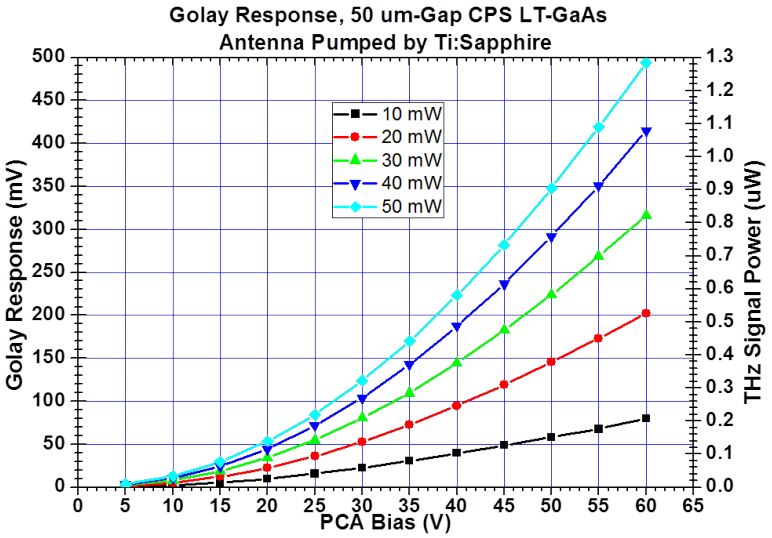

FIGURE 5.11: Golay cell-measured THz output power trend from a 50 μm-gap CPS LT-GaAs PCA pumped by the Ti:Sapphire laser with increasing applied voltage to the PCA.

The conversion saturation is also visible in this plot as the PCA E-field increases beyond $\sim$ 23 kV/cm. Structure 2 is the 25-layer QD sample and it was generally observed that conversion saturation was more common in this structure when pumped using the Ti:Sapphire laser. This could be attributed to the faster overall saturation of recombination sites than might be expected in the 40-layer samples due to the lower number of dots. Conversion saturation with increasing PCA E-field is an inherent part of the device operation. With reference to the equivalent circuits shown in Figure 1.11, we see that the potential-divider-type configuration of the PCA elements sets limits on the distribution of power throughout the antenna. This is determined by the pump power-dependent conductance of the PC medium and the corresponding balance between this and the antenna admittance [14]. The applied PCA bias field is also subject to screening effects by the generation of the photocarriers themselves, and their subsequent spatial separation in the photo-gap. The electric field generated by the separation of charge carriers is oriented in the opposite direction to the applied bias field and subsequently begins to screen it. If the bias across the antenna is increased much beyond this point, regardless of the PC surface material properties, the electrical breakdown of the photo-gap may then occur due to the build-up of the E-field across it. Photocarriers which have been captured by QDs will continue to screen the bias field until they recombine [14], which means that the recombination rate, QD density of states and subsequently the number of dot

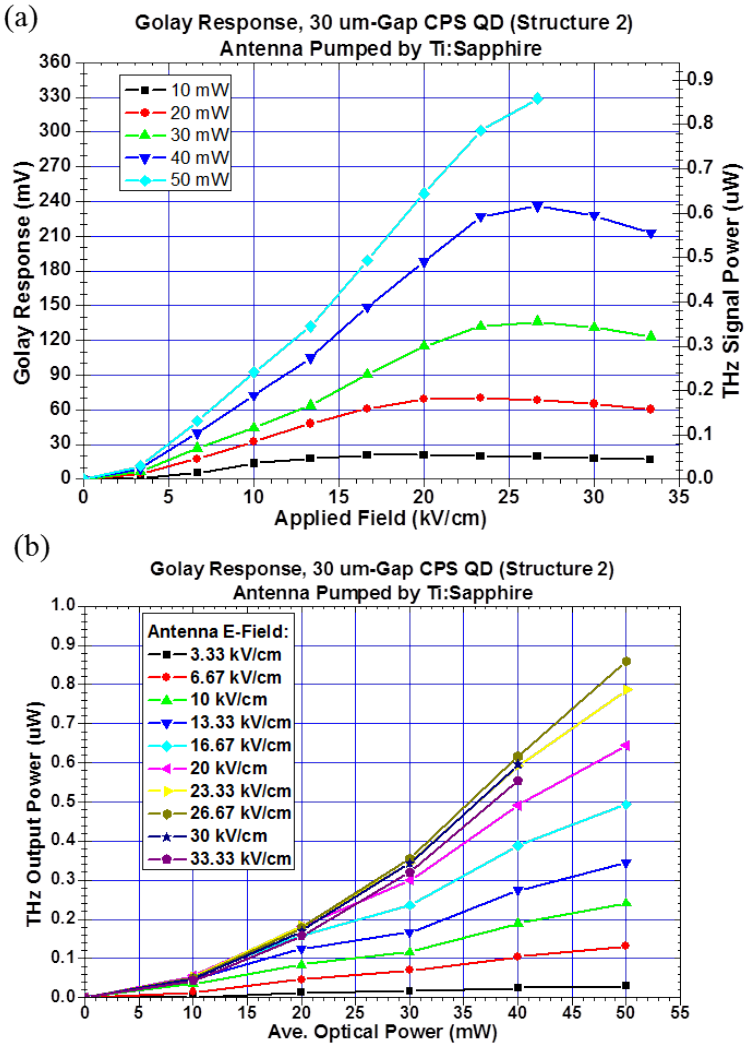

FIGURE 5.12: Golay cell-measured THz output power trend from a 50 μm-gap CPS PCA over QD Structure 2 pumped by the Ti:Sapphire laser with (b) increasing applied voltage to the PCA; and (b) increasing optical pump fluence.

layers in the structure will be primary factors in the saturation field level in a QD PCA.

With this in mind, it is intuitive that optimisation of PCA characteristics would preferentially involve increased tolerance to optical pumping rather than increased tolerance to field breakdown threshold. The InAs:GaAs structures used in these tests are ideally suited to strong optical pumping and indeed this is indicated by Figure 5.12(b), which is a re-plotting of the data in (a) with respect to optical pump power. The data indicates almost no evidence of saturation specifically due to increasing pump power at these levels. An upper limit to the

power generated at each respective pump power appears to be set by the E-field upper limit of $\sim 26.67\ kV/cm$ in this case, not the pump power level.

As such, the conversion performance of such QD PCAs was investigated while pumping at increasingly higher optical power, as shown in Figure 5.13(a). The average Ti:Sapphire optical power applied to a 50 μm-gap QD (Structure 3) CPS PCA was increased up to 315 mW as the PCA bias was held constant and the corresponding THz output power was monitored. Two different PCA bias levels were tested, at 6 kV/cm and 8 kV/cm. Tests at the 6 kV/cm bias level were made only up to a certain pump power as it was limited by the optical setup at the time. The PCA performed much better than expected, exhibiting no signs of saturation or breakdown. After these initial results, the optical scheme was re-configured to enable the use of the full Ti:Sapphire optical power for pumping the test PCA. The PCA bias was also increased to 8 kV/cm, and the device was pumped up to the maximum achievable Ti:Sapphire output power, 315 mW. Only slight signs of conversion saturation are observed at this extremely high pump power. Even this is in some doubt, as the uncertainty associated with the measurement of the Ti:Sapphire output power increases as the maximum is approached. At this point, the pump power was reduced back to 10 mW and the PCA continued to function as before. It should be noted that absolutely no external thermal management of the PCA was applied in these tests. The same PCA device was then re-tested using a pump power held constant at 240 mW, where THz output power was monitored with increasing PCA bias and the output trend in Figure 5.13(b) was observed. Interestingly, this indicates perhaps a more cubic-like output power function with respect to PCA E-field which very rapidly increased towards 0.5 μW as a field strength of 9 kV/cm was approached. It was just above this point, around 9.5 kV/cm, at which the PCA electrically broke down.

Figure 5.14 shows results obtained via the Golay cell measurement of THz output power from a 100 μm-length, 10 μm-gap QD (Structure 3) dipole PCA pumped using the Ti:Sapphire laser. Quadratic THz output power trends were observed with some saturation behaviour exhibited at E-fields above $\sim$45 kV/cm. There are two important observations to note here. Firstly, the saturation E-field in this case is around five times higher than that exhibited by the CPS-geometry antennas, which have a photo-gap five times wider. It should be noted that the field

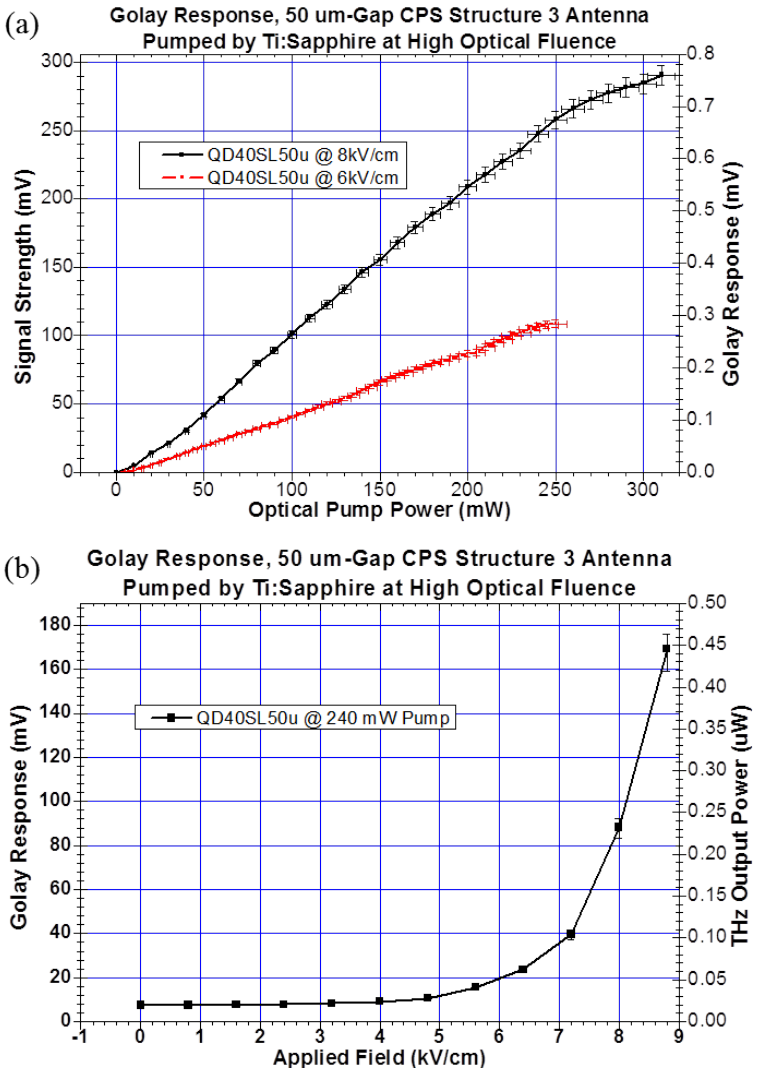

FIGURE 5.13: Golay cell-measured THz output power trend from a 50 μm-gap CPS PCA over QD Structure 3 pumped by the Ti:Sapphire laser at very high optical pump fluence with (a) increasing pump fluence; and (b) increasing PCA applied E-field.

enhancement level created by the five-fold reduction of the electrode separation ($E_{surface} \propto V_{bias}/d_{electrode}$) would demonstrably be enough to initiate saturation effects in the CPS antennas. As such, it is possible that the field-screening effects usually associated with PCA charge carrier capture could potentially be reduced and prevent breakdown in a QD structure. This could be explained in part by the multi-level nature of the QD energy structures which effectively exhibit a variety of electron degeneracies at each dot site which may be simultaneously 'accessed' by photocarriers, as discussed in Section 2.2.5. This allows for a broader range of carrier occupancy and relaxation channels in each QD capture site than would be

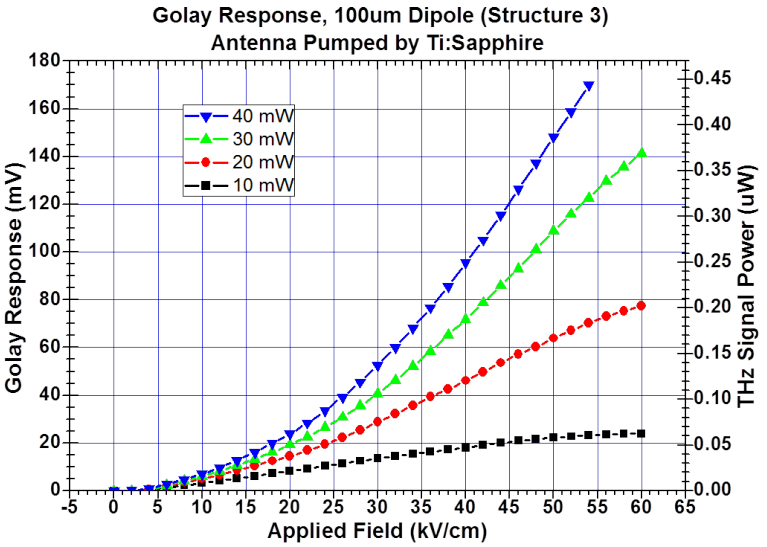

FIGURE 5.14: Golay cell-measured THz output power trend from a 100 μm-long, 10 μm-gap dipole PCA over QD Structure 3 pumped by the Ti:Sapphire laser with increasing applied voltage to the PCA.

in the defect sites that are implanted in bulk materials such as LT-GaAs. Therefor, the extent of carrier field screening effects may be more efficiently managed provided there is an adequate density of QD capture sites. Indeed, as mentioned previously it was observed that E-field-related conversion saturation and breakdown was reduced in QD structures with a greater number of layers (40 layers compared with 25). These results suggest that more fundamental investigation of this should be the subject of future work and future device optimisation. The second main observation is that the strength of the E-field required for output signal saturation appears to depend on the optical pump power in all QD PCA devices. As the pump power is increased, the corresponding E-field level at saturation also increases. The opposite scenario is normally the case for 'traditional' low-temperature grown semiconductors – lower field levels are required to saturate the output power at higher optical pump powers, regardless of *absolute* power level – and so this is an extremely interesting result.

This effect could be explained in part with reference to the analogy of QD-SESAMs discussed in Section 2.2.3, where the increase in applied pump power tends to reduce recombination times [15]. The rate of both radiative and Auger recombination at high carrier densities or with additional p-type doping within the dots has been shown to increase [16, 17], with a corresponding decrease in radiative [18] and non-radiative [17] lifetimes and PL intensity. This effect is

typically less significant in QDs than in bulk or QW medium (likely due to the relatively low volume of active medium), and the dots deposited in the samples tested here are undoped, but this effect should be present nonetheless and could reasonably account for the observed dependence of the screening field on the (photo)carrier-pair generation rate. With recombination times being reduced, screening carriers are removed at a higher rate. This would mean that the subsequent screening of the bias field will be reduced on average and a higher bias may be applied before saturation is observed. This, coupled with the high carrier mobility and comparatively high thermal conductivity of the InAs:GaAs structure, might explain the apparent demonstration of a THz PCA which operates more efficiently the harder it is pumped. A more detailed evaluation of the saturation behaviour can be made by considering the rate of change in the output signal power with respect to the emitter E-field ($\delta P/\delta E$). Figure 5.15 shows a plot of such data, which is the calculated derivatives of the curves in Figure 5.12(a). It was observed that the rate of change in output power increased linearly with emitter E-field, which is to be expected from a quadratic trend, and that this occurred up to a certain point at each optical pump power. The E-field level at which the derivative became a constant (saturation point) typically increases with increasing pump power, after which point the derivative is observed to actually decline. This plot further emphasises two main effects. Firstly, it is clear that the stationary points in each curve ($\delta P/\delta E = 0$) are also observed at increasingly higher E-field levels with increasing pump power. Secondly, the curves actually go negative. This indicates that after the saturation point the conversion efficiency of the QD structure begins to decrease as the PCA E-field is increased, which is also evident in Figure 5.12(a).

This is likely due to screening effects specific to the QD medium as the typically-employed bulk-type PC medium such as LT-GaAs tends to simply break down soon after saturation effects are initiated and so this should be the subject of further investigation. The carrier recombination processes which govern the conversion saturation are different in bandgap-engineered QD structures than in bulk low-temperature semiconductors, as discussed previously. It is possible that the balance between charge carrier screening and PCA E-field may favour the screening field if the optical pump is not strong enough to enhance recombination processes. Therefore, increasing the QD PCA E-field after saturation may

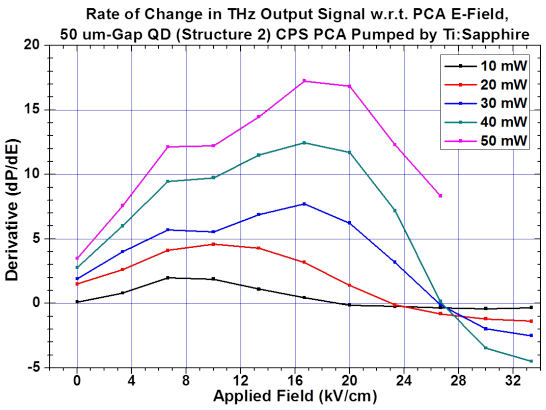

FIGURE 5.15: Derivative plots of the THz output power curves in Figure 5.12(a) with respect to emitter PCA E-field.

simply encourage the build-up of captured excitons which have yet to recombine and contribute to an increasing screening field.

This behaviour may also explain the seemingly ever-increasing THz output trend observed in Figure 5.13(a), for example, and further investigation using a higher power Ti:Sapphire laser would be useful in testing the upper pump power limit and PCA behaviour near this limit. It should be noted that the output power measured from the PCA in Figure 5.13(a) at the highest pump power level was nearly ten times that when pumped at the modest $10-50\ mW$ range, so further testing with more optimal samples and antenna configurations could yield output powers at least in the several μW range.

5.2.3 Golay Cell Detection of LT-GaAsBi-Based THz Antenna Signals

Figure 5.16 shows results obtained via the Golay cell measurement of THz output power from a 50 μm-gap CPS LT-GaAsBi PCA pumped using the a tapered, two-section mode-locked QD LD. The LT-GaAsBi device was used as a reference sample for longer-wavelength optical pumping and was a commercially-available pre-mounted THz PCA provided by TeraVil. LT-GaAsBi is a particularly interesting semiconductor blend for integration in THz PCA devices. Bi does not properly integrate with the alloy blend at normal MBE growth temperatures around say 580°C, but reducing the growth temperature to around 300°C and below allows a Bi percentage up to 10% to be integrated [19, 20]. Similarly to

LT-GaAs as described in Section 1.2.3, the necessarily low growth temperature and subsequent anti-site defect incorporation throughout LT-GaAsBi bulk allows the material to exhibit ultrashort carrier lifetimes necessary for THz operation [20, 21]. The relative volume of Bi incorporated into the blend is typically very small and excess As atoms will most likely occupy predominantly Ga rather than Bi antisites, which creates deep As_{Ga} donor levels [21]. The bandgap reduction which results from the incorporation of Bi allows efficient optical-to-THz signal generation when pumped at wavelengths up to 1.4 μm [22] and THz-to-optical signal detection at pump wavelengths up to 1.55 μm [23]. This made it particularly suitable for pumping via the longer-wavelength QD LDs operating at ultrashort pulsewidths, with the aim of developing an ultra-compact, all-semiconductor THz transceiver system.

The performance of this setup was limited primarily by the optical pulsewidths that were actually achievable using the two-section QD LDs which were available. The QD LD samples available at the time of acquiring the GaAsBi PCA devices exhibited minimum pulsewidths of 1.5–2 ps as discussed in Section 3.2.2. This was a relatively long photoexcitation time for the PC structure and this meant that any output signal generated by the PCA devices was very low, as it is proportional to the derivative of the rise time of the pump pulse. This may account for the very low output powers which were measured, but the output trend with increasing PCA bias was of a typical quadratic form as expected and even exhibited saturation behaviour at high PCA bias levels as would normally be the case in a functioning device. To measure these low output power signals, the automatic PCA bias control and measurement software was set to use a very long integration (averaging) time at the LIA, and any EM and thermal noise surrounding the experimental area was eliminated as much as possible. This was repeatable across multiple LT-GaAsBi devices as shown in Figure 5.16, so should be mentioned in this section as even these apparent proof-of-concept results were rather promising. However, to validate the system it would be interesting to further explore these THz output signals to evaluate their waveform and frequency spectrum properties. This may be done using an interferometric technique or coherent detection system, provided that the THz beam power is high enough to do so, and should be considered in future investigations.

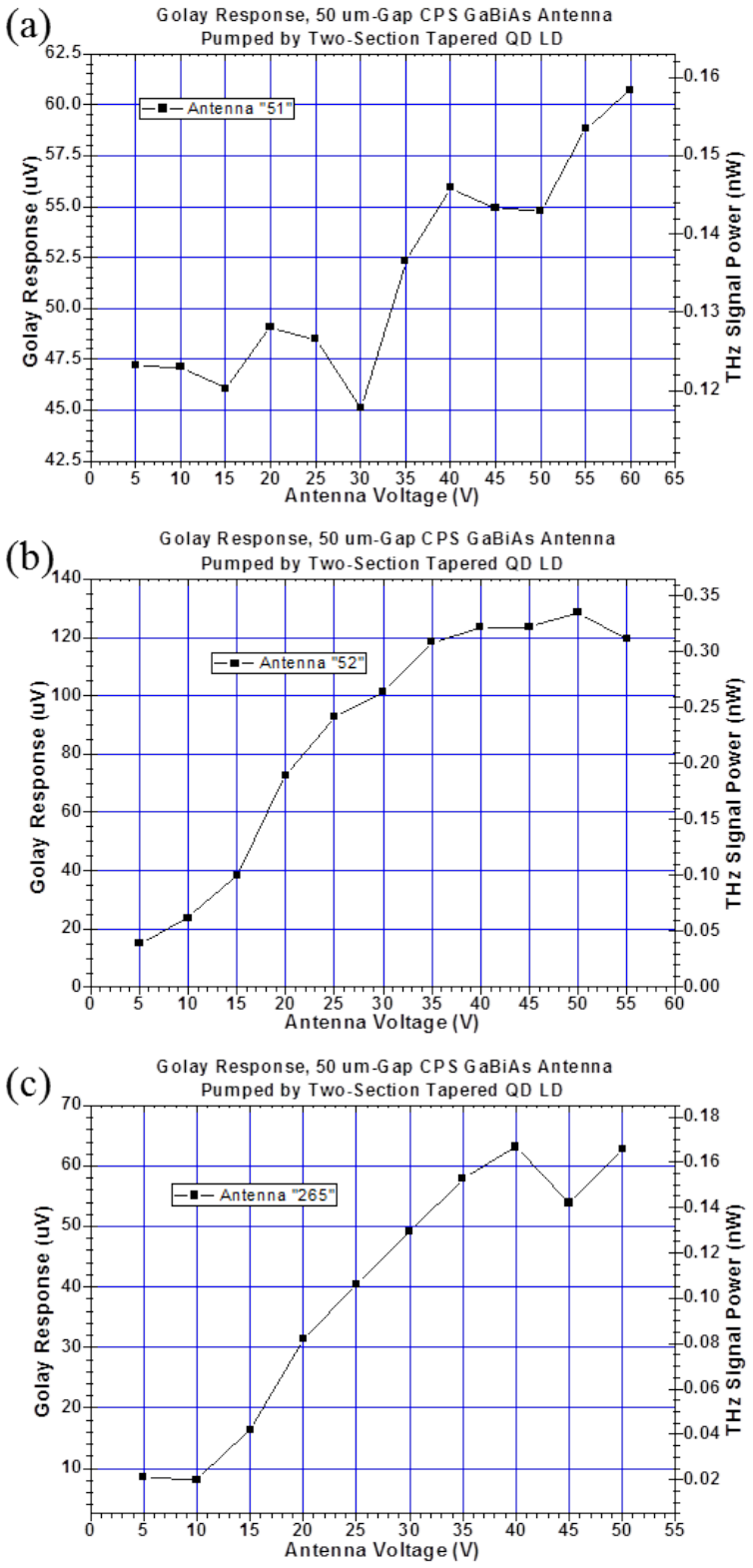

FIGURE 5.16: Golay cell-measured THz output power trend from a 50 μm-gap CPS PCA over LT-GaAsBi pumped by an ultrafast two-section tapered-gain quantum dot diode laser with increasing applied voltage to the PCA.

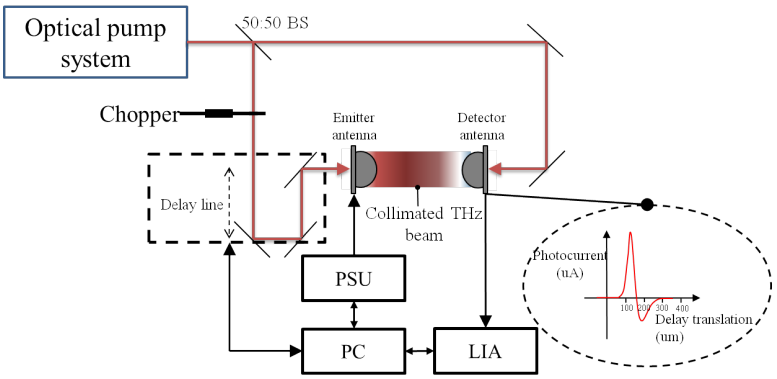

FIGURE 5.17: Schematic of the two-antenna coherent detection system. BS – beamsplitter; PC – computer system; PSU – power supply unit; LIA – lock-in amplifier.

5.3 Coherent Signal Detection

In the previous section, a relatively simple experimental setup for the 'direct' generation and detection of THz radiation from PCA devices was discussed. In this section, the experimental setup and methods for both the generation and detection of THz radiation using two PCA devices in a so-called 'coherent' detection scheme is described. This method relies on the optical pump phase coherence between two PCAs and the THz wave which propagates between them. This allows both an extremely sensitive method of detection and the ability to map the waveform of the THz signal in the temporal and frequency domains, as discussed in Section 1.2.4.1. A basic schematic of this experimental setup is shown in Figure 5.17.

As discussed in Section 1.2.4.1, the operation of both the emitter and detector antenna in a coherent scheme is of course dependent on the interaction of the pump beam with the active PC medium and integrated antenna so the system is still a reliable method for the testing of PCA devices for their optical-to-THz conversion performance and efficiency. However, this method introduced the additional parameter of the optical and THz pulse phase, which was predominantly controlled using the delay line. In the following sections, the implementation of this method is described and exemplary PCA characterisation data is given.

5.3.1 Complete Transceiver System

The results presented here are based on a coherent THz transceiver system using the LT-GaAs PCA provided by TeraVil as the detector antenna, and a range of test PCA devices as the emitter. The emitter voltage was varied in the same way as before; either manually or automatically swept using the PSU voltage control software described in Section 4.2. The system had a detection bandwidth, NEP and optical responsivity which was essentially defined by the limitations of the active PCA semiconductor material(s). The theoretical limitations on the signal chop rate is predominantly given by the lower limit of the pump pulse repetition rate because the relaxation time of the emitter and detector components are at sub-ps scales due to the very nature of the ultrafast PC device physics. It was found that using a high chop rate can help to eliminate low-frequency noise in the output measurements, so typically chop rates in this system were between $\sim 250\ Hz$ and $3\ kHz$.

Alignment was an even greater concern in this system for several reasons. Firstly, the alignment of the pump beam at the emitter relative to the positive and negative bias lines significantly affects the efficiency and movement of generated carrier pairs [24] and therefore can affect the output signal properties. The alignment and collimation of the outcoupled THz beam is then optimised using the abutted Si lens and the beam must then be refocussed at the 'rear' facet of the detector and aligned relative to the detector optical pump beam absorption region and antenna contacts. Misalignment of the collected THz beam can cause significant errors in the measurement of the signal power and frequency spectrum, as the focussed semi-Gaussian beam is relatively broad and consists of a very wide range of THz wavelengths with different focal spot limits [25]. Additionally, a motorised translation stage formed the basis of the delay line and the alignment of the retro-reflected pump beam through the line must be as constant and stable as possible at the PCA emitter pump spot throughout the sweep of the required delay length, which can be several cm.

Presented in Figures 5.18 and 5.19 are some exemplary THz signal measurements taken by scanning the delay line to the location where the output waveform peak was in phase with the detector pump and then sweeping the emitter voltage. As such, these measurements do not represent actual emitted signal 'power', but rather the peak amplitude as 'translated' by the photocurrent convolution within

the detector antenna. Still, the output signal trends that were observed agreed well with theoretical predictions, with THz signal amplitude increasing as the emitter voltage or the pump fluence was increased.

Figure 5.18 shows coherent THz signal measurements made while pumping similar 50 μm-gap LT-GaAs CPS emitter and detector PCAs using the Ti:Sapphire laser. A more linear output power trend with increasing PCA bias is observed in these measurements. This is because the photocurrent generated in each antenna is similarly proportional to the pump power and the THz electric field incident on the detector antenna is proportional to the bias field of the emitter antenna. Plot (b) again shows initial quadratic output power trend with increasing pump power and output saturation begins at around 40 mW.

Figure 5.19 shows coherent THz signal measurements made while pumping 50 μm-gap QD (Structure 3) CPS emitter and 50 μm-gap CPS LT-GaAs detector PCAs using the Ti:Sapphire laser. Interestingly, we observed a more sub-linear output signal strength dependence on emitter bias. The difference in the respective PCAs' response to optical pumping, emitter bias and incident THz field at the detector may account for the trends which were observed. For example, as discussed in the previous section, the optical-to-THz conversion in the QD PCA emitter saturates at higher bias field when pumped at higher optical power – but the response of the LT-GaAs detector PCA begins to saturate as the optical pump power is increased. As such, the resultant 'efficacy' of coherent signal emission/detection in this configuration may primarily be a complicated balance of these two competing factors. To investigate this further, a QD dipole emitter PCA was set up in the same configuration and the results of these tests are presented in Figure 5.20. The output trend with increasing optical pump power is also shown in Figure 5.19(b). At lower pump powers, this indicates a more linear dependence than the fully LT-GaAs coherent configuration and this slowly saturates with increasing pump power. This more linear dependence and slower saturation rate could be explained by the effect of only the LT-GaAs detector PCA optically saturating, but we can also still see the bias field saturation effects of the QD CPS antenna.

As presented earlier, the narrower photo-gap dipole antenna may be operated at higher bias fields before output saturation is observed. In this case, it was postulated that the inter-relationship between the QD emitter PCA bias field

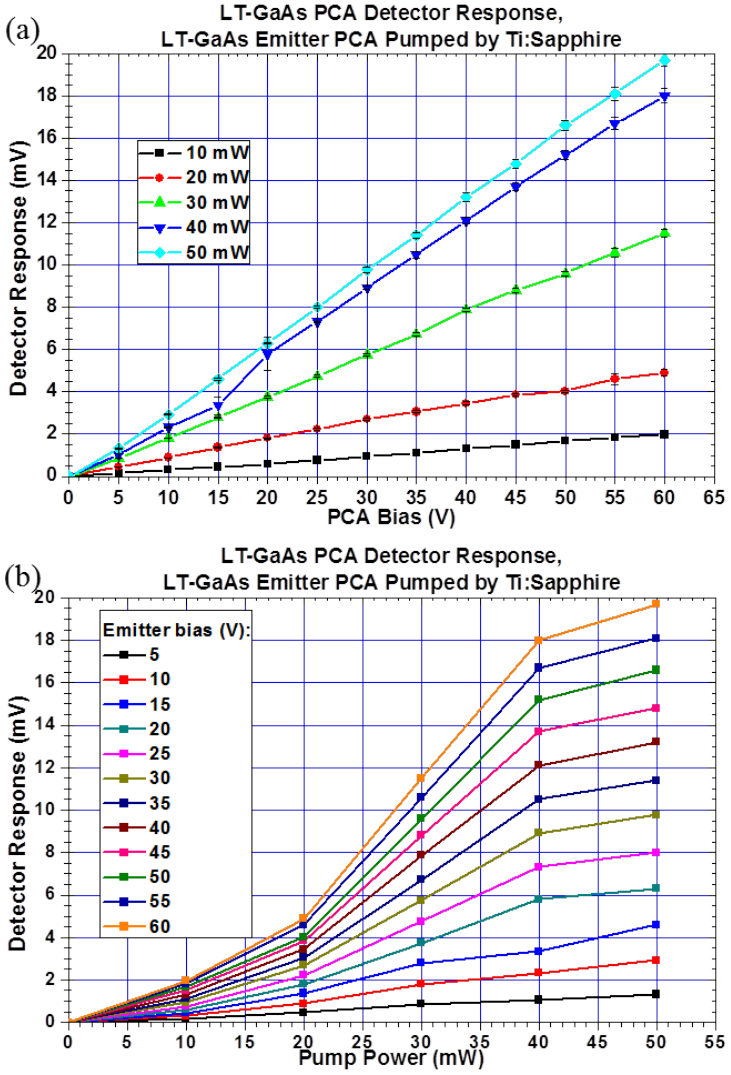

FIGURE 5.18: Exemplary THz signal peak output amplitude trends from a 50 μm-gap CPS LT-GaAs PCA emitter as detected by an LT-GaAs PCA detector with (a) increasing emitter voltage and (b) increasing optical pump fluence.

saturation and LT-GaAs detector optical pump saturation could be simplified. Indeed, Figure 5.20(a) shows that this configuration exhibits a more linear output power trend that is normally observed in the sub-saturated LT-GaAs-based coherent system – most likely due to the significantly reduced bias field saturation effects in the emitter. The output signal strength with respect to optical pump power is plotted in Figure 5.20(b). It is interesting to note that this trend is also a more linear form, compared with the CPS PCA emitter setup and the two-LT-GaAs antenna setup. The slowly saturating output signal again could be explained by the optical saturation of only the LT-GaAs detector PCA and, as

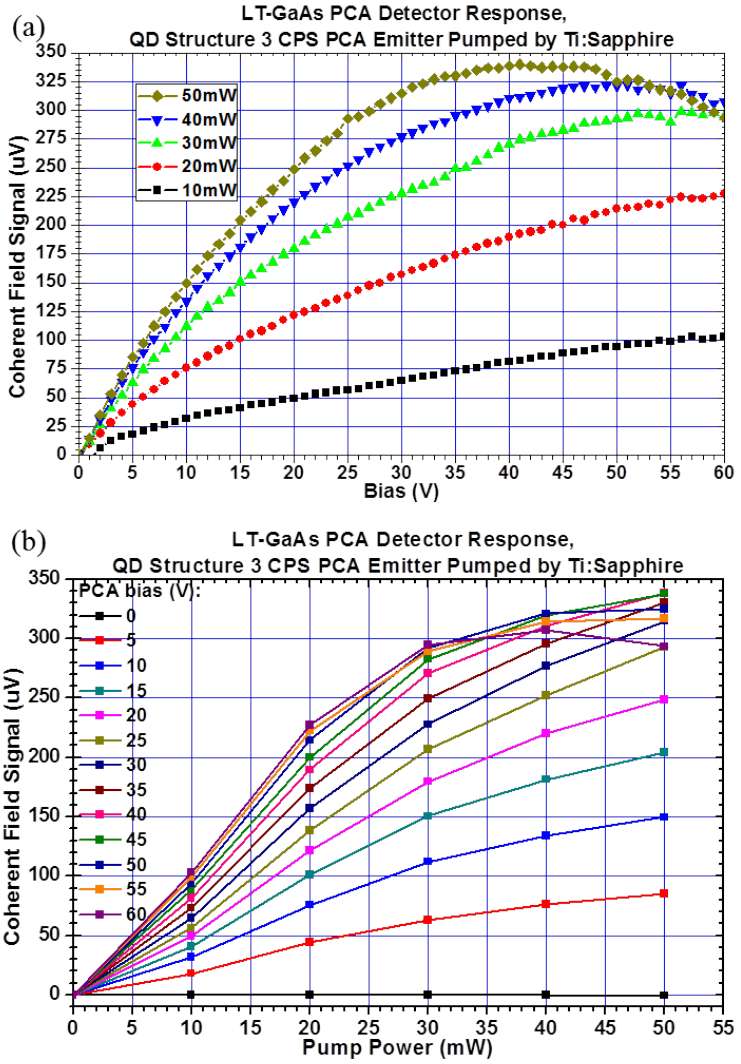

FIGURE 5.19: Exemplary THz signal peak output amplitude trends from a 50 μm-gap CPS 40-Layer QD (Structure 3) PCA emitter as detected by an LT-GaAs PCA detector with (a) increasing emitter voltage and (b) increasing optical pump fluence.

hypothesised, there is no significant emitter bias field saturation effects observed in this plot.

5.3.2 Frequency Response

In this section, a summary of THz spectrum measurements taken using the TDS method as introduced in Section 1.2.4.1 is presented. To implement this, a high-precision Thorlabs NRT100 motorised translation stage [26] was used for the delay line base. This was actuated by a BSC101 single channel stepper motor

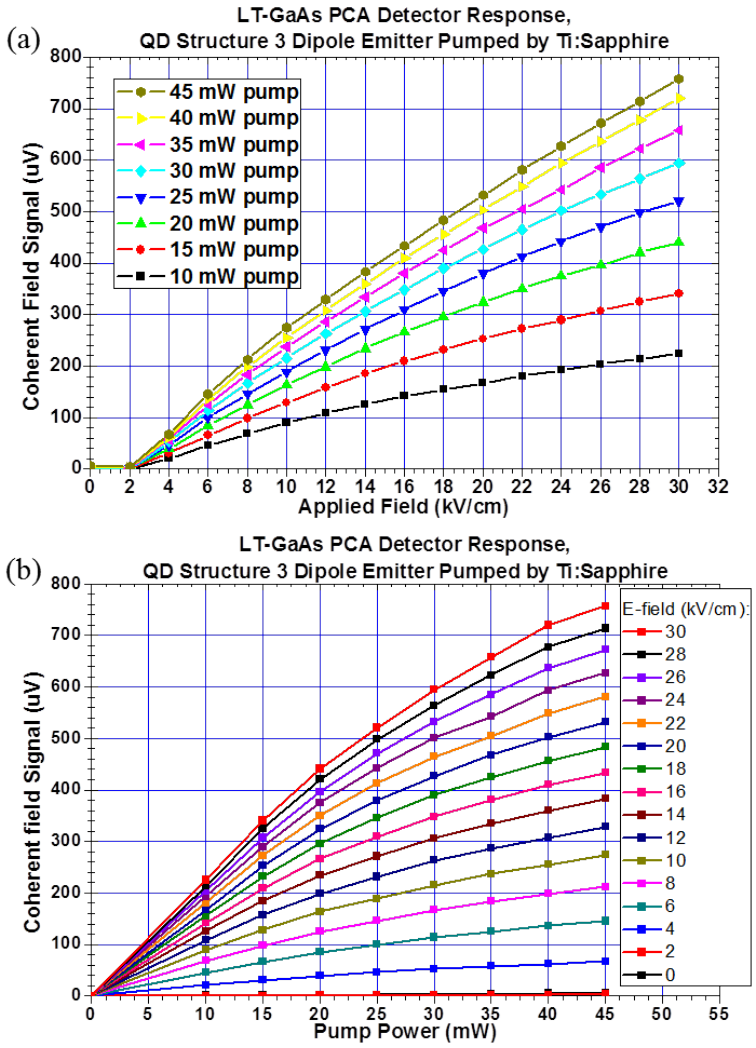

FIGURE 5.20: Exemplary THz signal peak output amplitude trends from a 100 μm-length, 10 μm-gap dipole QD (Structure 3) PCA emitter as detected by an LT-GaAs PCA detector with (a) increasing emitter voltage and (b) increasing optical pump fluence.

controller, which in turn was controlled using custom software written in LabVIEW. The software allowed complete control of the TDS parameters as well as real-time monitoring of results within the same package.

The precision, accuracy and repeatability of the delay line movement was very important and this setup allowed accurate minimum delay steps of 1 μm, which corresponds to a path length increment of 2 μm and time-of-flight resolution limit of 6.67 fs. This level of accuracy was not actually necessary, so typically the smallest delay step size was 2 μm corresponding to a temporal resolution of 13.34 fs. Temporal resolution and accuracy sets important limits on the spectral resolution of the resultant THz spectrum, as pulse-to-pulse jitter or offset will

blur and skew the Fourier transform features of the waveform. The accuracy of each consecutive delay step depends partly on the overall movement velocity and acceleration of the stage so at each step the system was given adequate time to settle as close as possible to the required position, which also gave the opportunity to use long signal integration times at the LIA if necessary. Longer integration times allow a more accurately-averaged signal measurement and it was also found that multiple complete spectral measurements when averaged would further increase the resultant S/N ratio of the obtained THz spectrum. Example screenshots of the THz TDS software, including sample waveform and FFT spectrum data, are presented in Figure 5.21. This software was developed with the help of Dr David Carnegie.

Figures 5.22-5.24 show some typical results obtained in the THz TDS measurements using a range of different PCA devices. Figure 5.22(a) shows the temporal profile of the THz output signal generated and detected by the 50 μm-gap CPS Lt-GaAs PCAs. This was measured at successive 6.67 fs intervals using the pump delay line at the emitter antenna. A zoomed view of the main pulse is shown inset, we can see the main peak at $\sim 32.5\ ps$ and we can estimate from this a FWHM of $\sim 600\ fs$. The FFT is taken over the entire temporal pulse length of course, including the long 'tail' of the pulse up to 100 ps and beyond, and is shown in plot 5.22(b). The spectrum has a noise floor around 2.5×10^{-6} but we can actually resolve spectral features to beyond 2.2 THz in this measurement. We can check the accuracy and precision of such spectral features by comparison with previously established measurements of THz spectral fingerprints of different chemicals as discussed in the next section. The signal spike at 2.75 THz is an example of an artefact that was occasionally observed after the FFT process was run on the obtained waveform, and is likely indicative of small, repeated inaccuracies in the delay line movement. This effect further emphasizes the importance of precision and accuracy in the delay line control, as recurring errors in sequential delay steps can emerge as resonant spectral features in the resultant FFT data.

Figure 5.23(a) shows the temporal profile of the THz output signal generated and detected by a 50 μm-gap CPS QD (Structure 3) emitter PCA and 50 μm-gap CPS LT-GaAs PCA detector. A zoomed view of the main pulse is shown inset and we can see the apparent main peak at $\sim 11\ ps$ and this exhibits a FWHM

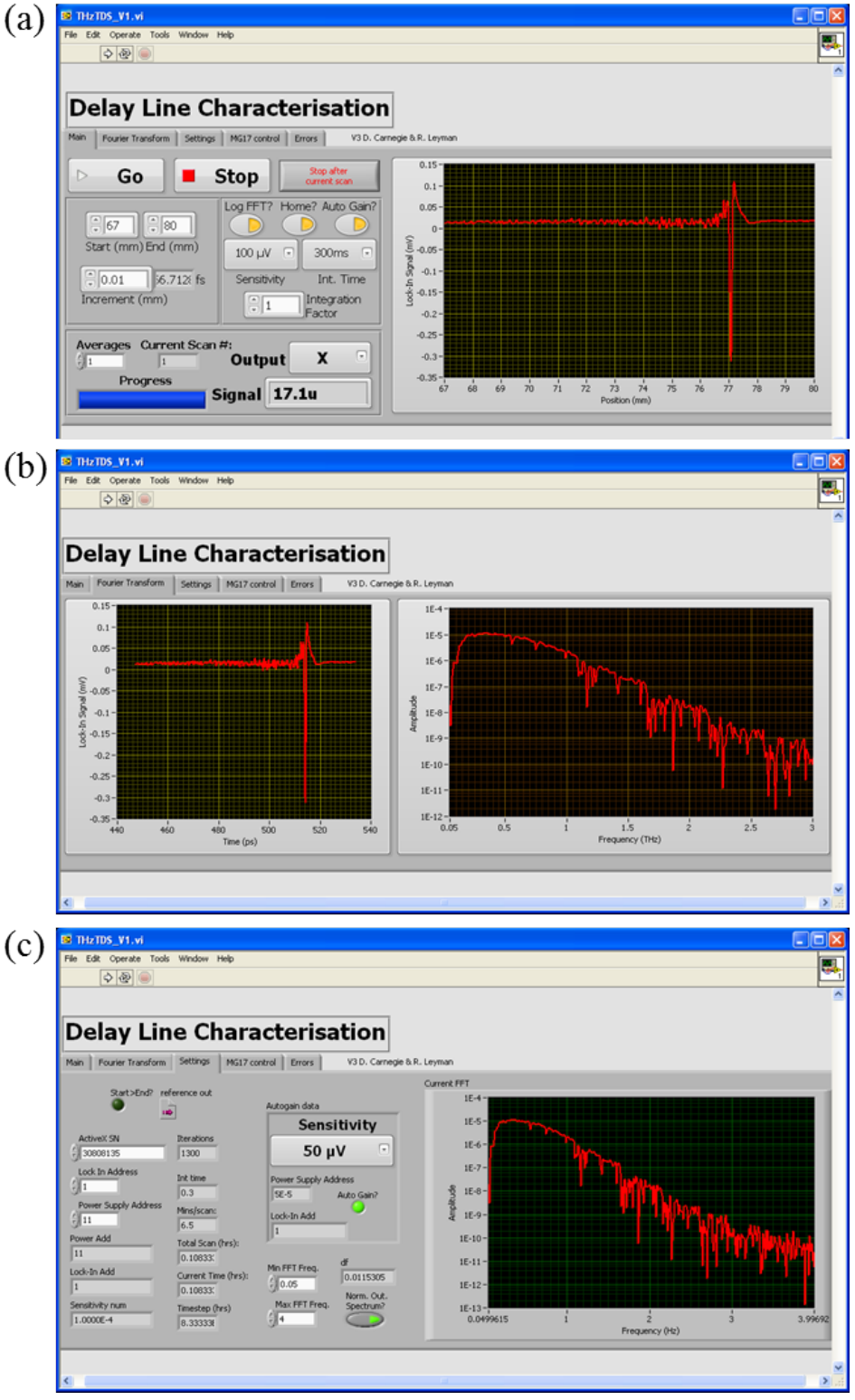

FIGURE 5.21: Screenshots of the THz TDS software: (a) is the main parameter definition panel; (b) is the 'results' panel which shows the averaged temporal THz waveform and normalised Fourier transform frequency power spectrum; and (c) shows the "Settings" panel which was used to monitor background data such as the overall scan progress, current frequency spectrum resolution, chosen spectrum cut-off frequencies and current LIA status.

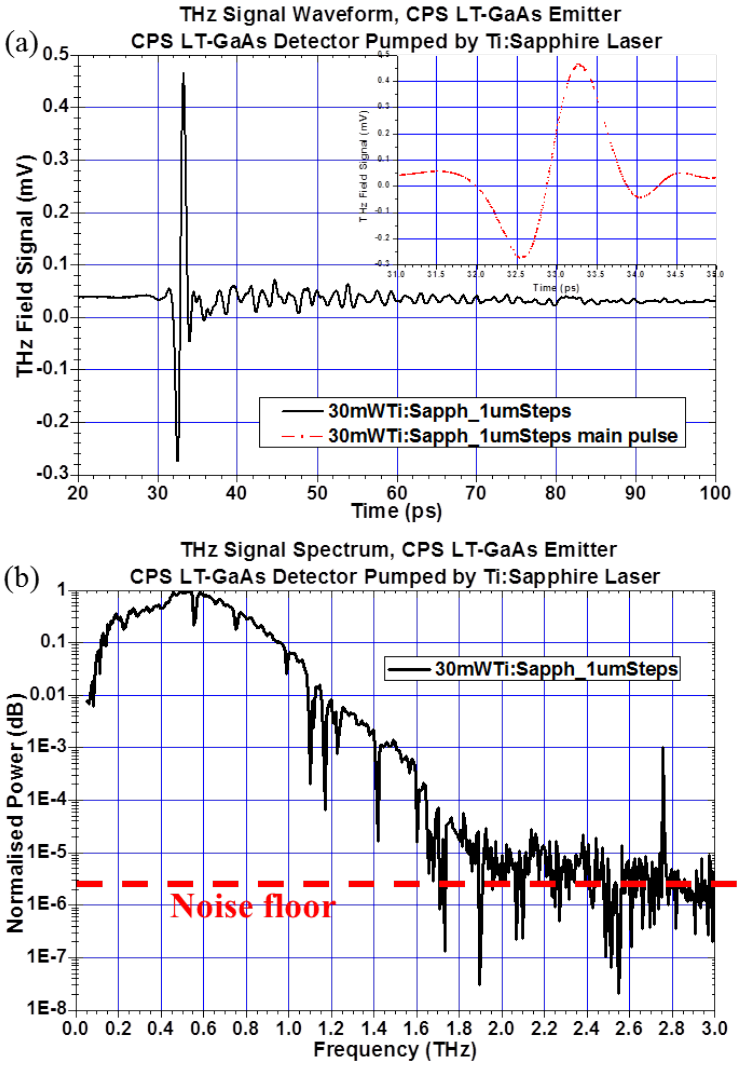

FIGURE 5.22: Exemplary output signals from a 50 μm-gap CPS LT-GaAs PCA emitter as detected by an LT-GaAs PCA detector showing: (a) the temporal signal waveform and zoom of the pulse (inset) obtained directly via scanning the delay line and continuously reading from the LIA; and (b) the corresponding signal frequency power spectrum obtained via FFT of the temporal waveform.

of $\sim$ 600 fs. However, this is closely followed by a secondary, shorter pulse of FWHM $\sim$ 500 fs that is generated 11.13 ps later. Multiple pulse features such as these were typically observed from QD PCA emitters. It was postulated that this could be due to the nature of the pump beam's propagation through successive layers throughout the active structure depth, shown for example in Figure 4.2. These layers are deposited via MBE as discussed in Section 2.1, which is to say they may be considered similarly to a QW superlattice – with the pump beam experiencing multiple material layer interfaces of varying refractive indices and

potential wells. It's possible that the multilayer nature of the beam path conveys a significant effect on the photocarrier dynamics. For example, the beam may experience some degree of reflection as an $n_{low} - n_{high}$ interface is reached and will also experience a very slight phase change through the barrier. Additionally, the DBR beneath the active region was still effective to some small degree at around the 810 nm pump wavelength so the beam may be retro-reflected and re-excite the active region once more. The 11 ps delay between the two main pulse peaks (at $\sim$ 11 ps and $\sim$ 22 ps) corresponds to a propagation distance of 1 μm for an 810 nm pump beam in GaAs ($n_{GaAs,810} \approx 3.31$). As such, this hypothesis may be accurate as the structure cavity length is roughly 1 μm. The extent of the effects of any retro-reflected optical pumping within the structure cavity would depend partly on the optical pump fluence and whether it was high enough to retain the necessary power required to excite enough photocarriers to generate a measurable signal effect. This could be a subject for future work and may potentially be used in a multi-THz pulse capacity if such an application required it.

The plot in Figure 5.23(b) shows the corresponding THz FFT power spectrum of this signal. We can see the appearance of water absorption features around 0.55 THz and 0.75 THz as we would expect, and we can also see many additional features in the spectrum which may be the result of the complicated temporal signal profile signal. Each THz spectrum measured from a QD-based PCA emitter exhibits absorption features around 0.3 THz and 0.4 THz for example, which presumably indicates some significant activity at this frequency in these structures which does not occur in the LT-GaAs PCAs, for example. It is difficult to say exactly what this may correspond to as results reported from THz spectroscopy of semiconductor materials is at present extremely limited (e.g. [27]).

Figure 5.24(a) shows the temporal profile of the THz output signal generated and detected by a 100 μm-length dipole QD (Structure 3) emitter PCA and 50 μm-gap CPS LT-GaAs PCA detector. Again, multiple main pulse features are observed as well as strong secondary pulses roughly 111 ps later. The frequency power spectrum shown in plot (b) again indicates many spectral features which are 'additional' to those expected from water-vapour-only absorption of the THz beam and so may be attributed to events within the QD PCA emitter. However, the output power and S/N ration for this PCA were both much larger than the

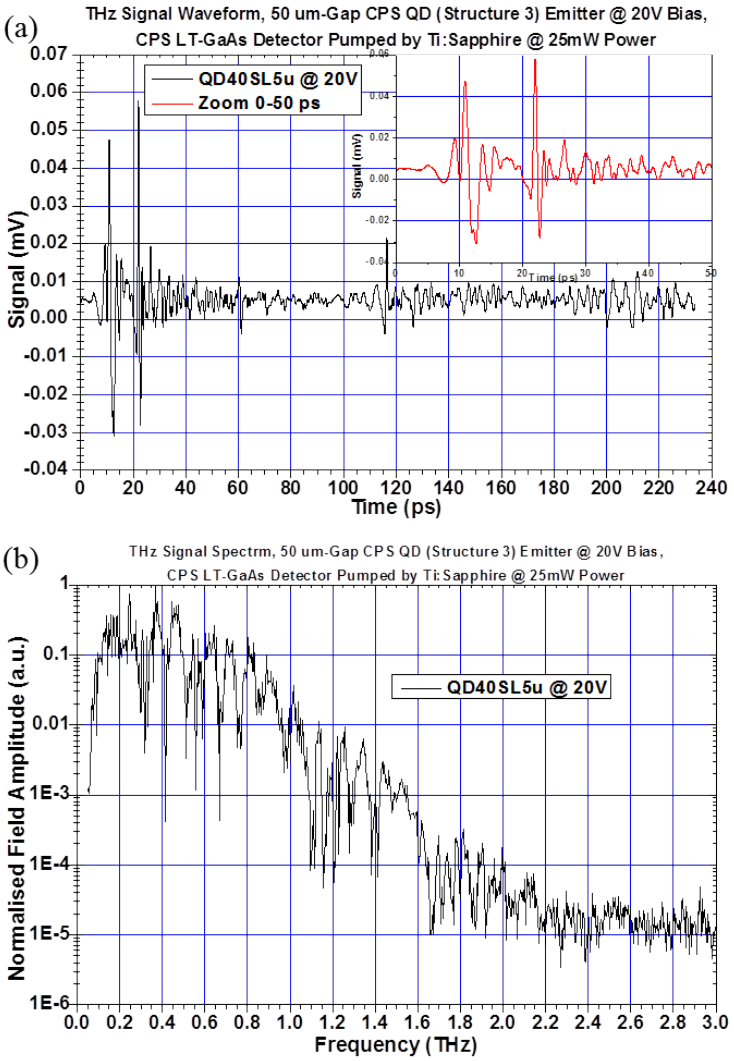

FIGURE 5.23: Examplary output signals from a 50 μm-gap CPS QD (Structure 3) PCA emitter as detected by an LT-GaAs PCA detector showing: (a) the temporal signal waveform obtained directly via scanning the delay line with main pulse area zoomed inset; and (b) the corresponding signal frequency power spectrum obtained via FFT of the temporal waveform.

CPS antenna in Figure 5.23 and the relative absorbed power from water-only interactions in the air is more prominent than these additional features. Note also that the peak power frequency is confined to roughly 0.2 THz, which is due to effects of the interaction between the fs pump beam and the resonant dipole antenna geometry. This demonstrates the relative tunability of a THz PCA as configured using antenna resonance features normally employed – the PCA is operating as predicted. Again, the power spike at 1.675 THz is an artefact from the delay line movement and FFT process and would be averaged out if multiple scans were taken.

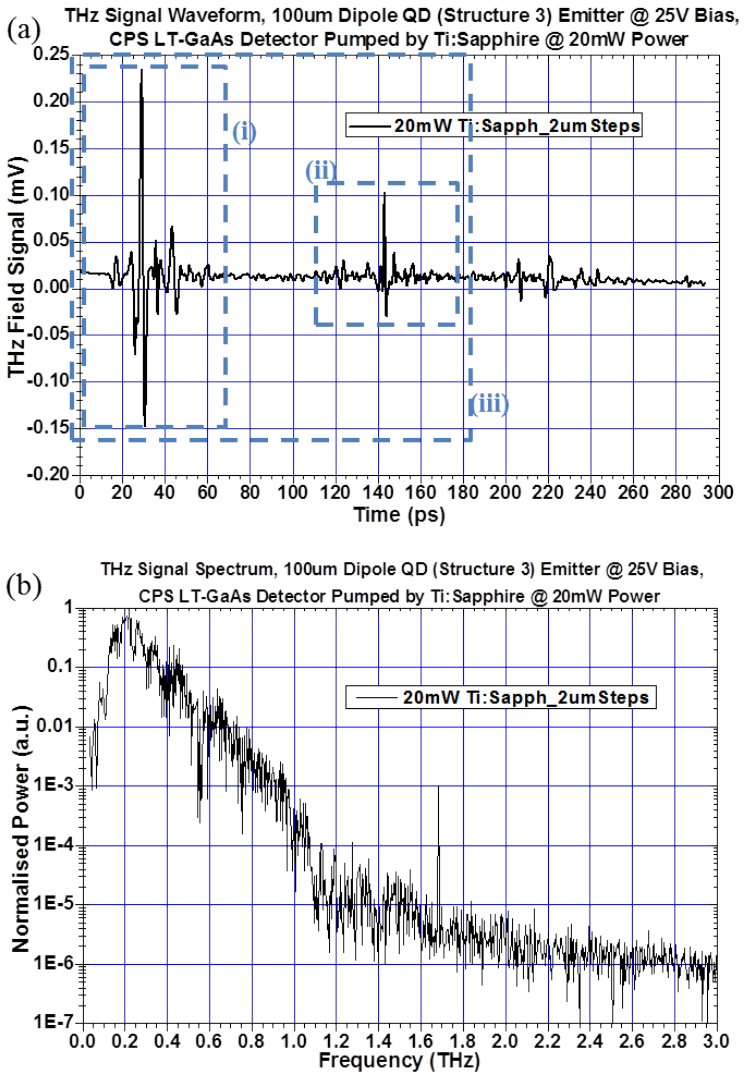

FIGURE 5.24: Examplary output signals from a 100 μm-long, 10 μm-gap dipole QD (Structure 3) PCA emitter as detected by an LT-GaAs PCA detector showing: (a) the temporal signal waveform obtained directly via scanning the delay line and continuously reading from the LIA; and (b) the corresponding signal frequency power spectrum obtained via FFT of the temporal waveform. Sections (i–iii) are marked in the waveform plot for separate spectral evaluation.

To further investigate the influence of the 'multiple-pulse' behaviour, evaluation of the spectral characteristics of each main 'section' of the output waveform was conducted, shown as (i)–(iii) in Figure 5.24(a). This was done because, intuitively, any 'parasitic' signal features (likely to be caused by events other than the primary optical pulse excitation of the PCA structure), for example, could potentially interfere with the original 'true' waveform profile, and cause corresponding artefacts in the Fourier spectrum. The rapidly oscillating (non-smooth) spectrum obtained from QD PCAs in these experiments is likely due to such pulse echoes and wave reflections. For example, the secondary set of features in section (ii) of plot 5.24(a) occurs roughly 110 ps after the main pulse event, which would correspond to a propagation distance of roughly 1 cm for a THz wave through GaAs or HRFZ Si. This happens to be roughly the beam path thickness of the HRFZ Si lens used at the PCA rear facet, and so reflections at the Si lens boundaries may be the cause of such features. The Si lens was abutted as carefully as possible to the PCA facet using small springs against the back mounting plate, but we could not confirm the extend of the planar contact between the two surfaces. To evaluate the overall effect this may have, the corresponding FFT power spectrum of the signal in regions (i)–(iii) were measured using software developed by Dr Andrei Gorodetsky.

This software was used because it included signal conditioning features such as: *0-offset*, whereby the waveform 0-signal level offset was measured and reduced to the true 0-point on the y-axis; waveform smoothing for FFT accuracy; and arbitrary selection of waveform time boundaries. As such, the three temporal regions of the output waveform from the QD dipole emitter PCA we analysed in the frequency domain as presented in Figure 5.25.

The main pulse is defined as temporal period within Region (i) and the FFT of this is given in plot (a). Region (ii) is the temporal region containing the 'echo' features. Region (iii) is the FFT measured across this entire 'pulse + echo' time period. The FFT power spectrum of all regions are compared in plot (b). It can be seen that the main pulse and echo FFT power spectrum are relatively smooth and exhibit clear absorption features around the expected values from water vapor absorption of the THz beam in the air in the laboratory. The amplitude of the smaller 'echo' signal appears greater than the main pulse here, but the spectra are plotted with a logarithmic y-axis as is usual for such data. As such,

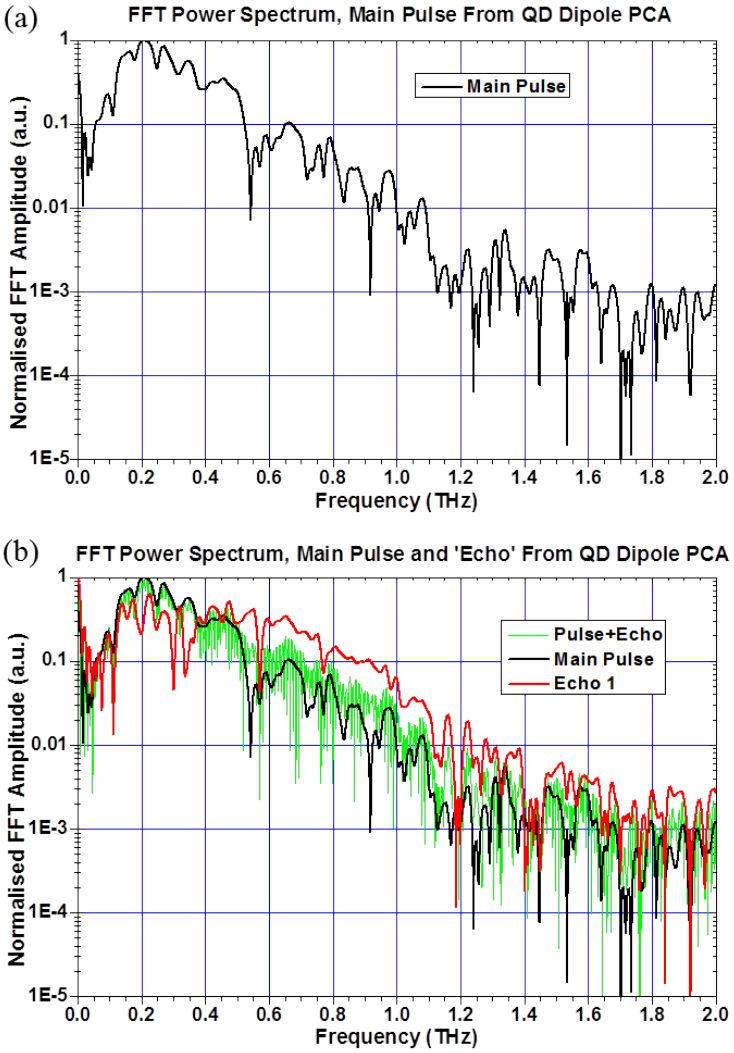

FIGURE 5.25: FFT power spectrum of extracted output signal waveform regions from a 100 μm-long, 10 μm-gap dipole QD (Structure 3) PCA emitter as detected by an LT-GaAs PCA detector showing. (a) shows the power spectrum of the 'main' pulse temporal region only. (b) shows power spectrum from: the main pulse region (black); the secondary 'echo' region (red); and over nearly the entire waveform (green).

the relative *dynamic range* (roughly defined as the bandwidth over which there is a significant difference between the FFT frequency amplitude and the noise floor) is the figure of merit here and it should be noted that the main pulse waveform exhibits a S/N ratio in this plot which is several times greater than the 'echo' signal at most frequencies. The FFT spectrum of the entire pulse and echo period (region [iii]) exhibits the jagged and noisy profile which are also observed in Figures 5.23(b) and 5.24(b). This spectrum is essentially the resultant FFT of all ultrafast processes in the PCA behaviour, combined with

the detected echoes and all such parasitic waveform effects. As such, to obtain an accurate frequency power spectrum from these particular QD PCA devices, the temporal range of analysis from signal outputs should be chosen so as to avoid such artificial features. Additionally, more careful methods of Si lens mounting should be employed in future – these calculations potentially demonstrate the extent of the effect on final THz spectral measurements which may be caused by improper device mounting.

With this in mind, measurements were made by taking temporal scans of THz output signals over periods corresponding only to the 'main' pulse. Examples of such measurements are given in Figures 5.26 and 5.27. This is the main output pulse signal (i.e. 'Region (i)' as before) from a QD-based (Structure 3) dipole PCA pumped by the Ti:Sapphire laser. We can see from the temporal plots inset that there is still evidence of the pulse echo behavior in this sample, but it is somewhat reduced (presumably due to better surface contact between the structure and the Si lens, for example). We observe that over these modest driving conditions a scan of only the main pulse region of the signal will yield a much smoother FFT power spectrum, but some spectral information is lost due to such confinement of the scan [28]. As such, we can see that water vapor absorption features that were previously very clear are now somewhat less distinct. This is an example of the compromise that is typically made between the factors of spectral resolution, S/N ratio, bandwidth and dynamic range [29] (which is a more in-depth evaluation of 'useful' spectral power with respect to bandwidth) when using such data processing techniques [28, 30].

Additionally, we can see from Figures 5.26 and 5.27 that at these 'modest' driving conditions the THz signal waveform and corresponding FFT power spectrum does not vary with either pump power or PCA E-field. With the exception of the signal amplitude, we see that the extracted spectral features and waveform are identical as both the pump power and PCA E-field is increased and this is indicative that the PCA is not being driven to any particularly 'extreme' conditions in this case. It would be interesting to measure such signal data when driving the PCA at both very low and very high optical pump power. However, this would require an even more sensitive detection setup in the former case and additional independent management of the emitter and detector beam powers in the latter case. This is because the Ti:Sapphire pump beam would be split

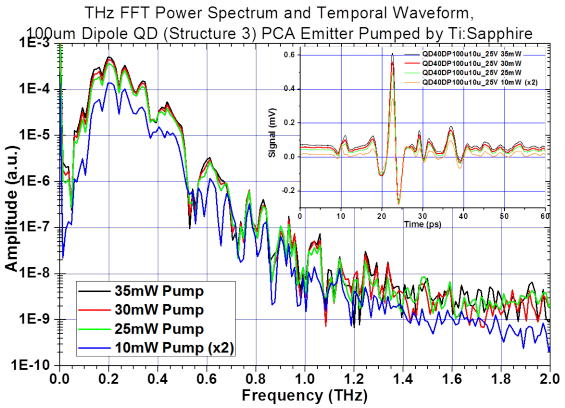

FIGURE 5.26: FFT power spectrum and corresponding output signal waveforms (inset) from a 100 μm-long, 10 μm-gap dipole QD (Structure 3) PCA emitter as detected by an LT-GaAs PCA detector. The PCA is pumped at a different optical power level in each plot.

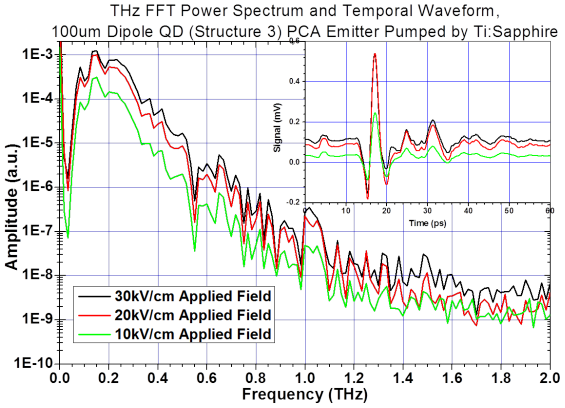

FIGURE 5.27: FFT power spectrum and corresponding output signal waveforms (inset) from a 100 μm-long, 10 μm-gap dipole QD (Structure 3) PCA emitter as detected by an LT-GaAs PCA detector. A different E-field is applied across the PCA in each plot.

into two components, each being several hundred mW in average power, but an LT-GaAs PCA detector in this configuration would saturate and break down when driven at pump beam powers above $\sim 60\ mW$ for an extended period of time. Hence, separate control of the pump power to the LT-GaAs detector in this setup would be needed, which would necessitate the use of an optical filter which may introduce further beam effects before the detector PCA and therefor a disparity between the emitter and detector optical pump signal properties.

5.3.3 Spectroscopy and Materials Testing

The results from the coherent THz TDS system developed in this work were evaluated partly via the comparison of previously obtained experimental and theoretical THz spectral data of various different chemicals and materials. The most convenient comparison could be made using the absorption spectrum of water because the TDS experiments were conducted at room-temperature in air and the water vapour naturally present in the test environment resulted in very clear spectral absorption features. These features were present in each THz spectrum in Figures 5.22-5.24 predominantly at or around frequencies of 0.54 THz, 0.75 THz, 1.1–1.25 THz, 1.4 THz and 1.7 THz (for comparison, see [31, 32]). As discussed in Section 1.2.4.1, absorption features like these are present in a wide range of chemicals, including illicit and explosive materials [33], and identification of such materials for security purposes using THz spectral 'fingerprint' identification like this was part of the motivation for this work. Absorption of EM waves in different chemicals at THz frequencies primarily results from resonant frequency absorption via molecular rotational transitions in vibrational ground- and/or excited-states, and so different chemicals may be identified 'at a glance' by examining the broadband transmission (reflection) spectrum as a THz beam is passed through (reflected from) it.

Another main motivation was to develop a practical and efficient, ultra-compact THz spectroscopy system for use in biomedical applications, such as the identification of cancerous cells in human tissue [34, 35]. During TDS system testing, there were several biologists within the research group (Scott Palmer and Dr Sergei Sokolovski) who were interested in the comparison and distinction of cancerous cells from healthy tissue. Although the THz TDS system presented here was of high accuracy and resolution, the implementation of a TDS method is not as trivial as simply passing the THz beam through the sample. Many elements and parameters must be calibrated and configured, such as: knowledge and selection of sample volume/thickness; estimate of expected frequency-dependent absorption coefficient(s); and the consequential necessary THz frequencies and power levels for adequate spectral distinction of different chemicals. Nevertheless, several THz TDS experiments were conducted using the Ti:Sapphire pump laser and QD-emitter/LT-GaAs-detector – partly as a demonstration of the novel QD-based transceiver system and also with the aim of potentially identifying the

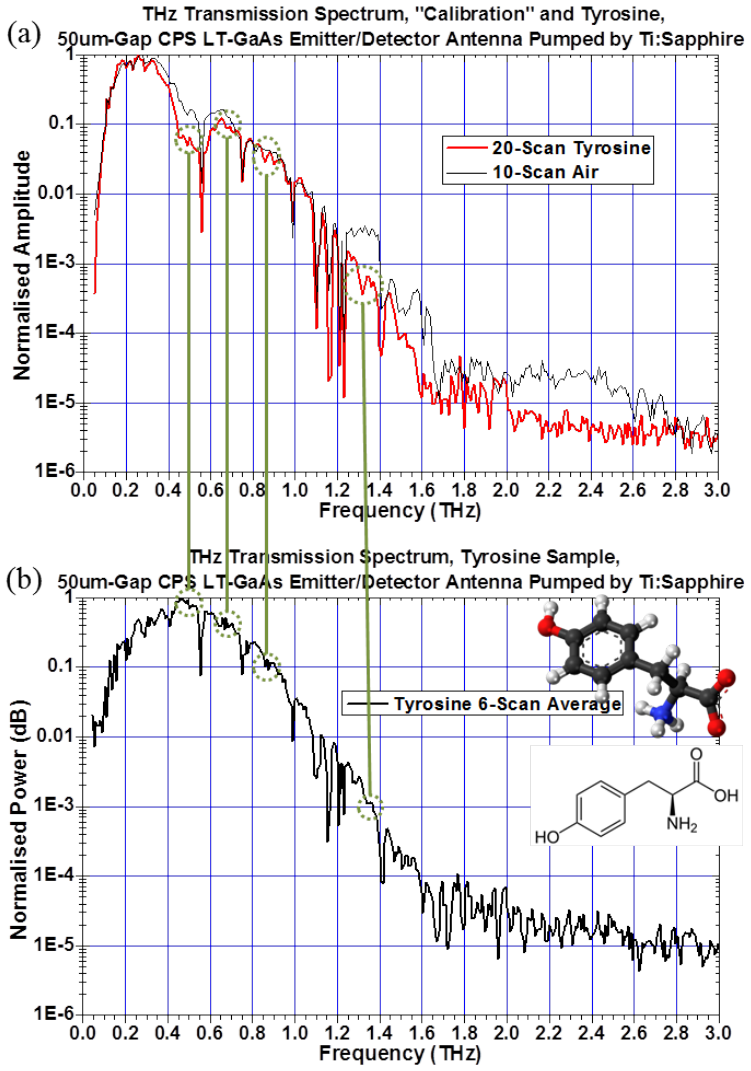

FIGURE 5.28: THz TDS transmission spectrum measurements from calibration tests of: (a) air and tyrosine; and (b) tyrosine after sample re-preparation and using multiple averaged complete scans. Skeletal formula and ball-and-stick molecular representation of tyrosine are also shown in (b,inset).

spectral fingerprint of tumorous cells. Some exemplary data from these tests are given in Figures 5.28 and 5.30.

These were the first reliable calibration TDS measurements taken of chemicals other than water vapour in air, and was conducted using both LT-GaAs CPS PCA emitter and detector pumped by the Ti:Sapphire laser. Tyrosine is an amino acid used by cells to synthesize proteins and can also be synthesized in the body from phenylalanine. It is found in many high-protein food products such as meat, cheese, nuts and seeds and is a polar molecule – making this common chemical a suitable choice as a calibration sample. For this reason, THz absorption spectrum

of tyrosine has been measured previously [36] and established results such as these were used as a reference for the accuracy of our measurements. The calibration method here was simple – to examine the obtained THz spectrum for evidence of absorption features which were not present in the 'air-only' spectrum, specifically at the frequencies of $\sim 0.53\ THz$, $\sim 0.66\ THz$, $\sim 0.83\ THz$ and $\sim 1.33\ THz$. Figure 5.28(a) shows the first obtained calibration spectrum that indicated the presence of tyrosine, and the spectral locations where the additional features from absorption in the spectrum are highlighted in the dashed circles.

A lot of preparation was made before the first measurable tyrosine spectral features were observed because the volume of the sample and even the geometry of the pile of dry tyrosine powder and subsequent scattering/refractive effects on the THz beam had to be accounted for and optimised. Finally, a sample was prepared by compacting a $\sim 3\ mm$-thick disk of powder into the sample dish, the system was re-aligned and a 6-scan averaged transmission spectrum was measured, shown in 5.28(b). Again, the expected tyrosine absorption features may just be resolved in the locations marked by the dashes circles. More information on the sample preparation process for these tests is given below. The absorption features of interest marked in both plots were only slight but indeed measurable. This was at least demonstration of function, but it would appear that a clearer THz spectral fingerprint should be taken using either: a thicker or denser powder sample for further absorption of the THz beam; or a higher power/sensitivity system. A plot of the signal temporal waveforms as transmitted through air with and without the tyrosine crushed powder sample in the beam path is shown in Figure 5.29.

This data conveys a lot of information about the sample, in particular the THz absorption coefficient and pulse phase shift through the sample, which can be used to determine the refractive index properties of the chemical at the detectable THz wavelengths. In-depth THz spectroscopic characterisation of chemicals or materials is outwith the scope of this work, but the occurrence and interpretation of these effects is intuitive. The THz beam will normally pass through the experimental setup without the sample in the beam path, so the measured waveform in this case is unimpeded by propagation effects through anything other than air (and maybe not even this, if the setup is enclosed in a dry N atmosphere for example). Once the sample is placed in the beam path, there scan

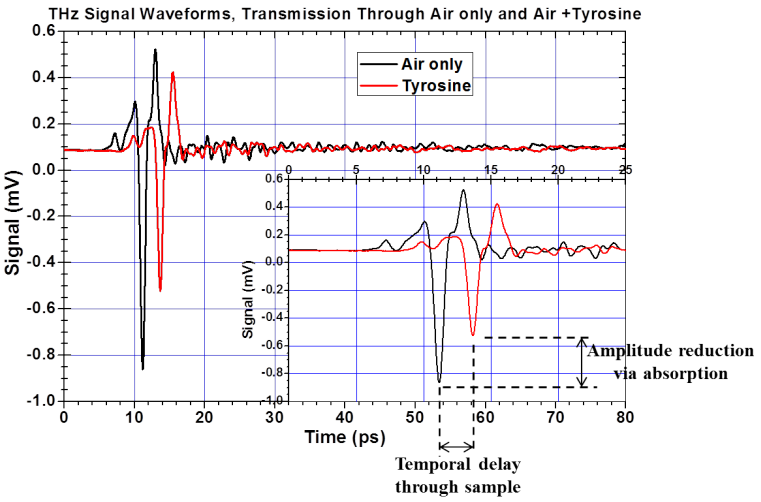

FIGURE 5.29: THz signal waveforms of the beam transmitted through air only (black) or air + tyrosine (red).

is once again made and a delay in the arrival of the pulse is observed. This delay corresponds to a frequency-dependent phase shift which may be measured and the corresponding refractive index over the test THz spectral range may be extracted. This is assisted by analysis of the frequency-dependent reduction of spectral power across the test range, which directly conveys a measurement of the absorption coefficient at the respective frequency.

Further calibration measurements were made using samples of common chemicals such as tryptophan and IPA, and preliminary measurements of cell cultures were even made when their preparation was completed at the biology lab. For this work, HaCaT keratinocyte cells were initially obtained by Sergei Sokolovski from the college of life sciences at the University of Dundee and grown to confluence on 35mm petri dishes (purchased from Becton Dickinson) using Dulbeccos modified Eagle Medium (DMEM) from Invitrogen. HaCaT keratinocytes were also grown to confluence in petri dish with a cover slip in an attempt to keep cells within medium and alive during testing for a longer period. In this case, the cell thickness was around 30 μm, cover slip thickness was 130 μm and the petri dish thickness was ~ 1 mm in all cases. HaCaT cells were also provided in cuvette chambers in suspension in DMEM at concentrations of 1.3×10^5 and 1.3×10^6 per ml. H1299 lung cancer cells were obtained by Dr Sokolovski and either grown to confluence in petri dish or removed from flasks using trypsin and suspended in DMEM to a concentration of 1×10^6. Suspension studies used tyrosine and tryptophan at 1M concentrations. Dry amino acid powders were purchased from

Sigma-Aldrich. Molar calculations were 181 g/L and 204 g/L which translated to 180 mg in 1 ml and 204 mg in 1 ml of tyrosine and tryptophan powder, respectively. 5 g of Amino acids were solubilised in 1 ml ethanol and pressed using petri dish lid to form the compact discs for study.

Some results of these preliminary measurements are shown in Figure 5.30. Plot (a) shows THz transmission calibration scans of air-only, tyrosine and tryptophan samples using an LT-GaAs CPS PCA emitter and detector pair. Plot (b) shows calibration scans of: air and sample holder window only; with petri dish included; with isopropyl alchohol added; and with a sample of cancerous living cells within DMEM medium, all made with the LT-GaAs PCA emitter/detector pair. Plot (c) shows calibration scans of: air-only; tryptophan; and a sample of H1299 lung cancer cells made using a QD (Structure 3) CPA PCA emitter and LT-GaAs PCA detector. All tests mentioned here were done using the Ti:Sapphire laser pump. Again, some additional absorption features are slightly evident in the tyrosine, tryptophan and cell sample spectra – but are not sufficiently beyond the error associated with the signal noise to make a decisive conclusion as to the THz spectral fingerprint of such samples. The demonstration of a THz TDS system based on QD-based PCA emitter devices was considered sufficient for the nature of the goals and research presented in this work.

5.4 Discussion and Conclusion

It should be noted that cell sample and tryptophan calibration tests were made without optimal alignment of the system and before the multi-scan averaging code had been included in the custom TDS system control software. Tests also had to be made over short time-scales – as the live cell cultures could only survive for a limited time in their environment before their nutrient medium dried up – which meant that only fast scans at limited resolution could be made. As such, the S/N ratio of these measurements was not so high, the spectral resolution was relatively poor (12.5 GHz) and a more suitable set of test conditions should be configured to obtain more conclusive measurements. The later improvements in the system sensitivity, speed, spectral range, data conditioning and sample preparation (e.g. thicker/denser cell samples which can live longer in the test chamber) could have yielded much clearer results, which would have been a

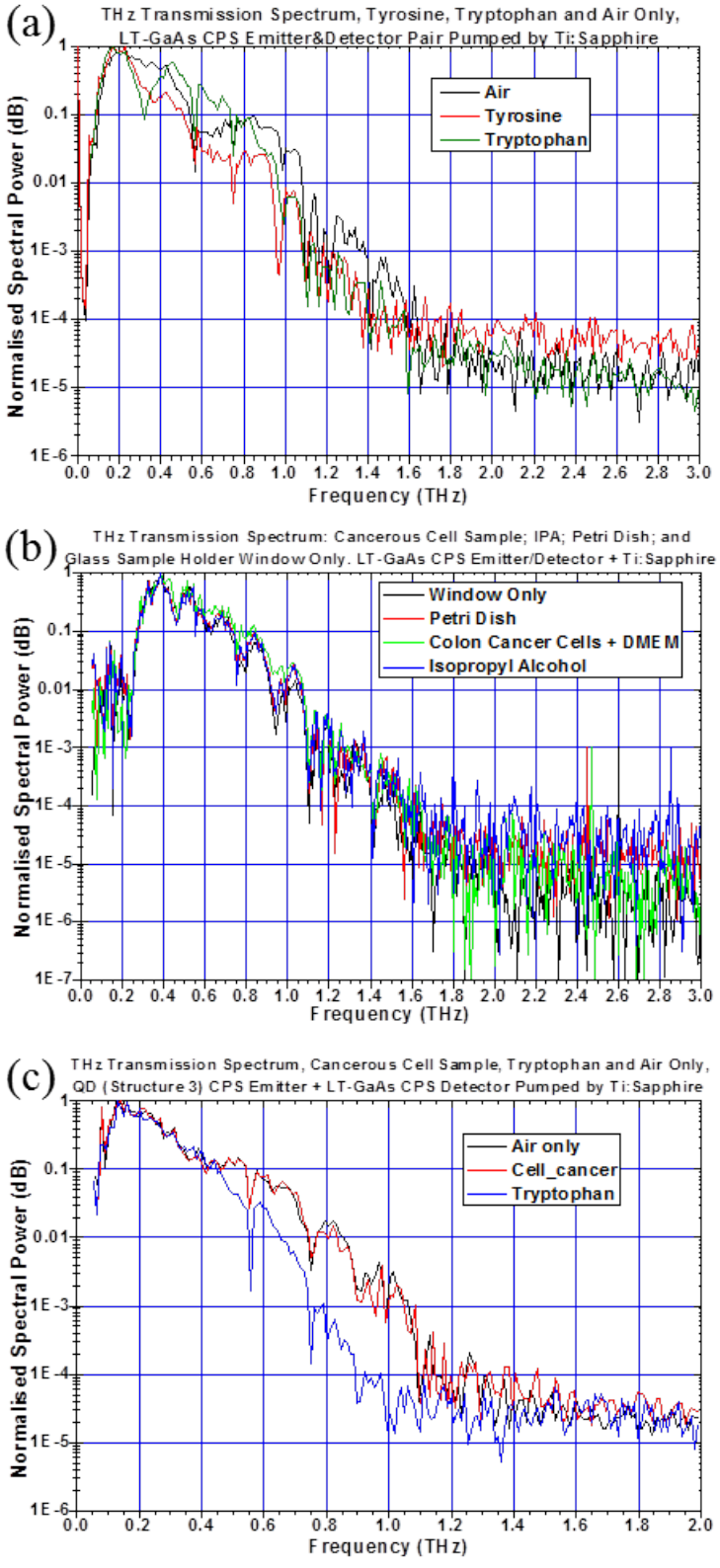

FIGURE 5.30: THz transmission spectrum of: (a) tyrosine, tryptophan and air only using CPS LT-GaAs PCA emitter+detector; (b) cancerous cell sample, IPA, petri dish, and glass sample holder window only using CPS LT-GaAs PCA emitter+detector; and (c) cancerous cell sample, tryptophan and air only using QD (Structure 3) CPS PCA emitter + CPS LT-GaAs PCA detector.

significant result for our THz biophotonics work and so should be the subject of continued work.

The absence of coherent system results taken using QD-based PCA devices as the *detector* element is also evident. It was observed that THz signal waveforms could not easily be distinguished while using QD-based PCAs in this configuration, regardless of the PCA *emitter* type which was used. The reason for this is unclear at present, but could potentially be described by reference to the importance of the lateral E-field in such QD semiconductor structures for ultrafast charge carrier modulation. The photocurrent in the PCA emitter is proportional to the time-varying amplitude of the incoming optical EM wave and the applied antenna E-field; whereas the photocurrent in a PCA detector is proportional to the time-varying amplitudes of the incoming optical EM wave and the THz E-field. The detector PCA must be able to sample each ultrafast EM field by sub-ps modulation of the corresponding electronic response. However, the observed strong dependence on photocarrier modulation speeds in QD structures could mean that the efficacy of the PCA detector is dependent upon the incoming THz field strength, particularly when at relatively low levels.

It should be noted that the the E-fields applied to QD-based PCA emitters in these tests are at comparatively high values compared with that expected of the generated THz E-field propagating between the two PCAs. Therefor, any such low-E-field-dependence of QD photocarrier generation and capture rate was not observed. It is possible that a relatively very high THz E-field is required to facilitate photocarrier modulation on the timescales necessary for accurate coherent THz signal sampling, but further work is required to ascertain this. Alternatively, an 'assisting' E-field across the QD-based PCA detector may be required to enhance carrier transport and allow sub-ps photoconductivity.

Further to this, it is worth discussing the results obtained in preliminary tests of such effects. THz surface emission and picosecond photoconductivity measurements of QD Structure 1 were made by Molis *et al.* [37] at Teravil Ltd and the Center for Physical Science and Technology, both of Vilnius, Lithuania. These tests were based on both coherent signal detection and emission regimes. An amplified Yb-doped potassium gadolinium tungstate (Yb:KGW) laser system (Light Conversion "PHAROS") operating at 1030 nm wavelength with a pulse duration of 160 fs and repetition rate of 200 kHz was the main optical pump

source. This laser was also used to drive a cavity-tuned optical parametric oscillator (OPO, Light Conversion "ORPHEUS") generating 140-160 fs duration pulses with a peak wavelength tunable from 640 nm to 2600 nm, for the purposes of wavelength-dependent probing of the QD structure optoelectronic response. For THz surface emission tests, the QD sample was pumped by the OPO signal and the THz output signal was detected by a sample of pre-characterised LT-GaAsBi, which in turn was pumped using the Yb:KGW beam. To investigate the picosecond photoconductivity of the QD structure, a 90 μm-long, 5 μm-gap dipole microantenna was integrated with the structure surface and this was pumped using the OPO beam. In this case, the QD PCA was used as a detector antenna for THz signals emitted by a pre-characterised p-InAs sample pumped by the Yb:KGW beam. The system schematic and preliminary results of these tests are given in Figure 5.31.

This figure describes the variation of the relative: ultrafast photoconductive response to incoming THz fields (as a THz PCA detector); THz output signal field amplitude (as a THz PCA emitter); and PL spectrum as a function of energy, for reference. It can be seen that the electrically biased QD-based PCA detector operates most efficiently as a THz signal detector when pumped around the GaAs barrier and InGaAs wetting layer absorption edges down to $\sim$ 1.3 eV, after which point the response rapidly falls off. The response then increases as the pump energy approaches $\sim$ 1.12 eV, which in fact corresponds almost exactly to the QD second ES energy as indicated by the PL spectrum shown by the green curve. The response then decays as the pump energy is decreased, but then is observed to recover as the pump energy approaches 1.05 eV. This energy corresponds almost exactly to the first QD ES level. The response then decays effectively to zero as the pump energy is decreased further, indicating no observable response at the QD GS energy. Interestingly, the photoconductive responses near the QD energy levels are most prominent at slightly blue-shifted energies relative to the PL peaks. The THz output signal from this structure is observed to be strongest when pumped at energies corresponding to the GaAs barrier absorption, similarly to the pumping regime involving the Ti:Sapphire laser as presented previously in this chapter. The output signal rapidly falls off as the pump energy decreases below the GaAs band edge, then remains relatively low until the pump energy approaches $\sim$ 1.13 eV. This again appears to occur at slightly blue-shifted energies relative to the second QD ES energy level. The

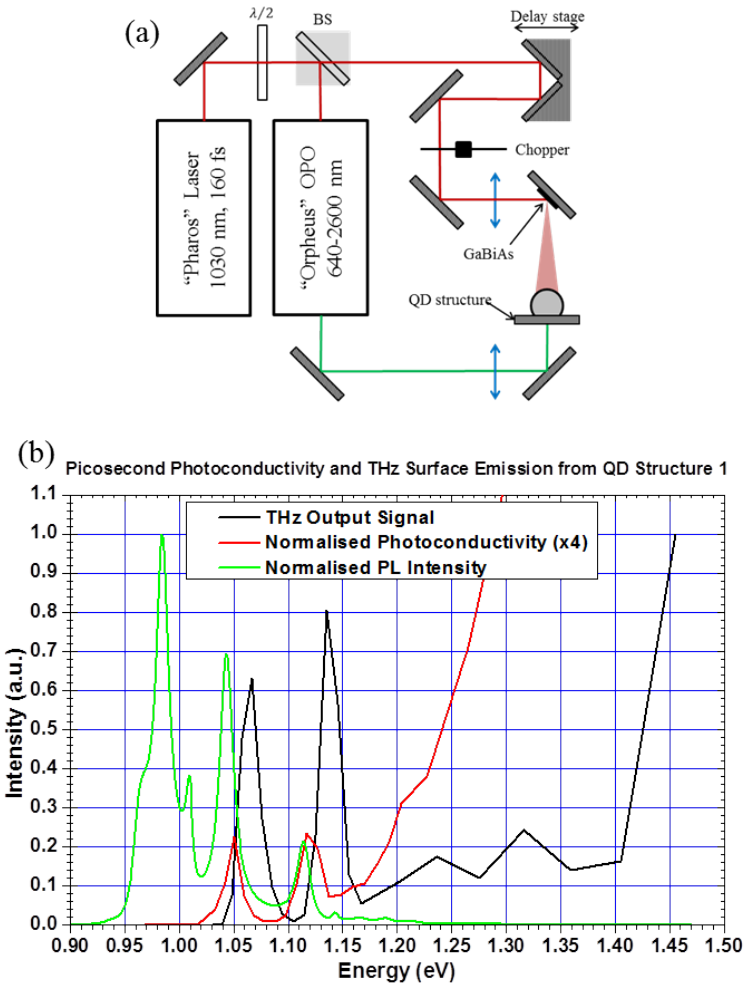

FIGURE 5.31: (a) experimental setup and corresponding (b) THz photoconductivity and emission spectrum measured from QD Structure 1 in wavelength-tunable coherent emission/detection regime using a broadly tunable fs pulse OPO pump source.

output signal again decays as the pump energy is decreased further and recovers as $\sim 1.06\ eV$ is approached, slightly blue-shifted with respect to the first QD ES energy level. Again, no observable output signal was measure when pumping the structure around QD GS energies. These preliminary results are very promising regarding long-wavelength optical pumping and even the potential option of multi-wavelength-range pumping of the same PCA device if implemented in a THz transceiver system. Further work into such systems will include characterisation of the THz output signal waveforms and frequency power spectrum.

Presented in this chapter were results which were taken in the measurement of THz signals generated by QD-based PCA devices pumped by a Ti:Sapphire laser

system. A description was made regarding output power behaviour with respect to input driving conditions such as optical pump power and PCA bias field, including discussion of the important factor of optical-to-THz conversion saturation behaviour. Results were presented from the measurement of the corresponding THz temporal and spectral response from such devices, and demonstrated the preliminary application of QD-based PCAs in a coherent THz transceiver system for spectroscopic analysis of chemicals and living cells. It was found that QD-based THz PCA devices operate comparably with state-of-the-art LT-GaAs PCA devices regarding THz signal output power, and additionally the major advantage of extremely high pump power tolerance and variable output saturation characteristics were demonstrated.

Also discussed were the preliminary results in the measurement of THz signal output from LT-GaAsBi PCA devices pumped by an ultrafast mode-locked QD LD. These results indicated that pumping of such devices for the generation of THz EM fields is demonstrably possible, albeit in this case at very low conversion efficiency. Further tests should be made using a mode-locked LD with much shorter temporal pulsewidth below 1 ps. An improvement in optical-to-THz efficiency for such a configuration would theoretically enable at least a working prototype of an ultra-compact, all-semiconductor, room-temperature THz transceiver system.

Measurements of the THz output signal from a QD PCA device were also presented, which indicates that photomixing in such devices at or near the excited energy level(s) may offer the conversion efficiency required to drive such a system potentially with a 'practical' output power – if some optimisation is made. For example, tests using interdigitated photomixer contacts are still ongoing, and promise further improvements in PC gain and output power.

5.5 References

[1] P.U. Jepsen, D.G. Cooke, and M. Koch. Terahertz spectroscopy and imaging – Modern techniques and applications. *Laser & Photonics Reviews*, 5(1): 124–166, 2011. ISSN 1863-8899. doi: 10.1002/lpor.201000011. URL http://dx.doi.org/10.1002/lpor.201000011.

[2] Joo-Hiuk Son. Principle and applications of terahertz molecular imaging. *Nanotechnology*, 24(21):214001, 2013. URL http://stacks.iop.org/0957-4484/24/i=21/a=214001.

[3] Stanford Research lock-in amplifier systems, 2013. URL http://www.thinksrs.com/products/SR810830.htm.

[4] Arnaldo D'Amico, CorradoDi Natale, FabioLo Castro, Sergio Iarossi, Alexandro Catini, and Eugenio Martinelli. Volatile Compounds Detection by IR Acousto-Optic Detectors. In Jim Byrnes, editor, *Unexploded Ordnance Detection and Mitigation*, NATO Science for Peace and Security Series B: Physics and Biophysics, pages 21–59. Springer Netherlands, 2009. ISBN 978-1-4020-9252-7. doi: 10.1007/978-1-4020-9253-4_2. URL http://dx.doi.org/10.1007/978-1-4020-9253-4_2.

[5] H. D. Drew and A. J. Sievers. A 3He-Cooled Bolometer for the Far Infrared. *Appl. Opt.*, 8(10):2067–2071, Oct 1969. doi: 10.1364/AO.8.002067. URL http://ao.osa.org/abstract.cfm?URI=ao-8-10-2067.

[6] P. L. Richards. BOLOMETERS FOR INFRARED AND MILLIMETER WAVES. *Journal of Applied Physics*, 76(1):1–24, 1994.

[7] QMC THz detector systems, 2013. URL http://www.terahertz.co.uk/index.php?option=com_content&view=article&id=204&Itemid=583.

[8] JamesW. Lamb. Miscellaneous data on materials for millimetre and submillimetre optics. *International Journal of Infrared and Millimeter Waves*, 17(12):1997–2034, 1996. ISSN 0195-9271. doi: 10.1007/BF02069487. URL http://dx.doi.org/10.1007/BF02069487.

[9] J. J. Kuta, H.M. van Driel, D. Landheer, and J.A. Adams. Polarization and wavelength dependence of metal-semiconductor-metal photodetector response. *Applied Physics Letters*, 64(2):140–142, 1994. ISSN 0003-6951. doi: 10.1063/1.111544.

[10] TeraVil photoconductive THz antenna devices, 2013. URL http://www.teravil.lt/emitter.php.

[11] DJHC Maas, AR Bellancourt, M Hoffmann, B Rudin, Y Barbarin, M Golling, T Südmeyer, and U Keller. Growth parameter optimization for fast quantum dot SESAMs. *Opt. Express*, 16(23):18646–18656, 2008.

[12] Tydex Golay cell detector systems, 2013. URL http://www.tydexoptics.com/products/thz_optics/golay_cell/.

[13] Marcel J. E. Golay. Theoretical Consideration in Heat and Infra-Red Detection, with Particular Reference to the Pneumatic Detector. *Review of Scientific Instruments*, 18(5):347–356, 1947. doi: http://dx.doi.org/10.1063/1.1740948. URL http://scitation.aip.org/content/aip/journal/rsi/18/5/10.1063/1.1740948.

[14] C Loata von Gabriel. *Investigation of low-temperature-grown GaAs photoconductive antennae for continous-wave and pulsed terahertz generation.* PhD thesis, 2007.

[15] E. U. Rafailov, S. J. White, A. A. Lagatsky, A. Miller, W. Sibbett, D. A. Livshits, A. E. Zhukov, and V. M. Ustinov. Fast quantum-dot saturable absorber for passive mode-locking of solid-State lasers. *Photonics Technology Letters, IEEE*, 16(11):2439–2441, 2004.

[16] J. Siegert, S. Marcinkevičius, and Q. X. Zhao. Carrier dynamics in modulation-doped InAs/GaAs quantum dots. *Phys. Rev. B*, 72:085316, Aug 2005. doi: 10.1103/PhysRevB.72.085316. URL http://link.aps.org/doi/10.1103/PhysRevB.72.085316.

[17] Y.D. Jang, T.J. Badcock, D.J. Mowbray, M.S. Skolnick, J. Park, D. Lee, H-Y Liu, M. Hopkinson, R.A. Hogg, and A.D. Andreev. Enhanced nonradiative Auger recombination in p-type modulation doped InAs/GaAs quantum dots. *Applied Physics Letters*, 93(10):101903–101903–3, 2008. ISSN 0003-6951. doi: 10.1063/1.2975961.

[18] Edmund Harbord, Peter Spencer, Edmund Clarke, and Ray Murray. Radiative lifetimes in undoped and p-doped InAs/GaAs quantum dots. *Phys. Rev. B*, 80:195312, Nov 2009. doi: 10.1103/PhysRevB.80.195312. URL http://link.aps.org/doi/10.1103/PhysRevB.80.195312.

[19] X. Lu, D.A. Beaton, R. B. Lewis, T. Tiedje, and M.B. Whitwick. Effect of molecular beam epitaxy growth conditions on the Bi content of $GaAs_{1-x}Bi_x$. *Applied Physics Letters*, 92(19):192110–192110–3, 2008. ISSN 0003-6951. doi: 10.1063/1.2918844.

[20] V. Pačebutas, K. Bertulis, G. Aleksejenko, and A. Krotkus. Molecular-beam-epitaxy grown GaBiAs for terahertz optoelectronic applications. *Journal of Materials Science: Materials in Electronics*, 20(1):363–366, 2009. ISSN 0957-4522. doi: 10.1007/s10854-008-9625-1. URL http://dx.doi.org/10.1007/s10854-008-9625-1.

[21] V Pačebutas, K Bertulis, L Dapkus, G Aleksejenko, A Krotkus, K M Yu, and W Walukiewicz. Characterization of low-temperature molecular-beam-epitaxy grown GaBiAs layers. *Semiconductor Science and Technology*, 22 (7):819, 2007. URL http://stacks.iop.org/0268-1242/22/i=7/a=026.

[22] K. Bertulis, A. Krotkus, G. Aleksejenko, V. Pacebutas, R. Adomavicius, G. Molis, and S. Marcinkevicius. GaBiAs: A material for optoelectronic terahertz devices. *Applied Physics Letters*, 88(20):201112–201112–3, 2006. ISSN 0003-6951. doi: 10.1063/1.2205180.

[23] Andrius Arlauskas, Polina Svidovsky, Klemensas Bertulis, Ramūnas Adomavičius, and Arūnas Krotkus. GaAsBi Photoconductive Terahertz Detector Sensitivity at Long Excitation Wavelengths. *Applied Physics Express*, 5 (2):022601, 2012. doi: 10.1143/APEX.5.022601. URL http://apex.jsap.jp/link?APEX/5/022601/.

[24] Ian S. Gregory, Colin Baker, William R. Tribe, I.V. Bradley, M.J. Evans, E.H. Linfield, Giles Davies, and M. Missous. Optimization of photomixers and antennas for continuous-wave terahertz emission. *Quantum Electronics, IEEE Journal of*, 41(5):717–728, 2005. ISSN 0018-9197. doi: 10.1109/JQE.2005.844471.

[25] P. Uhd Jepsen, R. H. Jacobsen, and S. R. Keiding. Generation and detection of terahertz pulses from biased semiconductor antennas. *J. Opt. Soc. Am. B*, 13(11):2424–2436, Nov 1996. doi: 10.1364/JOSAB.13.002424. URL http://josab.osa.org/abstract.cfm?URI=josab-13-11-2424.

[26] Thorlabs NRT100 motorised translation stage, 2013. URL http://www.thorlabs.de/thorproduct.cfm?partnumber=NRT100/M.

[27] Toshiaki Hattori, Satoshi Arai, Keisuke Ohta, Aya Mochiduki, Shin-ichi Ookuma, Keiji Tukamoto, and Rakchanok Rungsawang. Ultrafast semiconductor spectroscopy using terahertz electromagnetic pulses. *Science and technology of advanced materials*, 6(6):649–655, 2005.

[28] Matthias Clemens Hoffmann. *Novel techniques in THz-time-domain-spectroscopy*. PhD thesis, Universitätsbibliothek Freiburg, 2006.

[29] Mira Naftaly and Richard Dudley. Methodologies for determining the dynamic ranges and signal-to-noise ratios of terahertz time-domain spectrometers. *Opt. Lett.*, 34(8):1213–1215, Apr 2009. doi: 10.1364/OL.34.001213. URL http://ol.osa.org/abstract.cfm?URI=ol-34-8-1213.

[30] Timothy D. Dorney, Richard G. Baraniuk, and Daniel M. Mittleman. Material parameter estimation with terahertz time-domain spectroscopy. *J. Opt. Soc. Am. A*, 18(7):1562–1571, Jul 2001. doi: 10.1364/JOSAA.18.001562. URL http://josaa.osa.org/abstract.cfm?URI=josaa-18-7-1562.

[31] T. Suzuki, K. Takayama, S. Yamauchi, Y. Imai, and M. Tonouchi. Measurement of water absorption coefficient using terahertz time-domain spectroscopy. In *Infrared, Millimeter, and Terahertz Waves, 2009. IRMMW-THz 2009. 34th International Conference on*, pages 1–2, 2009.

[32] X. Xin, H. Altan, A. Saint, D. Matten, and R. R. Alfano. Terahertz absorption spectrum of para and ortho water vapors at different humidities at room temperature. *Journal of Applied Physics*, 100(9):094905–4, 2006.

[33] A. Giles Davies, Andrew D. Burnett, Wenhui Fan, Edmund H. Linfield, and John E. Cunningham. Terahertz spectroscopy of explosives and drugs. *Materials Today*, 11(3):18–26, 2008.

[34] Ruth M Woodward, Bryan E Cole, Vincent P Wallace, Richard J Pye, Donald D Arnone, Edmund H Linfield, and Michael Pepper. Terahertz pulse imaging in reflection geometry of human skin cancer and skin tissue. *Physics in Medicine and Biology*, 47(21):3853, 2002. URL http://stacks.iop.org/0031-9155/47/i=21/a=325.

[35] R. M. Woodward, V. P. Wallace, R. J. Pye, B. E. Cole, D. D. Arnone, E. H. Linfield, and M. Pepper. Terahertz pulse imaging of ex vivo basal cell carcinoma. *Journal of Investigative Dermatology*, 120(1):72–78, 2003.

[36] Cecil S. Joseph, Anna N. Yaroslavsky, Munir Al-Arashi, Thomas M. Goyette, Jason C. Dickinson, Andrew J. Gatesman, Brian W. Soper, Christopher M. Forgione, Thomas M. Horgan, Elizabeth J. Ehasz, Robert H. Giles, and William E. Nixon. Terahertz spectroscopy of intrinsic biomarkers for non-melanoma skin cancer. *Proc. SPIE*, 7215:72150, 2009. doi: 10.1117/12.809402. URL http://dx.doi.org/10.1117/12.809402.

[37] G. Molis, A. Arlauskas, A. Krotkus, R. Leyman, N. Bazieva, and E. Rafailov. THz emission spectroscopy of self-organized InAs quantum dot ensembles. In *Infrared, Millimeter, and Terahertz Waves (IRMMW-THz), 2012 37th International Conference on*, pages 1–2, 2012. doi: 10.1109/IRMMW-THz.2012.6380164.

Chapter 6

Summary and Outlook

6.1 Summary of the Work Presented

The work discussed in this thesis represents preliminary investigations into the construction of novel and versatile THz transceiver systems that utilise primary components consisting of QD-based semiconductor devices. This has involved the configuration, testing, calibration and/or programming of a broad range of optoelectronic device production methods and testing systems, as well as the fundamental design of novel PC semiconductor materials and devices. This included the characterisation of suitable ultrafast laser sources, many of which were relatively novel QD LD devices or configurations operating in both/either pulsed and/or CW regimes. The design and production methods for such semiconductor devices were described, including many standard and well-established procedures which are key steps in the fabrication of most optoelectronic devices in general.

Both 'direct' and coherent measurement techniques were used in this work. A major motivation for the work conducted in this project was the development of an ultra-compact, efficient, room-temperature THz source or full measurement system. This, ultimately, may result in the future development of an elegant, efficient and complete THz TDS system based on all-semiconductor elements in an ultracompact housing – which at this time is still a major goal in THz optoelectronics research and industry.

6.2 Future Work and Outlook

The fabrication methods of QD-based semiconductors were also briefly described. MBE was introduced here as it was the method of production for the samples used in this work, but there are other methods such as metalorganic chemical vapor deposition (MOCVD) that have been routinely used in the production of high-quality QD-based semiconductor heterostructures since the mid-1990's [1]. This process is typically less expensive, less complicated and can produce structures of comparable quality to MBE growth methods [2]. The details of this growth method are outwith the scope of this discussion, but it is mentioned here as an example of the widespread fabrication of QD-based semiconductors. This is promising for future work into the optoelectronic properties of such materials and suggests that the further development of ultrafast and THz QD-based devices will continue to be a thriving area of research.

It is the hope of the author that the work presented here will justify the inclusion of QD-based THz transceiver systems as part of this research effort. The implementation of QD LDs as pump sources could be a major step towards this, as these devices would not only enable the use of an ultracompact, electrically-controllable system but would also rapidly increase the scope of data analysis which THz TDS systems are capable of. This is predominantly due to the high pulse repetition rates and low timing jitter of such LDs [3], which could ultimately allow GHz-rate-averaged, real-time THz TDS and data acquisition and analysis through techniques such as ASOS [4]. This method is based on the principle of using two lasers with offset repetition rates as the emitter-detector pump delay mechanism, and would be especially suited to high repetition-rate mode-locked LD pump devices. The key future steps in the further development of such systems now lie in the further investigation and optimisation of QD-based THz PCA structures and devices, particularly with regards to their compatibility with QD LDs as optical pump sources.

The concepts and results discussed in this work has somewhat emphasised the respective energy-dependent optical and electronic characteristics of QD-based semiconductors for this reason. The tunability of the photonic energies of QD LD output signals and the versatile bandgap-engineering offered by QD-based PC materials and PCS devices presents a broad avenue for exploration of highly

configurable, ultrafast optoelectronic systems. For example, consider that the device structures for both the LDs and the PCAs used in this work may potentially be fabricated on the same epitaxial wafer. This of course would be effective only once an efficient configuration of the QD structure and material properties for both lasing and ultrafast carrier modulation had been designed. In fact, this is already conceivable if we consider that the two-section QD LDs discussed in Section 3.2.2 are based on similar principles. Investigations of such possibilities are now underway, and it seems reasonable to predict that complete transceiver system prototypes may be demonstrated within this decade.

6.3 References

[1] P.M. Petroff and S.P. DenBaars. MBE and MOCVD growth and properties of self-assembling quantum dot arrays in III-V semiconductor structures. *Superlattices and Microstructures*, 15(1):15, 1994. ISSN 0749-6036. doi: http://dx.doi.org/10.1006/spmi.1994.1004. URL http://www.sciencedirect.com/science/article/pii/S0749603684710044.

[2] Luo Shuai, Ji Hai-Ming, Gao Feng, Yang Xiao-Guang, Liang Ping, Zhao Ling-Juan, and Yang Tao. InAs/InGaAsP/InP Quantum Dot Lasers Grown by Metalorganic Chemical Vapor Deposition. *Chinese Physics Letters*, 30 (6):068101, 2013. URL http://stacks.iop.org/0256-307X/30/i=6/a=068101.

[3] D. I. Nikitichev, Y. Ding, M. A. Cataluna, E. U. Rafailov, L. Drzewietzki, S. Breuer, W. Elsaesser, M. Rossetti, P. Bardella, T. Xu, I. Montrosset, I. Krestnikov, D. Livshits, M. Ruiz, M. Tran, Y. Robert, and M. Krakowski. High peak power and sub-picosecond Fourier-limited pulse generation from passively mode-locked monolithic two-section gain-guided tapered InGaAs quantum-dot lasers. *Laser Physics*, 22(4):715–724, 2012.

[4] Takeshi Yasui, Eisuke Saneyoshi, and Tsutomu Araki. Asynchronous optical sampling terahertz time-domain spectroscopy for ultrahigh spectral resolution and rapid data acquisition. *Applied Physics Letters*, 87(6):061101–3, 2005.

Appendix A

The Opto-InGaAsP Software

The Opto-InGaAsP software is a brute-force calculation tool for the one-dimensional analysis of optical wave patterns through a $In_xGa_{1-x}As$-based semiconductor structure. This program considers the free-space longitudinal wavelength of the incoming optical mode(s) and evaluates the phase-dependent evolution of the mode(s) throughout the pre-set depth of the semiconductor structure. The main purpose of the software is for the design of semiconductor structures with regards to the behaviour of single or multi-modal optical pump beams as applied to PCA or SESAM applications, where the interaction of the optical pump beam with respective semiconductor features within the structure is crucially important.

Presented here are some results generated by a working version of the program. This version can analyse the propagation of any number of optical modes, and will calculate the superposition of them at each spatial calculation step. The spatial resolution of these examples are 1 nm, which also defines the temporal and wave phase resolution and should be more than sufficient for the parameters to be considered in this work. This spatial resolution was chosen somewhat arbitrarily, however, and may be altered to higher or lower values as appropriate.

The goal of the program was to simulate as accurately as necessary the behaviour of the pump beam in the structure, and so parameters including the wavelength-dependent refractive index, absorption coefficient and energy bandgap of every material and layer in the structure were considered. This was done by evaluating the Sellmeier equation for each layer at each wavelength and calculating the corresponding effect on wave phase and amplitude, then superposing this result with

results from all wavelengths. The Sellmeier equation for an $In_{1-x}Ga_xAs_yP_{1-y}$ quaternary semiconductor blend was derived from the commonly-used results of the studies carried out by Nahory *et al.* [1]. Material energy bandgaps are derived using Equation A.0.0.1, and the corrsponding refractive indices are calculated using the Sellmeier Equation A.0.0.2.

$$E_{BG}(x) = 1.425\ eV - x1.501\ eV + x^2 0.436\ eV \tag{A.0.0.1}$$

$$n = \sqrt{A + \frac{B}{1 - \left(C\frac{E_{BG,GaAs}}{\lambda E_{BG}(x)}\right)^2}} \tag{A.0.0.2}$$

This program allowed the arbitrary definition of semiconductor heterostructures composed of $In_xGa_{1-x}As$ layers up to any thickness and the corresponding optical wavelength response over a broad wavelength range covering the entire spectrum of laser systems used in this work, and beyond. An example calculation is given in Figure A.1. This is a simplified model of the propagation of two longitudinal modes at 847 nm and 850 nm through a bulk GaAs structure of depth $> 40\ \mu m$, for the test demonstration of photomixer modelling. Plot (a) shows the superposed down-converted wave beat signal and plot (b) shows the corresponding optical intensity. In this model, the effects of absorption are neglected and a DBR is not present at any point, so we see the phase evolution of the THz beat signal as it propagates for just over 0.5 wavelengths. The plot is scaled to this level so that the smaller oscillating features may be discerned. The free-space THz frequency and wavelength of the beat signal in this case is $1.25\ THz$ and 240 μm, respectively, which corresponds theoretically to a wavelength of $\sim 70\ \mu m$ in GaAs – depending upon the taken value of the refractive index (here $n_{GaAs,1.25THz} \approx 3.4$). Indeed, we observe the half wavelength to be roughly half this value in the simulation.

For comparison, presented in Figure A.2 is a more accurate model of the same simulation which takes absorption into account, and considers a DBR at the 'rear' facet of the semiconductor. The effects of the DBR are negligible in this case, however, as we can observe that the absorption is so strong at these wavelengths the reflected power is ineffectual.

Future iterations of the program will include improved accuracy and versatility by including features such as:

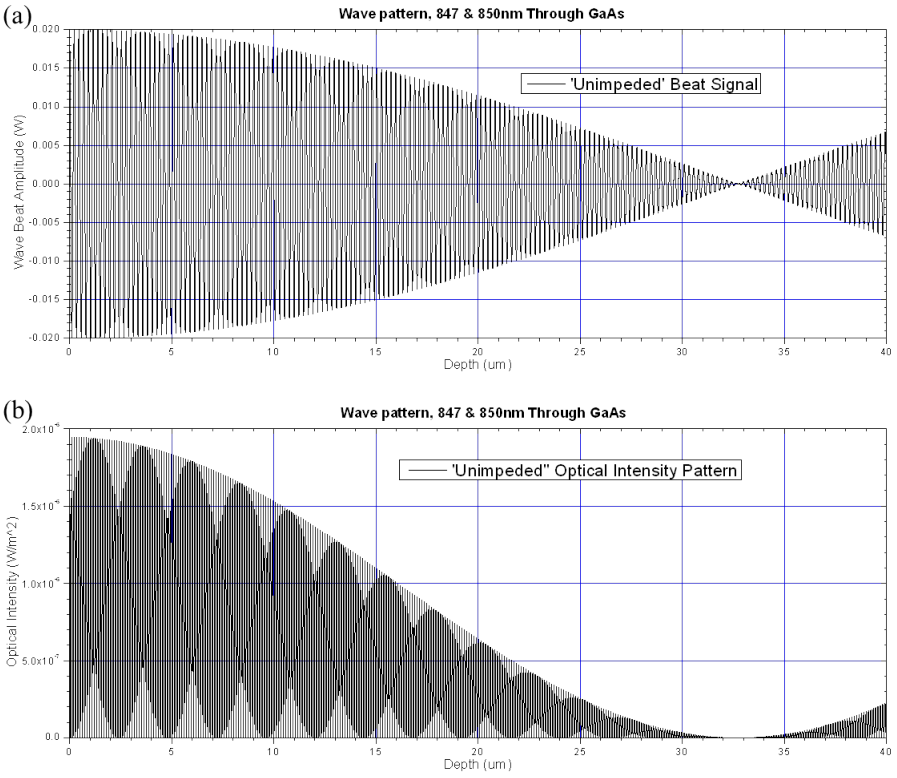

FIGURE A.1: Exemplary simulation results obtained in the modelling of a dual-wavelength (847 nm and 850 nm) pump beam propagating through GaAs bulk semiconductor. (a) shows the superposed down-converted wave beat signal and (b) shows the corresponding optical intensity. In this model, the effects of absorption are neglected and a DBR is not present at any point.

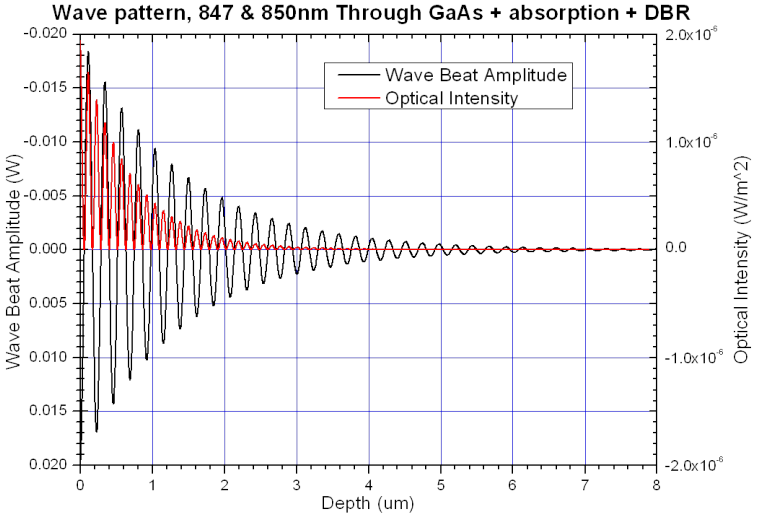

FIGURE A.2: Exemplary simulation results obtained in the modelling of the beat pattern and intensity of the dual-wavelength (847 nm and 850 nm) pump beam propagating through GaAs bulk semiconductor. Absorption effects are considered here, which are considerable.

- Rate equations for the absorptive medium for lasing analysis.
- Customisable DBR structures and simulated reflectivity plots.
- Inclusion of timestep analysis in addition to or instead of spatial/phase step calculation.
- A versatile window-based graphical user interface which allows arbitrary control of resolution and input parameters. Currently the program is a simple DOS-style executable which outputs files containing tables of data formatted for display using Origin graph software.
- Ability to import optical spectrum files for more application-specific analysis of expected optoelectronic performance.
- Extension of the analysis to three dimensions so that beam diameter influence may also be modelled.

The C++ code for this working version of the program is given overleaf.

```
// Heterodyne 5
// First "file-driven" C++ implementation of the InGaAsP optoelectronic mixer program

#include <iostream>
#include <fstream>
#include <sstream>
#include <stdio.h>
#include <cstdio>
#include <cstdlib>
#include <math.h>
#include <string>
#include <conio.h>
#include <stack>

using namespace std;

    const double pi = 3.141569;                 //Double-float defining global variable "Pi"
    const double c = 299792458;                 //Double-float defining global variable "Speed of Light"
    const double Eo = 8.85418782e-12;           //Double-float defining global variable "Permittivity of Free Space"
    double t = 0;                               //Double-float for defining the initial time t of simulation


void beatcalc (double c,double modes[][5],double t,int modenum)  //FUNCTION beatcalc: calculation of optical beat
pattern throughout structure
{
    const double Egaas = 1.425;                 //Define GaAs energy bandgap

    cout << "Beginning of structure:\n";        //Announce structure definition to begin
    cout << endl;                               //

    int rownum = 0;             //Integer which counts the current overall working table row number
    int rowcount = 0;           //Integer which counts the temporary current working row number
    string begsect;             //String for query: next structure section a repeated section?
    string strucend;            //String for query: end of structure definition?
    int repcounter;             //Integer which counts row increments in loops
    int reprowcountstart;       //Integer for storing row # which defines the beginning of repeated section loops
    int reprowcountend;         //Integer for storing row # which defines the end point of repeated section loops
    int repnum;                 //Integer for defining number of layers/materials in a repeated section
    int sectrep;                //Integer for defining number of consecutive repeats of a repeated section
    int i;
    double lamcount = 0;        //Double-float for storing average optical wavelength of modes
    double matdrep;             //Double-float for defining a repeated layer depth in um
    double x;                   //Double-float for defining a layer/material x-composition
    long double n;              //Long double-float for storing corresponding calculated refractive index of layer
    double Ex;                  //Double-float for storing corresponding calculated energy bandgap of layer
    double matdnorep;           //Double-float for defining a non-repeated layer depth in um
    string STRING;
    string DBR;
    double A, B, E, F;
    long double D;
    double V, W, Y, Z;
    long double X;

    for (i = 0; i < modenum; i++)               //Loop for calculating average optical wavelength of all modes
        {                                       //
            lamcount += modes[i][0];            //
        }                                       //
    double lamave = lamcount/modenum;           //Double-float for storing average optical wavelength of all modes

    fstream outfile;                                                        //Define file reference and type
        outfile.open ("Interference.txt", ios::in | ios::out | ios::trunc);       //Define file name and access rights
        fstream sectemp;                                                    //Define file reference and type
        fstream DBRfile;

    for (;;)                                                //Loop for defining and outputting structure details
        {
            int matd = 0;                                    //Integer for storing current material depth
            repcounter = 0;                                  //Reset row counter to 0
```

```
            cout << "Is next layer beginning of a repeated section? (y/n)\n";     //Query: next structure section a
repeated section?
            cin >> begsect;                                 //
            if (begsect == "y")                            //Loop for definition of layers within a repeated section
               {
               sectemp.open ("sectemp.txt", ios::in | ios::out | ios::trunc);     //Define file name and access rights
               reprowcountstart = 0;                       //Store row # for beginning of repeated layer definition
               reprowcountend = 0;                         //Reset end row # for current layer to 0
               cout << "How many different layers in this section?\n";           //Query: number of layers/materials
in this repeated section?
               cin >> repnum;                                                    //
               cout << "How many repeats of this section in the structure?\n";    //Query: number of consecutive
repeats of this repeated section?
               cin >> sectrep;                                                   //

               int secrow = 0;
               int secrowcount = 0;
               for (int i = 0; i < repnum; i++)          //Loop for defining properties of each repeated section layer
               {
                   sectemp.seekg (0, ios::end);
                   cout << "Enter next layer In(x)Ga(1-x)As material x-fraction, 0-1:\n";     //Query: layer/material
x-composition?
                   cin >> x;                                                     //
                   Ex = Egaas-(x*1.501)+(pow(x,2)*0.436);                        //Store layer/material energy bandgap
                   n = sqrt(8.95 + (2.054 / (1 - pow((0.6245*Egaas/(lamave*1e6*Ex)),2)) ));   //Store layer/material
refractive index

                   cout << "Enter material depth, in um:\n";                     //Query: repeated layer depth in um?
                   cin >> matdrep;                          //
                   matd = int(matdrep*1e3);                 //Increment current section depth in nm by [Layer Depth*1000]

                   for (int i = secrowcount; i < secrowcount+matd; i++)   //Loop for writing repeated layer within
section to temp table file
                   {                                                  //depths in nm over current layer depth/distance
                       sectemp << Ex << "\t" << n << "\t" << "0" << "\t" << "0" << endl;      //
                       secrow += 1;
                   }
                   secrowcount = secrow;
               }

               for (int i = 0; i < sectrep; i++)
                   {
                        sectemp.clear();
                        sectemp.seekg(0, ios::beg);      //Seek the pointer to the beginning of the sectemp file
                        outfile.seekg(0, ios::end);      //Move writing position to end of output file "outfile"
                        while(getline(sectemp,STRING))   //Runs through the whole of sectemp until end-of-file. This
                        {                                //     should get each line in sectemp, store into STRING,
                         rowcount += 1;                  //     then write STRING into outfile
                         outfile << rowcount << "\t" << STRING << endl;   //enters STRING into the main output file
                        }
                   }
               sectemp.close();
            }
            Else                                                  //Alternative: non-repeated section definition
            {
                outfile.seekg (0, outfile.end);                   //Move writing position to end of main output file
                cout << "Enter next layer In(x)Ga(1-x)As material x-fraction, 0-1:\n";    //Query: layer/material x-
composition?
                cin >> x;                                                                  //
                Ex = Egaas-(x*1.501)+((pow(x,2))*0.436);                 //Store layer/material energy bandgap
                n = sqrt(8.95 + (2.054 / (1 - pow((0.6245*Egaas/(lamave*1e6*Ex)),2)) ));  //Store layer/material
refractive index

                cout << "Enter material depth, in um:\n";        //Query: non-repeated layer depth in um?
                cin >> matdnorep;                //
                matd = int(matdnorep*1e3);       //Increment current layer depth in nm by [Layer Depth*1000]

                for (int i = 0; i < matd; i++)   //Loop for writing repeated layer within section to temp table file
                    {                            //depths in nm over current layer depth/distance
```

```
                    outfile << i+rowcount+1 << "\t" << Ex << "\t" << n << "\t" << "0" << "\t" << "0" << endl;
                }
            rowcount += matd;
                }

            cout << "Is this the end of the structure? (y/n)\n";          //Query: end of structure definition?
            cin >> strucend;                                              //
            if (strucend == "y")                                          //Exit structure definition loop if all layers are defined
            {                                                             //
               outfile.close();                                           //
               break;                                                     //
            }                                                             //
        }

        cout << "DBR?\n";
        cin >> DBR;
        if (DBR == "y")
        {
                DBRfile.open ("DBRfile.txt", ios::in | ios::out | ios::trunc);
                outfile.open ("Interference.txt", ios::in | ios::out);

                stack<string> lines;
                string temp;
                while(getline(outfile, temp)) lines.push(temp);
                while(!lines.empty())
                {
                DBRfile << lines.top() << endl;
                lines.pop();
                }
                DBRfile.close();
                outfile.close();
        }

        cout << "Evaluating interferometric pattern throughout entire region...";         //Message: beginning beat
pattern calculations
        cout << endl;                                                                     //

        fstream strucbeat;
        fstream DBRbeat;
        strucbeat.open ("Strucbeat.txt", ios::in | ios::out | ios::trunc);
        outfile.open ("Interference.txt", ios::in | ios::out);
        outfile.clear();
        if (DBR == "y")
        {
               DBRfile.open ("DBRfile.txt", ios::in | ios::out);
        }
        double step = 1e9;

        while(outfile >> V >> W >> X >> Y >> Z)
        {
              for (int j = 0; j < modenum; j++)  //Loop for calculation and storage of interference intensity at
current row/depth
                 {
                 //NOTE: absorption coefficient accounted for here only in GaAs @850nm - generalise later
                 modes[j][3] *= exp(-0.001375532612);
                 modes[j][4] += modes[j][1]*X*(1/step) - (2*pi*modes[j][2]*t);
                 Y += modes[j][3] * cos(modes[j][4]);
                 }
              Z = (c*Eo*X/2)*pow(Y,2);
              strucbeat << V << "\t" << W << "\t" << X << "\t" << Y << "\t" << Z << endl;
        }
        strucbeat.close();

        if (DBR == "y")
        {
           DBRbeat.open ("DBRbeat.txt", ios::in | ios::out | ios::trunc);

           while(DBRfile >> A >> B >> D >> E >> F)
           {
```

```
           for (int j = 0; j < modenum; j++)     //Loop for calculation and storage of interference intensity at
current row/depth
                  {
                        modes[j][4] += modes[j][1]*D*(1/step) - (2*pi*modes[j][2]*t);
                        E += modes[j][3] * cos(modes[j][4]);
                  }
           F = (c*Eo*D/2)*pow(E,2);
           DBRbeat << A << "\t" << B << "\t" << D << "\t" << E << "\t" << F << endl;
           }
        }

        outfile.close();

        fstream DBRflip;
        if (DBR == "y")
        {
        DBRbeat.close();
        DBRfile.close();
        DBRflip.open ("DBRflip.txt", ios::in | ios::out | ios::trunc);
        DBRbeat.open ("DBRbeat.txt", ios::in | ios::out);
        stack<string> DBRlines;
        string temp;
        while(getline(DBRbeat, temp)) DBRlines.push(temp);
        while(!DBRlines.empty())
        {
                DBRflip << DBRlines.top() << endl;
                DBRlines.pop();
        }
        DBRflip.close();
        DBRbeat.close();
        }

        fstream resultfile;
        resultfile.open ("Finalcalc.txt", ios::in | ios::out | ios::trunc);
        resultfile << "Depth" << "\t" << "Bandgap" << "\t" << "Index" << "\t" << "Wave Beat Amplitude" << "\t" <<
"Optical Intensity\n";   //Write tab-delimmed table column titles "Depth", “Bandgap”, “Index”, "Wave Beat Amplitude"
and “Optical Intensity”
             resultfile << "um" << "\t" << "eV" << "\t" << "" << "\t" << "W" << "\t" << "W/m^2\n"; //Write tab-delimmed
         column unit headings "um", “eV”, “”, "W" and “W/m^2\n”
        strucbeat.open ("Strucbeat.txt", ios::in | ios::out);
        if (DBR == "y")
        {
           DBRflip.open ("DBRflip.txt", ios::in | ios::out);
        }

        double G = 0;
        while (strucbeat >> V >> W >> X >> Y >> Z)
        {
              if (DBR == "y")
              {
                      DBRflip >> A >> B >> D >> E >> F;
              }
        G = (c*Eo*X/2)*pow(Y+E,2);
        resultfile << V/1e3 << "\t" << W << "\t" << X << "\t" << Y+E << "\t" << G << endl;
        }

        strucbeat.close();
        resultfile.close();
        if (DBR == "y")
              {
                      DBRbeat.close();
              }

    return;
}


int main()                              //Beginning of main program
{
```

```
        string begin;                   //String for query: begin calculations on structure?
        string quit;                    //String for query: quit program?

                int modenum = 2;

        cout << "How many longitudinal optical modes to simulate?\n";
        cin >> modenum;
        cout << endl;

        double modes [2][5];

        for (int i = 0; i < modenum; ++i)
        {
         cout << "Enter vacuum wavelengh of optical pump mode " << i+1 << " in um\n";
         cin >> modes[i][0];                            //modes[][0] are wavelengths
         modes[i][0] = modes[i][0]/(1e6);
         modes[i][1] = (2*pi)/modes[i][0];              //modes[][1] are wavevectors of wavelengths modes [][0]
         modes[i][2] = c/modes[i][0];                   //modes[][2] are frequencies of modes [][0]
         cout << "Enter optical power of pump mode " << i+1 << " in W\n";
         cin >> modes[i][3];                            //modes[][3] are optical powers of modes [][0]
         cout << endl;
         }

         double dcav;                   //Double-float for defining distance modes propagate before entering structure

         cout << "Enter optical cavity length BEFORE analysis region, in um\n";   //Double-float for defining mode
propagation distance before incident on structure
         cout << "This is the distance initially travelled by all modes before reaching the semiconductor surface:\n";
        //This can be useful for external cavity
         cin >> dcav;                                                                    //
         cout << endl;

         cout << "Calculating mode & interference starting conditions...\n";      //Message: beginning external cavity
measurements
         double t = 0;                          //Double-float to define/store starting time in seconds
         for (int j = 0; j < modenum ; j++)     //Loop for calculating optical mode phase(s) upon entering structure
             {
                  modes[j][4] = sin((2*pi*modes[j][2]*t) + modes[j][1]*(dcav/(1e6)));
             }
         cout << "Starting conditions acquired\n";               //Message: finished external cavity calculations
         cout << endl;
         cout << "Begin photomixer structure definition? (y/n)\n";       //Query: begin definition of semiconductor
structure?
         cin >> begin;                          //
         if (begin == "y")                      //If user begin="y" then pass variables to main calculation subsystem
            {                                   //
                  beatcalc(c,modes,t,modenum);  //
            }                                   //

    cout << "Exit program? (y/n)\n";             //Query: exit program?
    cin >> quit;                                                                     //
    if (quit == "y")                                                                 //
    {
       return 0;
    }
}
```

A.1 References

[1] R.E. Nahory, M.A. Pollack, W.D. Johnston, and R. L. Barns. Band gap versus composition and demonstration of Vegard's law for $In_{1-x}Ga_xAs_yP_{1-y}$ lattice matched to InP. *Applied Physics Letters*, 33(7):659–661, 1978. ISSN 0003-6951. doi: 10.1063/1.90455.

Appendix B

The THz TDS Software

The THz TDS software used in this work was developed using LabVIEW. The software has three main functions: to control the movement of the translation stage which forms the basis of the optical beam delay line; to measure the varying THz signal as the delay line is scanned in a coherent antenna setup; and to process the measured data into formats which may be directly examined as performance indicators of the coherent system in general. This software was developed with the help of Dr David Carnegie.

The control of the delay stage is done via the connection between the main computer and the stage actuator unit, the Thorlabs BSC101. The BSC101 supports USB connection, which is used as a port for communication between the unit and computer. Communication between the BSC101 and computer is done through a set of commands which is provided by the manufacturer, and allows continuous two-way control and monitoring of the delay stage location. The monitoring of the corresponding detected THz signal is done via GPiB connection between the SR830 lock-in amplifier and the main computer. Again, a set of commands is provided by the manufacturer which is used to issue commands to the SR830, query measurement values and check the unit status. Monitoring of the THz signal simultaneously with the scanning of the delay line via the BSC101 actuator allows the mapping of THz waveforms generated by the antenna device(s) in the setup. It is possible to do this manually point by point, but automation of this method reduces the complexity and measurement time dramatically while also

improving accuracy, precision and enables real-time data processing during the experiment.

The LabVIEW development environment also allows scope for complete mathematical exploration of the data, manipulation for output formatting, accurately repeated measurements and various averaging methods. Figures B.1–B.3 show the LabVIEW code in a fully operational version of the software. Figure B.1 shows the initialisation section, with each main element highlighted (a-e) and described as follows:

(a) Input parameters such as SR830 and power supply unit GPiB addresses, initial and final stage positions, stage movement increment and number of signal averages ('complete' measurements to take and average over).

(b) Mathematically translate the stage increment to corresponding temporal resolution for reference.

(c) Sets the SR830 signal sensitivity ranges, which are automatically adjusted according to the input signal strength.

(d) Send relevant information to the respective control units.

(e) Set up expected scan durations and reset progress monitor.

Figure B.2 shows the main stage control and signal measurement routines with each main element highlighted (a-i) and described as follows:

(a) Increments the movement of the stage at each step.

(b) Used at the very first data point to stop the stage, 'Auto-phase' the SR830 to to correct chopping phase, and wait for the signal to settle before beginning to measure.

(c) Used as one of the averaging mechanisms, applies a wait time of an integer number of integration periods (such as 100 ms) which the SR830 is set to.

(d) Translates the stage position (in mm) to time (in ps) for the FFT process.

(e) Sets the next incremental stage position to be moved to for the next measurement.

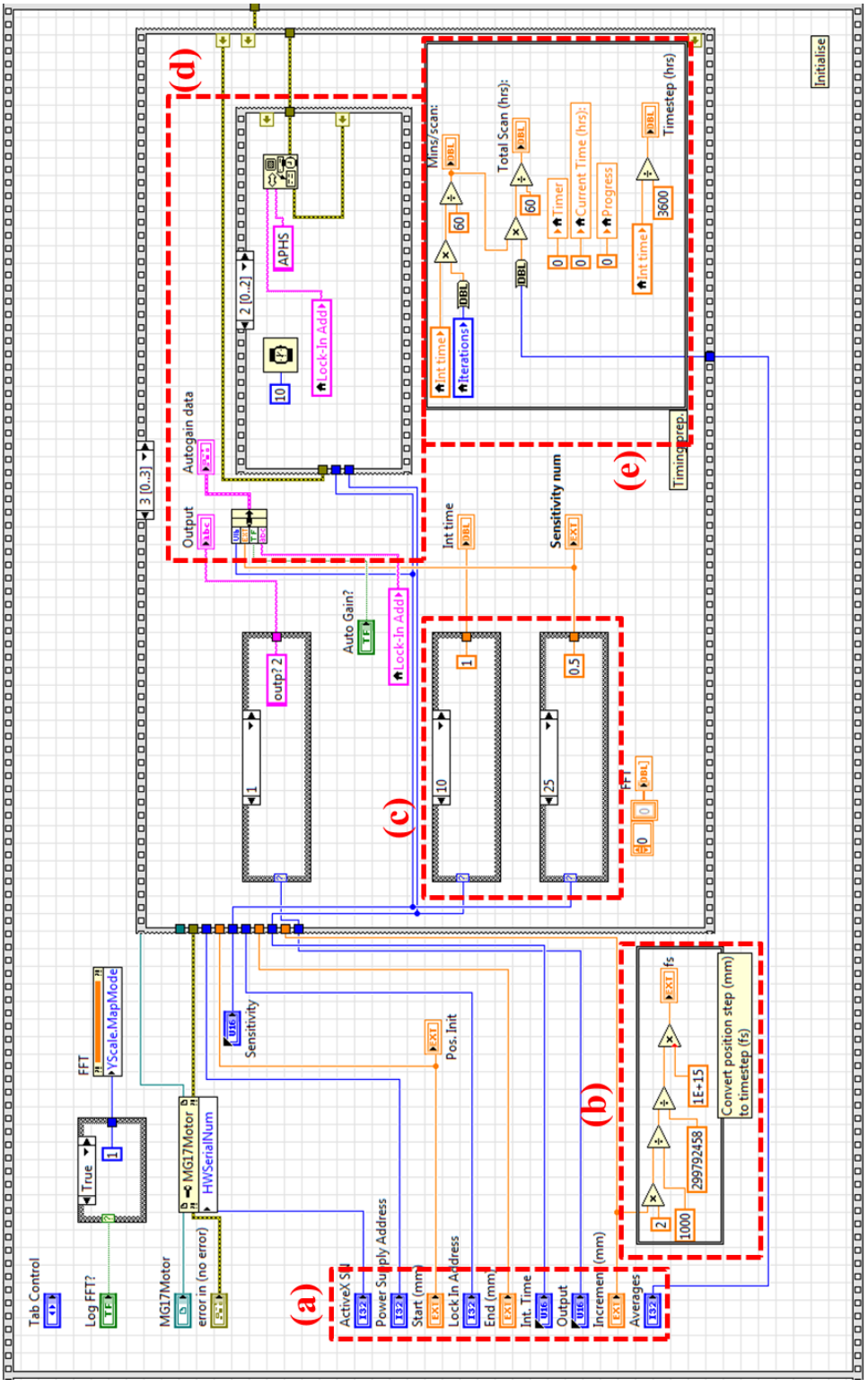

FIGURE B.1: LabVIEW block diagram of the initialisation code of the THz TDS software.

(f) Outputs Time- and Position-vs-Signal waveform graphs to the graphical user interface for reference.

(g) Runs the FFT process on the current Time-vs-Signal data and constantly updates in real-time.

(h) Adds the data from each measurement run to be averaged later.

(i) Outputs the final, averaged FFT power spectrum of the measured signal. The maximum and minimum extent of the x-axis (THz frequency) is set here.

Figure B.3 shows the signal data processing and output routines with each main element highlighted (a-g) and described as follows:

(a) Averages all measured FFT spectra simply by dividing each row value by the pre-set Averaging number.

(b) Compiles the x-axis data for the FFT plot. This takes in the FFT y-values data and uses this is the number of rows. The frequency increment δf in each data point is retrieved from the FFT subroutine in the previous stage and each successive data row is assigned a frequency value of $(row\ number) \times \delta f$.

(c) Averages all measured Time-vs-Signal data.

(d) Corrects the direction of Time-vs-Signal x-axis data. The stage moves the emitter pump beam 'backwards' through the THz signal and so the Time values may need to be reversed and set to 0 at $t = 0$.

(e) Removes the FFT spectrum data which is outwith the user-defined range. For example, the user may only be interested in the spectrum in the range $0 < f_{data} < 3\ THz$ which was usually the case in this work.

(f) Normalised the FFT power spectrum to 1.

(g) Output Time-vs-Signal and FFT spectrum data in tabular format and save to file.

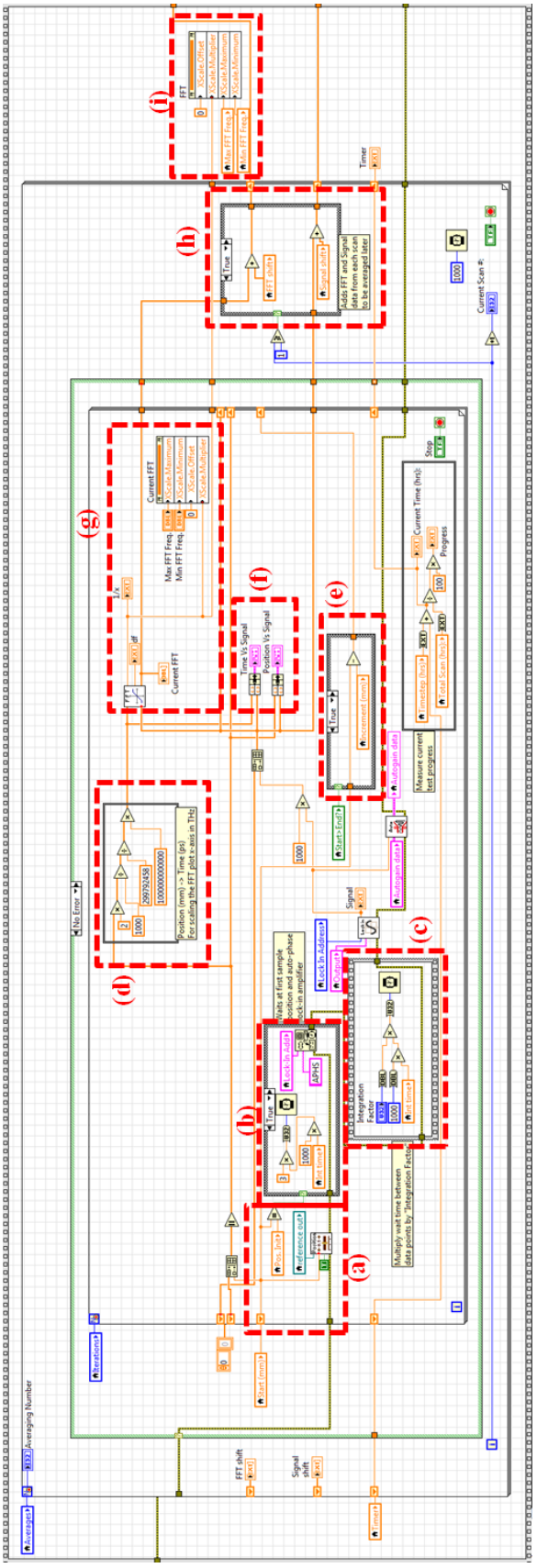

FIGURE B.2: LabVIEW block diagram of the main signal measurement and stage control code of the THz TDS software.

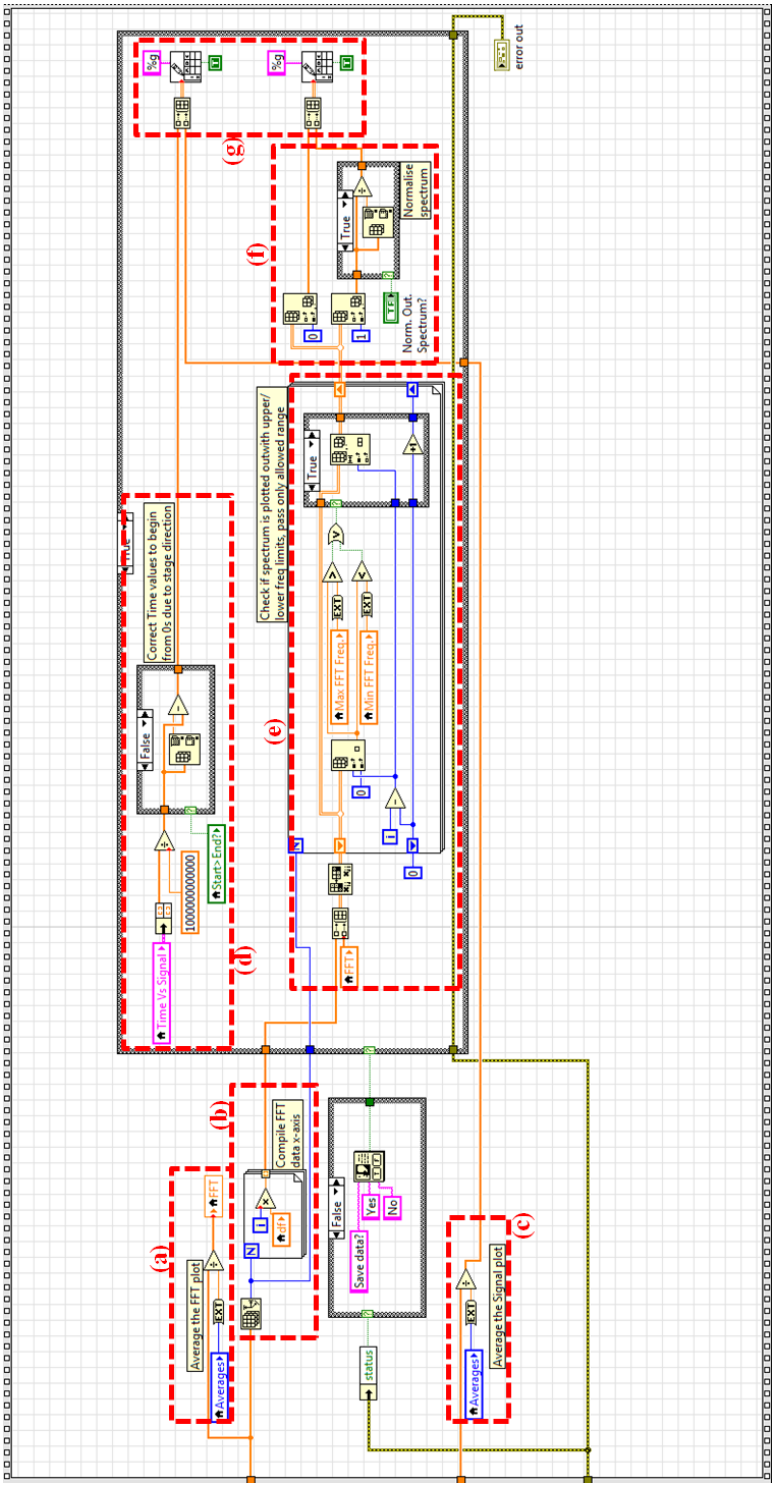

FIGURE B.3: LabVIEW block diagram of the THz signal data gathering, conditioning and output code of the THz TDS software.